Freie Universität Berlin
Fachbereich Physik

Tuning the Interactions of Magnetic Molecules on a Superconductor

Laëtitia Farinacci

Dissertation
zur Erlangung des Grades eines
Doktors der Naturwissenschaften

Berlin, 2019

Diese Arbeit entstand in der Arbeitsgruppe von Prof. Dr. Katharina J. Franke am Fachbereich Physik der Freien Universität Berlin.

Berlin, der 18.12.2019
Erstgutachterin: Prof. Dr. Katharina J. Franke
Zweitgutachter: Prof. Dr. Wolfgang Kuch
Datum der Disputation: 08.06.2020

Abstract

The interplay of magnetism and superconductivity leads to a variety of phenomena whose fundamental understanding is still under research. In this thesis we investigate the properties of the iron-porphine (FeP) molecules on a Pb(111) surface with scanning tunneling microscopy (STM), scanning tunneling spectroscopy (STS) and atomic force microscopy (AFM). A special focus is placed on how their electronic and magnetic properties are affected by their environment and on how to modify these properties by the presence of an STM tip and molecular neighborhood.

First, we characterize the molecular self-assembly of FeP-Cl molecules after sublimation on a Pb(111) surface. We show that by adjusting the sample temperature during and after evaporation one can tune the FeP/Cl ratio on the surface. This leads to the formation of different molecular phases in which the electronic and magnetic properties of the molecules are affected in various ways.

We first focus on the electronic properties of the molecules. We demonstrate that the presence of Cl adatoms leads to the appearance of two different molecular types that have different charge distributions and thereby electronic properties. Interestingly, some molecules display a peculiar feature that can be related to a local gating induced by the tip's electric field. This gating effect is attributed to modifications of image potential states and underlines their importance when considering the energy level alignment at interfaces.

The rest of the thesis is devoted to the study of magnetism and superconductivity. Focusing first on single impurities we demonstrate that by approaching the tip toward a FeP molecule it is possible to modify the magnetic coupling to the substrate and therefore the energy of a Yu-Shiba-Rusinov (YSR) state, allowing for an identification of the nature of the many-body ground state of the system. Furthermore, we tune the system through the quantum phase transition (QPT) on the single impurity level and identify its hallmark characteristics in STS. Finally, this experiment also allows for an identification of the various transport processes that happen through the junction as its conductance increases.

Another aspect of the YSR state is then investigated: the variation of its asymmetry across a molecule. This variation is identical to the one of the phase factor of the Kondo resonance when the substrate is in its normal state. We explain these with local modulations of the electron-hole asymmetry of the scattering of electrons at the impurity level caused by the spatial variations of the frontier orbitals.

Finally we study the coupling of YSR states within a Kagome lattice. By investigating building blocks of this lattice we show the YSR hybridization and discuss its possible origin. Molecular self-assembly is thus a promising alternative to atomic or molecular manipulation in order to engineer well-defined and large systems of coupled impurities. The conditions for the formation of a Kondo lattice in this Kagome arrangement are also discussed.

Kurzfassung

Das Zusammenspiel von Magnetismus und Supraleitung führt zu einer Vielzahl von Phänomenen, deren grundlegendes Verständnis noch erforscht wird. In dieser Arbeit werden die Eigenschaften von Eisen-Porphin (FeP)-Molekülen auf einer Pb(111)-Oberfläche mit Rastertunnelmikroskopie (STM), Rastertunnelspektroskopie (STS) und atomarer Rasterkraftmikroskopie (AFM) untersucht, insbesondere wie die elektronischen und magnetischen Eigenschaften der Moleküle durch ihre Umgebung beeinflusst werden und wie diese durch eine STM-Spitze und die molekulare Umgebung angepasst werden können.

Zu Beginn wird die molekulare Selbstorganisation von FeP-Cl-Molekülen nach Sublimation auf einer Pb(111)-Oberfläche charakterisiert. Wir zeigen, dass man durch Variieren der Probentemperatur während und nach dem Aufdampfprozess das FeP/Cl-Verhältnis kontrollieren kann. Dies führt zur Bildung verschiedener Phasen, welche die elektronischen und magnetischen Eigenschaften der Moleküle auf unterschiedliche Weise beeinflussen.

Zunächst wird auf die elektronischen Eigenschaften der Moleküle eingegangen. Cl-Adatome in der Nähe der Moleküle bewirken das Auftreten von zwei Molekültypen mit unterschiedlichen elektronischen Eigenschaften. Manche Moleküle zeigen interessante Merkmale, die sich auf das lokale Gating zurückführen lassen, welches durch das elektrische Feld der Spitze induziert wird. Dieser Gating-Effekt wird auf Veränderungen der Bildpotenzialzustände zurückgeführt und unterstreicht deren Wichtigkeit bei der Anpassung der Energieniveaus an Grenzflächen.

Der zweite Teil der Arbeit widmet sich der Untersuchung von Magnetismus und Supraleitung. Wir konzentrieren uns zunächst auf einzelne magnetische Störstellen und zeigen, dass es bei Annäherung der Spitze an ein FeP-Molekül möglich ist die magnetische Kopplung an das Substrat und damit die Energie eines Yu-Shiba-Rusinov (YSR)-Zustandes zu modifizieren, wodurch sich die Art des Vielteilchengrundzustandes des Systems identifizieren lässt. Außerdem beeinflussen wir das System durch den Quantenphasenübergang (QPT) einzelner Störstellen und identifizieren seine charakteristischen Merkmale in STS. Mit diesem Experiment lassen sich schließlich auch die verschiedenen Transportprozesse im STM-Kontakt bei zunehmender Leitfähigkeit identifizieren.

Außerdem ist die Asymmetrie der YSR-Zustände von der Position über dem Molekül abhängig. Diese Variation ist identisch mit der des Phasenfaktors der Kondo-Resonanz, wenn das Substrat sich in seinem Normalzustand befindet. Wir erklären diese Variation mit lokalen Modulationen der Elektron/Loch-Asymmetrie der an einzelnen Verunreinigungen gestreuten Elektronen, welche durch die räumlichen Variation der Grenzorbitale zustande kommt.

Schließlich untersuchen wir die Kopplung von YSR-Zuständen innerhalb eines Kagome-Gitters. Durch die Untersuchung der Grundbausteine dieses Gitters zeigen wir die YSR-Hybridisierung und erläutern ihren möglichen Ursprung. Wir zeigen die molekulare Selbstorga-

nisation als eine vielversprechende Alternative zur atomaren oder molekularen Manipulation um große und klar definierte Systeme von gekoppelten Störstellen zu generieren. Die Bedingungen für das Entstehen eines Kondo-Gitters in dieser Kagome-Anordnung werden ebenfalls diskutiert.

Contents

Chapter 1

Introduction

Pinky: Gee, Brain, what do you want to do tonight ?
Brain: The same thing we do every night, Pinky - try to take over the world!

Pinky and the Brain, 1995

Maybe the Brain would have had more success if it had scaled down its goal, or used the correct instruments. When they invented the scanning tunneling microscope (STM) in 1981 [25], G. Binnig and H. Rohrer gave us access to a new world, the atomic world, which Feynman envisioned two decades before in his famous lecture *"There's Plenty of Room at the Bottom"* [53]. The working principle of a STM is intriguingly simple: based on the tunnel effect, a scanning tip "sees" the atoms of a conducting surface in real space. Quite rapidly, the scientific community used this scanning tip not only to see the atoms but also to move and arrange them the very way they wanted, writing a company's name [47] or building small fences for electrons [36]. With a STM, one can exactly control (a very small part of) the world!

But there is more to STM than the exact control of the position of atoms or molecules. Despite, or maybe because of, the apparent simplicity of its working principle, several aspects of the adsorbates and substrates can be observed. Primarily, one measures with scanning tunneling spectroscopy (STS) the electronic properties of a sample. A considerable part of the research done with STM is thus dedicated to the development of nano-devices and towards a fundamental understanding of the quantum effects behind the failure of Moore's law in the last years: the sizes of transistors have reached a limit of a few nanometers, where the quantum nature of electrons cannot be ignored. Beyond electronic properties, one can also detect and characterize magnetic and vibrational fingerprints of substrates and adsorbates with STS by means of inelastic electron tunneling spectroscopy. From a technical point of view, great efforts have been made over the last years in order to combine STM with other measurement techniques. For instance, a combination of STM with X-ray magnetic circular dichroism (XMCD) [195] or Raman spectroscopy [230] allows us to gain chemical sensitivity, while pump-probe [134] and light-emission [145] set-ups as well as terahertz-STMs [34] are used to overcome the limits of time-resolution of STM set by current amplifiers. More recently, electron-spin resonance (ESR) STM [21] has been developed and shown to achieve high energy resolution (in the order of neV) on the atomic scale. With a STM, one can thus observe many aspects of the nanoworld.

These two features, a precise control of the investigated system and a versatility of the measurement technique, make STM an ideal tool for understanding, while not yet ruling, the nanoworld. Indeed, STM is particularly adequate to bridge the worlds of experimental and theoretical research. While the small size of the investigated systems is seen as a challenge for industrial applications, it is particularly suited for testing and confronting the hypotheses of fundamental models.

This thesis revolves around two themes: the energy level alignment of molecules deposited on a metal substrate and the interplay of magnetism and superconductivity. The first aspect is particularly relevant from the experimental point of view. As briefly mentioned above, the miniaturization of electronic devices faces the growing challenge of understanding interface phenomena. More precisely, it has been proposed that molecules serve as building blocks for electronic devices. In order to be contacted, the molecules have to be deposited on some sort of substrate and this often leads, unfortunately, to a modification of their structural and electronic properties. A better understanding of the various effects that can come into play at the interface is thus necessary in order to design functional devices.

The second aspect of this thesis, concerning magnetism and superconductivity, finds its foundations rather on the theoretical side. The ultimate goal of the miniaturization of data storage would be to encode information in the state of a single atom or molecule. For instance, classically, one could use the direction of the spin of an atom or molecule to define a bit: $|1\rangle$ would correspond to spin-up and $|0\rangle$ to spin-down. Yet, since the 1980s, theoreticians have demonstrated the many advantages of quantum computation [54, 22] and experimentalists have been challenged with finding viable systems for its implementation. In a quantum device, the information is stored in a *qubit*; that is a coherent superposition between (at least two) states $a|0\rangle + b|1\rangle$. The computation relies then on the wave nature of the qubits, inducing destructive or constructive interferences to modify the probabilities a^2 and b^2 of finding the qubit in a given state. A major challenge for the use of small bits or qubits in electric devices is to reduce the effects of external perturbations. If one wishes to store information in the spin states of atoms or molecules it is thus of fundamental importance to grasp the nature of their interaction with a metal substrate. A major limitation for the coherence lifetime of a quantum state on a metal substrate is the scattering of conduction electrons. Here again, theoreticians have proposed to circumvent this problem by engineering topologically protected states. Because they are protected by the topology of the system hosting them, these states are immune to local perturbations and qualify as promising candidates to form qubits. Since superconductivity and magnetism can serve as a platform to engineer such a state (a Majorana fermion) [110, 6], magnetic impurities on superconductors have been studied enthusiastically in the last years [86]. Although the fundamental mechanism behind the interaction is relatively well defined (exchange scattering of electrons at the impurities), experimental work is still necessary to characterize and address all aspects of the many-body states induced both by single as well as by multiple impurities.

These different aspects are treated in this thesis with the following outline.

In **chapter 2**, we introduce the working principle of STM and AFM, both from an experimental and theoretical point of view. In order to set a framework concerning the detection of gating phenomena, we propose at the end of the chapter a theoretical model to describe how charging events are detected in STS.

Chapter 3 presents the theoretical background concerning magnetic impurities adsorbed on metal and superconductors. The general description of a magnetic impurity and its interaction with a metallic surface, leading to the Kondo effect, is given. We also give an introduction to conventional superconductivity and the emergence of Yu-Shiba-Rusinov (YSR) states near magnetic impurities.

Chapter 4 shows our experimental results concerning the molecular self-assembly of iron porphine (FeP) molecules on a Pb(111) surface. By sublimating FeP-Cl molecules onto samples held at different temperatures and annealing either the preparations afterwards or not, we show that the FeP to Cl ratio can be adjusted. This leads to different molecular phases that affect the electronic and magnetic properties of the molecules. We give an overview of the various effects in each phase as these are then addressed specifically in the next chapters.

Chapter 5 describes two effects that affect the electronic properties of FeP molecules on a Pb(111) substrate. We show that the presence of chlorine adatoms modifies their electronic states leading to the presence of two different types of molecules. Furthermore, we identify a peculiar feature in STS that is attributed to a gating of the molecular system by image potential states.

The rest of the thesis is devoted to the study of magnetism and superconductivity. In **chapter 6**, we show that one can control the energy of a YSR state by means of a tip approach, allowing for an identification of the ground state of the system. Furthermore, we show that we can drive the system through a quantum phase transition (QPT) at the single impurity level. Finally, we analyze the variety of transport processes that are mediated by a YSR state as the junction conductance is increased.

In **chapter 7**, we study the correlation between the lineshapes of the Kondo and YSR state in STS. This study is performed over iron-tetra-pyridyl-porphyrin (Fe-TPyP) molecules on Pb(111) and we discuss the involvement of its highest occupied molecular orbital (HOMO) and lowest unoccupied molecular orbital (LUMO) in the scattering of electrons onto the magnetic levels. More precisely, we propose that these frontier orbitals effectively locally modify the electron-hole asymmetry of the scattering events.

Finally, **chapter 8** is devoted to the study of magnetic coupling on superconducting and metallic substrates. We demonstrate that when the FeP molecules and Cl adatoms are arranged in a Kagome-honeycomb lattice, the YSR states induced by the FeP molecule hybridize with one another, giving rise to YSR bands. This study demonstrates that molecular self-assembly is a valid alternative for designing large systems of coupled YSR states. The possibility of the formation of a Kondo lattice is also discussed.

Throughout this thesis a particular effort is made to propose models that describe effects which are not yet fully captured by the existing models in literature. Rather than aiming at a perfect description of the complex phenomena we observe, these models are introduced in order to propose other perspectives concerning current research topics, hoping that it will lead to a slightly better understanding of the nanoworld.

Chapter 2

Theoretical and experimental background

Surface science relies on a set of complementary techniques to determine structural and electronic properties of materials and adsorbates. Several techniques, such as angle-resolved photoemission spectroscopy (ARPES), low energy electron diffraction (LEED) and X-ray diffraction, are based on diffraction of electrons or light, giving direct access to the reciprocal space of the surfaces. Such techniques are particularly adequate for the investigation of crystalline and homogeneous samples as they result in non-local averaged quantities. The advantage of scanning probe techniques such as scanning tunneling microscopy (STM) and atomic force microscopy (AFM) is that they grant access to local characteristics of surfaces on the atomic scale. As a result, the specific role of impurities or defects can be addressed and singled out allowing for a more fundamental understanding of interfacial phenomena. In this chapter we present the basic concepts of the latter two techniques. The first section is dedicated to the working principles of a STM and the theoretical fundaments behind its high spatial resolution. In the second section, we show how one can access electronic properties of a sample by means of scanning tunneling spectroscopy (STS). Finally, we give a brief introduction to AFM and emphasize how charging phenomena are detected by both AFM and STS.

I. Scanning tunneling microscopy

In this section we present how the fundamental observable of a STM, the tunneling current, is handled in order to reach atomic resolution and discuss the theoretical background and derivation.

1. Working principle

As its name indicates, the scanning tunneling microscope is based on the tunneling effect of quantum particles: the wave-particle duality of electrons allows them to tunnel through a barrier (*e.g.* vacuum or air) between two materials. In its essence, the scanning tunneling microscope exploits this concept by placing a scanning tip in very close proximity of a conductive sample one wishes to investigate. Under the restriction that both materials are conducting, when the distance between the two is sufficiently small, one can measure

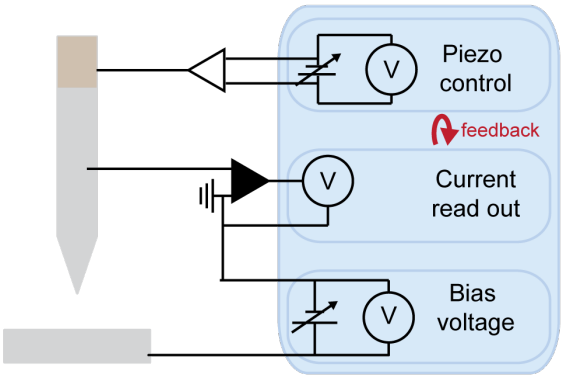

Figure 2.1.: Working principle of a STM. A scanning tip, whose position is controlled by piezoelectric-elements, is placed in very close proximity of a conducting sample. When a bias is applied to the junction, a tunneling current can be measured using a transimpedance amplifier. A feedback loop is commonly used to adjust the tip height in order to keep the tunneling current constant.

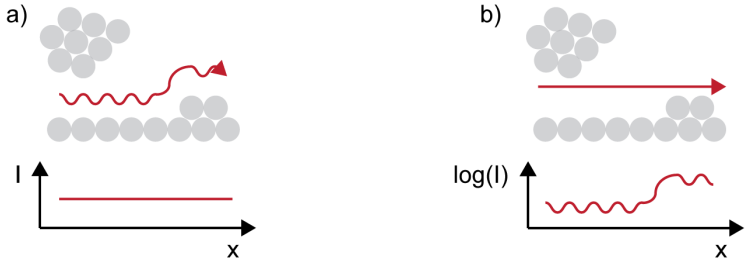

Figure 2.2.: The two scanning modes of a STM. a) Constant current mode: the height of the tip is regulated by a feedback loop in order to keep a constant tunneling current. The sample topography corresponds to these height variations. b) Constant height mode: the height of the tip is not regulated and the corrugations of the sample are directly reflected in the variations of the tunneling current.

a tunneling current (usually in the pico- to nanoampere regimes). Fig. 2.1 illustrates the implementation of this concept.

The position of the tip above the sample is controlled by piezo-elements to which high voltages are applied. A bias voltage is applied to the sample so that a measurable current flows through the junction. Because this current is small, we use an $I - V$ converter to amplify and convert it to a voltage signal. Additionally, a feedback loop is implemented to regulate the tip height in order to keep the current constant.

The tunneling current I depends exponentially on the tip-sample distance d: $I \propto e^{-kd}$, with $k > 0$ being a prefactor (as we show in section I.2). This exponential dependence is at the core of the atomic resolution of the scanning tunneling microscope: a change of tip height by a few Å is observed as a variation of around one order of magnitude of the tunneling current. To record topography images the tip scans line by line a predefined area under one of the two following modes (see Fig. 2.2):

Constant current mode. Via the aforementioned feedback loop, the height of the tip is adjusted such that the tunneling current is kept constant. As the tip scans the area, the variations of the tip height are recorded (the voltage signal sent to the z piezo is converted to the real height variations of the tip) and reflect the topography of the surface.

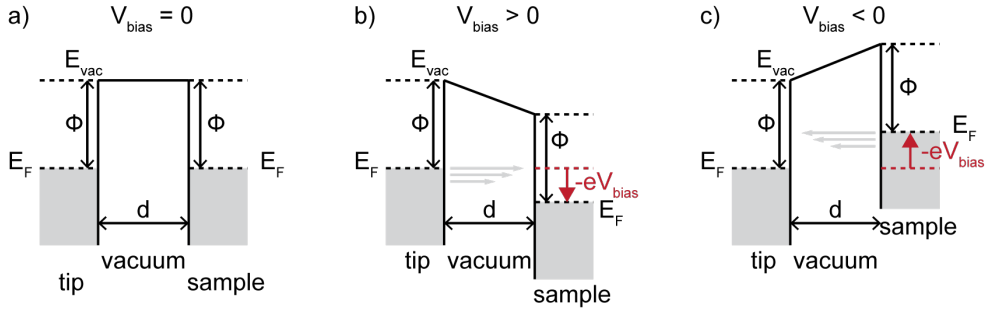

Figure 2.3.: Combined potential and energy diagram of the tunnel junction. The tip and sample are separated by a potential barrier whose width is determined by the vacuum gap and height by the electrodes work functions. a) When no bias is applied, the electrochemical potentials of the tip and sample are aligned so that no net current can be measured. b) A positive bias applied to the sample decreases its electrochemical by $-eV_{\text{bias}}$ which leads to an electron-flow from the tip to the sample. c) Oppositely, a negative bias applied to the sample leads to an electron-flow from the sample to the tip.

Constant height mode. In this mode, the height of the tip is not regulated. The roughness of the sample is detected directly by the variations of the tunneling current. In order to prevent the tip from contacting the surface, this mode is used only once the scanning conditions are stable (piezo creep or temperature changes would cause the tip to drift out of tunnel or into contact) and over pre-defined flat areas.

2. Theory of the tunneling effect

The key quantity probed by a STM is the tunneling current flowing through the junction. We present in Fig. 2.3 a schematic of the energy and potential landscape of such junction. The tip and sample are separated by a vacuum barrier of size d. To first approximation the height of this potential barrier is given by the work function Φ. The electronic occupation in both electrodes, given by the Fermi-Dirac distribution, is approximated by a step-function for simplicity and because of the low temperatures of our experiments (at or below 4.2 K). Classically, the electrons of both electrodes do not have the energy necessary to overcome the potential barrier and can not cross the junction. Yet, electrons are quantum particles and the exponential decay of their wavefunction towards to the vacuum side gives them a finite probability to tunnel through it. If no bias voltage is applied, the electro-chemical potential of tip and sample are equal and no net current is measured (Fig. 2.3a). Applying a bias voltage V_{bias} to the sample shifts the electric potential of its electrons by $-eV_{\text{bias}}$ and allows to measure a net current whose direction depends on the polarity of the bias: a positive bias leads to an electron flow from the tip to the sample (Fig. 2.3b), and a negative one causes an opposite flow (Fig. 2.3c).

We now derive the theoretical framework in which a derivation of the current can be carried out. Fundamentally, the application of a bias voltage through a junction drives the system *tip-vacuum-sample* out of equilibrium and different approaches can be adopted. Traditionally, the tip and sample are considered to be independent and the probability that an electron tunnels from a state ψ_μ in the tip to a state ψ_ν in the sample is given by Fermi's golden rule [20]:

$$T_{\mu\to\nu} = \frac{2\pi}{\hbar}|M_{\mu\nu}|^2\delta(E_\nu - E_\mu - eV_{\text{bias}}), \tag{2.1}$$

where E_μ (E_ν) is the energy of the state ψ_μ (ψ_ν) and $M_{\mu\nu}$ is the tunneling matrix element whose square modulus determines the probability of tunneling through the junction. The delta function accounts for energy conservation: we first consider only elastic tunneling.

By means of Pauli's principle, an electron can only travel from an occupied to an unoccupied state. Neglecting any interaction between the tunneling electrons, the current from the tip to the sample is obtained by considering all possible initial and final states with their occupation probabilities. The net total current flowing through the junction is then the sum of the current flowing from the tip to the sample and of the one flowing from the sample to the tip. We have:

$$I^{t\to s} = \frac{2\pi e}{\hbar}\sum_{\mu\nu}|M_{\mu\nu}|^2 f(E_\mu)[1-f(E_\nu)]\delta(E_\nu - E_\mu - eV_{\text{bias}}) \tag{2.2}$$

$$I^{s\to t} = -\frac{2\pi e}{\hbar}\sum_{\mu\nu}|M_{\mu\nu}|^2 f(E_\nu)[1-f(E_\mu)]\delta(E_\nu - E_\mu - eV_{\text{bias}}) \tag{2.3}$$

$$I = I^{t\to s} + I^{s\to t} \tag{2.4}$$

where f is the Fermi-Dirac distribution function and we considered the tunneling matrix element to be the same for both directions. If we further assume that $M_{\mu\nu}$ only depends on the two states ψ_μ and ψ_ν via their energy, we can replace the summation over all states by integrating them over their energy via the density of states (DOS) of the sample (ρ_s) and of tip (ρ_t). This leads to [7]:

$$I = \frac{2\pi e}{\hbar}\int_{E_\mu}\int_{E_\nu}|M_{\mu\nu}|^2[f(E_\mu)-f(E_\nu)]\rho_t(E_\mu)\rho_s(E_\nu)\delta(E_\nu - E_\mu - eV_{\text{bias}})dE_\mu dE_\nu \tag{2.5}$$

$$I = \frac{2\pi e}{\hbar}\int|M(E)|^2[f(E-eV_{\text{bias}})-f(E)]\rho_t(E-eV_{\text{bias}})\rho_s(E)dE \tag{2.6}$$

The second equation was obtained by evaluating the delta function. The essential problem is then the evaluation of the matrix element $M(E)$, for which we present two approaches. The first approach boils down to the one-dimentional scattering problem of textbooks. Despite its simplicity (it neglects any dependence of M on the wavefunctions of the tip and substrate), it accounts for the main characteristics of the tunneling current. The second approach is based on the work of Bardeen, Tersoff and Hamann who were the pioneers in the field of STM theory.

2.1. The Wentzel-Kramers-Brillouin approximation

In the simplest approach, the STM junction is described as a one-dimensional potential barrier whose width is the tip-sample distance d and height is defined by their work functions, Φ_t and Φ_s, and the applied bias voltage. In the Wentzel-Kramers-Brillouin (WKB) approximation, this trapezoidal shape of the barrier is furthermore approximated by a rectangle of height $\Phi_{\text{av}} + eV_{\text{bias}}/2$ with $\Phi_{\text{av}} = (\Phi_t + \Phi_s)/2$.

The scattering problem is treated by solving the Schrödinger equation in all three regions independently: tip, vacuum and sample. For the sample and tip one uses moreover a free-electron approximation) and it is required that the wavefunctions and their derivatives are equal at the two interfaces. One then obtains for the tunneling matrix element:

$$M(E) \propto \exp(-\frac{2d}{\hbar}\sqrt{2m(\Phi_{\text{av}} - E + eV_{\text{bias}}/2)}) \tag{2.7}$$

Inserting this expression into equation 2.6 with $\alpha(E) = \frac{4}{\hbar}\sqrt{2m(\Phi_{\text{av}} - E + eV_{\text{bias}}/2)}$ leads to:

$$I \propto \frac{2\pi e}{\hbar} \int e^{-\alpha(E)d}[f(E - eV_{\text{bias}}) - f(E)]\rho_t(E - eV_{\text{bias}})\rho_s(E)dE \tag{2.8}$$

In order to simplify this expression we now make use of several approximations. First of all, due to the low temperature of the experiments, the Fermi-Dirac broadening is often much smaller than the spectral features under investigation, we therefore approximate the Fermi-Dirac functions by step functions. The investigated energy range is usually such that $eV_{\text{bias}} << \Phi_s, \Phi_t$, therefore we consider $\alpha(E) \sim \alpha(E_F)$. Finally, assuming that the tip is metallic we can consider that its DOS around Fermi energy is constant: $\rho_t(E) \sim \rho_t(E_F)$. All in all, this leads to:

$$I \propto e^{-\alpha(E_F)d}\rho_f(E_F) \int_{E_F}^{E_F+eV_{\text{bias}}} \rho_s(E)dE \tag{2.9}$$

The tunneling current depends thus indeed exponentially on the distance between the tip and sample. Moreover, one can see from the integral that it is carried by all electrons within an energy range defined by the bias voltage and thus includes the contributions of the sample DOS throughout this energy range.

Here we should mention that the last assumption concerning the tip DOS fails in the case of a superconducting tip, in this case the total current is a convolution of both sample and tip DOS:

$$I \propto e^{-\alpha(E_F)d} \int_{E_F}^{E_F+eV_{\text{bias}}} \rho_s(E)\rho_f(E - eV_{\text{bias}})dE \tag{2.10}$$

Some care has then to be taken when analyzing the different contributions of the tip and sample to the observed features.

2.2. The Tersoff and Hamann approach

The second approach is based on the derivation of the tunneling matrix element by Bardeen [16]. To account for the transfer of electrons through the barrier, Bardeen considers two wavefunctions for the entire system *tip-barrier-sample*: Ψ_0 and $\Psi_{\mu\nu}$ that differ only by the transfer of an electron from a state ψ_μ of the tip to a state ψ_ν of the sample. The wavefunction ψ_μ is a solution of the Schrödinger equation in the *tip-barrier* region but it is not a valid solution in the *sample* region. Similarly, ψ_ν satisfies the Schrödinger equation in the *barrier-sample* region but not in the *tip* region. The transition matrix element $M_{\mu\nu}$ describes therefore the projection of the wavefunction ψ_μ, perturbed by the potential of the sample, onto the state ψ_ν. Bardeen shows then that [16]:

$$M_{\mu\nu} = \frac{\hbar^2}{2m} \int (\psi_\mu^\dagger \nabla\psi_\nu - \psi_\nu \nabla\psi_\mu^\dagger)d\mathbf{S} \tag{2.11}$$

where the integral is taken over any surface that lies entirely within the barrier.

In order to evaluate the transition matrix element, Tersoff and Hamann [211] assumed that the wavefunction of the tip has an s-wave character and is asymptotically spherical. As for the wavefunctions of the surface they are derived consistently with Bloch's theorem along it and have an exponential decay into the vacuum side. Considering, as we did previously, small temperature and voltage, this leads to the following expression for the tunneling current:

$$I \propto \rho_t(E_F) \sum_\nu |\psi_\nu(\mathbf{r}_0)|^2 \delta(E_\nu - E_F) \tag{2.12}$$

where $\mathbf{r}_0$ is the position of the tip (most precisely the center of the sphere it is approximated with). The sum represents the sample DOS at the position of the tip and carries thus the dependency $|\psi_\nu(\mathbf{r}_0)|^2 \propto e^{-2\kappa d}$ where κ is the decay length of the wavefunction. This expression shows therefore the same main characteristics of the tunneling current as in the WKB approximation.

II. Scanning tunneling spectroscopy

The STM is thus a powerful tool to reach atomic resolution. Yet, as we have seen, the tunneling current does not only depend on the tip-sample distance but also carries information about the electronic structure of the sample. In STS, one investigates specifically these electronic properties. We give in this section a brief theoretical and practical introduction to this technique.

1. Working principle

As we have seen in the previous section, the tunneling current involves electrons within the energy range $[E_F; E_F + eV]$. Yet, in order to have more insight into the electronic properties of the sample one would like to measure in a more direct way its DOS at a specific energy. In order to do so, the basic idea of STS is to record the differential conductance, $\mathrm{d}I/\mathrm{d}V$ of the current. Indeed, a derivation of equation 2.6 with respect to the bias voltage yields:

$$\begin{aligned}\frac{dI}{dV} \propto\ & \rho_s(eV_{\text{bias}} - E_F)\rho_t(E_F)\theta(eV_{\text{bias}} - E_F) \\ & + \int_E \frac{d|M(E)|^2}{dV}[f(E - eV_{\text{bias}}) - f(E)]\rho_t(E - eV_{\text{bias}})\rho_s(E)dE \\ & - e\int_E |M(E)|^2[f(E - eV_{\text{bias}}) - f(E)]\frac{d\rho_t}{dE_\mu}(E - eV_{\text{bias}})\rho_s(E)dE\end{aligned} \tag{2.13}$$

where $\theta(x) = \frac{1+(x-1)\exp(x)}{\exp(x)^2}$ is the temperature broadened step function obtained after taking the derivative of the integral over the Fermi-Dirac functions [119].

Here again, we assume that the tip DOS is constant in the energy range of interest, the third term reduces then to zero. As mentioned earlier, this assumption does not hold in the case of a superconducting tip, this case is specifically discussed in the next chapter. Furthermore, if the measurements are performed in constant height and under the assumption of small bias voltages, $eV_{\text{bias}} << \Phi_t, \Phi_s$, the tunneling matrix element can be considered to be constant as well and only the first term remains:

$$\frac{dI}{dV} \propto \rho_s(eV_{\text{bias}} - E_F)\rho_t(E_F)\theta(eV_{\text{bias}} - E_F) \tag{2.14}$$

Therefore the differential conductance obtained at a specific bias is a direct measure of the sample DOS at the corresponding energy. The $\mathrm{d}I/\mathrm{d}V$ signal is recorded via a lock-in amplifier in parallel of the tunneling current, as explained in the next subsection. We now present two types of measurements performed to investigate the electronic structure of a sample.

1.1. dI/dV spectra

A dI/dV spectrum consists in a scan in energy of the sample DOS at a given position in space. The tip is placed above the position of interest with a given current and bias voltage (set point parameters) that determine its height, the bias is then swept through a given range and the corresponding dI/dV signal is recorded. This measurement can be performed under two different modes:

Constant height mode. In this mode, the feedback loop is opened before the bias is swept. In this way, the position of the tip remains the same (i.e. the one defined by the set point parameters) throughout the spectrum and the variations of the dI/dV signal reflect, as we have seen, the sample DOS.

Constant current mode. There, the feedback keeps regulating the tip height to keep the current constant as the bias is swept. This mode is usually used in order to investigate the sample properties at high biases ($|V_{\text{bias}}| \gtrsim 2$ V). Yet, because the tip height changes throughout the spectrum, the tunneling matrix element cannot be considered to be constant and renormalization techniques should be employed in order to compensate for this effect [120, 201].

1.2. dI/dV maps

As we see next, the dI/dV signal can be recorded in parallel of the current channel. In a dI/dV map, one displays the variations of the dI/dV signal at a given bias voltage above an area of interest. Similarly to topography maps, one can choose different mode as for how the tip height is regulated, or not, while scanning.

Constant current mode. In a constant current dI/dV map, the tip height is regulated so that the current measured with the set bias voltage is kept the same. The variations in the tip height thus account for all electronic states at energies between Fermi energy and the bias energy. The dI/dV signal is then a convolution of both tip height variations and sample DOS distribution. dI/dV maps recorded in the constant-current mode are thus prone to artifacts and should be avoided.

Constant height mode. In the constant height mode, the feedback loop is opened and the tip is moved in a plane parallel to the surface plane. To a first approximation, the variations of the dI/dV signal reflect directly the distribution of the sample DOS at the energy of interest. Yet, for the investigation of adsorbates that have a $3D$ character the dI/dVsignal will be more intense above the protruding parts even without an increase of DOS of state above them.

Constant contour dI/dV maps. A way to circumvent the limitations of the constant height mode is to scan each line of an area twice. On the first scan, a topography of the sample is recorded as in a normal constant current scan with a given set point value. On the second scan, the bias is switched to the bias of interest and the tip position is set to follow the height profile of the first scan (with, if needed, an offset). The second scan yields then the dI/dV map. In this way, by choosing set point parameters that are below and far away from any electronic states, one can keep a constant tip-adsorbate distance throughout the investigated area.

Constant dI/dV mode - Iso-DOS dI/dV maps. The constant dI/dV mode is another alternative for the investigation of adsorbates with a $3D$ character. There, the feedback loop regulates the tip height on the dI/dV value. Similarly to topography images obtained in the constant current mode, a dI/dV map is then obtained by displaying the variations in tip height. Special care has to be taken when changing the regulation parameters while switching between the different regulating modes (current or dI/dV). This technique can only be

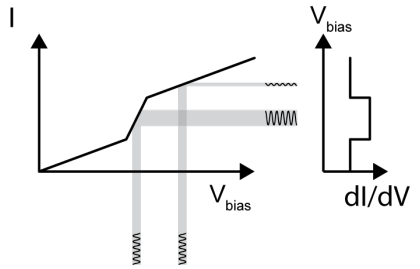

Figure 2.4.: Working principle of a lock-in amplifier. An AC voltage is added to the bias voltage so that higher slopes in $I - V$ curves are reflected in stronger variations of the modulated tunneling current yielding to a first approximation the sample DOS.

applied at energies for which there is a finite DOS above the whole area of interest as it would otherwise lead to a tip crash (it is therefore not usable within the gap of a superconductor for instance). Yet, introduced in [171], it is shown to yield the most accurate results.

2. Lock-in amplifier

As mentioned earlier, the $\mathrm{d}I/\mathrm{d}V$ signal is recorded parallel to the current channel by means of a lock-in amplifier. This technique indeed allows for a much better signal-to-noise ratio as compared to a numerical derivation of the current signal.

As illustrated in Fig. 2.4, a small AC voltage $V_m \sin(\omega_m t)$ is added to the bias voltage so that the tunneling current is now given by:

$$I(V_{\mathrm{bias}} + V_m \sin(\omega_m t)) \propto \int_0^{e(V_{\mathrm{bias}}+V_m \sin(\omega_m t))} \rho_s(E) dE \tag{2.15}$$

Since the amplitude of the modulation V_m is chosen to be small compared to the bias voltage V_{bias} (in this thesis we indicate the root-mean-square of the modulation amplitude by V_{rms}), one can expand the previous expression in a Taylor series:

$$I(V_{\mathrm{bias}} + V_m \sin(\omega_m t)) \approx I(V_{\mathrm{bias}}) + \frac{dI}{dV} V_m \sin(\omega_m t) + \mathcal{O}(V_m^2) \tag{2.16}$$

The second term, or first harmonic of the signal, is proportional to the $\mathrm{d}I/\mathrm{d}V$ signal and can be singled out by the lock-in amplifier. This is done using a mixer that multiplies this signal input by a reference signal $V_r \sin(\omega_r t + \theta_r)$ and thus gives the following output:

$$\begin{aligned} V_{\mathrm{out}} =& I(V_{\mathrm{bias}}) V_r \sin(\omega_r t + \theta_r) \\ &+ \frac{1}{2} \frac{dI}{dV} V_m V_r \cos((\omega_r - \omega_m)t + \theta_r - \theta_m) \\ &- \frac{1}{2} \frac{dI}{dV} V_m V_r \cos((\omega_r + \omega_m)t + \theta_r + \theta_m), \end{aligned} \tag{2.17}$$

where θ_m (θ_r) is the phase of the modulation (reference) signal.

Using a low-pass filter one then keeps only the DC component, which is proportional to the $\mathrm{d}I/\mathrm{d}V$ signal if $\omega_m = \omega_r$. The frequency of the modulation is chosen to be fast in order to have a short acquisition time ($\sim$ms) of the signal. With this technique, the $\mathrm{d}I/\mathrm{d}V$ signal can be measured in parallel to the tunneling current with a good signal-to-noise ratio as only one frequency is picked.

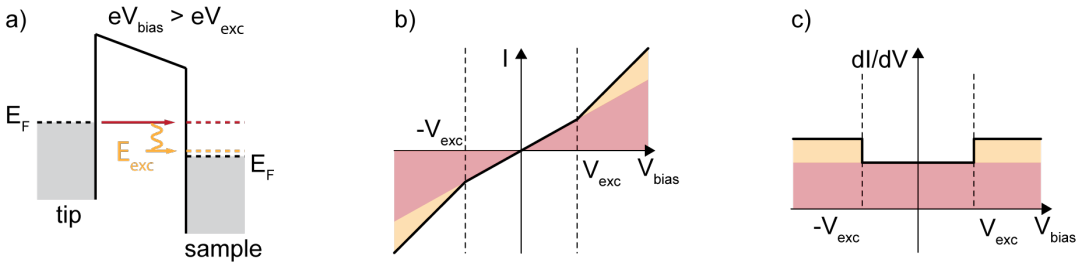

Figure 2.5.: Schematics of inelastic electron tunneling spectroscopy. a) When the energy of the tunneling electrons overcomes a threshold value eV_{exc}, corresponding for instance to a molecular vibration or a spin excitation, they can either tunnel directly through the junction (red path) or lose energy by exciting the system (yellow path). As a result, an additional tunneling path is opened when $|V_{\text{bias}}| \geq V_{\text{exc}}$ which is seen as a slope increase in the $I - V$ curve (b) and steps in $\mathrm{d}I/\mathrm{d}V$ (c).

3. Beyond elastic tunneling and independent electrons

Until now we have considered only elastic tunneling and shown that the $\mathrm{d}I/\mathrm{d}V$ signal was proportional to the sample DOS. We now explain how inelastic processes and interactions within electrons on the sample or tip side can be accounted for and how these are detected in STS.

3.1. Inelastic electron tunneling

In all generality, the tunneling electrons may couple to other degrees of freedom of the system that one wants to investigate: this can for instance be vibrational modes of a molecule or spin excitations for a magnetic impurity [93, 221, 81]. These vibrational modes or spin excitations are characterized by specific energies E_{exc} and detected by inelastic electron tunneling spectroscopy.

The principle of inelastic electron tunneling spectroscopy is illustrated in Fig. 2.5a. Once the bias voltage is high enough so that the energy of the tunneling electrons overcomes a certain threshold energy E_{exc}, these electrons can either tunnel elastically (red path) or lose this energy E_{exc} and bring the investigated system into an excited state (yellow path). In normal tunneling conditions, the system relaxes to its ground state before another electron tunnel through the junction so that effectively, for $V_{\text{bias}} \geq E_{\text{exc}}/e$, two tunneling channels are available for the tunneling electrons: an elastic and an inelastic one. This leads to a sharp increase of the current slope in $I - V$ curve and thus steps in $\mathrm{d}I/\mathrm{d}V$ at $V_{\text{bias}} = E_{\text{exc}}/e$ as illustrated in Fig. 2.5b. The step height in $\mathrm{d}I/\mathrm{d}V$ (or, equivalently, relative slope increase in $I - V$) is determined by the cross-section of the excitation process. The energy of these excitations processes can be used to identify vibrational modes of a molecule [198] or the spin state of a system [84].

3.2. Electron-electron interactions

Implicitly, we have until now neglected any eletronic interaction in the two electrodes. Indeed, we have derived the current as the sum of the amplitude of all processes involving the transfer of an electron from one occupied state on either of the two leads to an empty state on the other side of the barrier. In this description we consider that the energy of the sample or tip with $N \pm 1$ electrons is equal to its energy with N electron plus or minus the one of the state

whose occupation has changed.

Yet, as we show next, in the presence of an impurity spin or a superconductor, correlation effects should be taken into account. In particular, in these systems, the energy of a particle is not necessarily related to its momentum and both degrees of freedom have to be considered. The probability of a particle with an energy $\omega_{\mathbf{p}}$ to have the momentum $\mathbf{p}$ is given by the spectral function $A(\mathbf{p}, \omega_{\mathbf{p}})$. Therefore, considering interactions, the tunneling current is more correctly described by (neglecting the spin degree of freedom) [28]:

$$I = \frac{2\pi e}{\hbar} \sum_{\mathbf{p},\mathbf{q}} |M_{\mathbf{p},\mathbf{q}}|^2 \int \frac{d\omega_{\mathbf{p}}}{2\pi} \int \frac{d\omega_{\mathbf{q}}}{2\pi} [f(\omega_{\mathbf{p}}) - f(\omega_{\mathbf{q}})] A_t(\mathbf{p}, \omega_{\mathbf{p}}) A_s(\mathbf{q}, \omega_{\mathbf{q}}) \delta(\omega_{\mathbf{p}} - \omega_{\mathbf{q}} + eV_{\text{bias}}) dE \tag{2.18}$$

where $\omega_{\mathbf{p},\mathbf{q}}$ are energy variables to integrate over and $A_t(\mathbf{p}, \omega_{\mathbf{p}})$ ($A_s(\mathbf{q}, \omega_{\mathbf{q}})$) the spectral function of the tip (sample).

The transfer of an electron is thus to be understood as the probability to create a hole with given energy $\omega_{\mathbf{p}}$ and momentum $\mathbf{p}$ in one of the two leads and to create an electron with energy $\omega_{\mathbf{q}}$ and momentum $\mathbf{q}$ in the other lead. The contribution of this process to the current is weighted by the square modulus of the transition matrix element between the two different states.

In the absence of any interaction one can show that: $A(\mathbf{p}, \omega_{\mathbf{p}}) \propto \delta(\omega_{\mathbf{p}} - E_p)$ where E_p is the single-particle eigenenergy of the material. The spectral function reproduces the DOS of the material.

When the interactions are small, a perturbative approach can be adopted: it is for instance done in [208] for the scattering of electrons onto a magnetic impurity. Yet, often, strong electron correlations occur and cannot be captured within perturbation theory. In these cases, the scattering events are generally described within the framework of Green's functions [189]. These allow to consider infinite sums of scattering events of all orders and are used to determine the spectral function of many-body systems such as for the Kondo effect, as discussed in the next chapter.

III. Atomic force microscopy

The last two sections described how an STM can be used to achieve a high spatial resolution and investigate the electronic properties of a sample. Here we present a related technique, AFM, with which it is possible to investigate non-conducting materials. We use it in combination with STM in order to gain information about the forces acting between the tip and sample and thereby also about the charge distribution across the sample.

In an AFM, the tip is attached to a cantilever that behaves as an harmonic oscillator. As the tip is brought closer to the sample, the forces acting on the tip modify the eigenfrequency of the oscillator and it is this deflection that we measure and investigate in order to gain information about the sample.

An AFM can be operated in two different modes: the contact (or static) mode, in which the tip touches the surface and its deflection is directly measured, and the non-contact (or dynamic) mode, where the tip is kept at a certain distance from the surface [70]. In this mode, the cantiveler is driven at a given frequency with a given driving amplitude. The forces between the tip and sample modify the resonance frequency and thereby oscillation amplitude of the cantilever. In order to gain information about these forces one can then choose between the amplitude modulation and frequency modulation modes. In the amplitude modulation, the excitation frequency and driving amplitude are kept constant (with the

excitation frequency being close to the resonance frequency of the cantilever). The effect of local forces is then detected as a modification of the oscillation amplitude of the cantilever. In the frequency modulation mode, a phase-locked loop is used in order to drive the cantilever always at its resonance frequency. The frequency shift due to the local forces is then measured directly. Similarly, a feedback loop can be used in order to adjust the driving amplitude so that the oscillation amplitude is kept constant. Variations in the driving amplitude give then information about non-elastic deformation within the junction [135, 121, 148, 164].

In this thesis we use a non-contact AFM in the frequency modulation mode. The eigenfrequency of the tuning fork is $f_0 = 40.98$ kHz and we operate it to have oscillation amplitudes of $0.3 - 0.5$ Å. In this way, one stays in the tunneling regime and the STM and AFM can be used simultaneously.

1. Working principle

The tuning fork on which the tip is mounted is considered to be a damped oscillator which we drive by an external force F_D at frequency ω. Its equation of motion is then:

$$m\ddot{z} - 2\gamma m\dot{z} + k_0 z = F_D \cos(\omega t), \tag{2.19}$$

where m is the mass of the tuning fork and tip, γ the damping constant and $F_D = k_0 A_D$ the driving force with amplitude A_D. The damping constant γ is related to the quality factor Q of the tuning fork by $2\gamma = \omega_0/Q$, with $\omega_0 = 2\pi f_0 = \sqrt{k_0/m}$ the eigenfrequency of the oscillator.

The solution of equation 2.19 is an oscillator $z(t) = A(\omega)\cos(\omega t - \phi(\omega))$ whose amplitude and phase shift depend on the driving frequency ω:

$$A(\omega) = \frac{k_0}{m} \frac{A_D}{\sqrt{(\omega^2 - \omega_0^2)^2 + 4\gamma^2\omega^2}} \tag{2.20}$$

$$\phi(\omega) = \arctan\left(\frac{2\gamma\omega}{\omega_0^2 - \omega^2}\right) \tag{2.21}$$

At $\omega = \omega_0$, the oscillator is in resonance and one has $A(\omega_0) = A_D \cdot Q$ and $\phi(\omega_0) = \frac{\pi}{2}$.

The quality factor is either determined from the full width Δf_Q of the resonance curve at height $A_Q = A(\omega_0)/\sqrt{2}$ and using $Q = f_0/\Delta f_Q$ or by a linear fit of the slope of the phase shift at resonance that verifies $\frac{d\phi}{d\omega}(\omega_0) = -\frac{2Q}{\omega_0}$.

We now characterize how local forces between the tip and sample, F_{TS}, affect the motion of the cantilever. These forces modify the spring constant of the oscillator and if the gradient of the force is constant over an oscillation cycle (which is approximately true for small oscillation amplitudes) the modified spring constant is [69]:

$$k = k_0 - \frac{\partial F_{TS}}{\partial z} \tag{2.22}$$

The eigenfrequency of the cantilever shifts thus to a new frequency f':

$$f' = \frac{1}{2\pi}\sqrt{\frac{k_0 - \frac{\partial F_{TS}}{\partial z}}{m}} \tag{2.23}$$

For small force gradient with respect to the spring constant, a Taylor expansion gives for the frequency shift:

$$\Delta f = f' - f_0 \approx -\frac{f_0}{2k_0}\frac{\partial F_{TS}}{\partial z} \tag{2.24}$$

The frequency shift is thus directly proportional to the force gradient. In the frequency modulation mode, a phase-locked loop (PLL) adjusts the driving frequency to keep the phase shift at $\pi/2$ and thus the cantilever in resonance. In this way, the frequency shift is directly recorded.

To gain information about the forces acting on the tip one therefore measures the frequency shift as a function of tip-sample distance z. Under the previous assumptions one obtains:

$$F_{TS}(z) = -\frac{2k_0}{f_0}\int \Delta f(z)dz + const. \tag{2.25}$$

If the previous assumptions are not valid as in case of large oscillation amplitudes or strong variations of the force gradient, a more complex but accurate expression has to be used as explained in [185, 68].

2. Forces in AFM

In order to understand what is an AFM sensitive to and how local the measurements are, we now describe the three main types of forces that act on the tip when it is in the proximity of a sample.

Chemical forces

The chemical forces are short-range forces that characterize the interaction between the last atom of the tip apex and the substrate. The interaction is commonly modeled by a Lennard-Jones potential that describes the potential energy of two atoms as a function of the distance z separating them [100]:

$$E_{\mathrm{LJ}} = \epsilon\left[\left(\frac{z_0}{z}\right)^{12} - 2\left(\frac{z_0}{z}\right)^{6}\right], \tag{2.26}$$

where ϵ is the depth of the potential well at the equilibrium distance z_0.

At large distances, the interaction (shown in blue in Fig. 2.6a) is attractive as the second term, caused by van der Waals forces, dominates (long-dashed-blue line in Fig. 2.6a). The van der Waals forces are discussed next and describe the energy gain due to (permanent or induced) dipole-dipole interactions. At short distances, the interaction becomes repulsive (the repulsive contribution is shown as a short-dashed blue curve in Fig. 2.6a) because of Pauli repulsion: as the atoms are brought closer together their electron wavefunctions overlap and since they cannot occupy states with the same quantum numbers, they are forced to occupy states at higher energies.

As one can see in Fig. 2.6a, because of this repulsive component, the force (red curve) and consequently frequency shift (violet curve) derived from 2.26 are non-monotonic. Usually, the Δf measurements are performed only in the attractive regime. Strictly speaking, the repulsive regime starts only from $z \leq z_0$ (grey area in Fig. 2.6a). Yet, the minimum of the frequency shift curve (violet curve) indicates the region in which the repulsive forces starts to become consequent. For simplicity, we therefore use this minimum as the limitation between the attractive regime and the repulsive regime (which is then to be understood as attractive regime in which repulsive forces play a substantial role). In order to reach the repulsive regime without crashing the tip it is often necessary to functionalize the tip so that the interaction with the surface is increased while the tunneling current is kept (relatively) small.

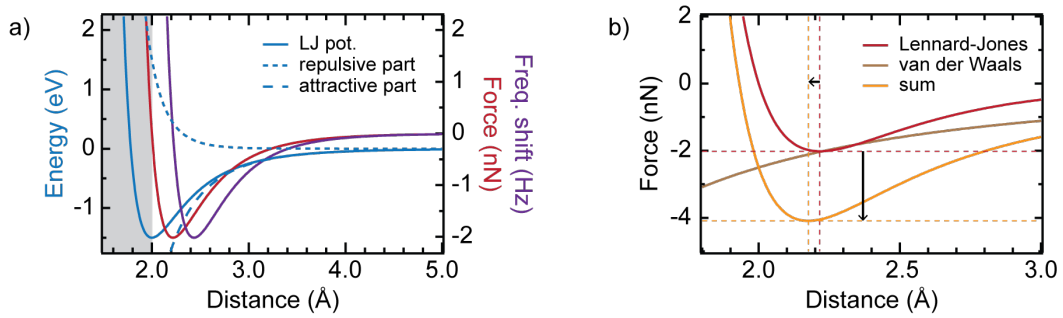

Figure 2.6.: a) Lennard-Jones potential energy (blue curve, we used: $z_0 = 2$ Å, $\epsilon = 1.5$ eV) with its repulsive (short-dashed line) and attractive (long-dashed). The corresponding Lennard-Jones force and frequency shift derived from it are shown along the right axis. The repulsive regime corresponds strictly speaking to the grey area where the force is positive. Yet, for simplicity, we use the minimum of the frequency shift curve to distinguish between the attractive regime and a repulsive regime that is to be understood as the attractive regime in which repulsive forces play a substantial role. b) The presence of van der Waals forces (brown curve) modify the total force (orange curve): compared to the Lennard-Jones force, the minimum of the force curve is shifted to a shorter distance and lower value.

The chemical forces are the only force that have a repulsive component, the repulsive regime is thus commonly used in constant height Δf maps to gain informations about the chemical structure of the investigated system [75].

van der Waals forces

The van der Waals forces arise due to dipole interactions between molecules and atoms. These interactions are classified in three categories depending on the type of dipole that are involved [2]. A Keesom force corresponds to a force acting between two permanent dipole moments. A Debye force describes the interaction between a permanent dipole and a corresponding induced dipole. Finally, the London dispersive force characterizes the spontaneous induction of dipoles moments in molecules that do not have a permanent moment.

The van der Waals potential between two atoms is rather short range and weak ($\propto 1/z^6$). Yet, these forces are additive and due to the mesoscopic nature of the tip and sample they yield a substantial attractive component to the total force. If one approximates the tip by a sphere of radius R at a distance z from the sample which is considered to be infinite, the formula established by Hamaker gives [78]:

$$F_{vdW}(z) = \frac{HR}{6z^2} \tag{2.27}$$

where H is the Hamaker constant that depends on the material. This formula is only an approximation and any modification of the tip shape leads to a different contribution of the van der Waals forces to the total force. The sharper the tip is, the smaller the van der Waals background becomes.

We illustrate in Fig. 2.6b the contribution of the van der Waals forces (brown curve) to the total force (orange curve). As one can see, compared to the Lennard-Jones force (red curve), the minimum of the total force is now shifted to shorter tip-sample distance and a more attractive (lower) value. As a result, if one wants to compare frequency shift values above different positions one should ensure that the tip is exactly the same for the two

measurements and that the contribution of the background van der Waals forces is similar (the two positions should be chosen close to each other). Otherwise, a background correction is necessary [75, 60, 205].

Electrostatic forces

Electrostatic forces are the most long-ranged forces and arise due to the different electrical potentials of the sample and tip. This difference in electrical potential is expressed in term of a voltage $V = V_{\text{bias}} - V_{\text{LCPD}}$ that includes both the bias voltage V_{bias} and the local contact potential difference (LCPD) V_{LCPD} whose origin is discussed in details in the next subsection. The STM junction can be described as a capacitor, the electrostatic force acting between the tip and the sample is then:

$$F_{el} = -\frac{\partial E_{pot}^{cap}}{\partial z} = \frac{1}{2}\frac{\partial C}{\partial z}V^2 = \frac{1}{2}\frac{\partial C}{\partial z}(V_{\text{bias}} - V_{\text{LCPD}})^2 \tag{2.28}$$

where $\frac{\partial C}{\partial z} < 0$ depends non trivially on the shape of the tip. This force depends thus quadratically on the bias voltage V_{bias}, and is minimized when the applied bias compensates the LCPD: $V_{\text{bias}} = V_{\text{LCPD}}$. This is the fundamental idea behind Kelvin probe force microscopy (KPFM) where the measurement of the LCPD is used in order to detect single-electron charging events [197, 217, 112] or probe the charge distribution of a molecule [151, 192].

3. Local Contact Potential Difference measurements

In this section we discuss the origin of the LCPD and present how its measurement yields information concerning the charge distribution of the investigated system.

We consider an isolated tip and an isolated sample, made out of different materials. Their work functions being different, they have different chemical potentials before being connected by a conducting wire or pulled in each others' vicinity (see Fig. 2.7a). Once connected or being close enough to allow for electron tunneling, the electrons will flow from the material with the lower work function to the material with the highest one (see Fig. 2.7b), shifting their chemical potentials with respect to one another (lower graph). Yet this leads to a charge accumulation at the surface of the two metals (Fig. 2.7c). These opposite space charges yield a potential difference, the contact potential difference, and consequently an electric field that tends to push back the electrons toward the material with the lowest work function. The tip being grounded, the LCPD is the electrical potential of the sample. An equilibrium is reached when the electrochemical potentials of the two materials are equal (Fig. 2.7d), or in other words when the difference in the chemical potentials of the materials is compensated by the difference in their electrical potential. Two equivalent pictures can thus be used to describe the energy level alignment at zero bias. The first one, shown in Fig. 2.7e, is the common picture used for instance in Fig. 2.3 that considers that the electrochemical potentials of the tip and sample are equal. The other one is less intuitive but will be instructive in the subsection III.4: there, the states of the tip and sample are occupied up to chemical potentials (blue rectangle) that are misaligned. Yet, because of the LCPD, if the electrons were to tunnel their energy will be affected by the potential energy of the local electric field and this energy shift compensate for the misalignement of the chemical potentials.

As we have seen in the previous subsection, this potential difference yields an electrostatic force that depends quadratically on the bias voltage. Since the frequency shift is proportional to the force gradient it shows the same quadratic dependence:

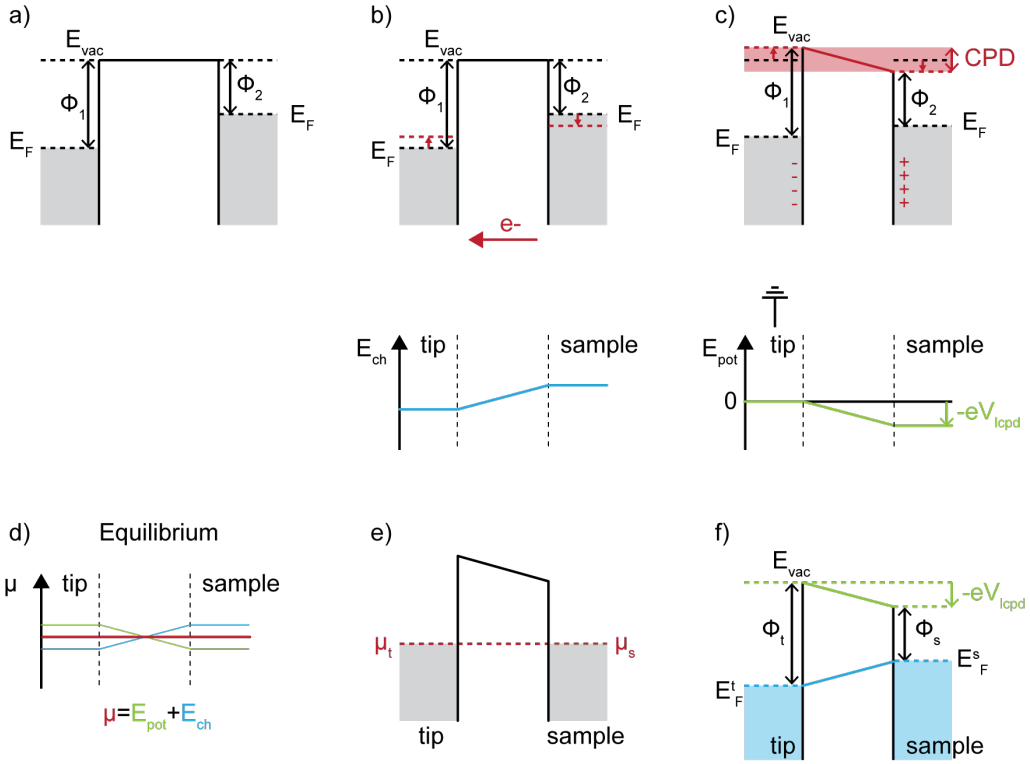

Figure 2.7.: Origin of the LCPD. a) Two different metals far away from each other have different work functions. b) When the distance between them is short enough, electrons tunnel from the material with the lower work function to the one with the higher one. This leads to a shift of their chemical potential potential (lower graph). c) Conjointly, this electron transfer leads to a charge accumulation at the surface of the metals. This yields a local electric field, or equivalently to a Contact Potential Difference (CPD). In the case of an STM, where the tip is grounded, the CPD corresponds to the electrical potential of the sample. d) An equilibrium is reached when the electro-chemical potentials of the two materials are aligned (red line): the chemical (blue) and electrical (green) shifts compensate each other. e) The common picture describes an STM junction with equal electro-chemical potential for the tip and sample. f) Alternatively, one can chose to represent the misaligned chemical potential but with a local electric field.

$$\Delta f(V_{\text{bias}}) = -\frac{1}{2}\frac{\partial^2 C}{\partial z^2}(V_{\text{bias}} - V_{\text{LCPD}})^2 + \Delta f(\bar{z}) \tag{2.29}$$

where $\Delta f(\bar{z})$ is the frequency shift due to all other forces (chemical and van der Waals forces) but the electrostatic one. The frequency shift as a function of bias voltage is thus a parabola, centered at the LCPD value and whose maximum accounts for all forces but the electrostatic ones.

As mentioned previously, the electrostatic forces are particularly long-ranged. In order to resolve the contribution of local charges on the sample, the oscillating tip must be brought in their very close vicinity. This is only achieved thanks to the high stiffness of the tuning fork and its small oscillation amplitudes. The first measurements of the charge state of a single atom was performed in 2009 by Gross et al. for Au and Ag atoms adsorbed on a NaCl layer on Cu(111) [73]. They observed a shift of the frequency shift parabolas for charged species.

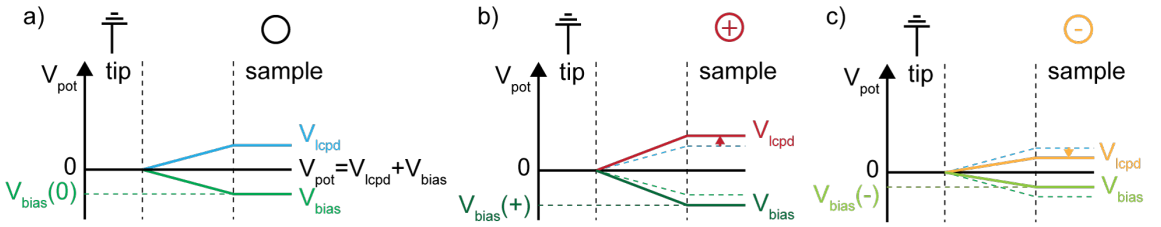

Figure 2.8.: Change of LCPD due to local charging. Compared to a neutral case (a), a positive charge (b) shifts the local potential up, and the LCPD is thus detected at a lower bias voltage. Inversely, a negative charge (c) decreases the LCPD which is seen at higher a bias voltage.

Namely, for both positive and negative charges, the parabolas are shifted to more negative Δf values indicating an additional attractive force. This attractive force is of van der Waals origin as it is caused by a polarization of the tip [73]. Most importantly, they observed that the shift in LCPD, when comparing the charged atom to the neutral one, could be directly related to the charge state of the atom: a positive charge leads to a decrease of the LCPD (i.e. more negative values) and a negative charge to an increase (more positive values), as illustrated in Fig. 2.8.

In general, special care must be taken in order to compare different LCPD values. In a plate capacitor model, the potential drops linearly with distance. As a result, the LCPD should be independent of the tip-sample distance z. Yet, in reality, the tip-shape influences the field lines and thus the LCPD value depends now on the exact shape of the tip and z [159]. Qualitative information is thus obtained by comparing relative changes of the LCPD, recorded with the same tip. Typically, if one wants to compare the charge distribution of two adsorbates, one records the value of the LCPD as a function of tip-sample plane distance z: far away, the LCPD is the same as it is averaged over an area larger than the two adsorbates and closer, contribution from the different adsorbates lead to relative changes in LCPD above the two positions.

4. Detection of charging processes

In order to set the framework in which gating processes are discussed in 5 we now describe how charging events can be induced and detected. Based on the previous section, it is quite straightforward to understand how these can be identified with AFM and we would like here to propose a model in order to explain why and how these are also seen in STS.

In the literature, several works report on the single electron charging or discharging of an atom or molecule. A requirement for such events to happen is the partial decoupling of the atom or molecule from the metal substrate. Typically this is achieved by the presence of a decoupling layer [168, 156, 130] but the presence of a molecular ligand might suffice [52, 113]. The tunneling junction is then described as a double tunneling barrier as sketched in Fig. 2.9. In this model, the decoupling of the adsorbate from the metal surface translates into a finite voltage drop between the two of them when a bias voltage is applied through the junction (Fig. 2.9b and d). As a result, when the bias voltage is swept to negative (positive) values, the energy levels of the adsorbate are pulled to lower (higher) energies with respect to the Fermi level of the substrate, as shown in Fig. 2.9b (Fig. 2.9d). Therefore, when the electric field induced by the applied voltage is sufficient to shift a level across the Fermi energy of the substrate, this one is charged (Fig. 2.9b) or discharged (Fig. 2.9d), depending on the original

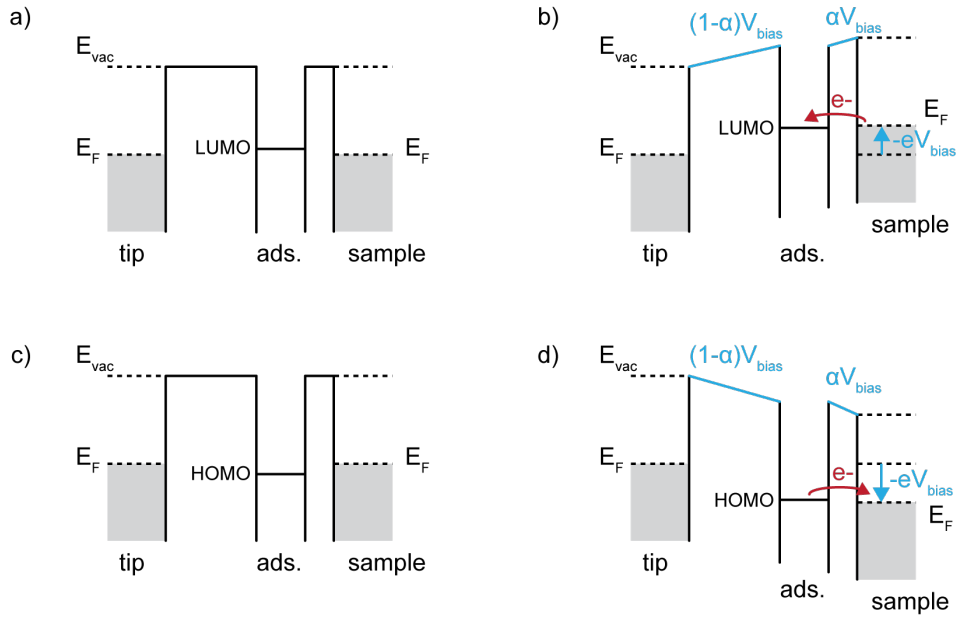

Figure 2.9.: The decoupling of a adsorbate, such as a molecule, from a metal surface is modeled with a double tunneling barrier. If the LUMO (HOMO) is close to Fermi energy at zero bias as shown in a (c), the voltage drop between the adsorbate and the surface might be enough to pull it across the Fermi level when the bias is swept to negative (positive) values. The LUMO (HOMO) is then occupied (emptied).

situation. Such an event can by identified by a sudden jump of the LCPD value: in frequency shift versus bias voltage curves the signal jump from one parabola to another [113].

These processes are detected as rings in constant height $\mathrm{d}I/\mathrm{d}V$ maps, whose radii increase with (absolute) applied bias. Such a dispersion can be explained by the fact that these events are triggered when the electric field induced by the bias voltage overcomes a threshold value at the position of the adsorbate. Indeed, the electric field lines are perpendicular to the surface of a metal. In the case of an STM, their path is thus mostly dictated by the shape of the sharp tip as shown in Fig. 2.10a. For this reason, we refer from now on to the electric field induced by the application of a bias voltage through the junction as the electric field of the tip. The value of electric field at the adsorbate depends on the bias value and position of the tip. To a first approximation, the apex of the tip can be considered to be spherical. For a given bias voltage, the iso-contours of the electric field of the tip are thus circles in the $x-y$ plane of the sample centered at the (projected) tip position. This is shown in Fig. 2.10b, where the red area shows electric field higher than a given threshold value (E_{th}). Similarly, considering that the electric field depends linearly on the applied bias, constant electric field lines for bias sweeps performed as a function of lateral tip displacement are parabolas (Fig. 2.10c): as the tip is brought further away from the adsorbate, the bias voltage required to achieve a given electric field increases.

These considerations explain how a charging event can be induced but not how and why such events are detected and affect the tunneling current. Indeed, it has to be highlighted that these charging events are detected in STS not only above but also far away from the adsorbate (a few nm), when any overlap with the tip wavefunctions has vanished. We propose here a model that rationalizes how the charge redistribution at the adsorbate gates its surrounding which leads to a sharp increase or drop of the tunneling current.

The main idea is to separate the contributions of the chemical and electrical potentials

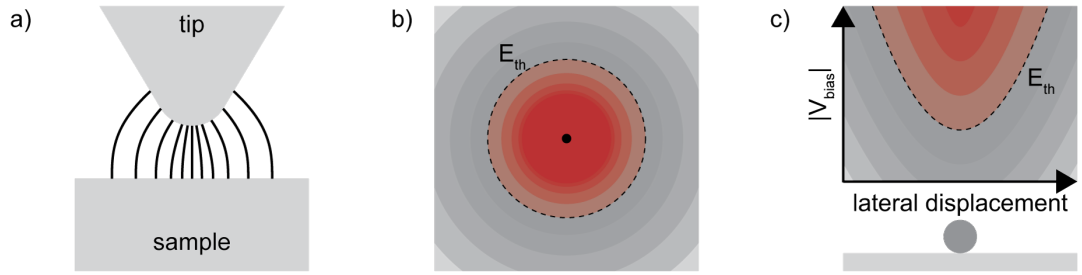

Figure 2.10.: Characterization of the field induced by the bias in an STM junction. a) The field lines are mainly dependent on the shape of the tip. b) In the $x-y$ plane of the sample, the field lines can be approximated by concentric rings centered at the projected position of the tip. We indicate in red the area of the sample for which the electric field is higher than a threshold value E_{th} for a given bias. c) A set of bias sweep along a constant height line above the adsorbate leads to a parabolic dispersion of the tip field at the adsorbate: when the tip is further away, more bias is required to reach a given electric field.

through the junction as illustrated in 2.11. As explained previously, when no bias is applied, the system is in equilibrium and the tip and sample have the same electro-chemical potential (Fig. 2.7d). We have:

$$\mu_t = \mu_s \tag{2.30}$$

$$E_F^t - eV_{\text{pot}}^t = E_F^s - eV_{\text{pot}}^s \tag{2.31}$$

where E_F^t (E_F^s) is the chemical potential or Fermi level of the tip (sample) and V_{pot}^t (V_{pot}^s) its electrical potential. Because the tip is connected to ground we set $V_{\text{pot}}^t = 0$.

In all generality, a charge redistribution has occurred in order to achieve this equilibrium: this corresponds to a potential drop (the LCPD, see previous subsection) across the junction (Fig. 2.11d): $V_{\text{pot}}^s = V_{\text{lcpd}}^0$. Therefore, at equilibrium, the chemical potentials of the two electrodes are shifted with respect to each other in order to compensate for this potential drop (Fig. 2.11c): $E_F^t = E_F^s - eV^0$. No current is observed: as sketched in Fig. 2.11e, electrons from the Fermi sea of the tip lose energy as they tunnel through the potential landscape of Fig. 2.11d: they follow the orange line of Fig. 2.11e and end up at the Fermi sea of the sample.

When a bias is applied, essentially the same picture as depicted in Fig. 2.3 applies. The electrical potential of the electrons in the sample is shifted to V^0+V_{bias} (Fig. 2.11i and Fig. 2.11 n). The chemical potentials of the two electrodes are not affected (Fig. 2.11h and m) but now, with $V_{\text{bias}} > 0$, electrons of the sample with energy E_{ini} such that $E_F^t - eV_{\text{bias}} < E_{ini} < E_F^t$ (orange rectangle in Fig. 2.11j) can tunnel through the junction gaining a potential energy of $e(V_{\text{lcpd}}^0 + V_{\text{bias}})$ and end up on the sample side with energy $E_{fin} = E + e(V_{\text{lcpd}}^0 + V_{\text{bias}})$ that satisfies

$$E_F^t - eV_{\text{bias}} < E_{ini} < E_F^t \tag{2.32}$$

$$E_F^t - eV_{\text{bias}} + e(V^0 + V_{\text{bias}}) < E_{ini} + e(V^0 + V_{\text{bias}}) < E_F^t + e(V^0 + V_{\text{bias}}) \tag{2.33}$$

$$E_F^s < E_{fin} < E_F^s + eV_{\text{bias}} \tag{2.34}$$

and corresponds thus to unoccupied states. We therefore find again that electrons within the energy range $[E_F^t; E_F^t - eV_{\text{bias}}]$ carry the tunneling current. The same applies for the

opposite bias regime (see Fig. 2.11k to o). Therefore, as long as the electrical potential is only modified by the bias, a description of the tunneling current based on the shift of the electro-chemical potential as in Fig. 2.3 is completely valid and sufficient: the sketches of Fig. 2.11a,f,k are totally equivalent to Fig. 2.11e,j,o.

We now show how the presence of an additional electron impacts the tunneling current. On the sample side, the sudden addition of an electron at a position $\mathbf{r}_0$ changes the electrical potential in its surroundings (see Fig. 2.8) from V^0_{lcpd} before its addition to $V_{\text{lcpd}} = V^0_{\text{lcpd}} + V_{\text{gate}}$, with, to a first approximation $V_{\text{gate}} < 0$ (a negative charge increases the potential energy of the electrons in its vicinity).

Considering that the charging happens instantaneously when the bias voltage reaches a threshold value $V^{\text{th}}_{\text{bias}}$, the gain of potential energy for the tunneling electrons changes sharply from $-e(V^0 + V^{\text{th}}_{\text{bias}})$ before the charging event (Fig. 2.12a) to $-e(V^0 + V^{\text{th}}_{\text{bias}} + V_{\text{gate}})$ after it (Fig. 2.12b). A similar calculation as carried out above shows that now electrons within the energy range $[E^t_F; E^t_F - eV^{\text{th}}_{\text{bias}} - eV_{\text{gate}}]$ carry the tunneling current.

As a result, upon the sudden charging event, electrons within the energy range $[E^t_F - eV^{\text{th}}_{\text{bias}}; E^t_F - eV^{\text{th}}_{\text{bias}} - eV_{\text{gate}}]$ are suddenly able to tunnel through the barrier (compare the areas of the orange and red rectangles in the right sketches of Fig. 2.12a and b). This leads to a sharp increase of the (absolute) current that manifests itself as a step in $I - V$ curves with a change of slope (Fig. 2.12c) and a peak in $\mathrm{d}I/\mathrm{d}V$ spectra (Fig. 2.12d). One can similarly verify that an electron removal with a positive bias sweep also lead to a sharp increase of the tunneling current and therefore also to a step and peak in $I - V$ and $\mathrm{d}I/\mathrm{d}V$ curves, respectively. To a first approximation, a change in the slope of the $I - V$ curve, reflecting the change of the height of effective potential barrier by $V_{\text{gate}}/2$, is also expected (Fig. 2.12c and d).

This effect is detected as long as the sample electrons are affected by the gating potential of the induced charge. Since it scales approximatively with $1/|\mathbf{r}|$ (screening potential), such effects are detected far away from the adsorbate, well after the overlap of their wavefunctions with the tip has vanished (exponential dependence). Assuming a constant density of states for both sample and tip, the change in current should scale linearly with eV_{gate} and thus be tip independent for a given position.

As a last remark we would like to underline that the electron added to (removed from) the adsorbate is only acting as an extra charge locally. It originates from (vanishes into) the Fermi surface of the substrate. In this sense, the charging rings have to be understood as the effect of a local charge redistribution (and not addition or removal) at the surface.

All in all, we have seen that STS was sensitive to the gating effects of charging events on the sample surface. We show in chapter 5 that another phenomenon, the addition or removal of image potential states, also induces a charge redistribution that effectively gates the adsorbates.

IV. Experimental details

The results presented in this thesis were obtained with three different ultra-high-vacuum (UHV) low-temperature (LT) STM. One of them is a Createc machine that operates at 4.2 K and was modified to allow for combined AFM and STM measurements. The other two, a Createc and a Specs Joule-Thomson (JT) STM, operate at 1.6 K and 1.1 K, respectively. The Specs STM is furthermore equipped with superconducting coils so that a magnetic field up to 3 T can be achieved in the direction perpendicular to the sample plane. The machines are conceived in similar ways and we present next their general set-up.

1. Experimental set-up

Fig. 2.14 shows the technical drawing of the Specs STM. Like other UHV-LT-STM it is composed of two chambers: the preparation chamber, and the STM chamber, which are separated by a gate valve. A manipulator allows to transfer the sample between the two chambers. The preparation chamber is equipped with several apparatus: metal and molecular evaporators, sputter gun, mass spectrometer and leak valves that are connected to different gas lines. The manipulator is also equipped with both thermo-couples and heating filaments that enable controlled annealing the sample. Several pumps are used in order to obtain and sustain ultra-high vacuum: ion pumps, turbo molecular pumps, titanium sublimation pump and cold traps.

In the STM chamber, in order to reduce the mobility of adsorbates and achieve high energy resolution, a temperature of 4.2 K is achieved by means of a cryostat composed of an outer liquid nitrogen Dewar (77 K) and an inner liquid helium (4.2 K) one. This cryostat further acts as a cold trap within the STM chamber. For the very low temperature-STMs ($T \sim 1$ K), the STM head is mounted on a further cooling stage allowing for these low temperatures.

Vibrations damping in STMs are crucial in order to reduce low-frequency noises. For this purpose the STM head is suspended by springs and the entire machine is lifted by pneumatic legs. In the Createc STMs, small magnets are also mounted on the cryostat to generate eddy current damping.

2. Sample preparation

The studies in this thesis were performed using Pb(111) substrates. The crystals are cleaned by repeated cycle of Ne^+ ion sputtering (parameters of ion gun: $HV = 0.9$ kV, $I = 10$ mA emission current) and annealing to ~ 430 K. In Fig. 2.15a, we show a topography image of a surface after this treatment. One can identify flat terraces with black dots, which correspond to subsurface Ne-filled nanocavities [118, 190, 179] (referred to as Ne impurities in the rest of this thesis). Fig. 2.15b displays an enhanced view of one of these impurities with atomic resolution. The hexagonal pattern of these Ne impurities reflects the orientation of the Pb lattice. Pb has a face-centered cubic (fcc) lattice and on its (111) surface, the atom spacing is 3.50 Å. It is a type-I superconductor with a critical temperature of 7.2 K which makes it suitable for studies at $T \leq 4.2$ K.

In the next chapter we introduce briefly superconductivity and highlight the advantage of using superconducting tips in order to improve energy resolution (see Fig. 3.12). The STM tips are made of tungsten and indented into the surface of Pb crystals while applying high voltage (100 V) to cover their apex with a superconducting Pb layer. The gap width of the tip is determined by the coating thickness and in order to ensure a bulk-like gap width we record $\mathrm{d}I/\mathrm{d}V$ spectra above the bare Pb substrate. Fig. 2.15c displays a $\mathrm{d}I/\mathrm{d}V$ spectrum of a good tip: one can distinguish two pairs of coherence peaks at ± 2.65 mV and ± 2.8 mV (see dashed lines) that correspond to the two superconducting bands of Pb [179] probed with a tip having a superconducting gap of $\Delta_t \sim 1.35$ meV.

The data was analyzed using the following softwares: SpectraFox [177], WSxM [94] and Igor Pro.

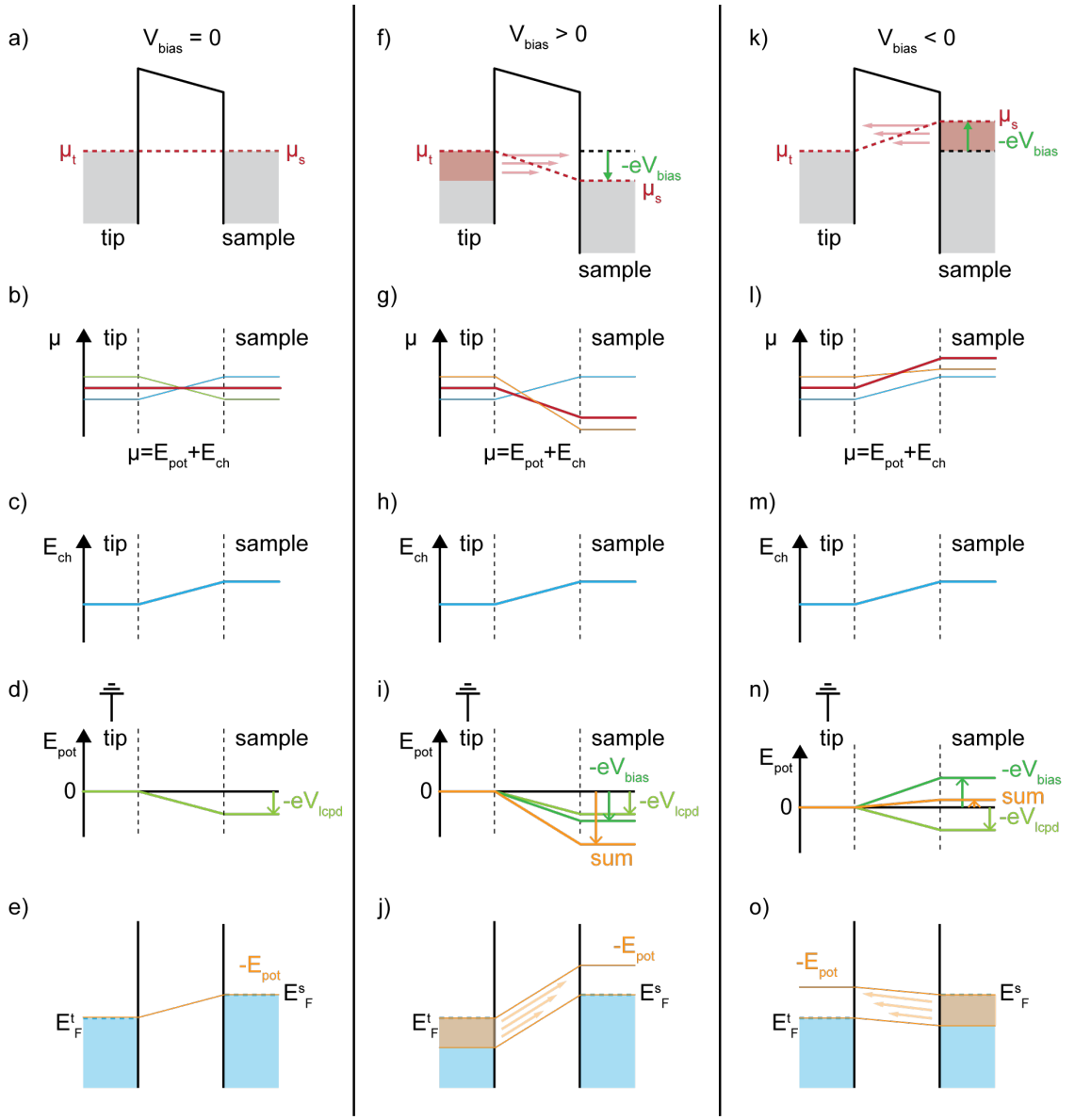

Figure 2.11.: Equivalent sketches of tunneling through an STM junction. In the absence of a bias (a-e), one can either consider that the electrochemical potentials of the tip and surface are aligned (a) or separated (b) their chemical (c) and potential (d) parts. Then, as shown in e, one can sketch misaligned chemical potentials but in a junction where the electrons energy vary according to the potential energy due to the electric field (orange curve). When a positive (f-j) or negative (k-o) bias is applied, the chemical potentials are considered not to be affected (h and m), but the electrical are (i and n). The potential lines along which electrons tunnel (orange lines in j and o) connect now occupied and occupied states so that a current flows. Comparing to the common electrochemical considerations (f and k), the sketched are totally equivalent.

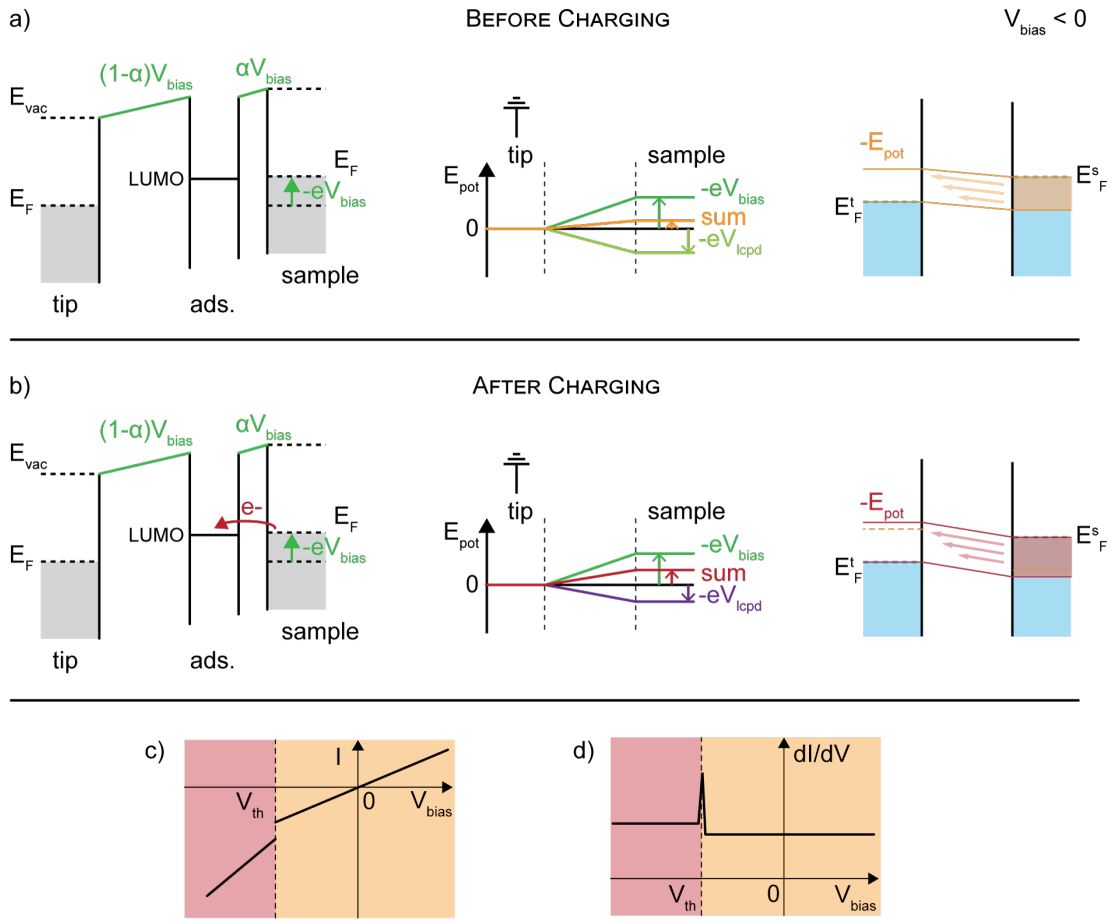

Figure 2.12.: We consider a double tunneling barrier as in Fig. 2.9a, just before (a) and after (b) an electron occupies the LUMO. The change in LCPD due to charging (as shown in Fig. 2.8) modifies the electric potential seen by the electrons (middle sketches). As a result, more electrons tunnel through the barrier after the charging event (compare the area of the orange and red rectangle in the right sketches). This leads to a sharp increase in the $I-V$ curve (c) and a peak in $\mathrm{d}I/\mathrm{d}V$ (d).

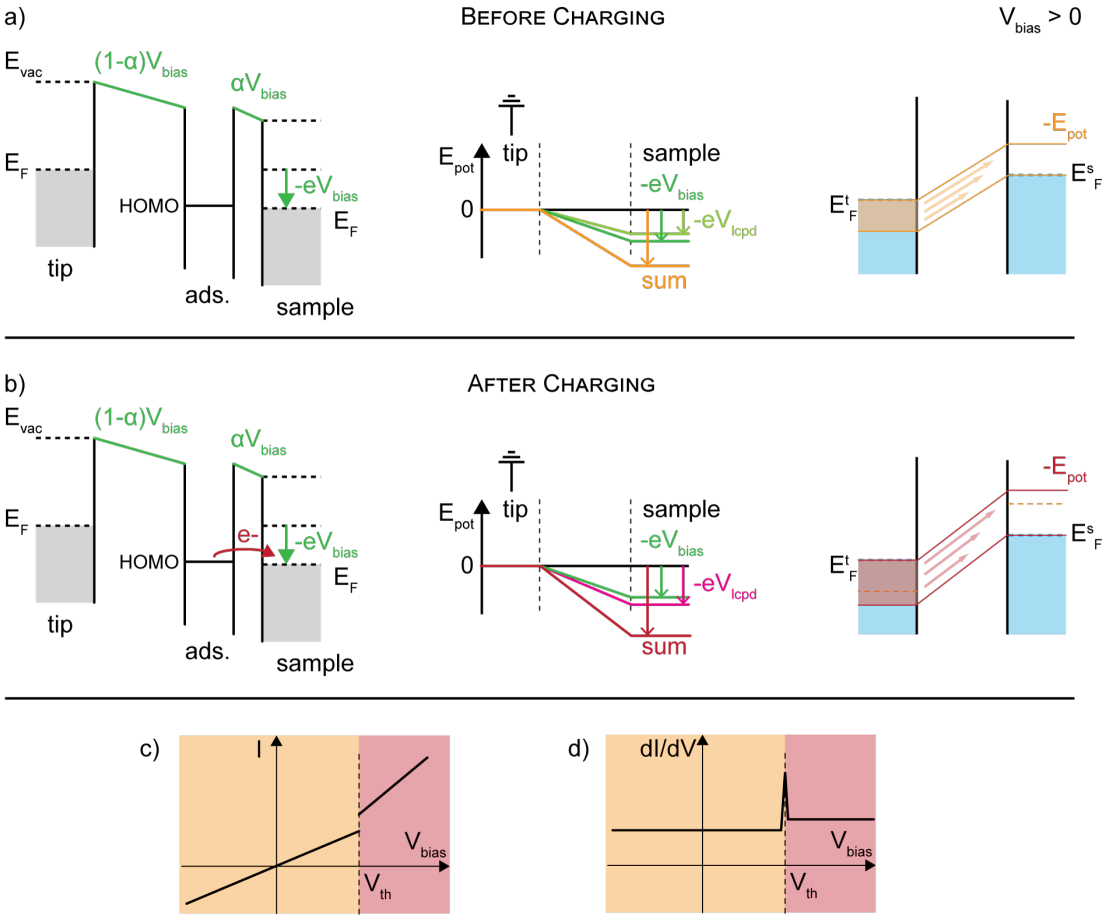

Figure 2.13.: We consider a double tunneling barrier as in Fig. 2.9a, just before (a) and after (b) an electron is removed from the HOMO. The change in LCPD (as shown in Fig. 2.8) modifies the electric potential seen by the electrons (middle sketches). As a result, more electrons tunnel through the barrier after the charging event (compare the area of the orange and red rectangle in the right sketches). This leads to a sharp increase in the $I-V$ curve (c) and a peak in $\mathrm{d}I/\mathrm{d}V$ (d).

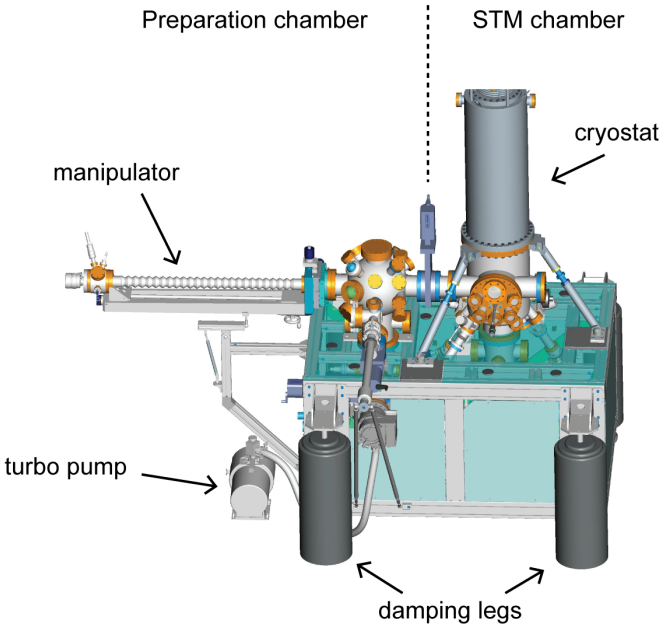

Figure 2.14.: Technical drawing of a LT-STM (original drawing made by Specs). A STM chamber is separated from the preparation chamber by a gate valve and a manipulator is used for sample transfer. The low temperature is achieved by a liquid nitrogen-liquid helium cryostat and high vacuum is created by a set of pumps. The machine is decoupled from the environment by damping legs.

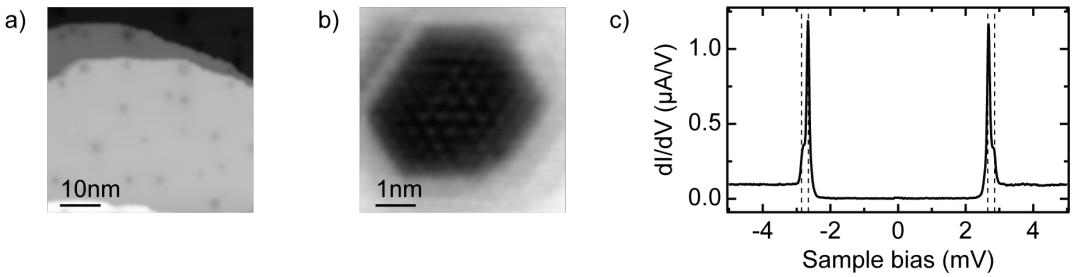

Figure 2.15.: a) Topography image ($V_{\mathrm{bias}} = 5$ mV, $I = 200$ pA) of a Pb crystal after cleaning cycles. The black dots are caused by subsurface Ne impurities. b) Atomic resolution above one of these impurities shows that their hexagonal pattern follows the lattice orientation ($V_{\mathrm{bias}} = 50$ pA, $V_{\mathrm{bias}} = 20$ mV). c) $\mathrm{d}I/\mathrm{d}V$ spectrum recorded with a superconducting tip above the bare Pb substrate (feedback opened at $V_{\mathrm{bias}} = 5$ mV, $I = 400$ pA and signal modulated with $V_{\mathrm{rms}} = 25$ μeV).

Chapter 3

Magnetic impurities on metals and superconductors

In this thesis, we study the interaction of the magnetic moments of porphine molecules with the electrons of the Pb surface, in its normal and superconducting state, as well as eventual coupling between them. Therefore, we first present the theoretical framework in which such a magnetic moment is described and review the different types of coupling between magnetic impurities on a metallic surface. In the second part of this chapter, we introduce the Kondo effect: the formation of a many-body state at low temperatures due to exchange coupling between a magnetic impurity and electrons of a metal surface. We also discuss the characteristic energy scales that have to be considered for the formation of a Kondo lattice. In the third part, we present the superconducting counterpart of the Kondo effect in the normal state: Yu-Shiba-Rusinov (YSR) states.

I. Description of a magnetic impurity

The magnetic moments discussed in this thesis stem from unpaired electrons of an Fe atom embedded in a magnetic ligand and deposited on a surface. We now present the formalism in which a magnetic moment in such a surrounding can be described. Moreover, because chapter 8 is dedicated to the study of magnetic coupling, we present the different types of interactions that can occur between two magnetic impurities.

1. Effective spin Hamiltonian

In gas phase, the spin of an atom is carried by unpaired electrons that occupy degenerate states: for an Fe atom ($[Ar]$ $3d6$ $4s2$), the six electrons of the $3d$ shell. The ground state configuration of the atom can be determined according to Hund's rule: first the spin quantum number $\mathbf{S}$ is maximized, then the angular momentum $\mathbf{L}$, and finally the total angular momentum $\mathbf{J} = \mathbf{S} + \mathbf{L}$ is either maximized or minimized, depending on if the shell is more than or less than hall-filled. The resulting ground state configuration of Fe in gas phase is thus ${}^5D_4$, as sketched in Fig. 3.1a. This ground state has moreover a nine-fold degeneracy $(2\mathbf{J} + 1)$ due to the quantum number m_J, which is the projection of $\mathbf{J}$ on the z-axis. Here, we note that the z-axis can be any axis in real space.

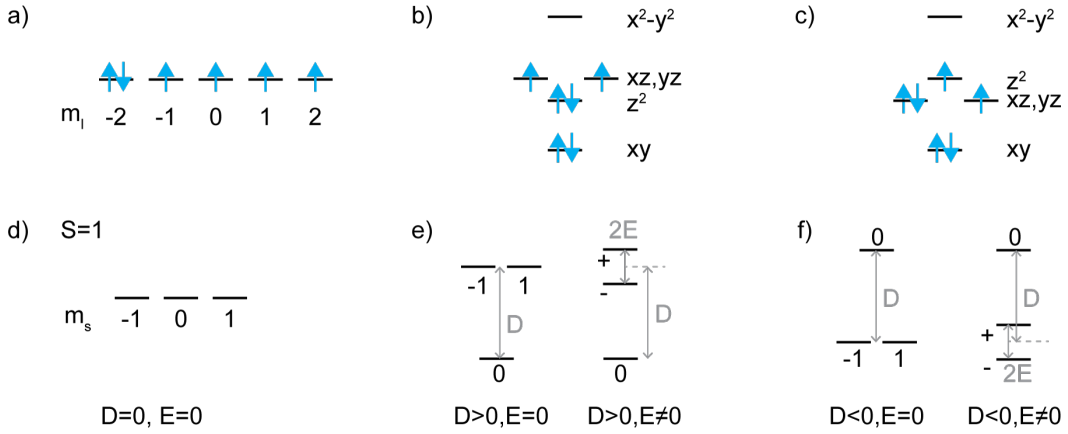

Figure 3.1.: a) Electronic configuration of the $3d$ shell of an Fe atom in gas phase. For the FeP molecule, the presence of the molecular ligand creates a crystal field that lifts the degeneracy of the d levels. These are then shifted in energy as sketched in b) or c). In both cases, this results in a spin $S = 1$ system. d) Without spin-orbit coupling, the spin levels m_s are degenerate. Spin-orbit coupling lifts this degeneracy and is usually described by means of an axial (D) and transversal (E) anisotropy parameters (see equation (3.2)). e) For $D > 0$, the ground state is $m_s = 0$, and in the presence of transversal anisotropy the $m_s = \pm 1$ are mixed to form new eigenstates $|\pm\rangle = |m_s = 1\rangle \pm |m_s = 1\rangle$. f) Splitting of the levels with $D < 0$, again in the presence of transversal anisotropy the eigenstates $m_s = \pm 1$ are mixed.

We now discuss the consequences of the presence of a molecular ligand: this leads, on the one hand, to a hybridization of the Fe d level with molecular orbitals and, on the other hand, to a local electric field -the crystal field- that shifts the energy of the orbitals. The hybridization with molecular orbitals is very specific to each molecular configuration and generally requires the use of density functional theory (DFT) calculations in order to determine the new hybrid orbitals. The occupation of these hybrid orbitals may then result in a change of the number of unpaired electrons and thereby spin state of the molecule. The new orbitals inherit the symmetry of the original d levels, we therefore only consider that the hybridization with a molecular ligand may change the number of electrons occupying the Fe levels.

In the case of the iron porphine (FeP) molecule, the oxidation state of Fe is 2+, meaning that the $4s$ shell is now empty and the six electrons of the $3d$ shell remain. The presence of additional charges in the vicinity of the Fe atoms shifts their d orbitals in energy depending on their spatial distribution. The Fe atom in the center of the porphine ring is subject mostly to the crystal field of the neighboring nitrogen atoms with a square planar symmetry. This results in a splitting of the d levels as shown in [5, 24]: the $d_{x^2-y^2}$ is shifted the highest in energy as it has the largest overlap with the nitrogen atoms while the d_{xy} orbital with the smallest overlap becomes the lowest orbital. The relative positions of the d_{z^2} and d_π orbitals may change depending on the fine details of the adsorption configuration of the molecule. The occupation of the d levels is now not only dictated by Hund's rule but also by the energy cost due to the occupation of a higher orbital. In the case of the FeP molecule, after filling all orbitals except $d_{x^2-y^2}$ with spin-up electrons, it is preferable to fill the remaining orbitals with spin-down electrons because the energy gain due to Hund coupling would not compensate the energy cost $E(d_{x^2-y^2}) - E(d_{xy})$. The two possible resulting electronic configurations for the ground state of the FeP molecule are shown in Fig. 3.1b and Fig. 3.1c. For simplicity, we consider here that Fig. 3.1b shows the ground state while Fig. 3.1c shows the electronic

occupation of the first excited state. As a result, the spin state of the system is $\mathbf{S} = 1$ and the orbital momentum is quenched ($\mathbf{L} = 0$). Here, the ground state is still three-fold degenerate with $m_S = -1, 0, 1$ and no preferential main axis in real space exists for the spin (see Fig. 3.1d).

We now present how spin-orbit coupling affects this configuration. Spin-orbit coupling is a relativistic effect that is described in classical quantum mechanics by [37]:

$$\mathbf{H_{SO}} = \lambda \mathbf{S} \cdot \mathbf{L} \tag{3.1}$$

where λ, the spin orbit coupling constant, is element specific and changes with the oxidation state. Due to the introduction of this additionnal term in the Hamiltonian of the system, the electronic configurations described above are no longer proper eigenstates. The new ground state is then an admixture of the various electronic configurations. If the ground state electronic configuration $|\psi_0\rangle$ is nondegenerate in $|LM_L\rangle$, then one can recast H_{SO} acting on $|LM_L\rangle|SM_S\rangle$ into a new effective Hamiltonian, called Spin Hamitonian, acting only on the spin basis functions $|SM_S\rangle$ [37]. The Spin Hamiltonian can be written as:

$$\mathbf{H_{zf}} = D\mathbf{S_z}^2 + E(\mathbf{S_x}^2 - \mathbf{S_y}^2) \tag{3.2}$$

where $D = \lambda^2/2(\Lambda_{xx} + \Lambda_{yy}) - 2\Lambda_{zz}$ and $E = -\lambda^2/2(\Lambda_{xx} - \Lambda_{yy})$ are the axial and transversal anisotropy parameters, respectively. These parameters arise since the angular momentum is now partially unquenched with [37]:

$$\Lambda_{ii} = \sum_{n}^{\text{exc. st.}} \frac{|\langle\psi_0|\mathbf{L_i}|\psi_n\rangle|^2}{E_n - E_0}, \quad i = x, y, z \tag{3.3}$$

As one can see from equation (3.2), the spin states with different m_S values are now split in energy; this is illustrated in Fig. 3.1e-f. This splitting occurs without the application of an external magnetic field and is therefore often referred to as the zero field splitting. Finally, we point out that the x, y and z axis are now well-defined in space because they are dictated by the symmetry of the crystal field.

The magnetic anisotropy is relevant for all spins larger than $\mathbf{S} = 1/2$ (Kramer's theorem ensures the double degeneracy of all eigenstates for a half-integer total spin due to time-reversal symmetry). In order to determine when or if these anisotropy parameters have to be taken into account one should compare their magnitude with the other energy scales (typically the coupling parameters) that come into play.

2. Coupling between magnetic impurities

We present here briefly the different mechanisms that can lead to a coupling between spin impurities. Because these mechanisms are not dependent on the type of spin involved, we consider for simplicity two spin 1/2 impurities. We focus on the three types of coupling that are relevant for our system and within our energy resolution: the exchange and super-exchange interaction as well as the Ruderman-Kittel-Kasuya-Yoshida (RKKY) interaction.

Exchange interaction

The exchange interaction between two impurities is caused by Coulomb repulsion due to their wavefunctions starting to overlap. This interaction favors parallel alignment of spins and is in essence the justification of Hund's first rule. Yet, such an interaction only becomes substantial when the impurities are in very close vicinity of each other and is therefore often much weaker than other types of interactions.

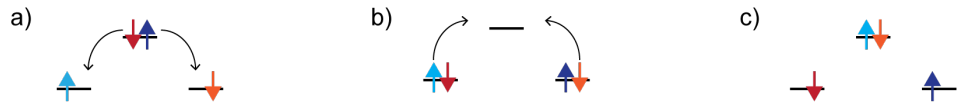

Figure 3.2.: Schematics of the superexchange interaction between two magnetic levels (left,right) via a non magnetic one (middle). a) At the beginning, the two magnetic levels are occupied by one electron each (light blue and orange arrows) and the non-magnetic one is doubly occupied (red and dark blue arrows). The two electrons of the non-magnetic level hop onto the magnetic ones. b) This leads to an intermediate state in which the non-magnetic level is empty. It is refilled by two electrons with opposite spins. c) This leads effectively to an exchange interaction between the two magnetic levels. Were the spins of the magnetic levels aligned, the hopping scheme from a) to b) would not be possible.

Superexchange interaction

The superexchange interaction between two magnetic impurities occurs via a non magnetic intermediate level that can either stem from a non-magnetic entity or be a non-magnetic level of one of the magnetic impurities. A series of hopping events, as sketched in Fig. 3.2, leads to an antiferromagnetic interaction between the two unpaired electrons of two magnetic levels. This type of interaction has for instance been observed between cobalt phthalocyanines molecules adsorbed on Pb(111) islands over a Si(111) substrate [29] or for manganese(II) phthalocyanine thin films [19, 222] as well as between Ni atoms coordinated by tetracyanoquinodimethane (TCNQ) molecules [1].

RKKY interaction

Two impurities deposited onto a metal substrate but separated by a finite distance usually do not interact directly with each other. Yet, as shown by M. A. Ruderman, C. Kittel, T. Kasuya and K. Yosida in the 1950s [183, 106, 226], they can interact indirectly via the conduction electrons of the substrate: the presence of an impurity polarizes the spin of the conduction electrons which then also interacts with the other impurity. We show in the next section that the coupling of each magnetic impurity $\mathbf{S_i}$ to the conduction electrons can be described by an exchange Hamiltonian of the form $J\mathbf{s_i} \cdot \mathbf{S_i}$, where $\mathbf{s_i}$ is the spin of the conduction electrons at the impurity position. The Hamiltonian of two impurities adsorbed on a metal substrate without direct interaction between them is thus:

$$\mathbf{H} = \mathbf{H}_{\text{sub.}} + \mathbf{H}_{\text{coup.}} = \sum_{\mathbf{k},\sigma} \epsilon(\mathbf{k}) c^\dagger_{\mathbf{k}\sigma} c_{\mathbf{k}\sigma} + J\mathbf{s_1} \cdot \mathbf{S_1} + J\mathbf{s_2} \cdot \mathbf{S_2} \tag{3.4}$$

Considering the Hamiltonian $\mathbf{H}_{\text{coup.}}$ as a perturbation of $\mathbf{H}_{\text{sub.}}$ and going to second order yields the following effective Hamiltonian:

$$\mathbf{H}^{\text{RKKY}} = J_{\text{RKKY}} \mathbf{S_1} \cdot \mathbf{S_2} \tag{3.5}$$

where J_{RKKY} depends on the distance r between the two impurities as follows:

$$J_{\text{RKKY}}(r) \propto J^2 \frac{k_F r \cos(2k_F r) - \sin(2k_F r)}{k_F^4 r^4} \tag{3.6}$$

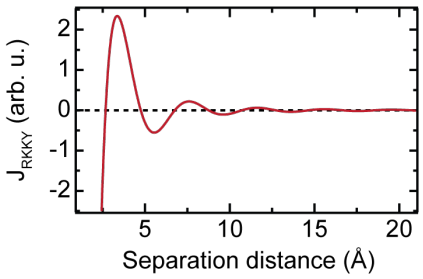

Figure 3.3.: Dependence of the RKKY interaction J_{RKKY} on the separation distance between two impurities (we use $k_F = 0.8\text{Å}^{-1}$). The sign of the exchange coupling changes with inter-impurity distance, and the coupling between impurities can therefore be ferromagnetic or antiferromagnetic.

As sketched in Fig. 3.3 the sign of the exchange coupling changes with inter-impurity distance, and the coupling between impurities can therefore be ferromagnetic or antiferromagnetic. This sign change has been evidenced by lateral manipulation of Co atoms on a copper surface [218] by investigating magnetization curves above Co atoms on a Pt(111) surface [140, 232].

II. Magnetic impurities on metals

The presence of magnetic impurities on a metal surface may lead to interesting phenomena since new correlated states can appear. Here, we follow the detailed approach of A. C. Hewson in [92] for the description of the interaction of a single impurity with the substrate electrons. We first derive the $s-d$ exchange Hamiltonian that explicitly expresses the spin-spin interaction between the two systems. Then, we show that this results in a new correlated state at low temperature: the Kondo effect. In the last subsection, we give a brief introduction to the theoretical framework of the Kondo lattice.

1. Interaction with a metal substrate

We now present how the interaction between a magnetic impurity and a metal substrate can be described. In Fig. 3.4a, we use the Anderson model [9] to illustrate how a magnetic moment can exist when adsorbed on a metal surface. The singly occupied level (we consider the impurity spin to be carried by a d level at energy e_d) lies below the Fermi level: $e_d < E_F$ while the Coulomb energy brings the doubly occupied level above it: $e_d + U > E_F$. As a result, in the ground state, the d level is singly occupied and has thus the two-fold degeneracy of a spin 1/2. We now consider that the impurity interacts with the substrate electrons via a potential scattering $V_{\mathbf{k},\mathbf{k}'}$, the Hamiltonian of the system is then [92]:

$$H = \sum_{\sigma} e_d n_{d,\sigma} + U n_{d,\uparrow} n_{d,\downarrow} + \sum_{\mathbf{k},\sigma} e_{\mathbf{k}} c^{\dagger}_{\mathbf{k},\sigma} c_{\mathbf{k},\sigma} + \sum_{\mathbf{k},\sigma} (V_{\mathbf{k}} c^{\dagger}_{d,\sigma} c_{\mathbf{k},\sigma} + V^{*}_{\mathbf{k}} c^{\dagger}_{\mathbf{k},\sigma} c_{d,\sigma}) \tag{3.7}$$

where $c^{\dagger}_{\mathbf{k},\sigma}$ ($c^{\dagger}_{d,\sigma}$) is the creation operation for an electron with momentum $\mathbf{k}$ (in the d level) and spin σ, and $n_{d,\sigma}$ the corresponding number operator. The two first terms describe the magnetic impurity, the third one the substrate and the fourth the interaction between the

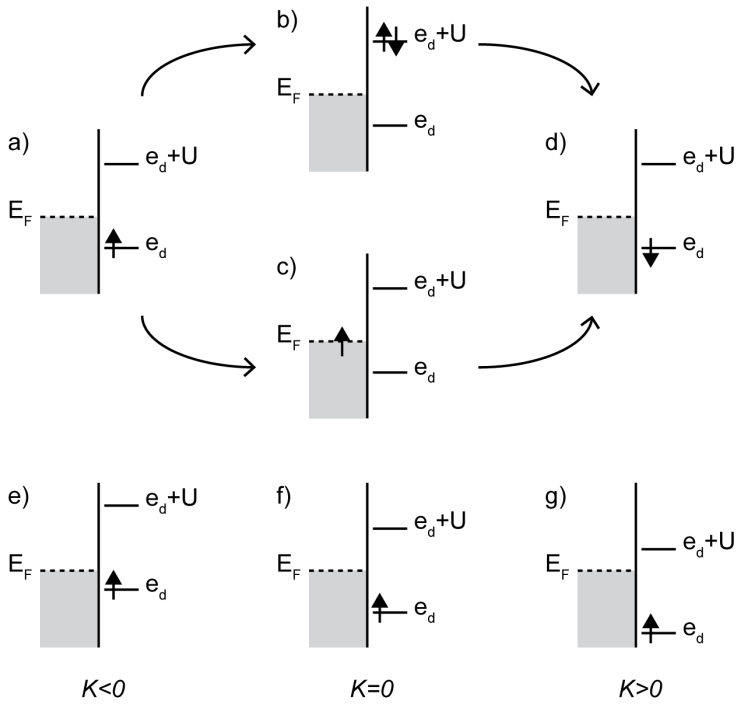

Figure 3.4.: a) Anderson model for the description of a magnetic impurity in front of a metal substrate: the singly occupied level at energy e_d lies below the Fermi level while the doubly occupied level at $e_d + U$ is above it, U being the Coulomb repulsion energy. Scattering of electrons onto the impurity leads to virtual excitations in which the impurity level is either doubly occupied (b) or empty (c). These excitations do not conserve energy and are thus only allowed within the Heisenberg uncertainty principle. d) A relaxation to the ground state configuration leads effectively to a spin flip interaction that is at the origin of the Kondo effect. e-g) The sign and magnitude of the potential scattering term K of the $s-d$ model depend on the relative positions of the singly and doubly occupied levels with respect to the Fermi level (see equation (3.15)).

two systems. If one approximates the substrate by a flat band with density of states (DOS) ρ_0 and neglects the $\mathbf{k}$-dependence of the potential scattering, this interaction leads to a broadening of the d level that then have a width $\Delta = \pi\rho_0|V|^2$. In the following we assume that $\Delta << |e_d|, |e_d + U|$, so that the magnetic moment is preserved.

The Hamiltonian of equation (3.7) does not explicitly show the interaction between the conduction electrons and the spin of the impurity. We now present the Schrieffer-Wolf transformation [191] that expresses the equivalence, under certain conditions, of the Anderson model (equation (3.7)) and the so-called Kondo or $s-d$ model.

One should consider the different occupation states of the d-level: ψ_0, with no electron, ψ_1 with one electron and ψ_2 with two electrons. As mentioned above, ψ_1 is the ground state of the system, ψ_0 and ψ_2 are excited states. The idea is to consider virtual excitations to these states, as shown in Fig. 3.4b and c, and treat them within first order perturbation theory. More precisely, we consider the total wavefunction of the system ψ as $\begin{pmatrix}\psi_0 & \psi_1 & \psi_2\end{pmatrix}$ and write the Schrödinger equation as:

$$\begin{pmatrix} H_{00} & H_{01} & H_{02} \\ H_{10} & H_{11} & H_{12} \\ H_{20} & H_{21} & H_{22} \end{pmatrix} \begin{pmatrix} \psi_0 \\ \psi_1 \\ \psi_2 \end{pmatrix} = E \begin{pmatrix} \psi_0 \\ \psi_1 \\ \psi_2 \end{pmatrix} \tag{3.8}$$

where $H_{nn'} = P_n H P_{n'}$, P_n being the projection operator onto the subspace with n electrons occupying the d level:

$$P_0 = (1 - n_{d,\uparrow})(1 - n_{d,\downarrow}) \tag{3.9}$$
$$P_1 = n_{d,\uparrow} + n_{d,\downarrow} - 2n_{d,\uparrow}n_{d,\downarrow} \tag{3.10}$$
$$P_2 = n_{d,\uparrow}n_{d,\downarrow} \tag{3.11}$$

We can consider that $H_{02} = H_{20} = 0$ since no term in the Hamiltonian of equation (3.7) describes the removal or addition of two electrons simultaneously. In order to obtain an effective Hamiltonian acting only on ψ_1 one can therefore rewrite the Schrödinger equation by eliminating ψ_0 and ψ_2:

$$(H_{11} + H_{12}(E - H_{22})^{-1}H_{21} + H_{10}(E - H_{00})^{-1}H_{01})\psi_1 = E\psi_1 \tag{3.12}$$

By going to lowest order in $V_{\mathbf{k}}$ one can then show that equation (3.12) is equivalent to the following Hamiltonian:

$$\begin{aligned} H = &\sum_{\mathbf{k},\mathbf{k}'} J_{\mathbf{k},\mathbf{k}'}(S^+ c^\dagger_{\mathbf{k},\downarrow} c_{\mathbf{k}',\uparrow} + S^- c^\dagger_{\mathbf{k},\uparrow} c_{\mathbf{k}',\downarrow} + S_z(c^\dagger_{\mathbf{k},\uparrow} c_{\mathbf{k}',\uparrow} - c^\dagger_{\mathbf{k},\downarrow} c_{\mathbf{k}',\downarrow})) \\ &+ \sum_{\mathbf{k},\mathbf{k}'} K_{\mathbf{k},\mathbf{k}'} c^\dagger_{\mathbf{k},\sigma} c_{\mathbf{k}',\sigma} \end{aligned} \tag{3.13}$$

where S_z and $S^\pm (= S_x \pm iS_y)$ are the spin operator for the spin S carried by the d level and $J_{\mathbf{k},\mathbf{k}'}$ the effective exchange coupling, and $K_{\mathbf{k},\mathbf{k}'}$ the potential scattering that are defined, respectively, as:

$$J_{\mathbf{k},\mathbf{k}'} = V^*_{\mathbf{k}} V_{\mathbf{k}'} \left(\frac{1}{U + e_d - e_{\mathbf{k}'}} + \frac{1}{e_{\mathbf{k}} - e_d} \right) \tag{3.14}$$
$$K_{\mathbf{k},\mathbf{k}'} = \frac{V^*_{\mathbf{k}} V_{\mathbf{k}'}}{2} \left(\frac{1}{e_{\mathbf{k}} - e_d} - \frac{1}{U + e_d - e_{\mathbf{k}'}} \right) \tag{3.15}$$

Equation (3.13) is usually written in a more concise way in real space as:

$$H = J\mathbf{s} \cdot \mathbf{S} + K\mathbf{I} \tag{3.16}$$

where J and K are the exchange and potential scattering at the impurity site in real space, $\mathbf{I}$ the identity matrix in spin space and $\mathbf{s}$ the local conduction electron spin at the impurity site defined as $\mathbf{s} = \sum_{\sigma,\sigma'} c^\dagger_\sigma \boldsymbol{\sigma} c_{\sigma'}$, with $\boldsymbol{\sigma} = (\boldsymbol{\sigma}_x, \boldsymbol{\sigma}_y, \boldsymbol{\sigma}_z)$ being the spin Pauli matrix.

We would like to point out here that the sign of the potential scattering K depends on the electron-hole asymmetry of the system. Assuming for simplicity that the conduction band and potential $V_{\mathbf{k}}$ are electron-hole symmetric, the asymmetry of the system depends only on the relative positions of the singly and doubly occupied levels with respect to the Fermi level of the substrate. As shown in Fig. 3.4e, when the singly occupied level is closer to the Fermi level than the doubly occupied level, one has $K < 0$. Conversely, when the doubly occupied level is closer to the Fermi level (see Fig. 3.4g) then $K > 0$, and lastly the symmetric case corresponds to $K = 0$.

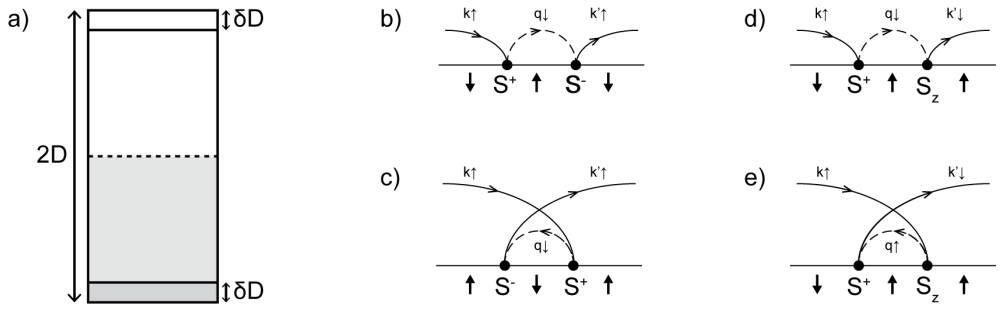

Figure 3.5.: Poor man's scaling approach. a) The band width of the conduction band is effectively reduced by removing the electron and hole states within the edges δD. The renormalization of the coupling coefficients is done by taking into account virtual excitations that involve an electron (b and d) or a hole (c and e) in an intermediate state q at band edge δD.

2. The Kondo effect

The Kondo effect is named after Jun Kondo who proposed in 1964 a theoretical explanation [115] for the observation of a resistance minimum at low temperatures for noble or divalent metals containing a small concentration of magnetic impurities [38]. The presence of this minimum was puzzling as, upon a decrease of the temperature, the number of phonons to which the electrons of the conduction band can couple decreases and thus one expects a continuous decrease of the electrons scattering rate and thereby also a decrease of the electrical resistance. Using perturbation theory up to 3$^{\text{rd}}$ order, Jun Kondo showed that this effect can be explained on the single impurity level by the scattering of the conduction electrons causing spin-flip events.

At temperatures below the so-called Kondo temperature, these spin-flip events lead to the formation of a many-body state. This state screens the impurity spin on energy scales defined by the aforementionned Kondo temperature. Following [92], we present here the so called 'poor man's scaling approach' that helps in understanding how the Kondo temperature is defined.

The idea is that, upon a decrease of the temperature, one would like to eliminate high excitation processes (that are not thermally activated), th same way as it is done in the previous section for the Schrieffer-Wolf transformation, and include the effect of these high energy excitation into a renormalization of the parameters of the Hamiltonian. Neglecting potential scattering, we consider a generalization of the $s-d$ model described above with the possibility for an anisotropic coupling if $J_\pm \neq J_z$:

$$H = \sum_{\mathbf{k},\mathbf{k}'} J_+ S^+ c^\dagger_{\mathbf{k},\downarrow} c_{\mathbf{k},\uparrow} + J_- S^- c^\dagger_{\mathbf{k},\uparrow} c_{\mathbf{k},\downarrow} + J_z S_z (c^\dagger_{\mathbf{k},\uparrow} c_{\mathbf{k},\uparrow} - c^\dagger_{\mathbf{k},\downarrow} c_{\mathbf{k},\downarrow}) \tag{3.17}$$

To carry out the scaling of the coefficients $J_\pm$ and J_z one separates the conduction band (assumed to be symmetric and of width $2D$) into two regions: states with $|e_k| < D - |\delta D|$ are retained and those at the edges $|\delta D|$ are eliminated (see Fig. 3.5a). In Fig. 3.5b-e we show the processes that have then to be considered for the scaling: these are those that involve the scattering of a particle (Fig. 3.5b and d) or a hole at the band edges, with (Fig. 3.5d and e) or without (Fig. 3.5b and c) an effective spin flip of the impurity. One can then show that the Hamiltonian retains the same form but with modified coupling parameters: $J_\pm \to J_\pm + \delta J_\pm$ and $J_z \to J_z + \delta J_z$. This leads to the following scaling equations that show how $J_\pm$ and J_z

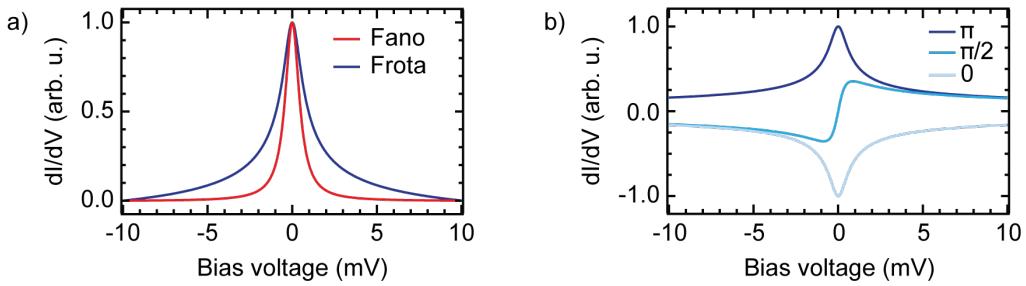

Figure 3.6.: a) Comparison of the Fano and Frota lineshapes with same phase factor π. The curves are normalized to have the same height. b) Fano-Frota lineshape for different values of the phase factor (see legend).

evolve with D [92]:

$$\frac{dJ_\pm}{d\ln D} = -2\rho_0 J_z J_\pm \tag{3.18}$$

$$\frac{dJ_z}{d\ln D} = -2\rho_0 J_\pm^2 \tag{3.19}$$

For an isotropic coupling we have $\frac{dJ}{d\ln D} = -2\rho_0 J^2$, and the integration of this equation leads thus to a scaling invariant that defines the Kondo temperature T_K:

$$De^{-1/(2J\rho_0)} \sim k_B T_K \tag{3.20}$$

Going to higher order in perturbation theory and including electron interaction on the impurity site leads to slight modification of this formula but the Kondo temperature remains defined as the energy scale that characterizes the emergence of a new correlated state in which the magnetic moment of the impurity is screened by the conduction electrons via coherent scattering. The presence of this many-body state manifests itself in $\mathrm{d}I/\mathrm{d}V$ spectra as a sharp resonance in the spectral function of the system [136]. This resonance has a width Γ that depends on temperature [155] and is localized near the Fermi level at ϵ_K [209]:

$$\epsilon_K = \Gamma \tan\left(\frac{\pi}{2}(1-n_d)\right), \tag{3.21}$$

where n_d is the average occupation of the d level: $n_d = -\frac{e_d}{U} + \frac{1}{2}$ (for an electron-hole symmetric substrate). The position of the resonance is thus related to the electron-hole asymmetry of the system.

The shape of the Kondo resonance in scanning tunneling spectroscopy (STS) is asymmetric [136, 209]. This asymmetry is due to interferences between two channels for the tunneling electrons: they can either tunnel into the many-body state or directly into the electron sea of the metal substrate. The resulting lineshape is typically described by a Fano-function [48]:

$$F_{\mathrm{Fano}}(\epsilon) = \frac{(q+E)^2}{1+E^2}, \tag{3.22}$$

where E is the reduced energy defined as:

$$E = \frac{\epsilon - \epsilon_K}{\Gamma/2}, \tag{3.23}$$

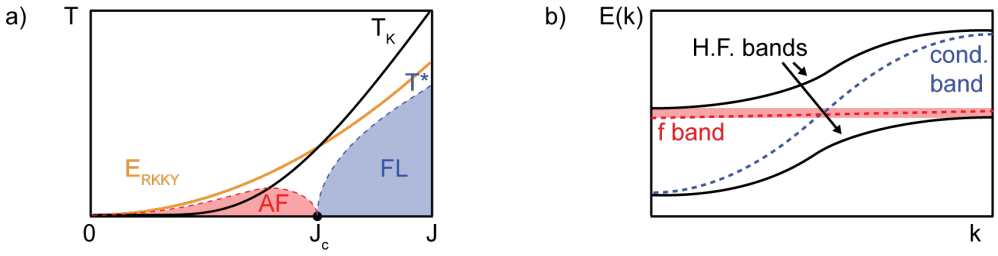

Figure 3.7.: a) Doniach's phase diagram. The Kondo and RKKY coupling both depend on the coupling strength of the impurity to the surface J but in different manners. As a result, at low coupling strength J, the RKKY coupling dominates and the system enters an ordered antiferromagnetic phase. At strong coupling, the Kondo screening dominates, and the system enters a Fermi liquid phase below a coherence temperature T^*. b) The formation of this phase can be understood as the hybridization between the dispersive band of conduction electrons and the weakly dispersive band of localized f (or d) electrons. This leads to a gap opening around the Fermi level.

ϵ being the energy variable. The parameter q is the interference factor that quantifies the asymmetry of the resonances. Over the last years, it has been shown that a Frota function can also be used to fit the Kondo resonance as it gives a better description of its lineshape [76] (the two lineshapes are compared in Fig. 3.6a). The interference between the two tunneling paths is then given by a phase factor ϕ [61]:

$$F_{\text{Frota}}(\epsilon) = -A \cdot \text{Re}\left(e^{i\phi}\sqrt{\frac{i\Gamma/2}{\epsilon - \epsilon_K + i\Gamma/2}}\right), \tag{3.24}$$

A being the amplitude of the resonance. This function is referred to as a Fano-Frota function.

As shown in [61], the phase factor ϕ is related to the interference parameter q by $\tan(\phi/2) = q$. The interference parameter is usually used to quantify the relative strength of the two tunneling paths: for $\phi = \pi$ ($q = \infty$) one obtains a peak (see Fig. 3.6b) indicating a tunneling of the electrons only to the Kondo resonance. Conversely, for $\phi = 0$ ($q = 0$), the obtained dip indicates that the tunneling path to the substrate dominates. Intermediate values are obtained when both paths have to be considered. In chapter 7, we discuss how the sign of the interference factor relates to the local electron-hole asymmetry of the system when the magnetic impurity is embedded in a molecular ligand.

3. The Kondo lattice

When several magnetic impurities are adsorbed on a metal substrate two competitive mechanisms come into play: the screening of each impurity by the substrate electrons as described above and a magnetic coupling between the impurities. Usually, the coupling between the impurities is considered to be mediated by RKKY interactions and scale thus with $\propto J^2$ (see subsection I.2), but since the Kondo temperature depends exponentially on $-1/J$, a transition with J exists between two regimes in which each effect dominates.

This is illustrated in Fig. 3.7a with Doniach's phenomenological phase diagram [42]. When RKKY coupling dominates, the ground state of the system has a magnetic order, but for large J, the magnetic impurities are Kondo screened. In this case, a Fermi liquid phase is formed below a coherence temperature T^* that is lower than the Kondo temperature T_K

associated with the screening of a single impurity. In this Fermi liquid phase, the d band formed by the localized moments couples to the conduction band of the metal. As illustrated in Fig. 3.7b, this leads to the opening of a gap around the Fermi level and thus to the emergence of heavy-fermion bands. For large J, therefore, different temperature regimes have to be considered: $T < T^*$ with a Fermi liquid phase, $T^* < T < T_K$ with independent screening of each impurity, and $T > T_K$ without screening.

In the literature, the competition between the RKKY and Kondo coupling is usually seen as a splitting of the Kondo resonance or emergence of a small gap around the Fermi level that disappears quickly with temperature [104, 15, 97, 193, 215, 14]. Modulation of the Kondo intensity for a small amount of impurities has also been reported [152].

III. Magnetic impurities on superconductors

We have seen that the exchange potential created by a magnetic impurity adsorbed on a metal substrate leads locally to the formation of a new ground state in which the impurity spin is screened. When the substrate is in the superconducting state, this very same interaction gives rise to bound states inside the superconducting gap, called YSR states. In this section, we first give a brief introduction to superconductivity, limiting ourselves to the case of BCS s-wave superconductors. We then describe in more detail how a YSR state is induced by a magnetic impurity and what its main characteristics are.

1. Superconductivity

Superconductivity is a state of matter discovered in 1911 by H. K. Onnes when he observed a sudden vanishing of the electrical resistance of mercury below a critical temperature (4.2 K) [160, 41]. This discovery was enabled only after he mastered the technical challenge of helium liquefaction in 1908. Indeed, the highest critical temperatures for elements within the periodic table remain below 10 K (for Niobium 9.5 K, technetium 7.8 K and lead 7.2 K) which hampered an earlier observation. A drop of the electrical resistance at low temperatures contradicted the expected saturation to a finite value due to the scattering of electrons at impurities. H. K. Onnes was thus awarded the Nobel prize in 1913 for the discovery of this intriguing state of matter.

Historical advances toward the understanding of this state were made by W. Meißner and R. Ochsenfeld in 1933 with the observation of the Meißner-Ochsenfeld effect (expulsion of external magnetic fields, this distinguishes superconductors from perfect conductors) [142] and the brothers F. and H. London in 1935 with the first phenomenological electrodynamic model of superconductivity [132]. In 1950, V. L. Ginzburg and L. Landau characterized the thermodynamics of superconductors by describing the phase transition from the normal to the superconducting state by means of a pseudo wavefunction Ψ for the superconducting electrons that serves as an order parameter [71]. Importantly for us, they introduced the concept of a coherence length ξ that defines the length-scale on which Ψ varies. Their theory also rationalized the existence of two types of superconductors as discovered in 1935 by Rjabinin and Shubnikov [173]. Yet, until 1957 and the Bardeen-Cooper-Schrieffer (BCS) theory [17, 18], the scientific community did not have a microscopic understanding of the effect. We present this theoretical description of the superconducting state in more detail in the following part but would like to emphasize that the research field of superconductivity is still blooming with, in particular, the discovery of high-T_c superconductors that cannot be explained within simple BCS theory that considers electron-phonon coupling.

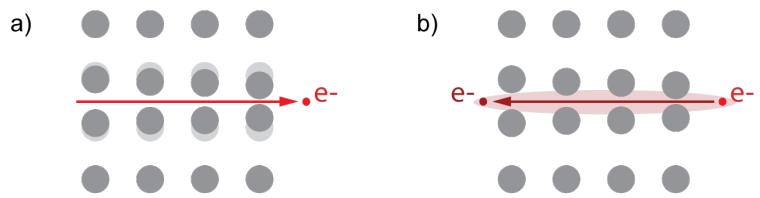

Figure 3.8.: Illustration of the electron-phonon coupling. a) The motion of an electron distorts the ion lattice due to Coulomb attraction. b) This creates a slightly favorable path for a second electron and effectively leads to a net positive interaction: the two electrons form a Cooper pair.

The Bardeen-Cooper-Schrieffer (BCS) theory

The BCS theory is based on the assumption of a net positive interaction between electrons. This is rather counter-intuitive as electrons tend to repel each other because of Coulomb repulsion. Yet, in 1950 it was observed that the different isotopes of mercury exhibit different critical temperatures: the phenomenon causing superconductivity should involve the mass of the nuclei [139]. J. Bardeen, L. Cooper and J. R. Schrieffer thus proposed that a coupling of the electrons to the phonon modes of the ion lattice leads to an attractive interaction between electrons [17, 18]. This idea is illustrated in Fig. 3.8: the motion of an electron within the lattice slightly modifies the position of the nuclei because of Coulomb attraction. These displacements create a slightly more favorable path for a second electron moving through the lattice. This effectively gives rise to a pair of bound electrons, called Cooper pair. The lifetime of an ion displacement (or phonon) is related to the inverse of the Debye frequency which gives for Pb 8.3×10^{-14} s. During this time, an electron with Fermi velocity can travel up to ~ 150 nm. The size of a Cooper pair is thus in the order of 100 nm, this explains why such a phonon mediated process is not hampered by the short-ranged Coulomb repulsion.

Assuming an arbitrarily small attractive interaction between electrons one can show that the Fermi sea is unstable against the formation of at least one pair of bound electrons [212]. This instability gives rise to a condensation of pairs of electrons until an equilibrium is reached when the state of the system is so greatly changed from the Fermi sea (because of the numerous bound pairs) that no energy is gained by bounding an extra pair of electrons. Because of the very large number of electrons involved, the BCS ground state is determined within a mean field approximation: the probability of a state $\mathbf{k}$ to be occupied depends only on the *averaged* occupancy of the other states. Effectively, one works within the grand canonical ensemble: only the averaged number of particles $\overline{N}$ is fixed. The BCS ground state is then given by [212]:

$$|\psi_G\rangle = \prod_{\mathbf{k}} (u_{\mathbf{k}} + v_{\mathbf{k}} c^\dagger_{\mathbf{k},\uparrow} c^\dagger_{-\mathbf{k},\downarrow}) |\phi_0\rangle, \tag{3.25}$$

where ϕ_0 is the vacuum state. The BCS ground state is thus made out of pairs of electrons that have a given probability to be occupied $|v_{\mathbf{k}}|^2$ or unoccupied $|u_{\mathbf{k}}|^2$ (we have $|u_{\mathbf{k}}|^2 + |v_{\mathbf{k}}|^2 = 1$), but no electron can exist alone. We notice from equation (3.25) that all pairs of electrons with opposite momentum are in phase, thus yielding a macroscopic wavefunction as in the Ginzburg-Landau theory. This phase coherence is achieved as the counterpart of the uncertainty concerning the particle number: we have $\Delta N \Delta\phi \geq 1$.

In scanning tunneling microscopy (STM), one does not measure the ground state of a system, rather, the technique relies onto the injection of single electrons or holes into the

sample (see chapter 2). We should therefore not only characterize the BCS ground state but also the single-particle excitations. The Hamiltonian of the interacting electrons is the so-called *pairing Hamiltonian* [212]:

$$H_{\mathrm{BCS}} = \sum_{\mathbf{k},\sigma} \chi_{\mathbf{k}} c^{\dagger}_{\mathbf{k},\sigma} c_{\mathbf{k},\sigma} + \sum_{\mathbf{k},\mathbf{l}} V_{\mathbf{k},\mathbf{l}} c^{\dagger}_{\mathbf{k},\uparrow} c^{\dagger}_{-\mathbf{k},\downarrow} c_{-\mathbf{l},\downarrow} c_{\mathbf{l},\uparrow} \tag{3.26}$$

where $\chi_{\mathbf{k}} = e_{\mathbf{k}} - \mu = \frac{\hbar^2 \mathbf{k}^2}{2m} - \mu$ is the energy of the electrons with respect to the chemical potential μ. $V_{\mathbf{k},\mathbf{l}}$ is the effective interaction potential due to electron-phonon coupling that describes the scattering of a Cooper pair with momentum $\mathbf{l}$ into a Cooper pair with momentum $\mathbf{k}$. The mean field approximation mentioned above is now performed by approximation the action of an operator A by its mean value: $A = \langle A \rangle + \delta A$, where δA are neglectable small fluctuations. Applying this transformation to the operators $A_1 = c^{\dagger}_{\mathbf{k},\uparrow} c^{\dagger}_{-\mathbf{k},\downarrow}$ and $A_2 = c_{-\mathbf{l},\downarrow} c_{\mathbf{l},\uparrow}$ one obtains:

$$\begin{aligned} H_{\mathrm{BCS}} = & \sum_{\mathbf{k},\sigma} \chi_{\mathbf{k}} c^{\dagger}_{\mathbf{k},\sigma} c_{\mathbf{k},\sigma} \\ & + \frac{1}{N} \sum_{\mathbf{k},\mathbf{l}} V_{\mathbf{k},\mathbf{l}} \left(\langle c^{\dagger}_{\mathbf{k},\uparrow} c^{\dagger}_{-\mathbf{k},\downarrow} \rangle c_{-\mathbf{l},\downarrow} c_{\mathbf{l},\uparrow} + c^{\dagger}_{\mathbf{k},\uparrow} c^{\dagger}_{-\mathbf{k},\downarrow} \langle c_{-\mathbf{l},\downarrow} c_{\mathbf{l},\uparrow} \rangle - \langle c^{\dagger}_{\mathbf{k},\uparrow} c^{\dagger}_{-\mathbf{k},\downarrow} \rangle \langle c_{-\mathbf{l},\downarrow} c_{\mathbf{l},\uparrow} \rangle \right) \end{aligned} \tag{3.27}$$

The last term is a constant that we name E_{BCS}. By introducing a gap parameter Δ_{k}:

$$\Delta_{\mathbf{k}} = -\frac{1}{N} \sum_{\mathbf{l}} V_{\mathbf{k},\mathbf{l}} \langle c^{\dagger}_{\mathbf{k},\uparrow} c^{\dagger}_{-\mathbf{k},\downarrow} \rangle \tag{3.28}$$

we finally obtain

$$H_{\mathrm{BCS}} = \sum_{\mathbf{k},\sigma} \chi_{\mathbf{k}} c^{\dagger}_{\mathbf{k},\sigma} c_{\mathbf{k},\sigma} - \sum_{\mathbf{k}} \Delta^{*}_{\mathbf{k}} c_{-\mathbf{k},\downarrow} c_{\mathbf{k},\uparrow} - \sum_{\mathbf{k}} \Delta_{\mathbf{k}} c^{\dagger}_{-\mathbf{k},\downarrow} c^{\dagger}_{\mathbf{k},\uparrow} \tag{3.29}$$

This Hamiltonian can be diagonalized by means of a Bogoluibov transformation which is a unitary transformation in electron-hole space. One defines new quasiparticle operators:

$$\gamma_{\mathbf{k},\uparrow} = u_{\mathbf{k}} c_{\mathbf{k},\uparrow} - v_{\mathbf{k}} c^{\dagger}_{-\mathbf{k},\downarrow} \tag{3.30}$$

$$\gamma^{\dagger}_{-\mathbf{k},\downarrow} = u^{*}_{\mathbf{k}} c^{\dagger}_{-\mathbf{k},\downarrow} - v^{*}_{\mathbf{k}} c_{\mathbf{k},\uparrow} \tag{3.31}$$

These are fermionic operators and the corresponding quasiparticles are a superposition of an electron and a hole. One has $|u_{\mathbf{k}}|^2 + |v_{\mathbf{k}}|^2 = 1$ for the transformation to be unitary, and in order to cancel the off-diagonal terms, $u_{\mathbf{k}}$ and $v_{\mathbf{k}}$ are further defined with:

$$|u_{\mathbf{k}}|^2 = \frac{1}{2} \left(1 + \frac{\chi_{\mathbf{k}}}{\sqrt{\chi_{\mathbf{k}} + |\Delta_{\mathbf{k}}|^2}} \right) \tag{3.32}$$

$$|v_{\mathbf{k}}|^2 = \frac{1}{2} \left(1 - \frac{\chi_{\mathbf{k}}}{\sqrt{\chi_{\mathbf{k}} + |\Delta_{\mathbf{k}}|^2}} \right) \tag{3.33}$$

$$u_{\mathbf{k}} v_{\mathbf{k}} = \frac{\Delta_{\mathbf{k}}}{2\sqrt{\chi_{\mathbf{k}} + |\Delta_{\mathbf{k}}|^2}} \tag{3.34}$$

The Hamiltonian is then finally

$$H_{\mathrm{BCS}} = \sum_{\mathbf{k},\sigma} E_{\mathbf{k}} \gamma^{\dagger}_{\mathbf{k},\sigma} \gamma_{\mathbf{k},\sigma} - E_{\mathrm{BCS}} \tag{3.35}$$

with the energy dispersion of the quasi-particles being

$$E_{\mathbf{k}} = \sqrt{\chi_{\mathbf{k}}^2 + |\Delta_{\mathbf{k}}|^2}. \tag{3.36}$$

In the case of an isotropic (s-wave) supercondutor the gap parameter is moreover independent of $\mathbf{k}$: $\Delta_{\mathbf{k}} = \Delta$.

The Hamiltonian is thus expressed in terms of non-interacting quasiparticles and the ground state defined by equation (3.25) consists of a state in which none of these quasiparticles is present. An excitation in the superconductor is thus to be understood as the creation of these quasiparticles. Indeed, these are defined as a superposition of an electron and a hole and therefore their DOS is thus what is to a first approximation what one measures in $\mathrm{d}I/\mathrm{d}V$ (see chapter 2). As one can see from equation (3.36) an energy gap Δ has to be overcome in order to create these quasi-particles and thus excite the system: the condensate of Cooper pairs in the ground state is protected against small perturbations which explains the vanishing resistance of superconductors. An increase of the temperature reduces the gap energy and at T_c, the BCS ground state is not favorable anymore over the Fermi sea of the metal. Because the gap parameter also depends on the strength of the pairing potential which stands for the electron-phonon coupling, different T_c are observed for different isotopes.

We now characterize in more detail the DOS of the quasiparticles, since it is, to a first approximation, what one measures in STS. The quasiparticles are created by the fermionic operators $\gamma_{\mathbf{k}}^\dagger$ that are in one-to-one correspondence with the electron operators $c_{\mathbf{k}}^\dagger$. The overall number of these states are thus equal and we have:

$$\rho_{\mathbf{SC}}(E)dE = \rho_{\mathrm{N}}(\chi)d\chi, \tag{3.37}$$

where ρ_{SC} (ρ_{N}) is the DOS of quasiparticles (electrons) in the superconducting (normal) state. For high energies, the energy dispersion of the quasiparticles with respect to the BCS ground state (equation (3.36)) is nearly identical to the free electron dispersion with respect to the Fermi level in the normal state ($\chi_{\mathbf{k}}$), so that the two DOS are considered equal. Close to the Fermi level, we can consider the ρ_{N} to be constant: $\rho_{\mathrm{N}}(\chi) = \rho_{\mathrm{N}}(0)$ (we take $\mu = 0$). Using equation (3.36), we therefore have [212]:

$$\rho_{\mathrm{SC}}(E) = \rho_{\mathrm{N}}\frac{d\chi}{dE} = \rho_{\mathrm{N}}(0)\begin{cases}\frac{E}{\sqrt{E^2-\Delta^2}}, & E > \Delta \\ 0, & E < \Delta\end{cases} \tag{3.38}$$

The finite lifetime of the quasiparticles ensures that the DOS is not actually divergent at $E = \Delta$, and one uses thus commonly the Dynes' formula with a broadening parameter Γ [45]:

$$\rho_{\mathrm{SC}}(E) = \left|\mathrm{Re}\left(\frac{E - i\Gamma}{\sqrt{(E-i\Gamma)^2 - \Delta^2}}\right)\right| \tag{3.39}$$

We show in Fig. 3.9a an illustrative picture of the transition from a metallic to a superconducting state. In the metallic state, an electron band (black dashed line) crosses the Fermi level. In the superconducting state, the quasiparticles DOS can be pictured as resulting from an effective coupling of the electron band with its hole band counterpart leading to an opening of a gap of size 2Δ around the Fermi level. The resulting DOS in the superconducting state (with a lifetime broadening) is sketched in Fig. 3.9b.

2. Yu-Shiba-Rusinov states

We now characterize how a superconductor is affected by the presence of magnetic impurities. We first treat the case of a single classical impurity and describe in detail the quantum phase

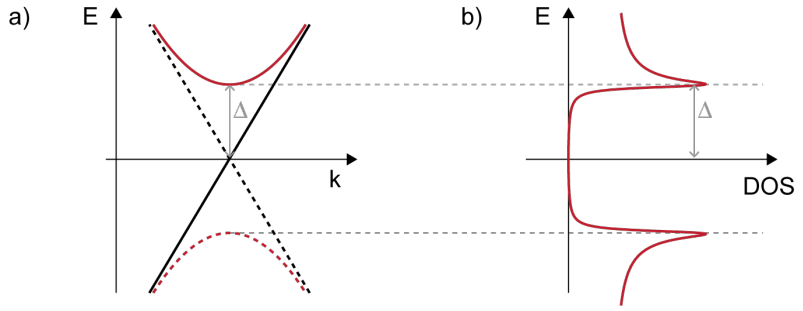

Figure 3.9.: a) Schematic drawing of an electron conduction band (black line) and its hole counterpart (black dashed line). The dispersion relation of quasiparticles $\gamma^\dagger$ in a superconductor (red line) can be understood as an effective coupling between these two bands (the red dashed line corresponds to γ and is the mirror image of the red line). b) Resulting quasiparticle DOS with gap 2Δ around E_F, taking into account the finite lifetime.

transition that is governed by the exchange coupling J. We briefly introduce the context of YSR coupling and important aspects of quantum impurities. Finally, we present the technical details concerning the measurement of YSR states with a superconducting tip.

Classical magnetic impurity

Magnetic impurities on superconductors, contrarily to non-magnetic entities, break time-reversal symmetry and thus locally perturb the Cooper pair condensate. An intuitive way to approach this problem is to consider a classical spin that creates a local magnetic field. This classical spin tends to attract electrons with spins of one flavor (*e.g.* spin down in Fig. 3.10a) and repel the other ones (*e.g.* spin up in Fig. 3.10a) thereby competing with the pairing of electrons. Depending on the strength of the local magnetic field with respect to the pairing energy Δ, a Cooper pair might be destroyed, or equivalently quasiparticles created, in the vicinity of the spin. More formally, the problem of the interaction of a classical spin with a superconductor has been addressed independently by Yu, Shiba and Rusinov in the 1960s (hence the name of the induced bound states) [227, 194, 184]. The Hamiltonian of the system is:

$$H = H_{\mathrm{BCS}} + J\mathbf{s}\cdot\mathbf{S} + V\mathbf{I}, \tag{3.40}$$

where H_{BCS} is the Hamiltonian of the substrate as introduced in the previous section (see for instance equation (3.29)) and the second and third terms come from the $s-d$ model as shown in equation (3.16): J and V are the exchange and potential scattering terms localized at the impurity. Considering a classical spin with a fixed orientation one finds that this Hamiltonian has a subgap solution with energy [161]:

$$E = \Delta\frac{1-\alpha^2+\beta^2}{\sqrt{(1-\alpha^2+\beta^2)^2+4\alpha^2}}, \tag{3.41}$$

where $\alpha = \pi\rho_{\mathrm{N}}(0)JS$ and $\beta = \pi\rho_{\mathrm{N}}(0)V$. Defining the impurity spin as spin-up and assuming an antiferromagnetic interaction, the wavefunction corresponding to this eigenvalue is a quasiparticle, called YSR state, with spin down $\gamma^\dagger = uc_\downarrow^\dagger - vc_\uparrow$. The electron ($u$) and hole ($v$) components of this quasiparticle are given by [161]:

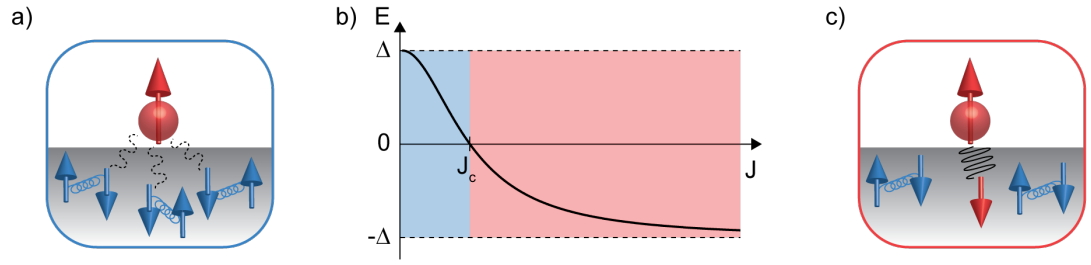

Figure 3.10.: Sketch of the interaction between a (classical) spin and a superconductor. a) The spin attracts electrons with spins of one flavor (here spin down) and repels the others (here with spin up), thereby competing with the superconducting order. This leads to the presence of a YSR bound state within the gap. b) Dependence of the YSR energy as a function of coupling strength J. At low coupling, the bound state is unoccupied and the Cooper pairs merely disturbed: the system is in a free-spin ground state as sketched in a). Upon an increase of the coupling strength, the energy of the YSR state crosses the Fermi level at a critical coupling strength J_c and the system undergoes a quantum phase transition to a screened-spin ground state. c) In the screened-spin state, the spin of the impurity is screened by the quasiparticle. The system has now a different fermionic parity.

$$u = \sqrt{1 + (\alpha + \beta)^2} \tag{3.42}$$

$$v = \sqrt{1 + (\alpha - \beta)^2} \tag{3.43}$$

This quasiparticle is a bound state within the gap of the superconductor. As one can see, the potential scattering V leads to an asymmetry of its electron and hole weights.

Next, we study in more detail the energy dependence of the YSR state and show that at a critical coupling J_c the system undergoes a quantum phase transition (QPT). Chapter 6 shows how this QPT can be induced with an STM on the single impurity level. We therefore present the theoretical framework within which the characteristic features of the transition in STS can be understood.

The Quantum Phase Transition

We display in Fig. 3.10b the evolution of the YSR energy with coupling strength J as given by equation (3.41). For very strong or vanishing coupling, the YSR energy merges with the gap edges at $\pm\Delta$ and it crosses the Fermi level at a critical crossing J_c. Thus, one can define two regimes that correspond to two different ground states: for $J < J_c$, the YSR state is not occupied by a quasiparticle and the Cooper pairs of the substrate are merely perturbed in the vicinity of the impurity, in this case the system is said to be in a *free-spin* ground state. On the other hand, for $J > J_c$, the YSR state is occupied by a quasiparticle. The presence of this quasiparticle means colloquially that a Cooper pair is broken by the exchange scattering potential at the impurity. This regime corresponds to the so-called *screened-spin* regime.

This transition can happen at $T = 0$ K and is therefore referred to as a quantum phase transition. Upon crossing this threshold the fermion parity of the ground state of the system changes. This change is detected as the $0 - \pi$ transition of the Josephson current in superconductor-quantum dot-superconductor junction [138]. The quantum phase transition has been more directly observed in asymmetric superconductor-quantum dot-normal metal junctions at mK temperatures in the Coulomb-blockade regime [40, 125, 124]. In chapter

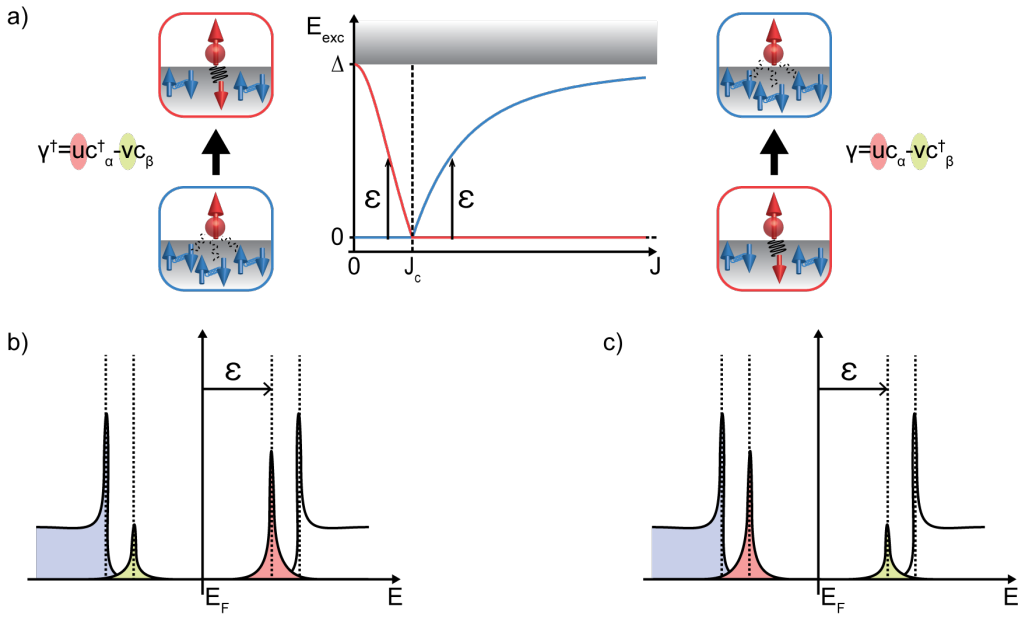

Figure 3.11.: a) Quasiparticle excitation spectrum corresponding to Fig. 3.10. Before the QPT, the excitation process creates the quasiparticle $\gamma^\dagger$. After the QPT, the ground and excited states have exchanged their roles and the excitation process corresponds now to γ. b-c) In STS, these excitation processes are seen as a pair of resonances symmetric in energy with respect to the Fermi level. The asymmetry of the resonance, related to the electron and hole weights of the YSR state, is reversed upon a crossing of the QPT.

6, we show that with STM one can also induce and detect this quantum phase transition on the single impurity level. In contrast to the other techniques, we are able to probe the discontinuous change in the spectral weights of electrons and holes in the addition spectrum of the system. But first, we give more insights into how a YSR state is detected in STS and explain how the QPT can be identified.

As explained for the case of a superconductor without impurities, in STS one does not measure the ground state of the system but rather the excitation spectrum of the quasiparticles. As shown in Fig. 3.11a (middle graph), the presence of a bound state within the superconductor gap at energy E (see equation (3.41)) is directly reflected in the excitation spectrum by an excitation at energy $|E|$. The nature of the excitation process depends on the nature of the ground state: in the free-spin regime, the excitation corresponds to a creation of the quasiparticle, the YSR state $\gamma^\dagger$. In the screened-spin regime, this quasiparticle is destroyed γ upon excitation.

Because the YSR state has both a hole-like and an electron-like component, these excitations processes are seen as two peaks at $\pm E$. The intensity of these peaks give information about the electron and hole spectral weights. More precisely, considering a YSR state $\gamma^\dagger = uc^\dagger_\alpha - vc_\beta$ (α and β being the spin indices), in the free-spin regime the excitation processes reflect $\gamma^\dagger$: the peak intensity at positive bias (electron excitation) is proportional to $|u|^2$, the electron weight of the YSR, and the one at negative bias (hole excitation) to $|v|^2$, the hole weight of the YSR state (see Fig. 3.11b). Conversely, in the screened-spin regime, the excitation process consists in the quasiparticle destruction $\gamma = uc_\alpha - vc^\dagger_\beta$, the intensity of the resonance at positive bias reflects $|v|^2$, and at negative bias $|u|^2$ (see Fig. 3.11c).

The hallmark of the QPT in STS is thus a crossing of the Fermi level of the YSR state

with a reversal of the YSR asymmetry of the resonances' intensities. We also highlight that the detection of a pair of resonances is not sufficient to determine the ground state of the system: in both cases one obtains a pair of resonances symmetric with respect to the Fermi level. We present in chapter 6 a technique that can be used to circumvent this problem.

Spatial extent of YSR states

In chapter 6 we are interested in the coupling of YSR states. The coupling model will be extensively discussed there and here we want only to briefly discuss why a coupling of these states comes into play.

The YSR state is localized at the impurity and has certain spatial extent. More precisely, for a $3D$ s-wave superconductor, the wavefunctions of its electron (ψ^+) and hole (ψ^-) components decay with lateral distance r as:

$$\psi^{\pm}(r) \propto \frac{\sin(k_F r + \delta^{\pm})}{k_F r} \exp\left[-|\sin(\delta^+ - \delta^-)|\frac{r}{\xi}\right], \tag{3.44}$$

where $\delta^{\pm}$ is the scattering of the two components given by:

$$\tan\delta^{\pm} = V \pm JS \tag{3.45}$$

This $1/r$ dependence allows for an overlap of the YSR states' wavefunctions when the impurities are a few nm apart, as shown for instance in [182]. Because these are fermionic states, the overlap of the wavefunctions leads to a hybridization and splitting of the states, if the YSR states have the same spin (i.e. if there is ferromagnetic coupling between the impurities) [107, 182, 31, 57]. When the YSR states have opposite spin (anti-ferromagnetic coupling), only an energy shift due to the influence of the neighboring magnetic field is expected.

Here we should mention that in case of a direct coupling of the impurities' states (*e.g.* the d levels of neighboring transition adatoms), the formation of coupled YSR bands also takes place, as observed for instance in [154, 178]. In this thesis we stay in the dilute limit where the impurity levels do not hybridize with one another and thus do not discuss this situation further.

Quantum impurities

Until now we have discussed the case of classical spins and thus neglected any internal degree of freedom of the impurities. In particular, we have neglected the spin-flip events that occur due to the exchange scattering potential and give rise to the Kondo effect, as explained in section II. Several experimental and theoretical works have studied the link between the YSR state energy and the Kondo temperature of the many-body states. Indeed, the Kondo effect and the YSR state induced by a quantum magnetic impurity are intrinsically related since they are caused by the same interaction. In chapter 7 we study the correlation between the lineshapes of the two effects.

The exact description of a quantum impurity adsorbed on a superconductor has to be done within the framework of many-particle theory with for instance numerical renormalization group (NRG) calculations; this goes beyond the scope of this thesis. Rather, we render the quantum character of the impurity by considering a spin-degeneracy of the induced YSR states. Indeed, for a quantum spin, time reversal is preserved, while it is broken by a classical spin. Typically, considering the spin of the impurity to be in the z direction, one rewrites equation (3.40) in the following form [161]

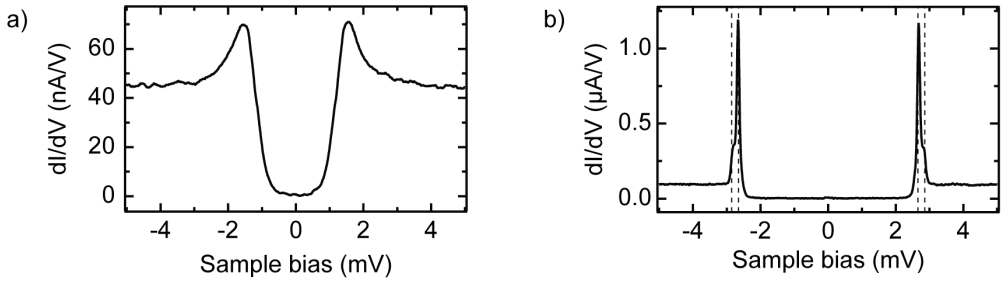

Figure 3.12.: a) $\mathrm{d}I/\mathrm{d}V$ spectrum taken with a normal tip at 1.6 K above a Pb(111) substrate (feedback opened at $V_{\mathrm{bias}} = 5$ mV, $I = 200$ pA and signal modulated with $V_{\mathrm{rms}} = 25$ μeV). b) $\mathrm{d}I/\mathrm{d}V$ spectrum taken at the same temperature with a superconducting tip (feedback opened at $V_{\mathrm{bias}} = 5$ mV, $I = 400$ pA and signal modulated with $V_{\mathrm{rms}} = 25$ μeV). The dashed lines indicate the two gaps of the Pb surface.

$$H = H_{\mathrm{BCS}} + J\sigma_z + V\tau_z, \tag{3.46}$$

where τ (σ) is the Pauli matrix in particle-hole (spin space) and fixes $\sigma_z = 1$ to find the first eigenvector with eigenvalue $E, -\Delta < E < \Delta$. The second YSR state at energy $-E$ is then determined by time-reversal symmetry.

The main consequence of the quantum nature of an impurity spin is thus the spin degeneracy of the induced YSR states [229]. In this case, a coupling between quantum impurities, whether ferromagnetic or antiferromagnetic, always leads to the observation of multiple YSR states within the superconducting gap [224, 187, 228, 104].

Probing YSR states with a superconducting tip

Finally, we present here the limitations caused by the use of superconducting tips. We use such tips in order to increase our energy resolution beyond the Fermi-Dirac broadening of metal tips [65]: at 1.1 K, one has $3.5k_BT = 330$ μeV and we reach a resolution of ~ 50 μeV with superconducting tips (compare spectra in Fig. 3.12). Yet, in this case, the $\mathrm{d}I/\mathrm{d}V$ spectra are now a convolution of both DOS of tip and sample (see chapter 2).

In order to facilitate the interpretation of the data we present here the different types of spectra obtained with a superconducting tip. We simulate in Fig. 3.13a-c different sample DOS with a pure BCS gap as expected for a bare superconducting surface as well as two DOS exhibiting one and two YSR states inside this gap. Simulating the DOS of our tip with equation (3.39) results in the $\mathrm{d}I/\mathrm{d}V$ spectra shown Fig. 3.13d-e. As one can see, we obtain a BCS-like spectrum for the bare surface but with a gap of size $2(\Delta_{\mathrm{tip}} + \Delta_{\mathrm{sample}})$. Indeed, as sketched in Fig. 3.13g, tunneling events only occur when the electron-like coherence peak of the tip (sample) is aligned with the hole-like coherence peak of the sample (tip). A single YSR state at energy E appears as a pair of resonances at $\pm(\Delta_{\mathrm{tip}} + E)$ (see Fig. 3.13h). Besides this energy shift by Δ_{tip} we notice the presence of a negative differential resistance (NDR) after the resonances. Indeed, at $|V_{\mathrm{bias}}| = |\Delta_{\mathrm{tip}} + E| + \delta V$, no current can flow through the junction leading to a current decrease. The presence of this NDR becomes relevant when probing YSR states close in energy as shown in Fig. 3.13c. Here, the two YSR state have the same weights (see Fig. 3.13c) but appear in $\mathrm{d}I/\mathrm{d}V$ with different intensities (see Fig. 3.13f). When analyzing the spatial variations of YSR states one should therefore take this effect into account. In order to circumvent this problem we use a deconvolution procedure as presented in appendix II.

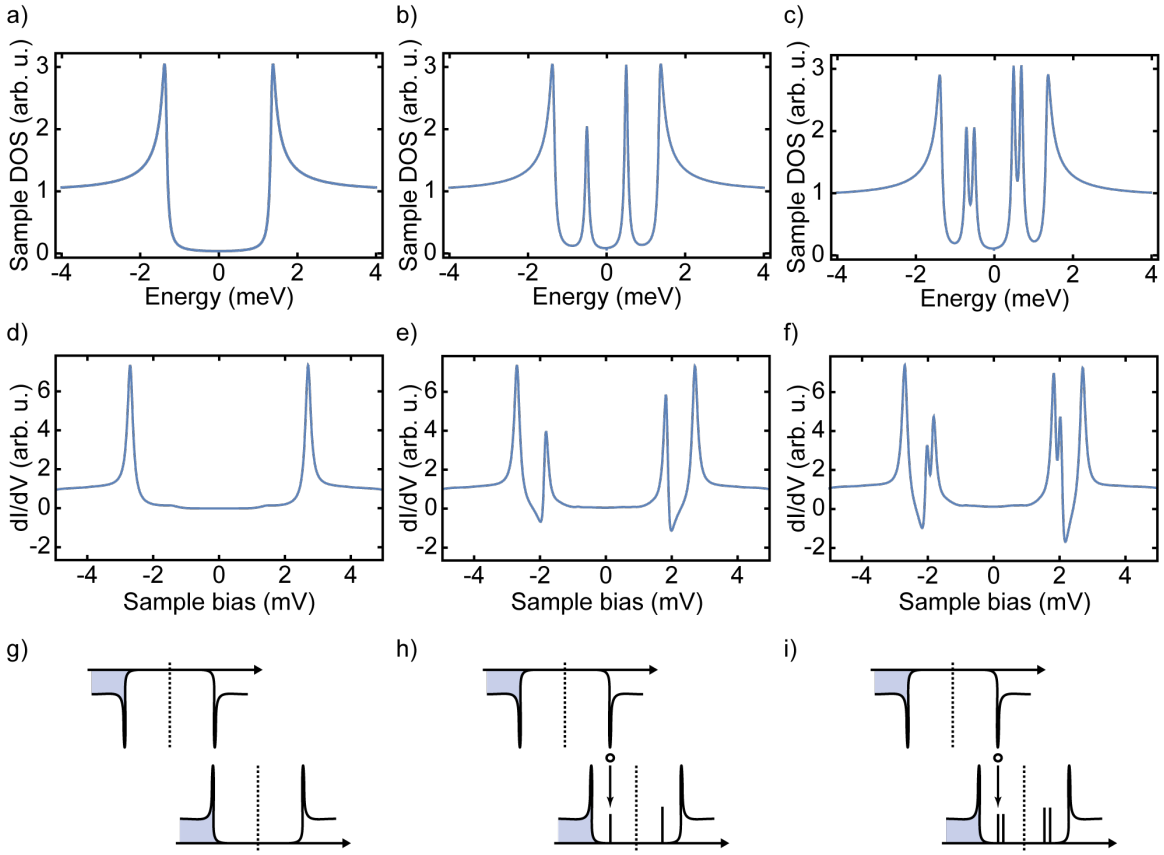

Figure 3.13.: Simulation of a sample DOS without (a), with one (b), and two (c) YSR states. Assuming a superconducting tip, the resulting $\mathrm{d}I/\mathrm{d}V$ spectra are simulated in (d-f), respectively. g-i) Sketches of the energy alignement required for tunneling that depict the observed energy shift of the features by Δ_t. Additionally to this energy shift we observe in e-f) NDR after the detection of YSR states.

Chapter 4

Fe(III)-porphine-chloride on Pb(111)

The results of this thesis concern the features observed above iron porphine (FeP) molecules on a Pb(111) surface. In this chapter, we first characterize the electronic properties of the FeP in the gas phase and give an overview of the different molecular arrangements that have been investigated. The molecules are obtained after sublimation of a powder of iron(III)-porphine-chloride molecules. We show that by adjusting the sample temperature during and after deposition of the molecules we can tune the ratio between Cl adatoms and FeP molecules. This gives rise to different molecular phases in which the molecules undergo subtle change in their environment which translates into different electronic and magnetic properties. This results in a rich variety of effects that are analyzed in details in the next chapters and presented here briefly for clarity.

I. The iron-porphin molecule

Fig. 4.1a displays the molecular model of the FeP molecule in gas phase. It consists of four pyrrole groups connected by four methine bridges and a central iron atom. The porphine molecule is the common building block of the broader family of porphyrin molecules: various functional groups (*e.g.* pyridil, ethyl or phenyl groups) can be attached to the macrocyclic ring and several elements besides Fe can be hosted in its center. This versatility is intensively used for various applications in hybrid molecular and photovoltaic devices [72, 127, 129, 225]. In this thesis, we show that the electronic and magnetic properties of the porphine molecule can be controlled without the need of a chemical modification but by a fine tuning of its environment.

We first discuss the electronic properties of the FeP molecule in gas phase. Fig. 4.1b shows the results of DFT calculations performed with *Gaussian 16* using the B3PW91 method and the 6-31++g(d,p) basis set. The energy of the orbitals is given with respect to the vacuum level and the black dashed line indicates the separation between the occupied and unoccupied orbitals. In accordance with previous theoretical studies of the FeP molecule in gas phase we find that the molecule carries a spin $S = 1$ [5, 24]. Orbitals of the majority (minority) spin channel are denoted with an a (b) index and displayed in the top (lower) part of Fig. 4.1b. We observe a strong hybridization of the Fe levels with the molecular ligand. In particular, as in [5, 24], a strong $\pi - \pi$ interaction mixes the Fe d_π levels with the N p_z orbitals. This leads to hybrid orbitals such as 92a and 92b that are localized both over the Fe atom and

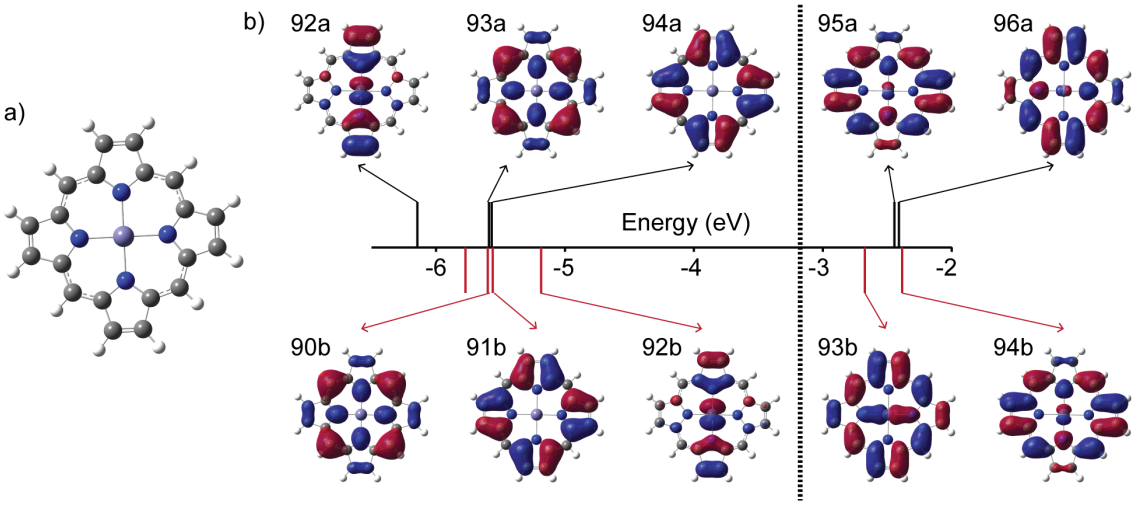

Figure 4.1.: a) Molecular model of the iron-porphine molecule. The central Fe atom (light violet) is surrounded by the four nitrogen atoms (blue) of the porphine ring made out of carbon atoms (grey) and with hydrogen atoms at its rim. b) DFT calculations performed for the FeP in gas phase. Orbitals of the majority (minority) spin channel are shown in the top (lower) part. The orbitals' energy are indicated with respect to the vacuum level and the black dashed line indicates the separation between occupied and unoccupied orbitals. A strong hybridization between the Fe d levels and the molecular orbitals is observed.

molecular ligand. Additionally, in-plane σ-bonds form between the vacant Fe $d_{x^2-y^2}$ level and the occupied p_z orbital of the N atoms. This effect leads to a partial occupation of the $d_{x^2-y^2}$ by electron back-donation from the occupied π-orbital [5]. It is shown in [24] that this results in an admixture of the electronic state with an electron occupancy of the Fe d-levels $N = 6$ to configurations with $N = 5$ and $N = 7$. All in all, this complex admixture renders the determination of the Fe ground state electronic configuration complicated and both configuration shown in Fig. 3.1b and c are valid candidates [5, 24]. Indeed, we would like to highlight that, here, the orbitals carrying the unpaired electron are not easily identified as Fe states lying close to Fermi energy.

II. Presentation of the different phases

In this section we show how the molecular self-assembly can be controlled by a modification of the sample temperature during and after evaporation of the molecules. We should mention that the sample temperature during the molecular deposition cannot be measured due to technical details but is estimated with respect to room temperature as the sample can be pre-cooled or pre-annealed before evaporation. For each of the obtained molecular phase, we describe the molecular arrangement and give a brief description of the various consequences for the electronic and magnetic properties of the molecules.

1. Tuning the FeP-Cl stoichiometry

Fig. 4.2a and d show topography images of preparations obtained after deposition of iron(III)-porphine-chloride molecules on a Pb(111) sample held above and below room temperature, respectively. The lower topography images show enhanced views of these preparations with

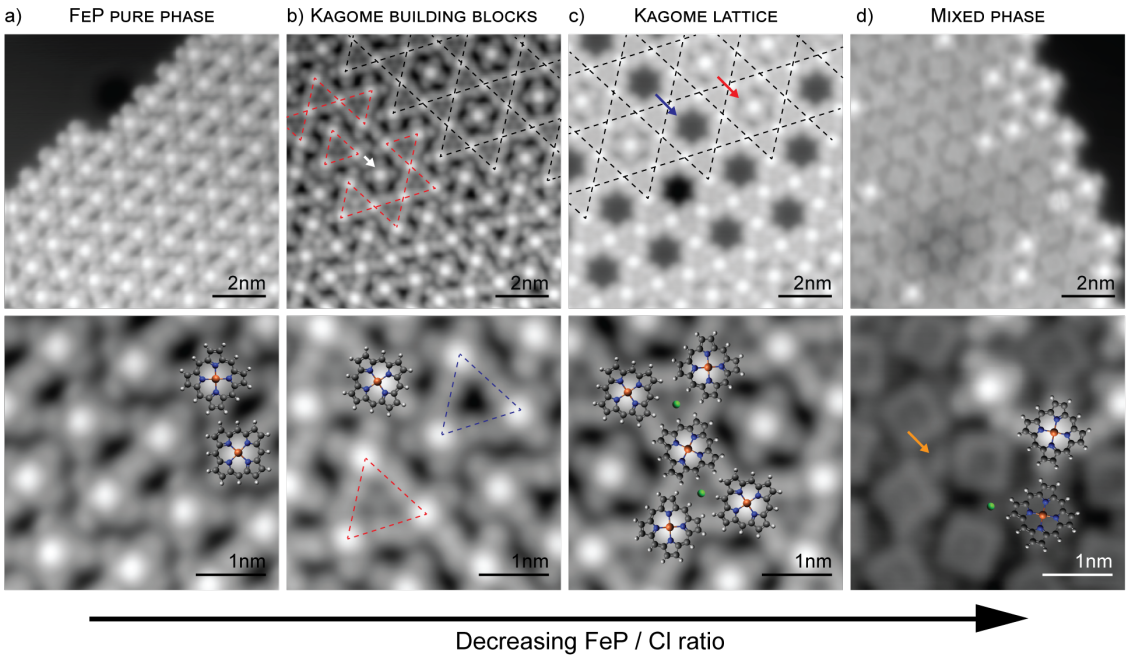

Figure 4.2.: Topography images of the different phases obtained after deposition of FeP-Cl molecules on Pb(111). a) After evaporation on a warm sample only FeP molecules are present ($V_{\text{bias}} = 5$ mV, $I = 200$ pA). b) Molecular phase obtained when the FeP/Cl ratio is below 1/2 ($V_{\text{bias}} = 5$ mV, $I = 200$ pA). c) A Kagome lattice (see black dashed lines) is fully formed when the FeP/Cl ratio is between 1/2 and 2/3 ($V_{\text{bias}} = 5$ mV, $I = 50$ pA). d) For higher ratio (after evaporation at low sample temperature), the molecules arrange in a hexagonal lattice with Cl adatoms randomly distributed between them ($V_{\text{bias}} = 20$ mV, $I = 500$ pA, see orange arrow).

overlaid molecular models. In both cases, the molecules form islands in which they arrange in a hexagonal lattice. Interestingly, we notice that small protrusions are present in-between the molecules on the preparation obtained after deposition on a cold sample (see orange arrow in the lower topography image of Fig. 4.2d), but absent on the other preparation. We assign these protrusions to the presence of Cl adatoms that desorb from the surface at high temperatures.

More precisely, Fig. 4.3 shows that additionally to the two types of molecules shown in Fig. 4.2d, a few molecules ($< 1\%$) display a high protrusion above their center (see height profile in Fig. 4.3b taken along the red line shown in Fig. 4.3a). As will be shown in the next chapter, the first two types differ mainly in their electronic properties and are both assigned to dechlorinated FeP molecules. On the contrary, the molecules with a high protrusion display in scanning tunneling spectroscopy (STS) (see Fig. 4.3c) a very similar spectrum to what has been observed for iron-octa-ethyl-porphyrin-chloride (FeOEP-Cl) on Pb(111) [85]: two pairs of peaks outside the superconducting gap assigned in [85] to spin excitations. As explained in chapter 3, the oxidation state of the Fe atoms as well as its spin state and magnetic anisotropy are dictated mainly by its direct surroundings. Because the FeP and FeOEP molecules only differ in that ethyl groups are attached at the periphery of the porphine ring for the latter, the Fe atoms in both molecules are subject to similar environments. Consequently, we assign the molecules with a high protrusion to FeP-Cl molecules. Most molecules have thus lost their chlorine ligand upon adsorption. We therefore assign the protrusions seen in between

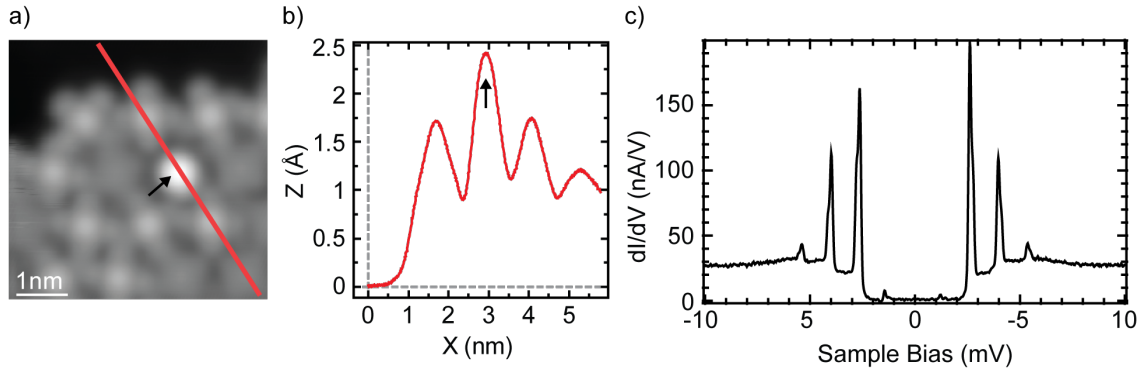

Figure 4.3.: a) Topography image of an island in which three types of molecules can be identified ($V_{\text{bias}} = -45$ mV, $I = 100$ pA) as shown by the height profile taken along the red line and shown in b). c) $\mathrm{d}I/\mathrm{d}V$ spectrum recorded above the center of a molecule with a very bright protrusion as the one indicated by an arrow in a (feedback opened at $V_{\text{bias}} = 20$ mV, $I = 500$ pA and signal modulated with $V_{\text{rms}} = 50$ μeV).

the molecules to Cl adatoms. Indeed, as shown in Fig. 4.4, we were able to manipulate one of these protrusions by approaching the tip above it: Fig. 4.4b shows the current traces upon approach (black) and retraction (red) of the tip above the position marked by a red cross in Fig. 4.4a (0 pm corresponds to the height at which the feedback was opened with $V_{\text{bias}} = -5$ mV and $I = 500$ pA). Scanning the area after the approach (see Fig. 4.4c and d) shows that no protrusion is present anymore at the position at which the manipulation was performed (red cross) and that the neighboring molecule displays now a round protrusion above its center similar to those observed for FeP-Cl molecules. We note that most molecules in the area changed their type upon the manipulation and investigate in more details in the next chapter the possible mechanisms underlying this phenomena.

One could argue that the protrusions seen in-between the molecules could correspond as well to Pb adatoms [4]. Nonetheless, as shown in Fig. 4.2a, no protrusion is observed when the molecules are evaporated on a sample held above room temperature for which the mobility of Pb atoms is higher. Moreover, Fig. 4.2b and c show topography images of the molecular phases obtained after annealing for several minutes to 373 K preparations such as the one depicted in Fig. 4.2d. On the preparation shown in Fig. 4.2c one can see that the molecules arrange in a Kagome lattice (see black-dashed lines) in which the holes of the lattice are either empty (blue arrow) or filled (red arrow) with a molecule. This Kagome lattice is made out of triangles in which the molecules are rotated by 60° with respect to each other (see molecular models overlaid on top of the lower topograph). On the preparation shown in Fig. 4.2b one can recognize the Kagome lattice in the top-right part of the image (see black dashed lines) and identify small structures made of only a few triangles (see red dashed lines) while other molecules do not adopt a specific orientation with respect to their neighbors (see white arrow). In the enhanced view of this preparation (lower topography image) we can notice that some triangles have a protrusion in their centers (red triangle) while other remain empty (blue triangle). By comparison, we see that the Kagome lattice is made of such triangles with a central small protrusion that we assign to the presence of an adatom. The overall amount of adatoms thus decreases upon annealing as one would expect in the case of Cl adatoms but not of Pb adatoms. Finally, we note that such Kagome lattices and small units were also obtained after hydrogen contamination of samples such as the one shown in Fig. 4.2d. There, the transition was interpreted as a reaction of the

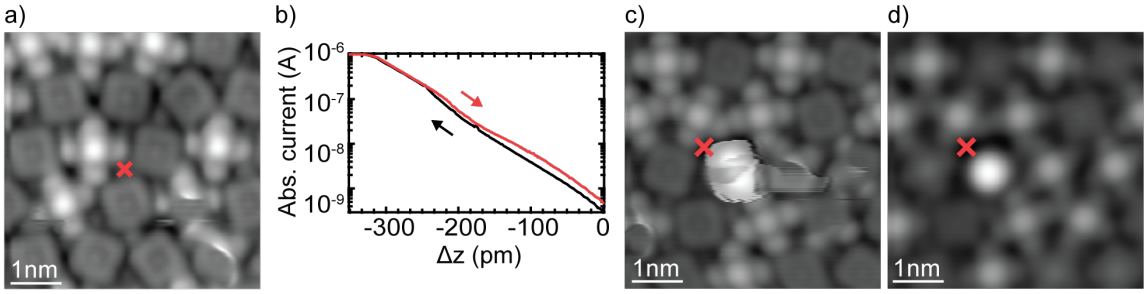

Figure 4.4.: a) Topography image ($V_{\text{bias}} = -5$ mV, $I = 500$ pA) before a tip approach at the position indicated by the red cross b) Evolution of the tunneling upon tip approach (black) and retraction (red) (feedback opened at $V_{\text{bias}} = -5$ mV, $I = 500$ pA) c) Topography image ($V_{\text{bias}} = -5$ mV, $I = 500$ pA) of the area after the manipulation (the apex of the tip had to be reshaped and the image is slightly shifted, the position of the vertical manipulation is indicated by a red cross and was identified in relation to the border of the island - not shown). d) Topography image of the same are as in c but with different scanning parameters ($V_{\text{bias}} = -50$ mV, $I = 100$ pA).

hydrogen with the Cl atoms on the surface and desorption of HCl molecules leading to a decrease of the amount of Cl adatoms. All in all, these findings are consistent with reports in the literature concerning FeOEP-Cl molecules on Pb(111) and Au(111) [85, 87, 89, 88] for which it was shown that the Cl ligands of the molecules are partially preserved when the molecules are evaporated on cold samples and desorb upon annealing. Indeed, this indicates a surface-assisted desorption mechanism of the Cl atoms that is consistent with the presence of Cl adatoms at low temperatures in our case.

We can therefore conclude that the different molecular arrangements shown in Fig. 4.2 are formed at different FeP-Cl stiochiometry and that the Kagome lattice appears to be the most stable phase. More precisely, after deposition on a cold sample the ratio of Cl atoms to FeP molecules is around one, and the excess of chlorine prevents the formation of the lattice. However, upon annealing, some of the chlorine adatoms desorb, so that as soon as the ratio goes at least locally below 2/3 the Kagome lattice starts to form. Upon a further decrease of this ratio, the excess of FeP molecules is accommodated in the holes of the Kagome. When this ratio goes below 1/2, corresponding to a Kagome lattice with all its holes filled with a molecules, FeP molecules are now in excess and smaller structures, that we refer to as Kagome building blocks, are formed. When no Cl is present on the surface, the FeP arrange as shown in Fig. 4.2a and no modification is observed upon annealing.

In the following we discuss in more details the organization of the different phases that are referred to as presented in Fig. 4.2. We also present the most characteristic spectroscopic features observed above the FeP molecules in these different phases in order to introduce the topics discussed in the next chapters.

2. The mixed phase

We first describe the phase obtained after evaporation on samples held below room temperatures. In these preparations, the FeP molecules appear at low biases either with a protrusion above their center or a depression. These two types are referred to as bright and dark molecules (see Fig. 4.2d and Fig. 4.5a). The origin behind these different appearances is discussed in the next chapter but one can already notice in the topography images of Fig. 4.2d and Fig. 4.5a that the molecules at the edge of the islands are bright while dark

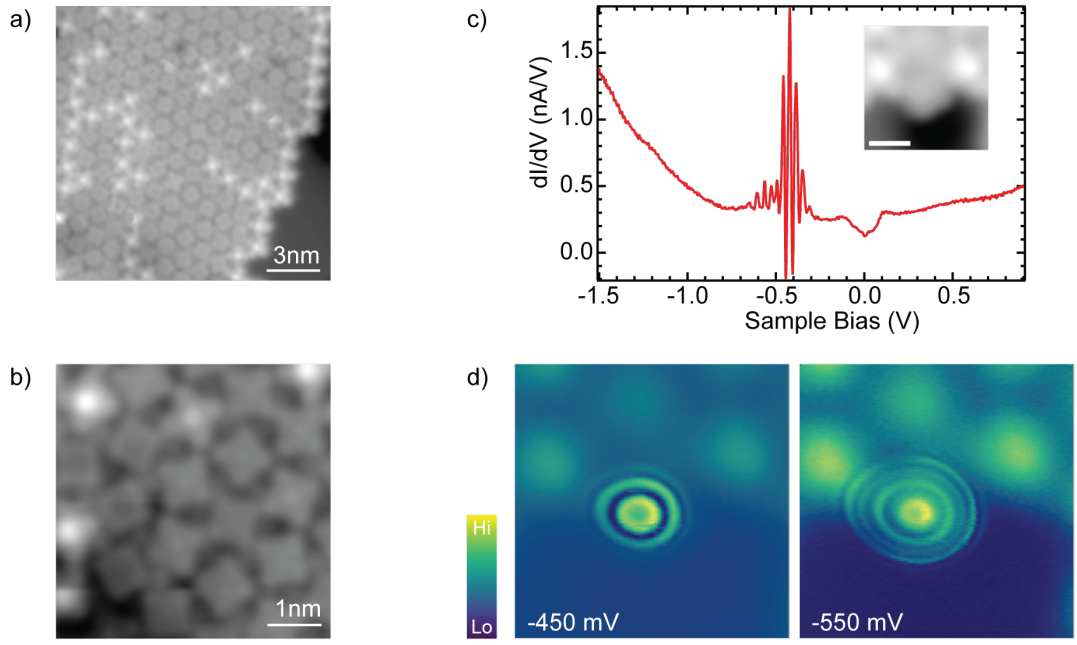

Figure 4.5.: a) Topography image ($V_{\text{bias}} = 5$ mV, $I = 200$ pA) of an island obtained after evaporation on a sample held at cold temperatures. b) The molecules arrange in a hexagonal lattice whose lattice vectors are along the Pb lattice orientations ($V_{\text{bias}} = 20$ mV, $I = 200$ pA). c) $\mathrm{d}I/\mathrm{d}V$ spectrum recorded above the center of the dark molecule shown in the inset (feedback opened at $V_{\text{bias}} = 900$ mV, $I = 300$ pA and signal modulated with $V_{\text{rms}} = 5$ mV). d) Constant height $\mathrm{d}I/\mathrm{d}V$ maps recorded above the area shown in the topography image in the inset of c.

molecules preponderate inside the islands. An enhanced view of the molecules inside an island is shown in Fig. 4.5b. The molecules arrange in a hexagonal lattice with a nearest neighbor distance of 1.2 nm. The lattice vectors are oriented along the Pb lattice orientation. The molecules do not seem to adopt preferred orientations with respect to these vectors which is most likely related to the presence of the Cl adatoms that are randomly distributed between the molecules.

The characteristics of the different molecular types are analyzed in the next chapter. The most striking fingerprint that we observe is the presence of oscillations in $\mathrm{d}I/\mathrm{d}V$ above certain molecules as shown in Fig. 4.5c. These oscillations appear as several rings in constant height $\mathrm{d}I/\mathrm{d}V$ maps whose radii depend on the applied bias (see Fig. 4.5d). This behavior resembles the one observed for charging rings as discussed in chapter 2, section III.4. However, we note that the absence of a decoupling layer as well as the presence of a multitude of these rings above a single molecule discard the scenario of an occupied level pulled below Fermi energy by the applied bias. Rather, we try to understand how the presence of chlorine adatoms can modify directly or indirectly the electric field at the surface. We then propose that the electric field of the tip modifies the latter which leads in some cases to new image potential states. We finally argue that such induced states gate the system locally, leading to steps in the current and peaks and/or dips in $\mathrm{d}I/\mathrm{d}V$.

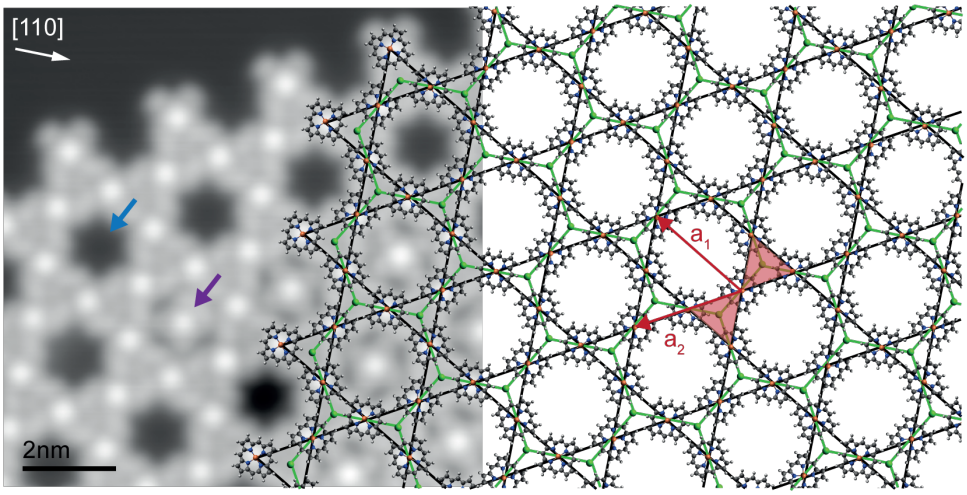

Figure 4.6.: Topography image ($V_{\text{bias}} = 5$ mV, $I = 50$ pA) of the Kagome phase. A molecular model is overlaid and extented to the right of the image for clarity. The FeP molecules arrange in a Kagome lattice as indicated by the black lines and the Cl adatoms in a honeycomb lattice as shown by the green lines. The unit cell of the honeycomb-Kagome lattice is shown in red along with the lattice vectors.

3. The Kagome lattice and its building blocks

We now present the molecular arrangements obtained after annealing to 373 K the previous phase. Fig. 4.6 shows a topography image of such a preparation. A model for the adsorption of the FeP molecules and Cl adatoms is partially overlaid to the image and extended to the right for clarity. There, it can be seen that the FeP molecules and Cl atoms arrange in a Honeycomb-Kagome lattice, with the FeP molecules (Cl atoms) occupying the Kagome (Honeycomb) sites (see black and green lines indicating the Kagome and Honeycomb lattices, respectively). The elementary cell consists of 3 FeP molecules and 2 Cl atoms, as shown by the red unit on the right part of Fig. 4.6. The Kagome lattice vectors $\vec{a_1}$ and $\vec{a_2}$ are rotated by 30° with respect to the Pb(111) lattice orientation (that is determined thanks to the Neon impurities patterns) and have a length of 2.4 nm. The three orientations of the molecules observed in the Kagome lattice are thus equivalent. Finally, we note that the holes of the Kagome can either be occupied by a FeP molecule (violet arrow) or empty (blue arrow). The proportion of occupied holes is related to the overall stoichiometry between FeP and Cl and varies between the different preparations. On preparations with a low amount of chlorine one can identify structures made of only a few triangles that compose the Kagome lattice. These structures are referred to as Kagome building blocks.

This phase is particularly suited for the study of Yu-Shiba-Rusinov states. As one can see in Fig. 4.7a, the molecule at the edge of the island displays one pair of sharp resonances inside the superconducting gap (black spectrum) that we attribute to the presence of a single YSR state. In comparison, the molecules inside the island show a broader resonance with different intensities (red and blue spectra). A $\mathrm{d}I/\mathrm{d}V$ map recorded inside this resonance shows that the signal is delocalized over the island. We assign this resonance to a YSR band arising from the coupling of YSR states between neighboring molecules that are part of the Kagome lattice. This is proven in the last chapter of this thesis (chapter 8) by a detailed analysis of the YSR states in small Kagome building blocks. The properties of the molecules in the normal states and the hypothesis of a Kondo lattice is also discussed.

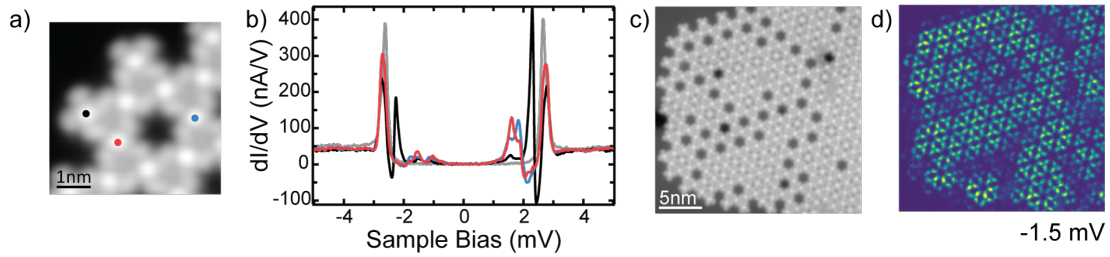

Figure 4.7.: a) Topography image ($V_{\text{bias}} = -45$ mV, $I = 100$ pA) of a border of an island of the Kagome phase. b) dI/dV spectra taken with a superconducting tip above the center of the molecules as shown by the dots in a (feedback opened at $V_{\text{bias}} = 5$ mV, $I = 200$ pA and signal modulated with $V_{\text{rms}} = 15$ μeV). A reference spectrum taken above the bare Pb substrate is shown in grey. c) Topography image ($V_{\text{bias}} = 5$ mV, $I = 50$ pA) of an island whose height profile was followed to record the dI/dV map at $V_{\text{bias}} = -1.5$ mV shown in d).

The study of the YSR states induced by the FeP molecules is first addressed in chapter 6 with the study of molecules that are not coupled and thus display only one YSR state. In particular, we show that the flexibility of the molecular ligand enables us to tune the energy of the YSR state. This allows us to identify the nature of the ground state (screened or free-spin state) but also to tune continuously the system through the quantum phase transition discussed in chapter 3 section III.2. Moreover, we investigate the transport properties of the junction in the presence of a YSR state. We show that the latter can be excited by single quasi-particles as well as by multiple Andreev reflections.

In chapter 7, we characterize the influence of the molecular orbitals on the lineshape of the YSR and Kondo states. For the FeP molecules, dI/dV spectra recorded above the centers and ligands of the molecules (see Fig. 4.8b) on a metallic substrate (external magnetic field of 200 mT) show the presence of a broad resonance in the negative bias regime that we attribute to the molecular HOMO but no resonance is detected in the positive bias regime (the feature around 100 mV is assigned to the tip as it is also present in the reference spectrum taken above the bare Pb surface). A sharp resonance is seen around Fermi energy on top of the HOMO. dI/dV spectra recorded over a smaller energy range (see Fig. 4.8c) show that it corresponds to a Kondo resonance. Interestingly, the lineshape of this resonance changes strongly between the center and the ligand of the molecule. We want to assign this lineshape change to the local variation of the electron-hole asymmetry of the scattering of electrons onto the impurity. In order to disentangle the role of transport through the frontier orbitals (HOMO and LUMO) and disentangle a possible interference between a tunneling path going to the HOMO of the molecule we present in chapter 7 the study of the YSR and Kondo lineshape on a similar molecule: the iron-tetra-pyridyl-porphyrin (Fe-TPyP) molecule on Pb(111).

4. The FeP pure phase

Finally, we examine the phase in which no chlorine adatoms are present on the surface. Fig. 4.9a shows a topography image of this phase with a corresponding molecular model below it. The molecules arrange in a hexagonal lattice with a nearest neighbor distance of 1.2 nm. Moreover, one can notice that the molecules adopt two different orientations that are rotated by 45° with respect to each other. As a result, the molecular arrangement consists of a hexagonal lattice with three molecules in its unit cell as indicated by the molecular model in

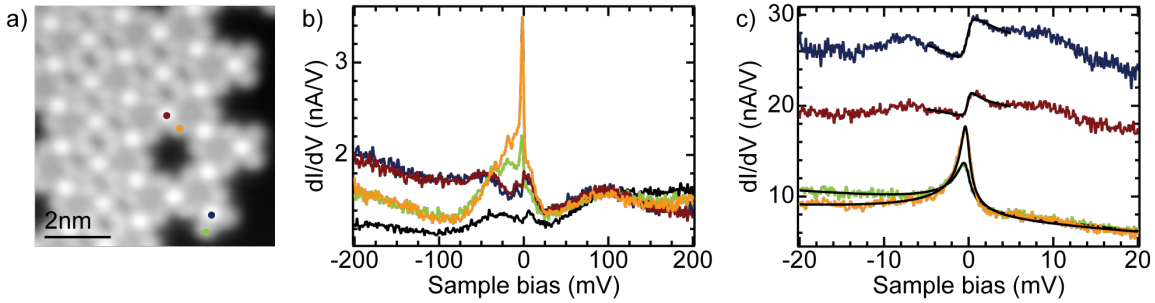

Figure 4.8.: a) Topography image ($V_{\text{bias}} = -45$ mV, $I = 30$ pA) of a molecular island in which a Kagome lattice is formed. b) dI/dV spectra (feedback opened at $V_{\text{bias}} = 200$ mV, $I = 300$ pA and signal modulated with $V_{\text{rms}} = 1$ mV) recorded above the centers and ligands of two molecules as shown in a. An external magnetic field of 200 mT was applied and a reference spectrum taken above Pb is shown in black (for the reference spectrum the magnetic field is 100 mT). c) dI/dV spectra (feedback opened above the ligand of the molecules -for both positions: center and ligand- at $V_{\text{bias}} = 20$ mV, $I = 150$ pA and signal modulated with $V_{\text{rms}} = 50$ μV) taken above the same positions as in b but recorded over a smaller energy range (still under an external magnetic field of 200 mT). The black curves are Frota-Fano fits of the resonances.

Fig. 4.9a. We note that the lattice vectors (red arrows) are parallel to the lattice orientation of the Pb(111) surface so that the two orientations of the molecules are not equivalent.

These different orientations do not lead to any difference in the spectroscopic signature of the molecules. More precisely, as is shown in Fig. 4.9b and c, no orbital is detected in the positive bias regime while a few resonances are to be seen in the negative bias regime: above the ligand, a resonance at $V_{\text{bias}} = -70$ mV and above the Fe center a broader one around $V_{\text{bias}} = -250$ mV as well as a shallow one around Fermi energy. In the superconducting state, besides a small asymmetry of the coherence peaks above the ligand (red curve) no difference with the reference spectrum recorded on Pb(111) is observed. The asymmetry of the coherence peaks can be caused by the presence of a YSR state at the gap edge but it can also be due to the onset of the orbital in the background. Since we do not observe the presence of the Kondo effect in the normal state (the spectra in c are recorded under an external magnetic field of 800 mT) and because the asymmetry is only present above the molecular ligand, the second scenario appears most likely.

This phase is not studied in more details in this thesis but used as a reference system to characterize more precisely the influence of the Cl adatoms on the electronic and magnetic properties of the molecules.

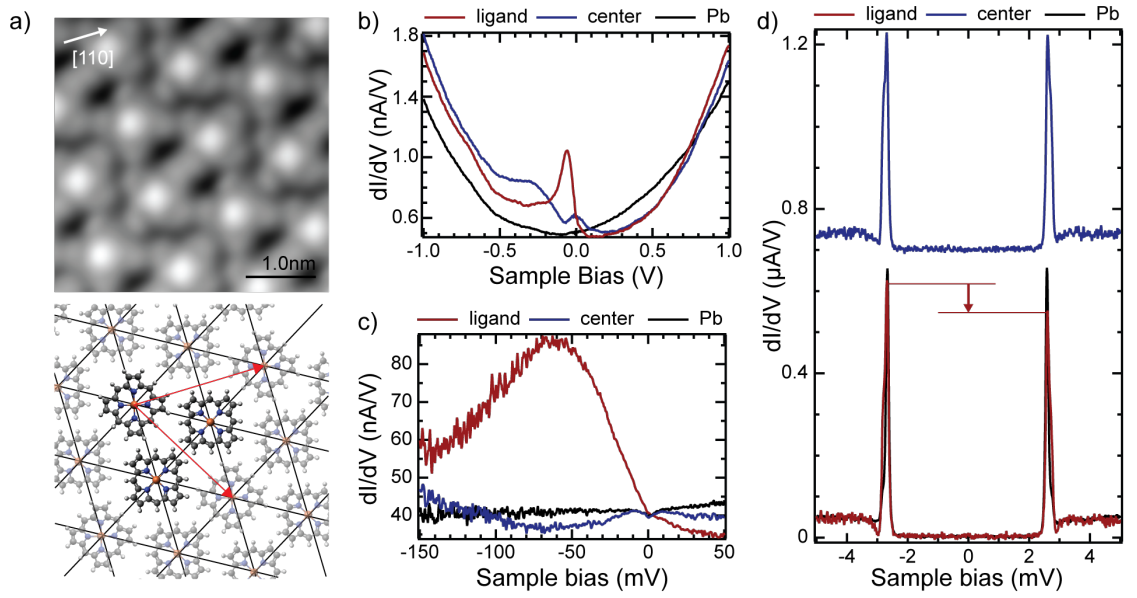

Figure 4.9.: a) Topography image ($V_{\mathrm{bias}} = 5$ mV, $I = 200$ pA) of the phase without Cl adatoms. A sketch of the molecular arrangement is displayed below the image. b) $\mathrm{d}I/\mathrm{d}V$ spectra recorded above the bare Pb surface (black), center and ligand of the molecules (feedback opened at $V_{\mathrm{bias}} = 1$ V, $I = 800$ pA and signal modulated with $V_{\mathrm{rms}} = 5$ mV). c) $\mathrm{d}I/\mathrm{d}V$ spectra recorded over a smaller energy range and with an external magnetic field of 800 mT (feedback opened at $V_{\mathrm{bias}} = 5$ mV, $I = 200$ pA and signal modulated with $V_{\mathrm{rms}} = 500$ μV). d) $\mathrm{d}I/\mathrm{d}V$ spectra recorded in the superconducting state with a superconducting tip (a reference spectrum is shown in black) show that no YSR state is detected inside the superconducting gap (feedback opened at $V_{\mathrm{bias}} = 5$ mV, $I = 200$ pA and signal modulated with $V_{\mathrm{rms}} = 15$ μV).

Chapter 5

Local gating by image potential states

Understanding the energy level alignment of molecules adsorbed on metal surfaces is one of the major challenges of molecular electronic nowadays. Often, the study of the interaction is done by incorporating a decoupling layer between the molecules and a metal substrate. Indeed, in this way one can better control the electronic properties and even charge states of adsorbates [172, 206]. In general, it is assumed that upon adsorption on a metal surface, the molecular levels are broadened and pinned to the Fermi or vacuum level which hinders any further alteration of the molecules' electronic properties.

Here, we study the properties of iron-porphine molecules when forming islands in which Cl adatoms are also present. We show that the random distribution of Cl adatoms alters the electronic properties of the molecules in a non-homogeneous way. This leads to the presence of two different molecular types that exhibit different charge distributions but also affect the fingerprints of the molecules in $\mathrm{d}I/\mathrm{d}V$ spectra. In particular, we show that in some cases a local gating can be induced by the electric field of the tip. We interpret this as caused by a modification of the number of image potential states trapped in front of the surface.

I. Molecular diversity and its origin

In this section, we characterize the two main types of molecules obtained after evaporation of iron-porphine-chloride molecules on cold Pb(111) samples (see chapter 4). In order to determine the origin of this diversity we analyze the electronic properties of the molecules as well as their structure and charge distributions by means of AFM measurements.

1. Influence of the bias on the appearance of the molecules

We first characterize the appearance of the molecules depending on the scanning conditions. Fig. 5.1a and b show topography images of the same area taken with different set points: $V_{\mathrm{bias}} = 5$ mV, $I = 200$ pA and $V_{\mathrm{bias}} = 700$ mV, $I = 200$ pA, respectively. The lower graphs show the corresponding height profiles of the molecules taken along the same line that is shown in red in the topography images. At low bias, one can identify two types of molecules depending on the appearance of their center as a protrusion (bright type, see green arrow in Fig. 5.1a) or a depression (dark type, see orange arrow in Fig. 5.1a). We note, however, that at high bias all molecules have the same apparent height. With a particularly sharp and/or functionalized tip one can moreover observe small variations in the appearance of

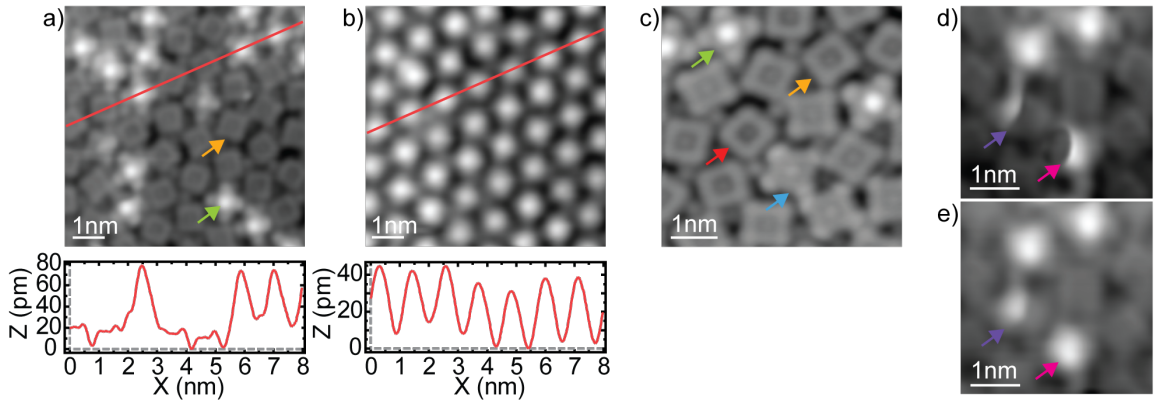

Figure 5.1.: a) Topography image recorded with $V_{\text{bias}} = 5$ mV, $I = 200$ pA in which bright (green arrow) and dark (orange arrow) can be identified. The lower graph displays the height profile of the molecules along the red line shown in the topography image. b) Topography image of the same area but recorded with a higher bias: $V_{\text{bias}} = 700$ mV, $I = 200$ pA. The height profile shown in the lower graph is recorded above the same line as in a) and illustrate that all molecules have now the same apparent height. c) Topography image recorded with a functionalized tip ($V_{\text{bias}} = 20$ mV, $I = 50$ pA). d-e) Topography images of the same area recorded with different biases (d)$V_{\text{bias}} = 5$ mV, $I = 200$ pA and e)$V_{\text{bias}} = 20$ mV, $I = 200$ pA) showing the presence of hybrid molecules on the surface.

molecules of the two different types. This is for instance the case in the topography image shown in Fig. 5.1c (set point: $V_{\text{bias}} = 20$ mV, $I = 50$ pA). There, one can identify bright molecules with a central protrusion and a clover shape (green arrow) and dark molecules with a central depression and a square shape (orange arrow). The height of the depression on the center of dark molecules varies slightly from one molecule to another (compare molecules indicated by red and orange arrows). Also, a few molecules appear to inherit partially the appearance of the two types with a very small protrusion on their center and an overall square shape with faint protrusions at the corners (blue arrow). Interestingly, we also observe molecules that have a hybrid appearance as shown in Fig. 5.1d (see violet and pink arrows, scanning parameters $V_{\text{bias}} = 5$ mV, $I = 200$ pA). There, depending on the position of the tip, the molecules appear either bright or dark. Scanning the same area at a higher bias ($V_{\text{bias}} = 20$ mV, $I = 200$ pA), as shown in Fig. 5.1e, changes the appearance of these hybrid molecules: one of the molecule appear now entirely bright (pink arrow) and the other shows a different position of the boundary between the two types (violet arrow). These results indicate that the molecules should vary mainly in their electronic properties and not drastically in their composition.

During measurement, we observed switching processes between the different types. This is for instance shown in Fig. 5.2, where we show sequential topography images recorded after positioning the tip at the crosses' locations and switching the bias from 900 mV to −900 mV in constant height mode with the feedback opened at $V_{\text{bias}} = 900$ mV and $I = 300$ pA. We observe switching of a dark molecule to a bright molecule (see red arrow in Fig. 5.2a and b) but also reversed processes (red arrow in Fig. 5.2b and c) as well as a dark molecule switching to a hybrid molecule (green arrow in Fig. 5.2b and c). The mechanism behind these switching phenomena could not be identified as they happened not in a controlled manner. Yet, interestingly, these switching events seem to be correlated to different positions of the protrusions in between the molecules (see orange arrows in Fig. 5.2). These protrusions are assigned to Cl adatoms but unfortunately, we cannot identify the exact position and

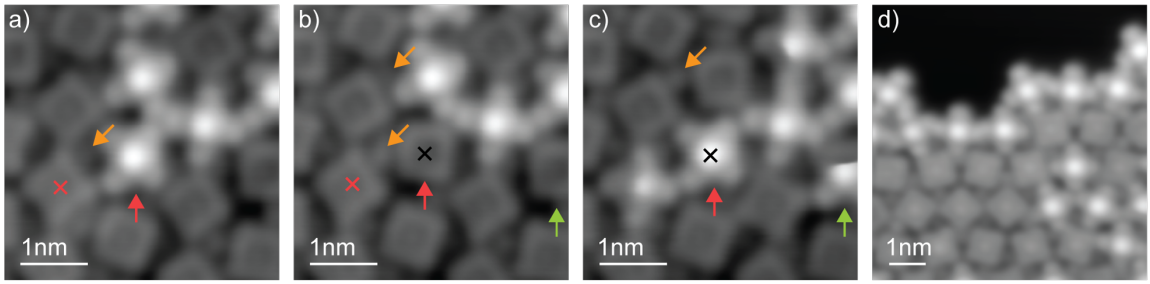

Figure 5.2.: a-c) Topography image of the same area recorded with the same set point: $V_{\text{bias}} = 5$ mV, $I = 200$ pA. Molecules switched their appearance after the tip was placed at the crosses' locations (red cross from a to b and black cross from b to c), the feedback opened with $V_{\text{bias}} = 900$ mV, $I = 300$ pA and the bias sweeped from 900 mV to -900 mV. d) Topography image ($V_{\text{bias}} = -45$ mV, $I = 500$ pA) of a border of an island.

number of all Cl adatoms on the preparation. The orange arrows in Fig. 5.2 indicate positions in which there is a clear change between the topography images but in general it is often hard to exactly distinguish all protrusions. Besides, it is impossible to tell if one protrusion corresponds to one or several Cl adatoms. Therefore, we restrict ourselves to a qualitative observation: the switching events are related to changes in the positions of Cl adatoms.

The fact the presence of Cl adatoms in the vicinity of the molecules influences their type is indeed consistent with the observations made in chapter 4: in the other phases when less or no chlorine is present the molecules are bright. Also, we observe here that the molecules at the edges of the islands are mostly bright, as shown in Fig. 5.2d. Since no protrusion is detected on the boundary toward the bare Pb(111) surface these molecules are surrounded, on average, by fewer Cl adatoms than inside the island where the dark type dominates. The Cl adatoms appear thus to trigger the appearance of the dark type.

All in all, these results point toward different electronic properties of the molecules rather than different chemical compositions. This is in accordance with our observation made in chapter 4 of a third type molecule that we identified as FeP-Cl, the other molecules being thus all assigned to FeP. The presence of Cl adatoms in their proximity most likely lies at the root of the observed molecular diversity.

2. AFM measurements

In order to confirm the identical chemical composition of bright and dark molecules we now characterize them with atomic force microscopy (AFM).

As we have seen in chapter 2 section III, frequency shift approach curves ($\Delta f(z)$) allow to characterize the interaction between an adsorbate and the tip apex. More precisely, it has been shown in literature that differences in the short range forces can be used to identify the different nature of adsorbates on a surface [203, 74, 75].

We record $\Delta f(z)$-curves above the centers of a bright and a dark molecule as shown in Fig. 5.3b. Following the procedure described in [185], we then extract the interaction forces between the molecules and the tip apex in Fig. 5.3c. The spectra are offset in z to compensate for the different apparent height of the molecules at the parameters used to open the feedback before each spectrum. Δz corresponds to the (relative) distance between the tip and the sample plane (we define arbitrarily $\Delta z = 0$ as the height at which the feedback was opened above the center of the bright molecule with $V_{\text{bias}} = 20$ mV and $I = 50$ pA). The tip was functionalized in order to be able to reach the repulsive regime [79] (see chapter 2 section

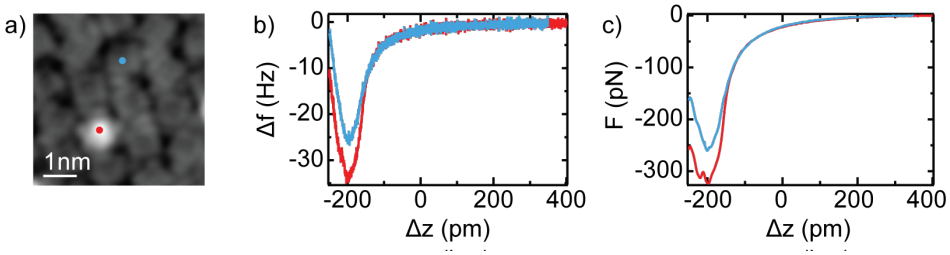

Figure 5.3.: a) Topography image ($V_{\text{bias}} = 20$ mV, $I = 50$ pA) recorded with a functionalized tip. b) Evolution of the frequency shift Δf with tip offset Δz (feedback opened at $V_{\text{bias}} = 20$ mV $I = 50$ pA, applied bias $V_{\text{bias}} = -100$ mV oscillation amplitude $A_{\text{osc}} = 50$ pm) above the center of a dark (blue) and a bright (red) molecule as indicated in the topography image in a. c) Forces between the molecules and the tip obtained from the frequency shift approach curves in b following the Sader-Jarvis deconvolution procedure [185].

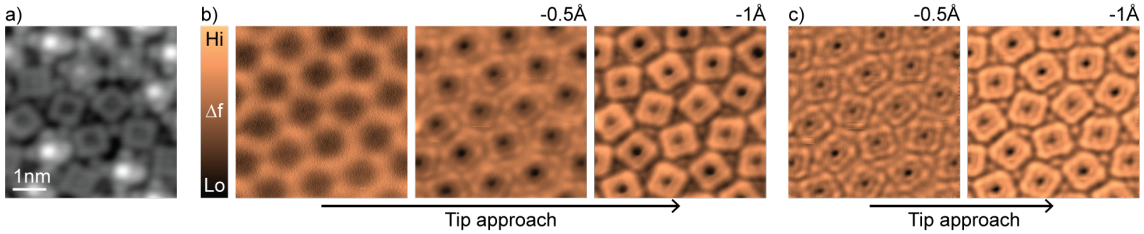

Figure 5.4.: a) Topography image ($V_{\text{bias}} = 20$ mV $I = 50$ pA) recorded with a functionalized tip. b) Constant height frequency shift maps obtained at different tip heights. c) Laplace-filtered images of the two maps at close tip-sample distances in b.

III). Finally, we note that since the molecules are close to each other, the background forces are similar and we can compare the force curves without a background correction.

One can see that both force curves show a minimum around $\Delta z = -200$ pm that can be used as a distinctive point to characterize the chemical interaction (see chapter 2 section III). This confirms that the two centers have the same chemical nature and that none of them posses an extra ligand. Indeed, in both cases, the onset of the chemical bonds would otherwise be at different heights and the minima of the curves would be shifted with respect to each other.

Interestingly, the bright molecule exerts a stronger attractive force onto the tip apex; this was observed irrespective of the tip termination. As we show next, the molecules have different electronic properties and we therefore interpret this stronger interaction as the manifestation of their different electronic configurations: the electronic density is different which leads to differences in the interaction strength with the tip apex during the bond formation.

We now characterize the molecules by means of constant height frequency shift maps in Fig. 5.4b. Here again, the tip is functionalized in order to enhance our resolution [79, 75, 50]. When the tip is relatively far away (left map), the frequency shift above the molecules is negative indicating an attractive force, due to van der Waals interactions between the molecules and the tip apex (see chapter 2 III.2). As the tip is brought closer (middle and right maps), repulsive interactions due to Coulomb repulsion gain importance and lead to a contrast inversion of the frequency shift above the molecular ligands. In order to have a better resolution of the molecular structure we show in Fig. 5.4c the Laplace filtered images of these two maps. There, one can distinguish the four pyrrole groups of the molecules similarly to what was observed for the free-base porphine molecule in [50]. While no difference is observed

above the ligands of the molecules, the frequency shift recorded above their center varies with more negative values and thus stronger attraction above molecules of the bright type; consistently with what is observed in Fig. 5.3. Since these variations between molecules is only observed above the molecules' centers we speculate that the differences in the electronic properties of the molecules stem mainly from differences in the hybridization and/or energy positions of the Fe *d*-levels with it surroundings. Indeed, the magnetic fingerprints of the molecules (Yu-Shiba-Rusinov (YSR) states for bright molecules and inelastic excitation for dark molecules - see appendix 9 section II) indicate different hybridization strength with the surface.

3. Electronic properties

We have established in the previous section that the different appearance of bright and dark molecules at low biases is not due to differences in their chemical composition but should rather be related to their electronic properties. Interestingly, these different types are related to the presence of Cl adatoms inside the molecular islands. In this section, we characterize in detail the electronic properties of the molecules and show in particular that the dark molecules display a variety of fingerprints in scanning tunneling spectroscopy (STS). The second part of this chapter is dedicated to the study of one of these fingerprints that we attribute to local gating effects. In this part, we focus on the characterization of the electronic differences between bright and dark molecules.

3.1. Variety of fingerprints in STS

We display in Fig. 5.5b typical spectra obtained above the center of bright (blue spectrum) and dark (red spectrum) molecules (see topography image of Fig. 5.5a) as well as a reference spectrum taken on Pb in black. The bright molecule shows a broad resonance around -250 mV that crosses Fermi energy. Above the dark molecule we observe a V-shape of the spectrum with two broad symmetric steps at around ± 100 mV (the dip around Fermi energy corresponds to the superconducting gap of Pb). In both cases we do not detect any clear resonance in the positive bias. A spectrum recorded above a Cl adatom is aditionally shown in green. Shallow changes in the differential conductance are observed compared to the spectrum taken above the Pb surface but no clear resonance is to be seen in $\mathrm{d}I/\mathrm{d}V$. This seems to indicate a rather indirect interaction (no formation of chemical bond) between the chlorine adatoms and the molecules. This is consistent with the fact that the Cl adatoms may change their position as shown in Fig. 5.2.

Before investigating in more detail the differences between bright and dark molecules we illustrate the variety of features that can be detected in STS above dark molecules. Indeed, the spectrum of Fig. 5.5b has been chosen because it displays the common features of all dark molecules but we show in Fig. 5.5d that the fingerprints of the dark molecules in the negative bias regime are very diverse. For some molecules, no resonance is observed in the spanned energy range (top violet spectra (i)). Other show a resonance whose position in energy can vary strongly from one molecule to another (compare the light violet (ii) and blue spectra (iii)). Finally, additional features are sometimes detected on top of this resonance (four lowest spectra (v - viii)). The resonance in the negative bias most likely corresponds to the highest occupied molecular orbital (HOMO) of the molecules. However, the fact that its position changes significantly in energy from one molecule to another is rather surprising.

We now characterize the additional features observed on top of the HOMO of the dark molecules. These can be grouped into two categories as illustrated in Fig. 5.5e-f and g-h. For some molecules, the modulation seen on top of the resonance stems from a bistability.

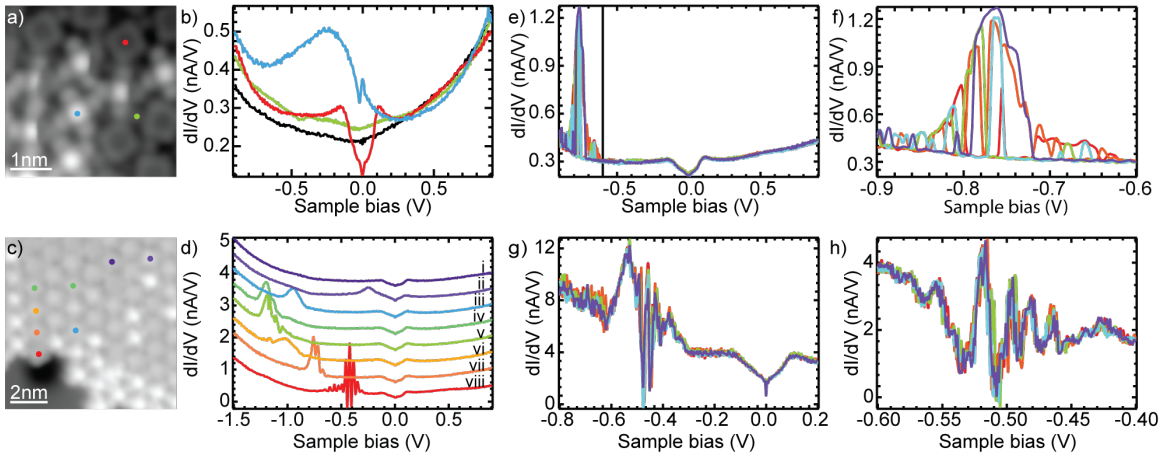

Figure 5.5.: a) Topography image ($V_{\text{bias}} = 5$ mV, $I = 200$ pA) of the molecules above which the dI/dV spectra in b) are recorded (feedback opened at $V_{\text{bias}} = 900$ mV, $I = 300$ pA and signal modulated with $V_{\text{rms}} = 5$ mV). c) Topography image of a molecular island ($V_{\text{bias}} = -45$ mV, $I = 100$ pA) which the location of the dI/dV spectra of d) (feedback opened at $V_{\text{bias}} = 900$ mV, $I = 300$ pA and signal modulated with $V_{\text{rms}} = 5$ mV) that illustrate the variety of fingerprints observed above dark molecules. e) dI/dV spectrum obtained from consecutive bias sweeps (feedback opened at $V_{\text{bias}} = 900$ mV, $I = 300$ pA and signal modulated with $V_{\text{rms}} = 5$ mV) above a molecule showing a bistable behavior. f) Enhanced view of the dI/dV traces of e). g) dI/dV spectrum of a molecule showing oscillations ($V_{\text{bias}} = 200$ mV, $I = 200$ pA and signal modulated with $V_{\text{rms}} = 1$ mV) with each trace corresponding to a bias sweep with a sweep rate of 0.2 mV/sec. h) dI/dV spectra recorded above the same molecule as in g) but with a decreased sweep rate (0.04 mV/sec).

In Fig. 5.5e we show dI/dV traces recorded by sweeping the bias several times between 900 mV and −900 mV. The signal switches randomly between two traces in which only one of them exhibits the resonance. This is seen more clearly in the enhanced view of these traces shown in Fig. 5.5f. Such bistable behavior has already been observed in the literature [116] and is to be related to the finite temperature of the experiment (1.6 K in our case) in the following fashion: two different configurations are available for the system and the barrier between them may be thermally overcome. As a matter of fact, we know that the Cl adatoms influence the electronic properties of the molecules and most probably affect the position of the HOMO. Since they have been observed to change position (see Fig. 5.2) it is rather logical that a few molecules show a bistability. Anticipating on observations made later in this section we note that the presence of the tip might also affect this bistable behavior.

The second type of modulation of the resonance intensity is shown in Fig. 5.5g-h. There, oscillations are observed on top of the resonance (Fig. 5.5g) with well-defined position and intensity that do not vary from one sweep to another. This can be seen more clearly in Fig. 5.5h where the sweeping rate was decreased by almost one order of magnitude (from 0.2 mV/sec for the left panel to 0.04 mV/sec for the right panel). This behavior is rather uncommon: to the best of our knowledge such fingerprints have not been reported in the literature for molecules adsorbed directly on a metal substrate. We focus on this feature in the second part of this chapter.

We can already speculate that the different fingerprints of the dark molecules are related to differences in their environments since they otherwise appear to be quite similar. More precisely, because the Cl adatoms are randomly distributed within the island they influence

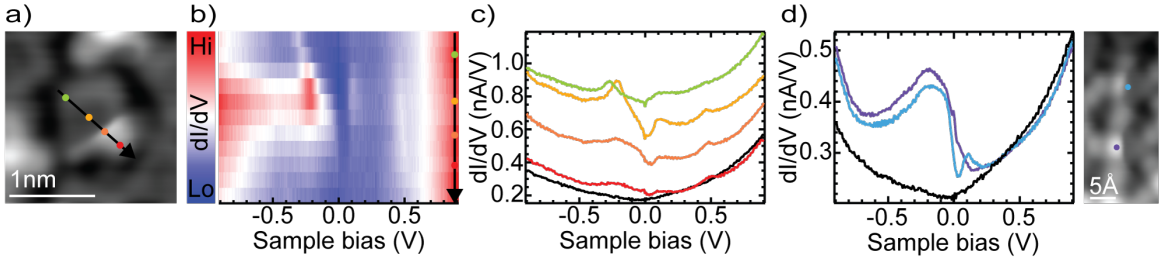

Figure 5.6.: a) Topography image of a hybrid molecule ($V_{\text{bias}} = 5$ mV, $I = 200$ pA). b) $\mathrm{d}I/\mathrm{d}V$ spectra taken along the line shown in a) (feedback opened at $V_{\text{bias}} = 900$ mV, $I = 300$ pA and signal modulated with $V_{\text{rms}} = 5$ mV). c) Exemplary spectra of the set shown in b along with a reference spectrum above the bare Pb substrate (black). d) $\mathrm{d}I/\mathrm{d}V$ spectra (feedback opened at $V_{\text{bias}} = 900$ mV, $I = 300$ pA and signal modulated with $V_{\text{rms}} = 5$ mV) taken above other hybrid molecules (set point of topography image $V_{\text{bias}} = 5$ mV, $I = 200$ pA).

the molecules in different ways but, as explained earlier, since we cannot precisely identify their number and positions we cannot relate each features to specific Cl dispositions.

3.2. Hybrid molecules

In order to have a better understanding of the electronic differences between bright and dark molecules we study now the properties of hybrid molecules since they should display the features of both types.

This is confirmed by the set of $\mathrm{d}I/\mathrm{d}V$ spectra taken across a hybrid molecule (see Fig. 5.6a) as shown in Fig. 5.6b. The top-left and central parts of the molecule exhibit the properties of the dark type with a V-shape around the Fermi level and a resonance in the negative bias regime (green and yellow spectra in Fig. 5.6c). As for the spectra taken on the bottom-right corner of the molecule, they show the feature of the bright type with a broad orbital around -200 mV that extends close to Fermi energy (orange and red spectra in Fig. 5.6c).

Overall the molecule shows dominantly the electronic properties of the dark type but we show in Fig. 5.6d that this depends on the investigated molecule. Indeed, there, one hybrid molecule displays a clear bright character (violet spectrum) while the other one (blue spectrum) shows a spectrum similar to the orange and red spectra of Fig. 5.6c: a broad orbital similar to the bright type but with a remaining V-shape around Fermi energy. Here again, these different behaviors are most likely related to different Cl surroundings.

While the transition between the bright and dark is sharp and well-defined in the topography images, it appears rather smooth and continuous in $\mathrm{d}I/\mathrm{d}V$. In this respect one should keep in mind that the $\mathrm{d}I/\mathrm{d}V$ spectra are taken at a different set points ($V_{\text{bias}} = 900$ mV, $I = 200$ pA) than the topography images ($V_{\text{bias}} = 5$ mV, $I = 200$ pA) and that the latter show a clear voltage dependence (see Fig. 5.1d and e). The presence of the tip and the applied bias seem thus to play a decisive role in the transition between the two types. More precisely, the orbital in negative bias regime shifts in energy in Fig. 5.6d. This orbital is assigned to the HOMO of the molecule that has a well defined and unique energy. Therefore, the apparent shift seen in Fig. 5.6b must be related to the presence of the tip.

This influence is investigated in more detail in Fig. 5.7 where we present the effect of a tip approach above the center of the hybrid molecule shown in Fig. 5.6a. We define 0 pm as the height at which the feedback is opened with $V_{\text{bias}} = 900$ mV and $I = 300$ pA and positive (negative) Δz offsets for a tip retraction (approach). The evolution of the tunneling current is shown in Fig. 5.7b exhibiting the stable and expected exponential dependence with

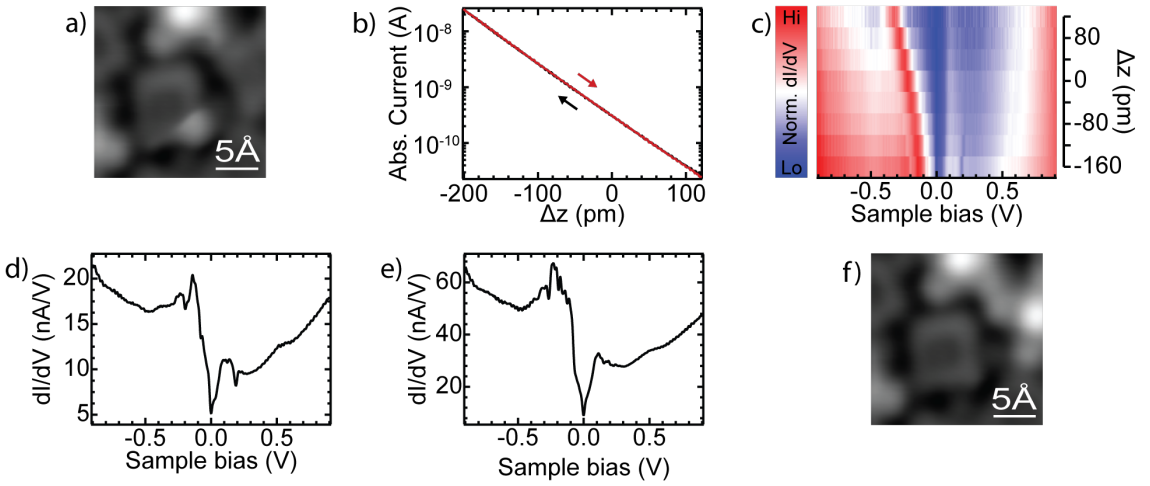

Figure 5.7.: Tip approach above the center of a hybrid molecule. a) Topography image ($V_{\text{bias}} = 5$ mV, $I = 200$ pA) of the molecule under investigation. b) Evolution of the tunneling current (with an applied bias of $V_{\text{bias}} = 900$ mV) as a function of the tip offset Δz (feedback opened at $V_{\text{bias}} = 900$ mV, $I = 300$ mV). c) Set of $\mathrm{d}I/\mathrm{d}V$ spectra normalized to their conductance at $V_{\text{bias}} = 900$ mV (feedback opened at $V_{\text{bias}} = 900$ mV, $I = 300$ pA and signal modulated with $V_{\text{rms}} = 5$ mV). d) $\mathrm{d}I/\mathrm{d}V$ spectrum recorded with an offset $\Delta z = -160$ pm. e) $\mathrm{d}I/\mathrm{d}V$ spectrum with $\Delta z = -200$ pm after which the molecule appears dark, as shown by the topography image in f) ($V_{\text{bias}} = 5$ mV, $I = 200$ pA).

the tip-sample separation. In Fig. 5.7c we present as a 2D color plot the $\mathrm{d}I/\mathrm{d}V$ spectra recorded with Δz offsets down to -160 pm (the spectra are normalized to their conductance at $V_{\text{bias}} = 900$ mV). A clear shift of the HOMO toward Fermi energy is observed upon tip approach. Moreover, as the tip is brought closer, we see small dips developing in both bias polarities. This is seen more clearly in Fig. 5.7d where we display the spectrum recorded with an offset of -160 pm. Fig. 5.7e shows a spectrum recorded with $\Delta z = -200$ pm. There, additional features are clearly seen in the negative bias and we notice similarities to the oscillations observed in Fig. 5.5d. The origin of such features is discussed in detail in the second part of this chapter. Interestingly, the topography image recorded after this last spectrum and displayed in Fig. 5.7f shows that the molecule appears now dark and that its neighbor switched from dark to bright.

These observations further support a strong influence of the electric field of the tip on the properties of the molecules. Indeed, the HOMO energy changes significantly even at large tip-sample distances where its energy shift appears rather linear with Δz. By contrast, the energy shift tends to diminish when the orbital merges with the onset of the step in the negative bias. This speaks against modifications of the spectroscopic signature due to a deformation of the molecule under the tip. Such an interaction would be stronger at close distances and should have a vanishing influence as the tip is brought away from the molecule (see chapter 2 section III.2 and chapter 6). Besides, we note that the switching processes happen before contact and were observed in Fig. 5.2 even without the need of a tip approach.

As a result, we conclude that the difference between dark and bright molecules is directly reflected in the energy position of the HOMO. Since the chlorine adatoms influence the molecular types they should therefore have an impact on the energy of this resonance. Interestingly, we showed that the position of this orbital can be modified by the electric field of the tip. It is therefore of interest to gain more insight into the charge distribution inside

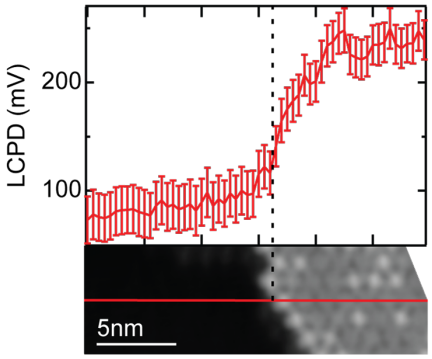

Figure 5.8.: Evolution of the LCPD along the line shown in the topography image. The measurements are performed in a constant height with an oscillation amplitude of the AFM tuning fork of 50 pm. The LCPD values are obtained by fitting parabolas to $\Delta f(V_{\text{bias}})$-curves and the error bars correspond to the standard deviations of the fits.

the molecular islands.

4. LCPD measurements

As explained in chapter 2 section III, different charges on the surfaces exert different electrostatic forces on the tip and these can be detected with AFM by means of local contact potential difference (LCPD) measurements: by recording the frequency shift as a function of bias voltage one can extract the value of the applied bias for which the electric field induced by the tip minimizes the electrostatic force between the tip and the sample.

Electrostatic forces are particularly long-ranged so we first characterize the differences of LCPD between the bare Pb substrate and a molecular island in Fig. 5.8. The measurements are carried out in constant height mode. Indeed, while the value of the LCPD does not depend on the tip-sample distance in a plate capacitor model, this model is not a realistic description of the tip shape. It has been shown in literature [159] that the tip electric field and thus LCPD value depends both on the tip shape and height (especially at close distance). The LCPD values in Fig. 5.8 are thus obtained by recording $\Delta f(V_{\text{bias}})$ curves in constant height mode and fitting these with parabolas; the error bars in Fig. 5.8 correspond to the standard deviation of the fits. The LCPD is higher above the molecular island than above the bare Pb(111) surface. This indicates that the tip interacts with more negative charge above the island than above the bare Pb(111) substrate (see chapter 2 section III Fig. 2.8). This is rather surprising; in most cases, the adsorption of molecules on a metal surface leads to the so-called push-back or pillow effect [83, 102, 103, 111, 214]: the electronic wavefunctions of the adsorbates repel the ones of the substrate so that the latter decay faster into vacuum giving rise to a lower LCPD value than above the bare substrate. Here, this effect seems to be compensated by other phenomena. More precisely, we propose in the next section that the increase of the LCPD above molecular islands is related to the presence of Cl adatoms within them. Yet, the non-local character of the measurement (see 2 section III.2) prevents us from singling out their specific contribution.

We now want to characterize in more detail if the differences between the dark and bright molecules are reflected by variations in the electrostatic forces they exert on the tip apex. In order to do so we investigate in Fig. 5.9 the evolution of the LCPD above two such molecules as a function of tip height Δz. We record $\Delta f(z)$ curves along the line shown in the topography

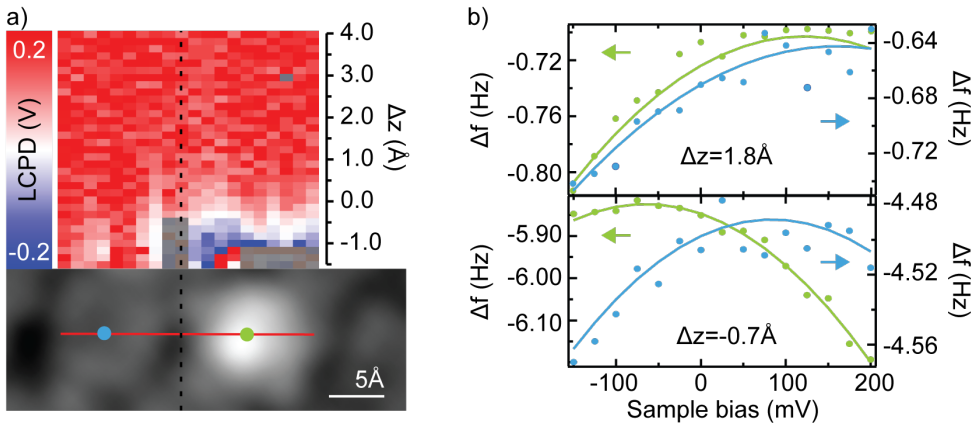

Figure 5.9.: a) Evolution of the LCPD as a function of tip-sample plane separation ($\Delta z = 0$ pm arbitrarily chosen) along the red line drawn in the topography image ($V_{\text{bias}} = 20$ mV, $I = 50$ pA). The LCPD values were obtained by fitting parabolas to the frequency shift vs. bias curves at the various distances (amplitude of the AFM oscillation $A_{\text{osc}} = 50$ pm). b) Exemplary data at two different heights above the centers of the bright (green) and dark (blue) molecules. The measured frequency shifts are shown by dots and the parabolic fits with lines.

image of Fig. 5.9a at different bias values ($V_{\text{bias}} = 200, 175, 150, \ldots, -125, 150$ mV) and then reconstruct the $\Delta f(V_{\text{bias}})$ curves for the various tip-sample plane distances Δz (here again $\Delta z = 0$ pm is arbitrarily chosen as the height at which the feedback loop was opened). These $\Delta f(V_{\text{bias}})$-curves are finally fitted with parabolas to obtain the LCPD values. Those values are displayed as a function of tip height Δz as a 2D color plot in Fig. 5.9a. The grey pixels are regions for which no reasonable fit could be performed due to noise issues. Fig. 5.9b shows four exemplary $\Delta f(V_{\text{bias}})$-curves (dots) along with their parabolic fits (curves) above the molecules' center at two different heights.

When the tip is far away, no difference in LCPD is observed between the two molecules. The two curves in the upper panel of Fig. 5.9b illustrate the equivalence of the frequency shifts measured above the centers of the two molecules. This is caused by the non-local character of the measurements as mentioned earlier. Only when going closer to the molecules do we detect deviations in the LCPD indicating different charge distributions. More precisely, at close distances, the LCPD becomes negative only above the bright molecule. This is clearly seen in the lower panel of Fig. 5.9b and cannot be accounted for by differences in the tip-molecule distances: as shown in the previous section the Fe centers are at the same height within our resolution. Also, variations solely due to different heights of the Fe centers should only shift the observed LCPD variations to lower/higher Δz offsets. Yet, we do not observe any negative LCPD values above the dark center. Therefore, the higher LCPD measured above the dark molecule indicate that the tip interacts there with more negative charges than above the bright molecule.

5. Energy level alignment

The bright and dark molecules have different electronic configurations. These are related on the one hand to differences in their charge distribution and, one the other hand to the presence of Cl adatoms in their surroundings. It is therefore of interest to consider what mechanisms govern the energy level alignment of molecules when they are adsorbed on a

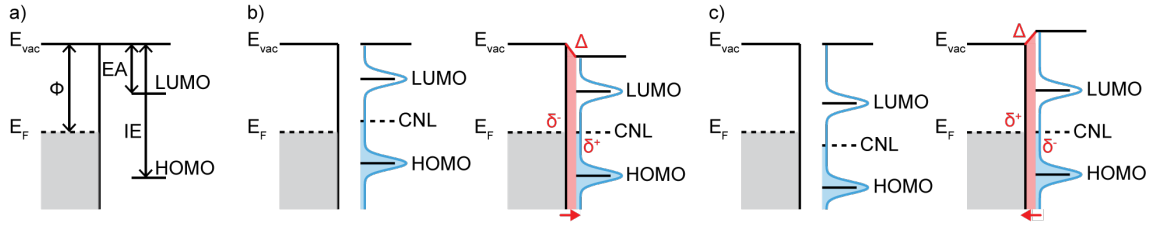

Figure 5.10.: Energy alignement. a) The HOMO and LUMO are pinned to the vaccum level. b) Before equilibrium the CNL of the molecule is above the Fermi energy of the metal (left). Upon adsorption a partial charge transfer occurs resulting in an interface dipole Δ pointing toward the vacuum. c) In the opposite case, if the CNL of the molecule lies below Fermi energy before equilibrium the resulting interface dipole points toward the surface.

metal surface.

In the simplest case, one considers a very weak interaction between the molecule and the substrate so that the molecular levels are pinned to the vacuum level. This is illustrated in Fig. 5.10a: the energies of the HOMO and lowest unoccupied molecular orbital (LUMO) with respect to the Fermi energy of the metal are determined by the work function of the metal Φ, the Ionization Energy (IE) and the Electron Affinity (EA) as follows

$$E_{\mathrm{HOMO}} = \mathrm{IE} - \Phi$$
$$E_{\mathrm{LUMO}} = \Phi - \mathrm{EA}$$

However, in general, even if the molecules do not hybridize strongly with the substrate there is a charge redistribution at the interface leading to a surface dipole. One frequent example is the push-back effect mentioned above: due to Pauli repulsion the electron wavefunctions of the substrate are pushed back toward the bulk. Another phenomenon is the image force effect [117]: the electron charge of the molecules are attracted by their image charge in the metal leading to polarization effects. Both effects lead to a lowering of the work function. Additionally, one should consider possible charge transfer between the adsorbate and the metal. This phenomenon can be described by the induced density of interface states (IDIS) model. The hybridization of the molecular levels with the metal substrate leads to their broadening and induces a density of states within the HOMO-LUMO gap. The charge neutrality level (CNL) of the molecule is then defined such that the integrated density of states (DOS) up to the CNL gives the charge of the isolated molecule. By comparing the metal work function and molecular CNL one can deduce the direction and intensity of the interface dipole. The possible cases are shown in Fig. 5.10b and c. In Fig. 5.10b, before equilibrium (left panel), the CNL of the molecule is higher than the Fermi level of the surface. To reach equilibrium there is therefore a partial charge transfer with an electron donation from the molecule to the substrate which results in an interface dipole pointing to the vacuum side (right panel). The reversed situation is displayed in Fig. 5.10c, when the CNL is below the Fermi level before equilibrium, the charge transfer gives rise to an interface dipole pointing toward the surface. Finally, we note that a permanent dipole moment of the adsorbate may affect this energy level alignment as well.

The AFM measurements presented in the previous section indicate a higher LCPD (and thus higher work function) above the molecular islands than above the bare Pb(111) surface. It is thus most likely that a charge transfer takes place as depicted in Fig. 5.10c; namely, a transfer of electrons from the Pb surface to the molecules. The relatively low work function of

Pb ($\Phi = 4.25$ eV) as compared to other metals such as Au ($\Phi = 5.1$ eV) or Cu ($\Phi = 4.65$ eV) [147] seems consistent with this behavior. The presence of chlorine adatoms within the island contributes similarly to an increase of the work function since this element tends to accept electrons.

The fact that the LCPD is higher above dark molecules than above bright molecules is however not captured within this simple model: since Cl adatoms tend to attract electrons, molecules in their vicinity should see a higher work function than on the bare surface. This would lead to a reduction of the charge transfer and thus of the work function for dark molecules as compared to bright molecules. In order to understand the exact interplay between chlorine and the FeP molecules one would need to perform density functional theory (DFT) calculations. Indeed, the interface dipole due to chlorine adatoms creates an electric field that might influence the electronic properties of the molecules in a non trivial way. The approach measurements presented in Fig. 5.7 and Fig. 5.14 show that the energy of the HOMO orbital shifts toward Fermi energy as the electric field of the tip becomes stronger. A possible explanation may be that the HOMO orbital carries a dipole moment $\vec{\mu}$: to first approximation, its energy would then vary with the electric field as $E_{\mathrm{HOMO}} = E^0_{\mathrm{HOMO}} - \vec{\mu} \cdot \vec{E}_{\mathrm{loc}}$, with E^0_{HOMO} the energy of the HOMO in the absence of electric field and $\vec{E}_{\mathrm{loc}}$ the local electric field. Besides explaining this energy shift under tip approach such an assumption may explain why the HOMO orbital is seen at very different energies depending on the investigated molecule (see Fig. 5.5): the distribution of chlorine adatoms within the island is random so that variations in the local electric field experienced by the molecules are to be expected. In any case, we note that the presence of a higher LCPD above dark molecules indicates that the surface dipole, present generally above the island, is therefore higher above these molecules.

II. Local gating by image potential states

We now want to investigate in detail the oscillations seen in STS above some of the dark molecules. In particular, we characterize their spatial dispersion and argue that it cannot be accounted for by models reported in literature that describe the emergence of peaks in $\mathrm{d}I/\mathrm{d}V$. Indeed, we finally propose to relate the appearance of the observed features to local gating effects.

1. Characterization of the oscillations

Fig. 5.11b shows a $\mathrm{d}I/\mathrm{d}V$ spectrum recorded above the center of a dark molecule as indicated in Fig. 5.11a. The forward and backward traces of the spectrum are identical indicating that the sharp features seen in the negative bias regime are well defined in energy and not related to a bistability in the junction. The constant height $\mathrm{d}I/\mathrm{d}V$ maps of Fig. 5.11c show that these peaks correspond to dispersive ring-like features. In order to know if the distribution of the molecules displaying such features is regular we recorded $\mathrm{d}I/\mathrm{d}V$ maps at various bias voltages above a molecular island as shown in Fig. 5.11d. No systematic pattern can be identified; the molecules displaying such ring-like features are randomly distributed across the island and the bias voltages at which these rings are detected vary from one molecule to another. Here again, we attribute this lack of uniformity to the random distribution of Cl adatoms within the molecular island.

We characterize in more detail the dispersion of the oscillations above the central molecule of the topography image in Fig. 5.12a. This molecule lies above a Ne impurity and is dark despite being at the border of an island. We choose this molecule because the oscillatory behavior in its $\mathrm{d}I/\mathrm{d}V$ spectrum is particularly prominent and regular (see Fig. 5.12b), making

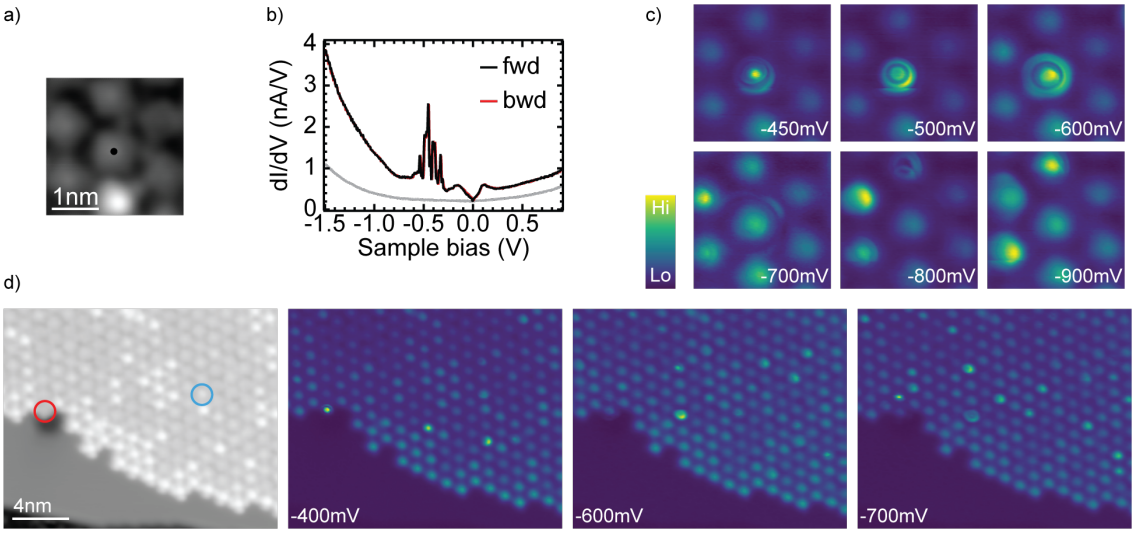

Figure 5.11.: a) Topography image ($V_{\text{bias}} = -45$ mV, $I = 100$ pA) of a dark molecule showing oscillations as shown in b) dI/dV spectra (feedback opened at $V_{\text{bias}} = 900$ mV, $I = 300$ pA and signal modulated with $V_{\text{rms}} = 5$ mV) recorded above the center of the molecule (black forward sweep from 900 mV to -1.5 V, red backward spectrum from -1.5 V to 900 mV) and the bare Pb surface (grey). c) Constant height dI/dV maps recorded above the area shown in a). d) Topography image (left, set point: $V_{\text{bias}} = -45$ mV, $I = 100$ pA) of a molecular island and corresponding constant height dI/dV maps.

it easier to identify its characteristics. This might be due to the particular environment of the molecule but we want to emphasize that the conclusions drawn concerning the behavior of the oscillations are valid for all investigated molecules. As explained in chapter 2 section III.4, peaks in dI/dV correspond to steps in $I - V$. The enhanced view of the dI/dV spectrum displayed in the inset of Fig. 5.12b along with its corresponding current trace shows that it is indeed the case between -400 mV and -500 mV where the relative change in the conductance is the strongest (the steps correspond to ~ 25 % relative increase of the current). Outside of this bias window the current changes are too shallow to be detected within our resolution. Overall, the peaks intensities seem to be modulated by an envelope function that corresponds to an orbital (as a guide to the eye we sketch in the inset of Fig. 5.12b a Gaussian function with a dashed blue line). This is corroborated by the observation of the HOMO above other dark molecules in this energy window as shown in Fig. 5.5. Yet, we would like to point out that we still detect peaks in dI/dV at higher voltages but with much lower intensity.

The spatial extent of these oscillations is investigated in Fig. 5.12c and d with constant height dI/dV maps recorded above the areas shown in the topography images of Fig. 5.12a and d, respectively. As the voltage is increased, concentric rings develop in the dI/dV maps. The radii of these rings increase with increased bias voltage and reach around 2 nm before the intensity of signal vanishes within our resolution. Such a behavior is similar to the charging rings described in chapter 2 section III.4. However, in our case, not only one ring is detected but several of them. Moreover, one can see in Fig. 5.12d that the intensity of the rings is spatially modulated. Namely, in the left dI/dV map, recorded with $V_{\text{bias}} = -650$ mV, above the molecule on top of the one at the center of the rings the signal appears to be inverted with respect to its surroundings: a high intensity signal becomes a low one and reciprocally. Upon a careful inspection, this reversal of the ring intensity can also be seen in the other

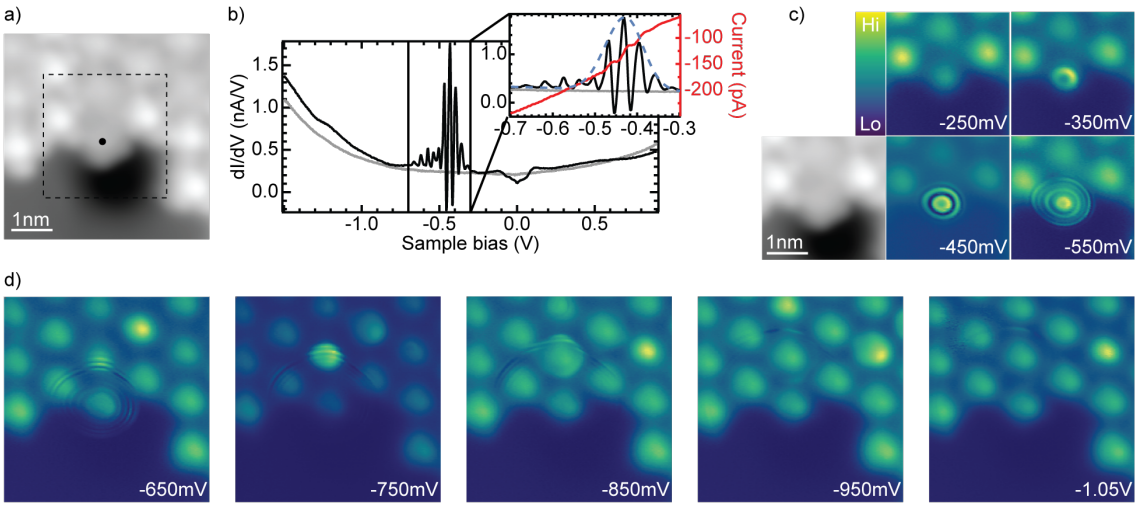

Figure 5.12.: a) Topography image $V_{\text{bias}} = -45$ mV, $I = 100$ pA. b) $\mathrm{d}I/\mathrm{d}V$ spectrum (black) and $I - V$ curve (red) recorded above the center of a dark molecule as shown in a) (feedback opened at $V_{\text{bias}} = 900$ mV, $I = 300$ pA and signal modulated with $V_{\text{rms}} = 5$ mV). c) Constant height $\mathrm{d}I/\mathrm{d}V$ maps recorded above the area shown in the topography image (grey color-scale, set point $V_{\text{bias}} = -45$ mV, $I = 100$ pA). d) Constant height $\mathrm{d}I/\mathrm{d}V$ maps recorded above the area shown in a).

$\mathrm{d}I/\mathrm{d}V$maps of Fig. 5.12d. Finally, one should remark that, if the rings extent relatively far away above the molecular island, their decay is much faster above the substrate: once their radii reach the size of the neon impurity underneath the molecule their intensity vanishes (compare the $\mathrm{d}I/\mathrm{d}V$ maps Fig. 5.12d taken with $V_{\text{bias}} = -650$ mV and $V_{\text{bias}} = -750$ /mV).

Complementary to these $\mathrm{d}I/\mathrm{d}V$ maps, we present as a 2D color-plot in Fig. 5.13b the evolution of the $\mathrm{d}I/\mathrm{d}V$ spectra recorded in constant height mode along the line shown in the topography image of Fig. 5.13a. In agreement with the observation made above, one can see that as the tip is moved further away from the molecule's center, the position of the oscillations in $\mathrm{d}I/\mathrm{d}V$ shifts to higher energies. More specifically, it appears that this shift has a parabolic dispersion with the lateral position of the tip (a parabola is drawn as a red dashed line in Fig. 5.13b as a guide to the eye). This reinforces the correlation with the charging rings reported upon in literature [52, 168, 156, 130, 113]. As a matter of fact, as explained in chapter 2 section III (Fig. 2.10), the observed parabolas in [52, 168, 156, 130, 113] correspond to constant electric field lines in bias-xy-space: below/above a specific electric field the system is in different states corresponding to different conductances. In our case, the electric field of the tip must thus play a crucial role in the mechanism underlying these oscillations.

This can be confirmed by comparing $\mathrm{d}I/\mathrm{d}V$ spectra recorded before (black) and after (red) a modification of the tip apex as shown in Fig. 5.13c. As one can see, the overall position of the oscilations is now shifted to lower energies and their lineshape is less regular (see enhanced view of the $\mathrm{d}I/\mathrm{d}V$ spectra in the inset). The electric field of the tip seems thus to affect those two characteristics.

To further characterize the influence of the tip field we study the evolution of the $\mathrm{d}I/\mathrm{d}V$ traces upon a tip approach. The measurements are performed above the molecule shown in the topography image of Fig. 5.14a and the set of $\mathrm{d}I/\mathrm{d}V$ spectra as a function of tip height Δz is displayed in Fig. 5.14c as individual spectra and Fig. 5.12d as a 2D color plot. We define 0 pm as the height at which the feedback is opened (with the following parameters:

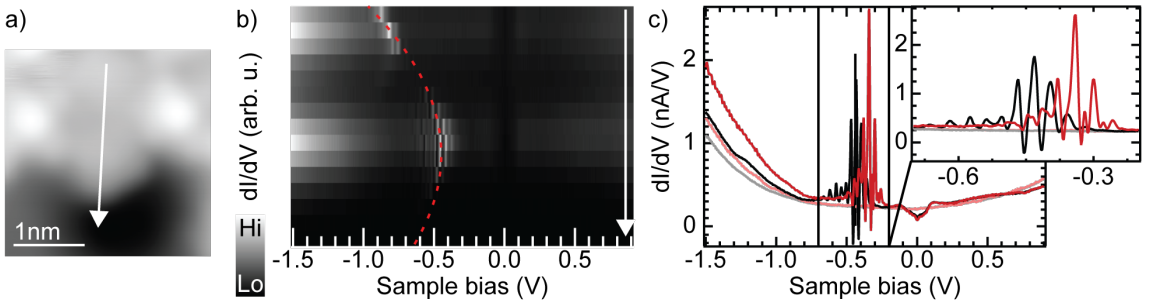

Figure 5.13.: a) Topography image ($V_{\text{bias}} = -45$ mV, $I = 100$ pA) of the investigated molecule. b) Set of $\mathrm{d}I/\mathrm{d}V$ spectra recorded in constant height mode along the line shown in a (signal modulated with $V_{\text{rms}} = 5$ mV). c) $\mathrm{d}I/\mathrm{d}V$ spectra (feedback opened at $V_{\text{bias}} = 900$ mV, $I = 300$ pA and signal modulated with $V_{\text{rms}} = 5$ mV) taken above the center of the molecule (black and red) and above the bare Pb surface (grey and light red) with two different tip apexes (black and grey spectra taken with the same tip apex and red and light red spectra with another one).

$V_{\text{bias}} = 900$ mV and $I = 300$ pA) and a positive (negative) offset Δz indicates an increase (decrease) of tip-sample distance. The $I - Z$ curve shown in Fig. 5.14b shows that the approach experiment is stable and reproducible. Moreover, we note that we remain in the tunneling regime throughout the experiment so that structural deformation of the molecule can be excluded. As the tip is brought closer to the molecule the overall signal (resonance and oscillations) shift to lower energies. More strikingly even, the lineshape of the $\mathrm{d}I/\mathrm{d}V$ spectra change significantly. At $\Delta z = 0$ pm the oscillations are rather faint and seen mostly as four small peaks preceding the broader resonance corresponding to the HOMO of the molecules. Upon tip approach, these oscillations gain in intensity and gradually obscure the HOMO resonance. At $\Delta z \leq -160$ pm one sees dominantly a series of peaks and dips and it is hard to make out the presence of a resonance behind them. The change of lineshape of the oscillations is drastic (the four small peaks at $\Delta z = 0$ pm are replaced at $\Delta z = -220$ pm by a main dip/peak feature at around $V_{\text{bias}} = -200$ mV followed by a succession of smaller peaks) but continuous as illustrated in Fig. 5.14e. There, the enhanced view of some of the spectra shows that a series of four peaks, shifting closer together, can be followed through the approach

All in all, this confirms that the electric field of the tip modifies both the position and the lineshape of these oscillations. Before discussing the possible origins of this oscillatory feature we would like to mention that it can also be observed at positive biases (see appendix 9 section I) and that both peaks or dips can be observed in $\mathrm{d}I/\mathrm{d}V$ spectra.

In the literature two models are usually used to account for the presence of sharp peaks in $\mathrm{d}I/\mathrm{d}V$: the excitation of vibronic modes of a molecule [93, 114, 122, 163, 109, 158, 64, 141] and charging peaks or dips as described in chapter 2 section III.4.

In the first case, the excitation of vibronics usually takes place via a resonant tunneling through an orbital. The vibronic peaks are then detected at the energy of this orbital plus the one of the excited vibration. The peaks must not have an equidistant spacing as they could be caused by different vibrational modes but their energy is well defined and should not vary strongly from one molecule to another. In particular, a modification of the tip apex is not expected to change strongly the observed lineshape in STS. Also, these are only detected as long as the tip apex has an overlap with the orbital through which the resonant tunneling processes occur. Last but not least, these are usually detected for molecules on an insulating

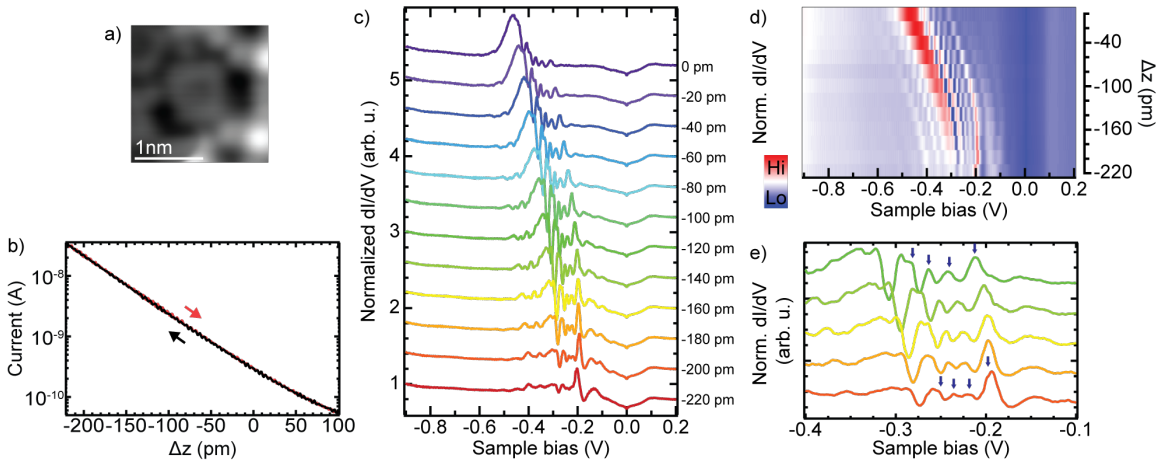

Figure 5.14.: Tip approach above the center of a molecule showing oscillations. a) Topography image ($V_{\text{bias}} = 5$ mV, $I = 200$ pA) of the investigated molecule. b) Evolution of the current (applied bias $V_{\text{bias}} = 900$ mV) with tip offset Δz (feedback opened at $V_{\text{bias}} = 900$ mV, $I = 300$ pA). c-e) Set of $\mathrm{d}I/\mathrm{d}V$ spectra normalized to their conductance at $V_{\text{bias}} = 200$ mV and recorded at different tip offset Δz (feedback opened at $V_{\text{bias}} = 900$ mV, $I = 300$ pA and signal modulated with $V_{\text{rms}} = 5$ mV).

layer as a direct adsorption on a metal surface quenches the lifetime of these vibrations. Such excitations are thus unlikely to occur and would not account for the influence of the tip field on the features.

The second phenomena, the detection of charging peaks, bears more similarities with our observations. In particular, as we noticed, the dispersion of the oscillations is very similar to the one of charging rings. However, as explained in 2 section III.4, the presence of a decoupling layer is usually a key ingredient to induce charging events since it allows a voltage drop between the molecule and the substrate. These charging events are moreover related to the presence of an orbital near the Fermi level that can then be shifted across it. Here, we have neither a decoupling layer nor any indication of a voltage drop across the molecules (see for instance the approach experiments presented in Fig. 5.14, a voltage drop would lead to a shift of the V-shape feature). Most importantly, we observe several peaks in $\mathrm{d}I/\mathrm{d}V$. Under the assumption of charging of molecular levels, this would correspond to too many orbitals to shift across the Fermi level to be realistic. All in all, the similar dispersion of charging rings and the observed oscillations indicate that a charge redistribution must be induced by the electric field of the tip. Yet, we should try to understand how such a charge redistribution can occur without the need of a decoupling layer or a shift of molecular levels across the Fermi level.

2. Proposed model

We propose to relate the observed oscillations to modifications of the number of image potential states induced by the electric field of the tip.

Image potential states arise due to the location variations of the potential near a metal surface. Indeed, the potential barrier seen by the electrons of a metal surface on the vacuum side is not an abrupt step but shows a smooth increase toward E_{vac} as shown in Fig. 5.15. A general formula for this increase is [46]:

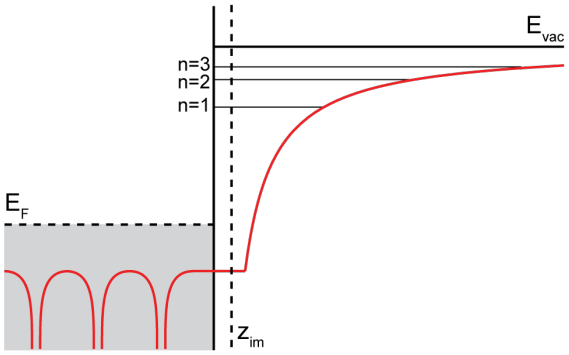

Figure 5.15.: The shape of the potential at the surface of a metal (red curve) leads to the presence of a image potential states in front of the surface.

$$V(z) = -\frac{1}{4(z - z_{\mathrm{im}})} \tag{5.1}$$

where z_{im} is the so-called image potential plane.

This leads to the presence of an infinite Rydberg-like series of states, called image potential states, trapped in front of the metal surface, as sketched in Fig. 5.15. These states have been observed with two-photon photoemission spectroscopy [67, 33, 66], inverse photoemission spectroscopy [43, 200] as well as with STM [219, 101, 202, 44]. In the latter case, they are probed resonantly by applying a high positive bias voltage to the sample. As it is shown in [202, 44], the electric field of the tip modifies the potential line-shape within the barrier so that a Stark shift in energy of these image potential states is observed.

As shown in Fig. 5.16a, the presence of the tip modifies the potential barrier so that the Rydberg-like series is truncated to a finite number. In our case, the interface dipole observed above the molecular islands (see first section of this chapter) will further affect the potential landscape. Specifically, the charge distribution is not homogeneous across the islands; this is (at least partially) due to the random distribution of Cl adatoms and evidenced by the LCPD measurements of Fig. 5.9. Therefore, the potential landscape in front of the surface is modulated locally across a molecular island and differs from molecule to molecule. We argue that in some cases, this modulation is such that the number of image potential states accommodated in front of the surface can be altered by the electric field of the tip.

More precisely, we show in Fig. 5.16b that a negative bias sweep broadens the effective potential well in which the image potential states lie. Therefore, it is possible that at a given threshold value, an extra state is accommodated in the junction, as sketched in Fig. 5.16d. This would then lead to a charge redistribution at the interface that is very similar to the charging effects described in chapter 2 section III.4. Namely, there, when the LUMO of an absorbate is shifted through the Fermi level by a negative bias sweep (see Fig. 2.12), an electron from the Fermi sea is then trapped in front of the surface in this orbital. Here, a hole from the continuum above the vacuum level is now trapped in the induced image potential state. Effectively, in both cases, a charge redistribution occurs and leads to a modification of the electrical potential in the surroundings of the trapped state. As explained extensively in chapter 2 section III.4, this effectively affects the number of electrons that tunnel through the junction. We illustrate this again in Fig. 5.16e-f: two different potential landscapes through the junction modulate the net flow of electrons. Because the change of potential landscape occurs sharply at a threshold value when the bias is sweeped, this results in steps in $I - V$

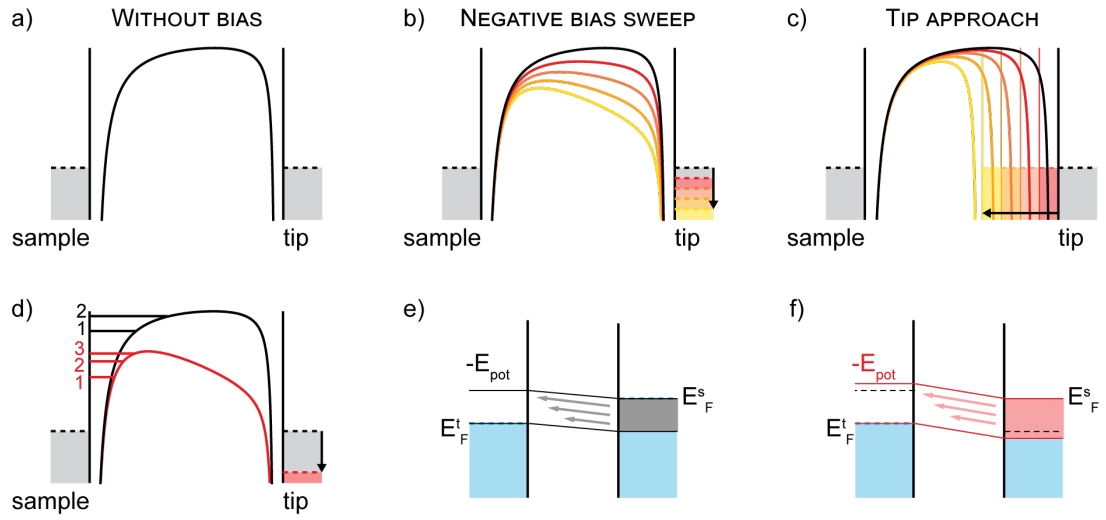

Figure 5.16.: Modification of the potential landscape by the tip. a) Sketch of the barrier without an applied bias. b) A negative bias sweep broadens the effective potential well in which the image potential states lie. c) An approach of the tip has a similar effect. d) As a result, the number of image potential states accommodated in front of the junction can change. e-f) Before and after a threshold value (either for the bias voltage or tip position) changing the number of image potential states, the potential landscapes in which the electrons tunnel are different. This gives rise to a step in $I-V$ curves and a peak or dip in $\mathrm{d}I/\mathrm{d}V$ spectra.

curves and peak or dips in $\mathrm{d}I/\mathrm{d}V$ spectra, depending on if the net flow of electron is increased or decreased, respectively. A similar change of local potential would happen if one of the image potential states is removed from the potential. Now that we exposed the fundamental ideas of model we would like to make two main remarks.

First of all, the inducement of new image potential states is related to the electric field of the tip and depends thus on the tip position. This is illustrated in Fig. 5.16c where we show that a tip approach leads to a broadening of the effective well of the image potential states. This explains the dispersion of the features as seen in Fig. 5.12 and Fig. 5.13b. But more than that, we notice that as the tip is brought closer, the confinement of the image potential states increases. Although it is not shown for a tip approach but a bias sweep, since both affect the potential landscape in a similar manner, one can compare in Fig. 5.16d the sizes of the states labeled 1 and 2 for the black and red cases. This increased confinement translates in a smooth modification of the image potential state wavefunctions. In all likelihood, as their wavefunctions change their effects on their surroundings is also affected. Modifications of the local gating potential will then be reflected in modified step height in $I-Z$ curves and thus lineshape of the $\mathrm{d}I/\mathrm{d}V$ spectra. This would then explain the change in lineshape observed upon tip approach as seen in Fig. 5.14. In general, a change of the tip apex modifies the overall landscape in which the image potential states are confined. This leads therefore to an energy shift and a lineshape modification of the oscillations in conformity with what is observed in Fig. 5.13c.

Second of all, the gating potential affects its local surroundings differently depending on their charge state: an electrical potential has an opposite effect on the potential energy of opposite charges. To some extent this may be the reason for the intensity inversion observed

for the rings of Fig. 5.12 and the fact that one can detect peaks as well as dips in dI/dV spectra. Still, one should notice that we considered an extremely simplified model of the effect of the tip field on the sample side. Indeed, we only described it via its direct modification of the electrical potential. Yet, as we have seen in the previous section, the charge distribution at the molecular interface cannot be trivially explained and the electric field of the tip may affect it also in a non-trivial way, by modifying for instance the interface dipole. In more detail, the inducement of new image potential states of our model gives this right trend for the peaks positions in dI/dV under tip approach: as the tip is brought closer to the sample these peaks move together since the induced field for a given bias sweep is stronger. It is however not clear if our model predicts the correct law for the peak position: it seems to be roughly linear and we cannot determine if we would not rather get a power law.

All in all, a local gating by image potential states can explain the main characteristics of the observed feature. Probably, DFT calculations would be necessary to help define the exact details of the energy alignment of the molecules at the interface and this would be necessary to determine how the electric field of the tip modify the potential landscape at the interface.

III. Conclusion

In this chapter we have investigated the properties of the molecules after deposition on a cold sample. The FeP molecules form islands in which chlorine adatoms are randomly distributed. This random distribution influences the electronic properties of the molecules in a non homogeneous way and leads to the presence of two different molecular types (dark and bright) on the surface. AFM measurements show that those two molecular types are related to different charge distributions and indicate the presence of a surface dipole at the interface between the substrate and molecules. Interestingly, a wide variety of features are exhibited by dark molecules in their dI/dV spectra. In particular, some show oscillations that cannot be accounted for by models reported in the literature so far. A characterization of their dispersion in space indicates that a gating phenomenon is most likely at the origin of these. In order to explain its origin we postulated that the potential landscape at the molecular interface is such that the electric field of the tip may modify the number of image potential states. This effectively leads to a charge redistribution and would thus explain the observed features in dI/dV.

Chapter 6

Yu-Shiba-Rusinov State: Quantum Phase Transition and Transport

The results presented in this chapter have been published as

L. Farinacci et al. *Tuning the Coupling of an Individual Magnetic Impurity to a Superconductor: Quantum Phase Transition and Transport.* Phys. Rev. Lett. **121**.19 (2018), p. 196803. DOI: 10.1103/PhysRevLett.121.196803

A magnetic impurity adsorbed on a superconductor induces a Yu-Shiba-Rusinov (YSR) bound state in its vicinity. The energy of this YSR depends on the coupling strength between the impurity and the substrate. At weak coupling, the bound state is unoccupied and the system is a free-spin ground state. Upon increase of the coupling strength, the system undergoes a quantum phase transition to a screened-spin ground state in which the YSR state is occupied. The quantum phase transition (QPT) is of first order and has been observed in quantum dots either indirectly via Josephson current measurements [137] or more directly in a transport regime where Andreev reflections dominate [39, 126, 123]. Here, we show that we can drive the quantum phase transition on the single impurity level.

We investigate the properties of molecules in the Kagome phase that display one YSR state which is not coupled to any other YSR state. In the first section we show that by approaching the tip toward the molecule we are able to modify the YSR state energy. We interpret this as the result of a molecular distortion upon tip approach and argue that the energy change is mainly driven by a modification of the coupling strength J of the impurity to the surface. This enables us to identify the screened-spin nature of the ground state. Moreover, we show that the flexibility of the molecule not only allows for a controlled tuning of the YSR state energy but also enables us to drive the system through the QPT. In the second section we analyze the variety of transport processes that occur as the junction conductance is increased by this tip approach. We show that the YSR state can be excited by single-quasiparticles but also via (multiple) Andreev reflections.

I. Tip approach over a FeP molecule

We investigate the properties of the molecule shown in the topography image displayed in the inset of Fig. 6.1a [1]. One can see that a single YSR state is detected above both its Fe center

[1] This molecule is at the edge of an island in which a Kagome lattice is formed (see chapter 4). We show in chapter 8 that such molecules have only one YSR that does not couple to its neighbors. The same

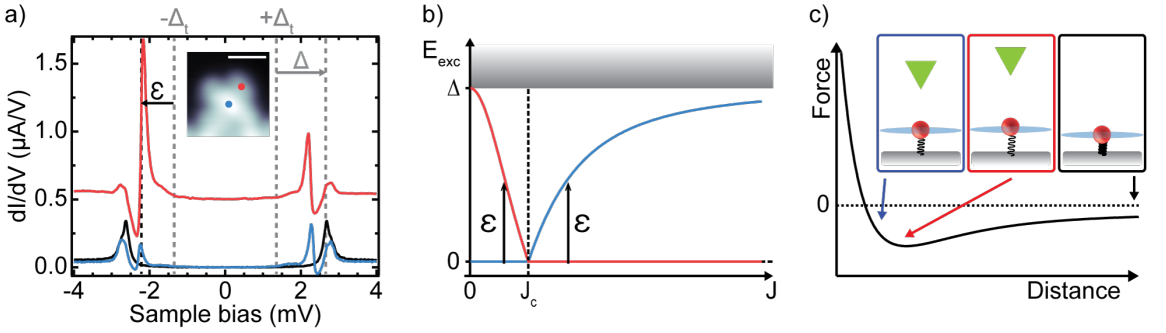

Figure 6.1.: a) dI/dVspectra taken with a Pb tip above the bare Pb substrate (black), the center (blue) and ligand (red, offset for clarity) of a FeP molecule (see topography image in the inset). Feedback opened with $V_{\text{bias}} = 5$ mV, $I = 200$ pA and signal modulated with $V_{\text{rms}} = 20$ μeV. b) The energy dependence of the YSR state leads to a QPT at a critical coupling J_c. A pair of resonances in the excitation spectrum with energy ϵ can therefore correspond to either a free-spin ground state ($J \leq J_c$) or a screened-spin state ($J \geq J_c$). c) The force between the tip and the molecule is derived from a Lennard-Jones potential: at large distances, attractive forces pull the molecule away from the surface and, at short distances, repulsive interactions set in pushing the molecule back to the substrate.

(blue curve) and molecular ligand (red curve) with the presence of a pair of resonances at $V_{\text{bias}} = \pm 2.2$ mV inside the superconducting gap (a reference spectrum taken on Pb is shown in black along with two vertical lines that indicate to the gap size Δ_t of our superconducting tip). As explained in chapter 3 section III.2 and illustrated again in Fig. 6.1b, one cannot identify the ground state of the system only by the detection of this pair of resonances. They could correspond both to an excitation from a free-spin ground state to a screened-spin excited state (left ϵ arrow) or oppositely to an excitation from a screened-spin ground state to an excited free-spin state (right ϵ arrow). The idea of the experiment is thus to modify the coupling strength J of the impurity to the substrate by approaching the tip toward the molecule and identify the ground state from the shift of the YSR state. Indeed, the interaction of the molecule with the tip can be qualitatively described by a Lennard-Jones potential resulting in a force-distance curve as sketched in Fig. 6.1c. As explained in chapter 2 section III.2, at large distances, van der Waals forces dominate and the molecule is attracted toward the tip. As a result, the distance between the molecule and the substrate is slightly increased (black and red insets of Fig. 6.1c) which leads to a decrease of the coupling strength[2]. As the tip is brought in the close vicinity of the molecule, repulsive interactions set in (red to blue insets of Fig. 6.1c) resulting in a decrease of the molecule-substrate distance and thus increase of the coupling strength J. We present in the following the results of such a tip approach above the Fe center and molecular ligand of the molecule shown in Fig. 6.1a.

1. Approach above the Fe center and quantum phase transition

Fig. 6.2a shows the evolution of the junction conductance as the tip approaches the Fe center of the molecule. Throughout this chapter we define the tip offset Δz from the height at which the feedback was opened with $V_{\text{bias}} = 5$ mV and $I = 200$ pA with positive (negative) values corresponding to a retraction (approach) of the tip. The evolution of the conductance shows the expected exponential increase at large tip-sample distances (the small deviations

observations are made for molecules in different environment [49]

[2]We discuss in the following how other parameters are also affected.

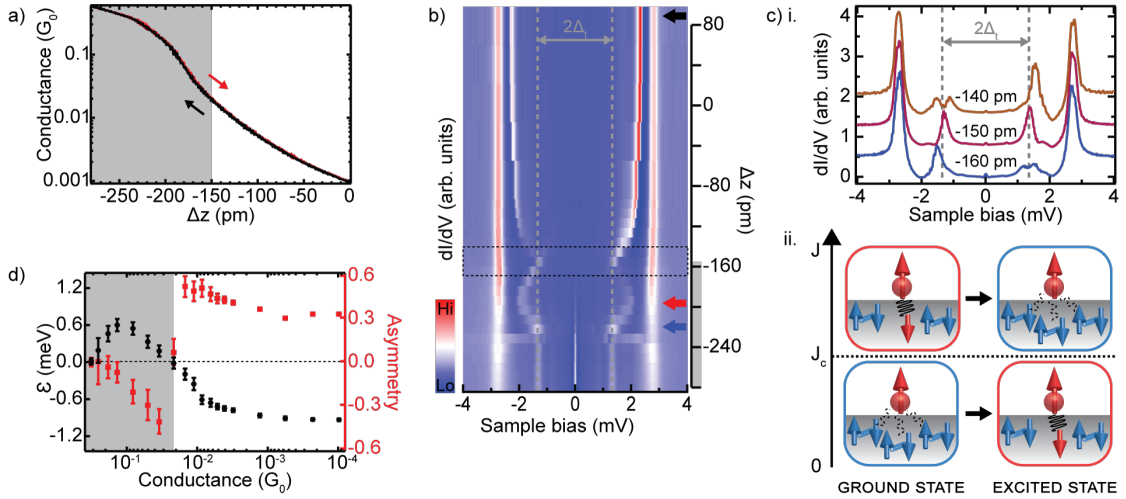

Figure 6.2.: Tip approach over the Fe center. a) Evolution of the junction conductance (in $G_0 = 2e^2/h$) as a function of tip offset Δz. b) 2D color plot of a set of spectra, normalized to their conductance at $V_{\text{bias}} = 5$ mV, taken at different tip offset Δz after opening the feedback with $V_{\text{bias}} = 5$ mV, $I = 200$ pA (modulation with $V_{\text{rms}} = 20$ μeV) c.i) Spectrum before ($\Delta z = -140$ pm), at ($\Delta z = -150$ pm) and after ($\Delta z = -160$ pm) the QPT (offset for clarity). ii)The asymmetry reversal is due to the different excitation processes probed: before (after) the QPT the quasiparticle is destroyed (created) as sketched for $J \geq J_c$ ($J \leq J_c$). d) Extracted energy (black) and asymmetry (red) of the YSR as a function of the junction conductance.

are due to non-linearities of the $I - V$ converter for small currents). Around $\Delta z = -150$ pm we detect a superexponential increase of the conductance with then a gradual saturation that indicates a smooth transition to contact [99]. The forward (black) and backward (red) traces are identical which ensures the reproducibility and reversibility of the experiment.

We now analyze the evolution of the dI/dV spectra (normalized to their conductance at $V_{\text{bias}} = 5$ mV) along this tip approach as shown in the 2D-color plot of Fig. 6.2b. As one can see, the pair of resonances initially shifts away from the gap edge and toward the Fermi level. At $\Delta z = -150$ pm, the energy of the YSR crosses the Fermi level and its asymmetry is reversed around this crossing point. This is shown in more detail in Fig. 6.2c, where the three spectra with $\Delta = -140, -150, -160$ pm are displayed. Beyond this turning point the YSR state resonances first shift away from Fermi energy and then revert at $\Delta z = -190$ mV back toward it. From $\Delta z = -240$ pm on, the dI/dVspectra are dominated by resonances at $V_{\text{bias}} = 0$ mV and $V_{\text{bias}} = \pm\Delta_{\text{t}}$.

The qualitative change of the YSR state energy can be fully captured by the modifications of the coupling strength J described above and allows for an identification of the system's ground state (see chapter 3 section III.2 for a detailed description of the YSR energy dependence). Indeed, the initial shift toward the Fermi level (black arrow in Fig. 6.2b) is ascribed to a decrease of J so that the system must be in a screened-spin ground state (see Fig. 6.1b). As the tip is brought closer, J decreases more substantially and the system crosses the QPT at $\Delta = -150$ pm (this point is addressed in details in the next paragraph). The coupling strength further decreases with thus a shift of the YSR state resonances away from Fermi energy. At $\Delta z = -190$ pm (red arrow in Fig. 6.2b) the system enters the repulsive regime and the coupling strength is increased leading to a shift of the YSR state energy back toward

Fermi energy. As a result, we can plot the evolution of the YSR state energy as shown in Fig. 6.2d (black dots) with $\epsilon < 0$ ($\epsilon > 0$) indicating a screened-spin (free-spin) ground state.

We now discuss in more details the crossing of the QPT at $\Delta z = -150$ pm. Anticipating on the discussion of the next section we can consider only single-electron tunneling because of the low conductance of the junction. We can ascertain the crossing of the QPT by investigating the YSR asymmetry $(I_+ - I_-)/(I_+ + I_-)$ with $I_{+/-}$ being the intensity of the YSR resonance at positive and negative bias voltages (see chapter 3 section III.2). Its evolution throughout the approach is shown in Fig. 6.2d (red dots) and shows a clear correlation with the YSR state energy ϵ: a sharp sign reversal of the asymmetry occurs as the latter crosses Fermi energy. This reversal can be understood when considering the different excitation processes as sketched in Fig. 6.2d. Before the QPT the excitation corresponds to the annihilation of the bound quasi-particle at the impurity (top sketch). The excitation process relates then to $\gamma = uc_\alpha - vc^\dagger_\beta$ where γ (c_α) is the annihilation operator of the bound quasi-particle (electron with spin α) and u (v) the electron component of the YSR state (see chapter 3 section III.2). The resonance of the YSR state in the positive bias regime corresponds to an electron-like excitation and its intensity before the QPT is thus proportional to $|v|^2$. The intensity of the resonance in the negative bias regime is proportional to $|u|^2$. At $\Delta z = -150$ pm the energy of the excitation is zero and the YSR resonances overlap with their thermal replica (see Fig. 6.5 and discussion in section II.1) so that the resulting $\mathrm{d}I/\mathrm{d}V$spectra is symmetric (see purple spectrum of Fig. 6.2c). After the transition, the excitation processes involve now the creation operator of the bound quasi-particle $\gamma^\dagger = u^* c^\dagger_\alpha - v^* c_\beta$ (see Fig. 6.2d). Consequently, the intensity of the electron-like resonance in the positive bias regime is now proportional to $|u|^2$ while the one of the hole-like resonance in the negative bias regime is proportional to $|v|^2$. As a result, we can conclude that the sharp sign reversal of the YSR asymmetry shown in Fig. 6.2c that happens conjointly with the crossing of Fermi energy by the YSR energy is the hallmark of the QPT.

Before investigating the effect of a similar approach experiment above the ligand of the molecule we address in more details the validity of the assumptions of our model. First of all, we point out that the magnetic impurity was treated within the framework of the simple spin 1/2 model. With scanning tunneling microscopy (STM), the spin of an entity cannot be measured directly so that density functional theory (DFT) calculations would be necessary to have more information about the spin state of the molecules. We should also remark that in gas phase the FeP molecule has a spin 1 and that bright molecules in the mixed phase can display up to three YSR states (see appendix 9). Nonetheless, here, we argue that the investigated YSR state is due to an effective spin 1/2 impurity. As a matter of fact, we notice that in the mixed phase the various YSR states were assigned to unpaired electrons that couple individually to the substrate. Here, it seems that if the total spin of the impurity can be larger than 1/2 only one unpaired electron couples efficiently to the substrate to give rise to a single YSR state. Indeed, we observe in the normal state a Kondo resonance as shown in chapter 4 Fig. 4.8. The presence of the Kondo effect is usually associated with half-integer spins with $|m_s = \pm 1/2\rangle$ as a ground state to allow for a spin flip of the substrate electrons. A spin 1/2 is thus more likely. Moreover, under tip approach we do not observe a splitting of the YSR resonance into several resonances, neither above the center of the molecule nor above its ligand (see next subsection and Fig. 6.3). This discards the unlikely case of two different YSR states lying at the same energy at $\Delta z = 0$ pm as different orbitals would have their coupling strength affected in different ways when the molecule distorts.

We now justify the fact that J is the key parameter for the driving of the system through the QPT. As we have seen in chapter 3 section III.2, in all generality, the energy of a YSR state depends on the substrate gap energy Δ and density of states at Fermi energy in the

normal state ρ_0 as well as on the exchange potential J and potential scattering V as follows:

$$\epsilon = \pm\Delta\left(\frac{1-\alpha^2+\beta^2}{\sqrt{(1-\alpha^2+\beta^2)^2+4\alpha^2}}\right), \tag{6.1}$$

where $\alpha = \pi\rho_0 SJ$ and $\beta = \pi\rho_0 V$.

Here, we note that the exchange potential and potential scattering have been obtained by a Schrieffer-Wolff transformation from the Anderson model as explained in chapter 3 so that they include the hybridization between the impurity orbital and the substrate. Although all parameters (Δ, ρ_0, J, V) should in principle be considered to explain the energy shift of the YSR state we argue that J is the most relevant one for the driving the QPT shown in Fig. 6.2.

As a matter of fact, ρ_0 is a bulk parameter and it can safely be assumed that it remains constant throughout the tip approach. Self-consistent calculations have shown that the gap energy Δ is affected by the coupling strength J: the bound quasi-particle at the impurity perturbs locally the Cooper pairs of the substrate [188, 59, 144]. However, calculations made by F. von Oppen in the framework of a collaboration show that the energy shift of the YSR state due to this dependence of Δ on J is negligible within our energy resolution of the order of ~ 100 μeV [49]. The scattering potential V depends on the relative position of the energies of singly and doubly occupied orbitals with respect to the Fermi level (see chapter 3 section II Fig. 3.4). It thus reflects the charge transfer between the molecule and the substrate. Furthermore, it is proportional to the hybridization strength between this impurity orbital and the substrate. Therefore, since the presence of the tip modifies the distance between the impurity and the substrate and thereby this hybridization strength, V is modified upon tip approach. Nevertheless, a driving of the QPT solely under the action of V would require a sign change of this parameter. This would imply a substantial shift of the singly and doubly occupied impurity levels (see Fig. 3.4) corresponding to a considerable charge transfer that is very unlikely. The exchange potential or coupling strength J is also proportional to the hybridization strength of the impurity orbital to the substrate (see equation (8.11)). It is therefore affected by the approach of the tip as described previously and its variation suffice to explain qualitatively our results.

2. Approach above the molecular ligand

As we have seen in Fig. 6.1a, the YSR state is also detected above the ligand of the molecule. We therefore performed a similar approach experiment on the location marked with a red dot in the topography image of the inset of Fig. 6.1a and present the results in Fig. 6.3.

The evolution of the conductance is displayed in Fig. 6.3a and shows the same behavior as above the center with first an exponential increase and then a smooth transition to a contact regime with a saturation of the conductance. Here again, the forward and backward traces are identical to one another which ensures the stability and reproducibility of the experiment. The evolution of the $\mathrm{d}I/\mathrm{d}V$spectra (normalized to their conductance at $V_{\mathrm{bias}} = 5$ mV) is shown as a 2D-color plot in Fig. 6.3b. At large tip-sample distances, the YSR state is at the same energy as above the Fe center and shows the same shift away from the gap edge under tip approach. This confirms that it is the same YSR state that is detected throughout the molecule and that it is in a screened-spin ground state. We note that the asymmetry of the YSR state is reversed as compared to above the Fe center and refer to the next chapter for a discussion about the origin of this reversal.

The initial shift of the YSR resonances is followed at $\Delta z = -150$ pm by a turn-back toward the gap edges that occurs before the energy of the YSR state reaches the Fermi level. Also,

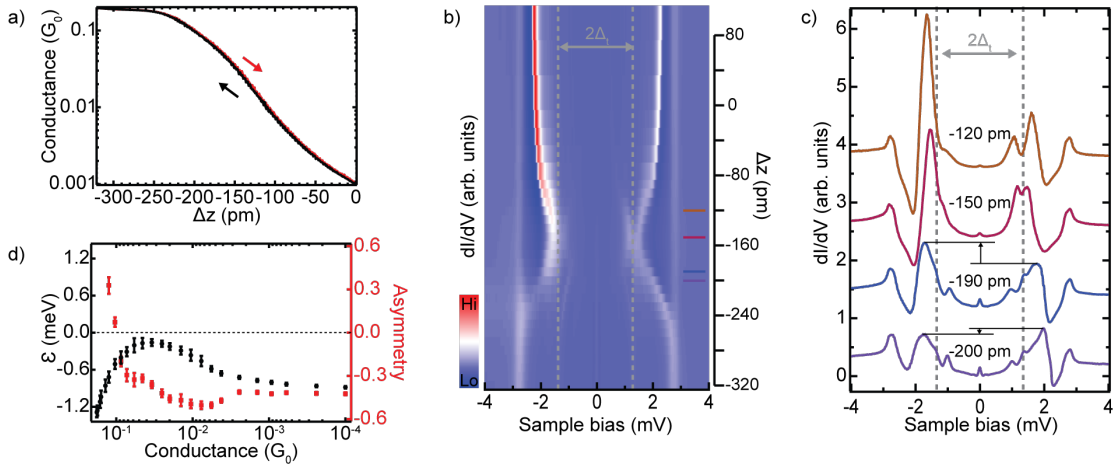

Figure 6.3.: Tip approach above the molecular ligand. a) Evolution of the junction conductance (in $G_0 = 2e^2/h$) as a function of tip offset Δz. b) 2D color plot of a set of spectra, normalized to their conductance at $V_{\text{bias}} = 5$ mV, taken at different tip offset Δz after opening the feedback with $V_{\text{bias}} = 5$ mV, $I = 200$ pA (modulation with $V_{\text{rms}} = 20$ μeV). c) Four spectra of the approach set (offset for clarity) that show that the YSR does not reach Fermi energy and only reverses its asymmetry at $\Delta z = -200$ pm when Andreev reflections become dominant. d) Extracted energy (black) and asymmetry (red) of the YSR as a function of the junction conductance.

we note that at this turning point the asymmetry of the YSR state keeps the same sign. This is illustrated in more detail in Fig. 6.3c where we display four exemplary spectra of the approach set. The YSR resonance at negative bias has a higher intensity than the one at positive bias up to $\Delta z = -190$ pm and the asymmetry reverses only at $\Delta z = -200$. In Fig. 6.3d we display the evolution of the YSR energy (black dots) and asymmetry (red dots) throughout the approach.

The energy shift of the YSR state can be understood in an identical manner as above the Fe center: at first the interaction of the molecule with the tip is attractive which lifts the molecule and thus decreases the exchange coupling J and then at $\Delta = -150$ pm repulsive forces set in so that the distance of the molecule to the sample is reduced and J increases again. As one can see, the system is this time not driven through the QPT. This is due to differences in the local forces between the molecule and the tip as well as in the molecular deformation under these different force fields.

The change in the asymmetry of the YSR at $\Delta z = -200$ pm state is due to the growing importance of Andreev reflections through the junction [181]. As the tip is brought closer to the molecule we can see both above the Fe center and the ligand of the molecule that peaks develop inside the bias window defined by the tip gap. These are a fingerprint of higher order tunneling processes that occur through the junction. In the next section we analyze therefore in more details the transport properties of the junction.

II. Transport through a YSR state

Until now we have focused on the most prominent peaks inside the superconducting gap that corresponds to the standard YSR resonances. However, as one can see from both of the approach sets above the Fe center (Fig. 6.2) and molecular ligand (Fig. 6.3) others peaks are

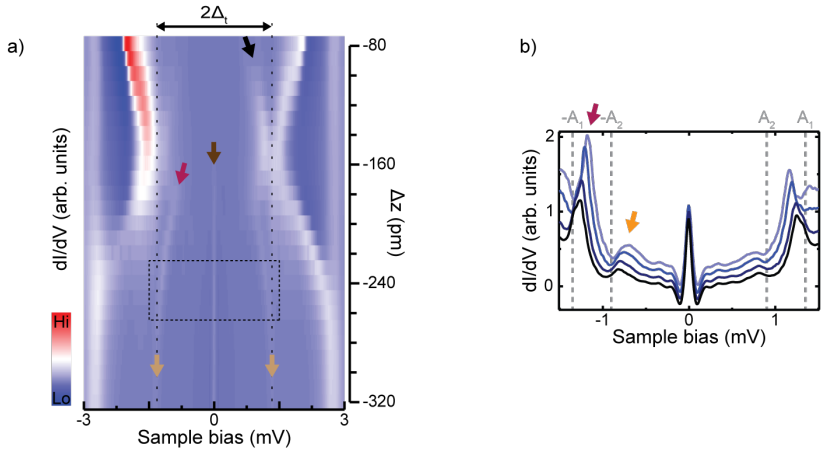

Figure 6.4.: a) Enhanced view of the approach set of Fig. 6.3b. b) Four spectra (offset for clarity) of this set that show peaks due to Andreev reflections mediated by the YSR state.

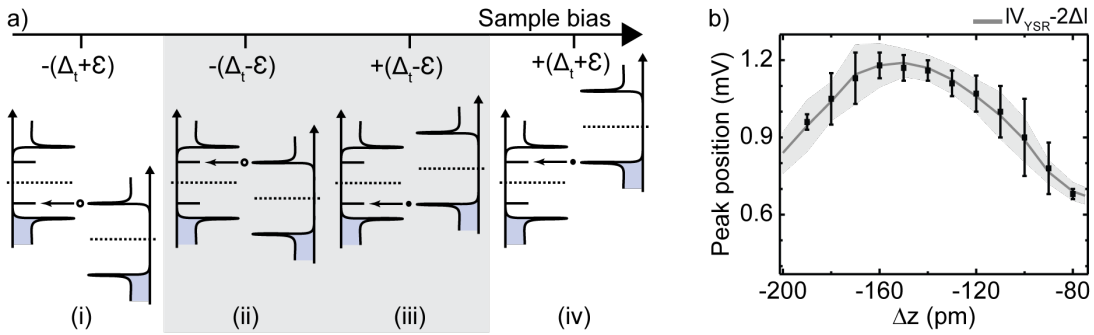

Figure 6.5.: a) Single electron or hole tunneling processes involving the YSR state. The two main YSR resonances are probed at $V_{\text{bias}} = \pm(\Delta_t + \epsilon)$ (i. and iv.). Thermal excitations of the YSR state are seen at $V_{\text{bias}} = \pm(\Delta_t - \epsilon)$ (ii. and iii.). b) Extracted positions of the series of peaks marked with a black arrow in Fig. 6.4a (black dots) compared to the expected positions of the thermal excitations of the YSR state (black trace) as a function of tip offset Δz.

detected within the bias window defined by the tip gap Δ_t. Fig. 6.4a shows an enhanced view of the approach set recorded above the ligand where we indicate these different peaks with colored arrows. We first identify a series of peaks marked by a black arrow that shift in an opposite manner to the main YSR resonances. Then, around $\Delta z = -200$ pm a peak develops at zero bias. Upon further tip approach we can identify two series of peaks that shift similarly to the main YSR resonances: the most intense series is shown with a purple arrow in Fig. 6.4a and the second series is less intense and shown by a yellow arrow in the enhanced view of Fig. 6.4b. Conjointly to these series of peaks we detect resonances at $V_{\text{bias}} = \pm\Delta_t$ (see for instance blue spectrum of Fig. 6.3c). In the following we address the origin of these different peaks by analyzing the various tunneling processes that take place as the junction conductance is increased.

1. Single quasi-particle tunneling

When the junction conductance is low single-electron tunneling processes dominate the transport properties of the junction [181]. The YSR state is probed at $V_{\mathrm{bias}} = -(\Delta_{\mathrm{t}} + \epsilon)$ [$V_{\mathrm{bias}} = +(\Delta_{\mathrm{t}} + \epsilon)$] as sketched in Fig. 6.5a.i (iv): when the hole-like (electron-like) coherence peak of the tip is aligned with the YSR excitation energy below (above) the Fermi level it can be transmitted and excites the system as shown in Fig. 6.1b. On the sample side, this hole (electron) excitation relaxes to the quasi-particle density of states (DOS) of the substrate via the adsorption or emission of a photon or phonon [181]. Due to the finite temperature of the experiments, the YSR state can also be thermally excited. As a result, the thermally excited YSR state can be probed by a hole (electron) excitation at negative (positive) bias as sketched in Fig. 6.5a.ii (iii). Consequently, the asymmetry of the thermal resonances is opposite to the one of the main YSR resonances. Moreover, the biases at which these resonances related to one another follows $V_{\mathrm{thermal}} = \pm|V_{\mathrm{YSR}} - 2\Delta|$.

The series of peaks indicated by a black arrow in Fig. 6.4a has an opposite asymmetry as the one of the main YSR resonances. In Fig. 6.5b we therefore compare the position of these peaks (black rectangles) to the expected position of the thermal excitation of the main YSR resonances (grey trace). The error bars correspond to the uncertainty with which we read the position of the peaks. We find a good agreement between the two data sets and can thus assign this series of peaks in Fig. 6.4a to the thermally excited YSR. We note that these thermal excitations are mostly seen when the energy of the YSR state is close to the Fermi level which is in accordance with the Fermi-Boltzmann statistic that governs the probability of its thermal excitation.

2. Higher order processes

As the tip is brought closer to the surface tunneling processes that involve more than one electron gain importance. We analyze these processes in the following by focusing first on those that are typical for superconductor-superconductor junctions and then study those that involve the YSR state.

2.1. Josephson effect

The zero bias peak marked by a dark brown arrow in Fig. 6.4 is the manifestation in scanning tunneling spectroscopy (STS) of the Josephson effect [169]. At close tip-sample distances, the wavefunctions of Cooper pairs of the sample and tip overlap with one another which allows for Cooper-pair tunneling through the barrier. The Cooper-pair current is dissipationless and thus not driven by a voltage drop at the junction but by the phase difference between the two superconductors. This effect is therefore observed at zero bias.

2.2. Multiple Andreev reflections

The resonances at $\pm\Delta_{\mathrm{t}}$ can be assigned to conventional Andreev reflections [210]. When the electron-like coherence peak of one of the two leads is aligned with the Fermi level of the other lead an electron can be transmitted through the junction, be reflected as a hole (since there is no DOS for it to tunnel to) whose energy is then also at Fermi energy (this effectively creates a Cooper pair). This hole tunnels then to the electron-like coherence peak. In total two electrons are transmitted through the junction and these onset of two-electrons processes lead to the observed resonances at $V_{\mathrm{bias}} = \Delta_{\mathrm{t}}$ (in general $V_{\mathrm{bias}} = (\Delta + \Delta_{\mathrm{t}})/2$ but here we have $\Delta_{\mathrm{t}} = \Delta$). Higher order processes that involve the reflection of $n \geq 2$ electrons lead

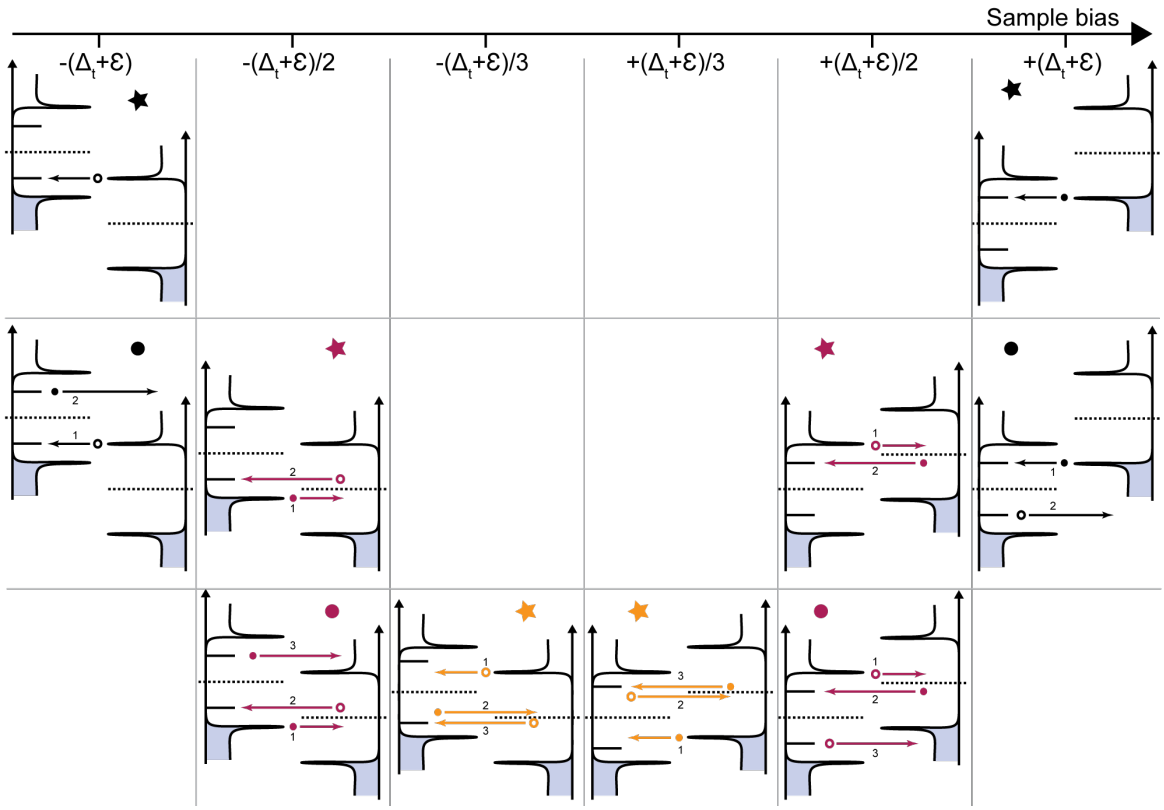

Figure 6.6.: Tunneling processes involving the YSR state as a function of bias voltage (horizontal axis) and number of electrons and/or holes involved (vertical axis). For more than two tunneling particles the processes are referred to as Andreev reflections: electrons and holes are reflected through the junction until their energy matches the position of the YSR state. They can then either excite the system (processes marked with a star) or be resonantly reflected back (processes marked with a dot, named *resonant* Andreev reflections).

similarly to peaks at $V_{\text{bias}} = \pm(\Delta + \Delta_t)/n$. We note the position of these Andreev multiple reflections by grey dashed lines in Fig. 6.4b.

We now discuss the two series of peaks that are marked by purple and yellow arrows in Fig. 6.4. Their position does not correspond to the Andreev reflections described above and their shift under tip approach indicate that they are related to the presence of a YSR state in the junction. We show that these are related to Andreev reflections mediated by the YSR state [169].

We show in Fig. 6.6 the various tunneling processes that involve the YSR state. They are sorted horizontally according to the bias voltage at which they occur and vertically according to the number of quasi-particles transferred through the junction. The first line corresponds to the standard tunneling to the YSR state described above. The other processes are Andreev reflection processes that involve the YSR: electron and holes are reflected through the junction until they can either excite the YSR state (sketches marked with a star) or be transmitted to the continuum of the DOS of the quasi-particle (sketches marked with a disk). In the first case, the occupation of the YSR state is modified and the current that is allowed to flow through these processes is limited by the rate at which the quasi-particle relaxes to the continuum. In the second case, the YSR state is merely an intermediate step for the reflection processes and these Andreev reflections are called *resonant* [181]. Each voltage $V_{\text{bias}} = (\epsilon + \Delta_t)/2$ correspond to the onset of two types of processes: one resonant and one

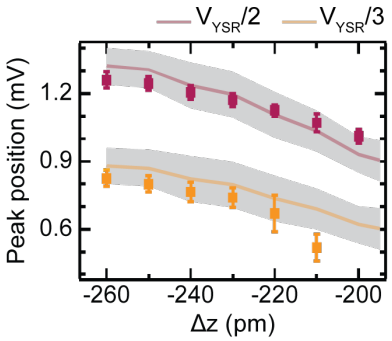

Figure 6.7.: Positions of the series of peaks indicated by a pink and yellow arrows in Fig. 6.4 (dots) compared to the expected position of the Andreev reflection processes shown in pink and yellow in Fig. 6.6 given the position of the main YSR resonances.

non-resonant. At first, the current is carried mostly by non-resonant Andreev reflections as they involve one particle less than their resonant counterpart. The pair of resonances corresponding to these processe therefore inherit the asymmetry of the YSR state. However, as the junction conductance is increased, the current carried by such processes saturates and the resonant Andreev reflections become dominant.

In the graph shown in Fig. 6.7 we compare the energy positions of the peaks belonging to the series marked with a purple and yellow arrow in Fig. 6.4 (rectangle of the corresponding color) to the positions at which the multiple Andreev reflections sketched in Fig. 6.6 are expected to take place given the position of the main YSR state resonances. The good agreement allows us to ensure that these resonances correspond indeed to Andreev reflections mediated via the YSR state.

2.3. Contact regime

When the tip reaches the contact regime the YSR main resonances merge with the gap edges and consequently the multiple Andreev reflections mediated by the YSR state merge with the conventional ones (see Fig. 6.4). In this regime the coupling of the impurity to the tip competes with the one of the impurity to the sample. As a result, the two leads are effectively coupled to each other and the usual assumption that the current can be derived from Fermi's Golden rule fails. The applied bias drives the coupled system *substrate-molecule-tip* out of equilibrium so that local excitations can no longer be detected in spectroscopic measurements [8].

III. Conclusion

In this chapter we have made use of the flexibility of the FeP molecule to tune the coupling of a magnetic impurity to a superconductor. By taking into account the nature of the forces between the tip and the molecule we have shown that one can unambiguously identify the nature of the ground state of the system. Moreover, we were able to tune continuously and reversibly the system through the QPT on the single impurity level. By investigating in detail the characteristics of the YSR excitation in STS we have shown that the QPT can be identified by a sharp reversal of the YSR asymmetry. Finally, we have considered the various tunneling processes that take place when the junction conductance is varied through three orders of magnitude. Notably, we identified Andreev reflections mediated by the YSR state.

Chapter 7

Modulation of the Kondo and Yu-Shiba-Rusinov lineshapes by orbital cotunneling

The Kondo effect and the formation of a Yu-Shiba-Rusinov (YSR) state share the same origin: the scattering of substrate electrons at a magnetic impurity. Previous studies have investigated the relation between the characteristic energy scales of both effects: the YSR state energy and the Kondo temperature are correlated [62, 82] since they both depend on the exchange coupling strength J between the impurity and the substrate electrons. In this chapter, we investigate another aspect of the scattering problem: besides an exchange interaction, the substrate electrons are also subject to a potential scattering K (see chapter 3). This potential scattering is related to the local electron-hole asymmetry of the system and affects the lineshapes of both many-body states in scanning tunneling spectroscopy (STS).

In a previous study by G. Ahmadi [3], there have been indeed hints of a correlation between the variations of the YSR asymmetry and Kondo interference factor across an iron-tetra-pyridyl-porphyrin (Fe-TPyP) molecule on a Pb(111) surface. Here, we investigate this correlation in more detail and propose to explain the observed variation by an effective change of the scattering potential K over the Fe-TPyP molecule. More precisely, we establish that the localization of the induced Kondo resonance and YSR state are almost identical and bear similarities with the pattern given by the relative intensities of the highest occupied molecular orbital (HOMO) and lowest unoccupied molecular orbital (LUMO) of the molecule. We therefore propose that these orbitals serve as intermediate states in a cotunneling description of the scattering of electrons onto the magnetic impurity, thereby modulating locally the electron-hole asymmetry of the system.

I. FeTPyP on Pb(111)

In this section we characterize the electronic properties of the Fe-TPyP molecule and, in particular, the spatial distribution of its HOMO and LUMO.

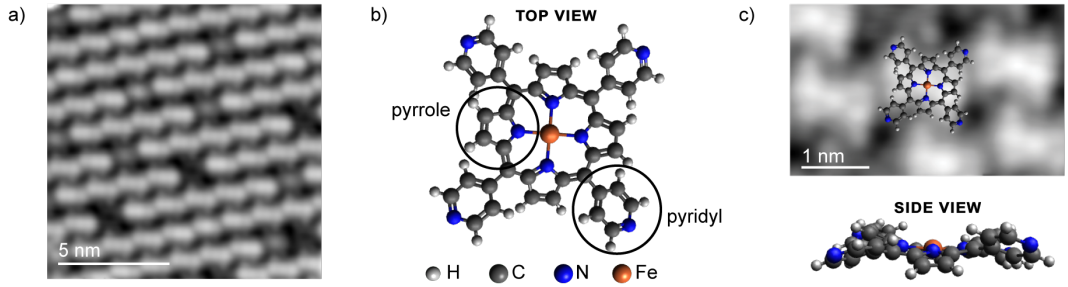

Figure 7.1.: a) Topography image after molecular deposition showing two types of molecules that appear either bright or dark at $V_{\text{bias}} = -800$ mV, $I = 20$ pA. b) Molecular model of the FeTPyP molecule. c) Imaging the molecules of the majority type with $V_{\text{bias}} = 5$ mV and $I = 100$ pA shows the saddle deformation of the molecules upon adsorption as illustrated by the molecular model below.

1. The FeTPyP molecule

The molecules are evaporated from a Knudsen cell held at 673 K on a Pb(111) crystal with $T_{\text{sample}} = 313$ K. The topography image of Fig. 7.1a shows that the molecules assemble in densely packed islands with two molecular types. The molecules appear either bright or dark at a bias voltage of -800 mV. The Fe-TPyP molecule consists of four pyridyl groups attached to a central porphin ring as shown in Fig. 7.1b. It is known from other studies [12, 72, 96, 166, 10, 11, 30] that these molecules adopt a saddle conformation when deposited on a surface. More precisely, in gas phase the pyridyl groups are rotated by 90° with respect to the flat porphin ring. On a surface, these pyridyl groups rotate in order to increase their interaction with the substrate. Steric hindrance between adjacent hydrogen atoms of the porphine ring and pyridil groups leads to deformation of the molecule as sketched in Fig. 7.1c. The four pyrrole groups are partially tilted with respect to the substrate and the central porphin ring is deformed with two opposite pyrrole groups pointing upwards and the two other ones downwards. It is argued in [3] that small variations in the conformations of the molecules are at the origin of the different types of molecules. Here, we focus on the majority type. Fig. 7.1c shows a topography image of such molecules taken with $V_{\text{bias}} = 5$ mV and $I = 20$ pA with a molecular model overlaid. We see that the saddle deformation reduces the $C_{4\text{v}}$ symmetry of the molecules in gas phase to a $C_{2\text{v}}$ symmetry on the surface: protrusions are present at the Fe center and four pyridyl groups as well as at two of the pyrrole groups that are thus assumed to be the two up-tilted groups.

2. Electronic properties

The electronic properties of the molecules are investigated in Fig. 7.2. We display in Fig. 7.2a the $\mathrm{d}I/\mathrm{d}V$ spectra taken above the center (blue) and the ligand (red) of a molecule as shown in the topography image of Fig. 7.2c. A reference spectrum taken above the bare Pb substrate is also shown in black. We detect in the positive bias a broad resonance around $V_{\text{bias}} = 1.08$ V and in the negative bias one at $V_{\text{bias}} = -360$ mV along with a smaller peak at $V_{\text{bias}} = -45$ mV (see grey dashed lines). This last one is better resolved in Fig. 7.2b where we show spectra recorded at the same locations as in Fig. 7.2a but over a smaller energy range. In order to gain more insight into the origin of these spectral features it is of interest to investigate their spatial distribution. The molecules have a 3D character due to their saddle deformation, we therefore recorded *iso-DOS* $\mathrm{d}I/\mathrm{d}V$ maps by regulating the feedback loop on the lock-in

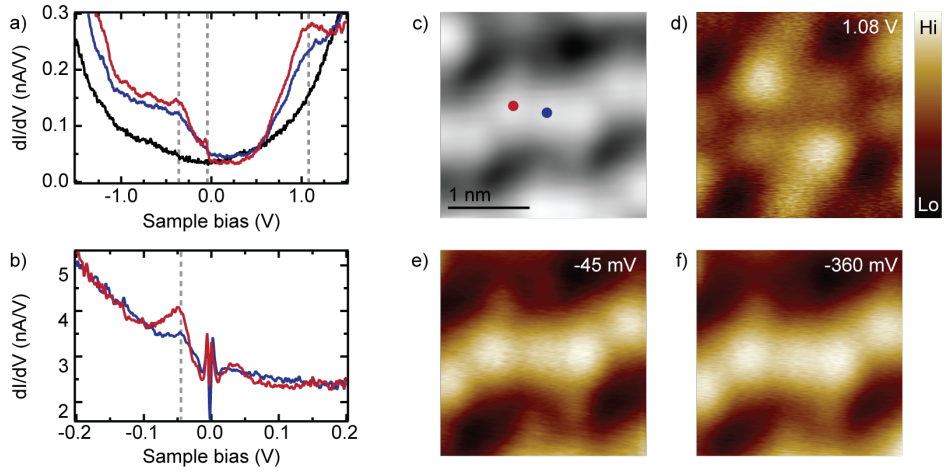

FIGURE 7.2.: a) $\mathrm{d}I/\mathrm{d}V$ spectra recorded above the bare Pb surface (black), the center (blue) and ligand (red) of a FeTPyP molecule (feedback opened at $V_{\mathrm{bias}} = 2$ V, $I = 500$ pA and signal modulated with $V_{\mathrm{rms}} = 10$ mV) as shown by the topography image in c) ($V_{\mathrm{bias}} = -800$ mV, $I = 50$ pA). b) $\mathrm{d}I/\mathrm{d}V$ spectra recorded within a smaller energy range that highlight the presence of a small resonance at $V_{\mathrm{bias}} = -45$ mV (feedback opened at $V_{\mathrm{bias}} = 200$ mV, $I = 500$ pA and signal modulated with $V_{\mathrm{rms}} = 2$ mV). d-f) *iso-DOS* maps of the molecule recorded under different bias voltages as indicated in the top-right corners.

($\mathrm{d}I/\mathrm{d}V$) signal and recording the modulations of the tip height as explained in [171]. The *iso-DOS* maps (taken above the same area as shown in the topography image of Fig. 7.2c) are displayed in Fig. 7.2d-f. The map recorded with $V_{\mathrm{bias}} = 1.08$ V (Fig. 7.2d) shows four protrusions above the pyridyl groups of the molecules with variations in intensity that reflect the $C_{2\mathrm{v}}$ symmetry of the molecules. The maps taken at $V_{\mathrm{bias}} = -360$ mV and $V_{\mathrm{bias}} = -45$ mV have identical patterns with the presence of three protrusions: one above the Fe center and two above the two up-tilted pyrrole groups. We assign the resonances at $V_{\mathrm{bias}} = -360$ mV and $V_{\mathrm{bias}} = 1.08$ V to the HOMO and LUMO of the molecule. The resonance at $V_{\mathrm{bias}} = -45$ mV is most likely caused by a molecular vibration. Indeed, the intensity of this resonance is relatively small and its distribution is identical to the one of the HOMO. A mediation of a vibrational excitation by the HOMO [175, 122, 163, 109, 133, 165, 63] would explain their identical distribution. The absence of a vibrational resonance in the positive bias regime could then be due to the higher energy position of the LUMO with respect to Fermi energy. Also, we note that the energy of this resonance lies in a range where vibrational modes of the Fe-TPyP molecule have been observed on Au(111) [175]. Inelastic processes due to spin excitations can be excluded as they are usually observed at lower energies [176].

The distributions of the HOMO and LUMO are very similar to what has been observed for the same molecule on Au(111) [174] and in agreement with other studies of similar porphyrin derivatives on metal surfaces [220, 13]. In none of these studies were these frontier orbitals observed to carry a spin. This seems also the case here. A singly occupied orbital gives rise to two resonances in $\mathrm{d}I/\mathrm{d}V$ a singly occupied molecular orbital (SOMO) and a singly unoccupied molecular orbital (SUMO), in each of the bias polarities that have thus the same spatial distribution [170]. We have not observed such pair of orbitals in the investigated energy range of Fig. 7.2. The orbital carrying the unpaired electron giving rise to the magnetic fingerprints that are analyzed in the next section is not well-resolved in STS. This indicates that the singly and doubly occupied level of this orbital lie outside the energy range we

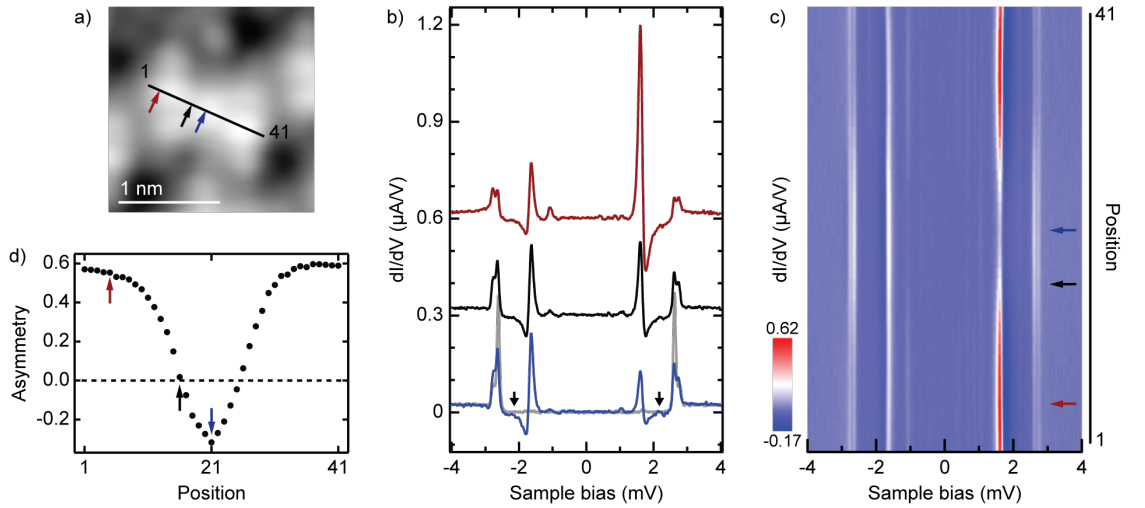

Figure 7.3.: a) Topography image of the investigated molecule ($V_{\text{bias}} = 5$ mV, $I = 100$ pA). b) dI/dV spectra recorded above the bare Pb substrate (grey) and above the molecule as indicated in a) (feedback opened with $V_{\text{bias}} = 5$ mV, $I = 100$ pA and signal modulated with $V_{\text{rms}} = 15$ μeV). c) Set of dI/dV spectra recorded along the line drawn in a). d) Asymmetry of the YSR state extracted from the set of spectra shown in c).

investigate or that their decay into vacuum is steeper than the one of the frontier orbitals. Despite their lack of magnetic character we will see that the HOMO and LUMO play a role in the detection of the magnetic fingerprints of the molecules.

II. Magnetic fingerprints

We now study the magnetic fingerprints of the molecules first when the substrate is in a superconducting state and then when it is a normal metal. In gas phase the Fe center of the molecules is in an oxidation state of +2 and carries a spin 1. Upon adsorption onto the substrate the charge and spin state of the molecule may be affected but we see in this section that the molecules conserve a magnetic moment that gives rise to a YSR state or a Kondo resonance when the substrate is superconducting or metallic, respectively.

1. Characterization of the YSR state

We first characterize in Fig. 7.3 the properties of the molecules on a superconducting substrate. The spectra are recorded with a superconducting tip and a reference spectrum taken on the bare Pb surface is shown in grey in Fig. 7.3b. A pair of resonances at $V_{\text{bias}} = 1.6$ mV indicates the presence of a YSR state above both the Fe center (blue spectrum) and ligand (red spectrum) of the molecule. A faint signal is also seen around $V_{\text{bias}} = 2.1$ mV (see arrows) but as we will see in the next paragraph it is caused by a neighboring molecule and not relevant here. In order to get a better insight into the spatial distribution of the YSR state we record a set of dI/dV spectra (see Fig. 7.3b) along the line shown in the topography image of Fig. 7.3a. The YSR state does not shift in energy but shows variations in its resonances' intensity. This is also clearly seen in Fig. 7.3b: above the Fe center the resonance at negative bias is more intense than the one at positive bias (blue spectrum) and the situation is reversed above the ligand of the molecule (red spectrum). This intensity change is smooth and continuous; we

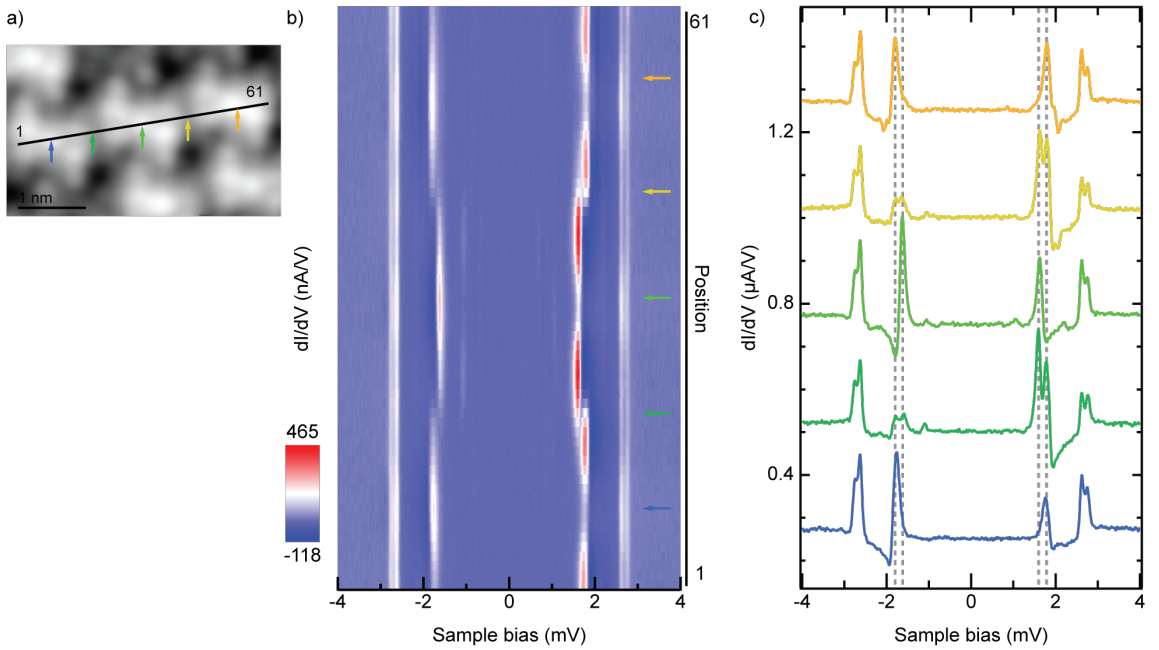

Figure 7.4.: a) Topography image of three neighbohring molecules ($V_{\text{bias}} = 5$ mV; $I = 100$ pA) along which the set of dI/dV spectra shown in b) was taken (feedback opened with $V_{\text{bias}} = 5$ mV, $I = 100$ pA and signal modulated with $V_{\text{rms}} = 15$ μeV). c) Exemplary spectra of this line taken above the centers of and in-between the molecules.

observe positions for which the YSR state is fully symmetric (black spectrum in Fig. 7.3b). This evolution is shown more precisely in Fig. 7.3d where we display the evolution of the asymmetry of the YSR state (defined as $(I_+ - I_-)/(I_+ + I_-)$ with $I_{+/-}$ being the intensity of the resonances at the positive and negative bias) as extracted from the data set of Fig. 7.3b.

Before analyzing in more detail the evolution of the YSR asymmetry above the molecule we show that only one YSR state is detected per molecule. We present in Fig. 7.4b a 2D color plot of dI/dV spectra taken along the line shown in Fig. 7.4a that extends over three molecules. Exemplary spectra taken above the centers and in between the molecules are shown in Fig. 7.4c. Each molecule is the host of one YSR state that is only faintly seen above its neighbor. The energy of the YSR state is slightly different from one molecule to another because of small variations in their adsorption site [3]. Importantly, we do not observe a splitting or delocalization over several molecules of the YSR states that would have indicated a coupling between the YSR states of neighboring molecules. Each molecule acts thus as an independent scatterer with only YSR state. Finally, we note that the change of the asymmetry of the YSR state seen in Fig. 7.3 is observed above all molecules.

We show in Fig. 7.5b dI/dV maps of the two resonances of the YSR state of the molecule investigated in Fig. 7.3 that were recorded while following the topography profile of Fig. 7.5a. The resonance in the negative bias is more intense above the Fe center of the molecule and shows four protrusions above the molecular ligand. In the positive bias, the YSR state has a high intensity above the same four protrusions as the one in the negative bias but seems to be almost absent over the Fe center. A comparison with the blue dI/dV spectrum of Fig. 7.3b shows that the resonance in the positive bias is still present above the Fe center but with much less intensity than above the ligand. All in all, the two resonances of the YSR state appear to follow the same pattern with five pockets (one over the Fe center and four over the

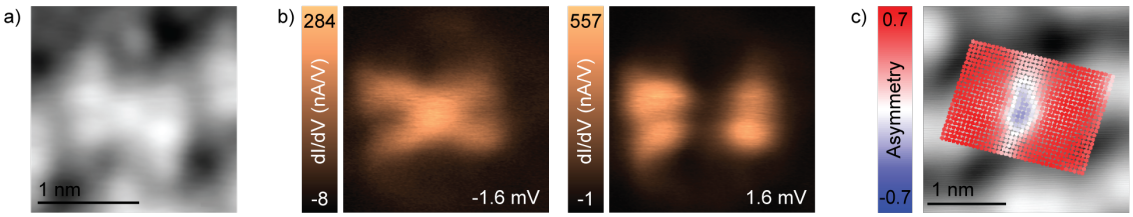

Figure 7.5.: a) Topography image ($V_{\text{bias}} = 5$ mV, $I = 100$ pA) whose apparent height profile was followed when recording the $\mathrm{d}I/\mathrm{d}V$ maps shown in b) ($V_{\text{rms}} = 15$ μeV). c) Asymmetry of the YSR state extracted from the spectra taken at each point of the grid.

molecular ligand) but show clear differences in their signal intensity inside them.

We present in Fig. 7.5c an alternative representation of these intensity variations: we record at each point of the displayed grid a $\mathrm{d}I/\mathrm{d}V$ spectrum and extract the asymmetry of the YSR state. The main characteristic of the asymmetry is a sign reversal between its center and ligand.

It has been shown in [180, 32] that the YSR states induced by magnetic atoms on superconducting substrate inherit the symmetry of the orbital carrying the unpaired electrons they stem from. Interestingly, in our case, the pattern of the YSR shares quite some similarities with both the HOMO and LUMO of the molecule: it appears to result from a convolution of both. We propose in the last section that these orbitals are involved in the scattering of the electrons onto the impurity even though they are not the one carrying the unpaired electron. We should note moreover that in the case of single atoms adsorb on Pb, only one of the two components of the YSR state could be clearly related to its corresponding d orbital. More precisely, it is argued in [32] that a phase shift of some of the Fourier components of the electron part of the YSR leads to the observed discrepancy between its lineshape and the one of the hole component. We do not observe such a discrepancy for the two components of the YSR state in the case of the Fe-TPyP molecule which seems consistent with a different scattering model.

2. Investigation of the Kondo resonance

We now investigate the properties of the same molecule on a metallic substrate (we apply an external magnetic field of 1.5 T). The YSR state is now replaced by a Kondo resonance (Fig. 7.6) whose lineshape varies across the molecule. More precisely, in analogy to Fig. 7.3, we display in Fig. 7.6c a 2D color plot of spectra taken along the line shown in the topography image of Fig. 7.6a. Three exemplary spectra, taken above the center (blue), ligand (red) and in-between (black), along with a reference spectrum taken above the bare Pb(111) surface (grey), are shown in Fig. 7.6b. These three spectra illustrate the variations of the Kondo resonance lineshape throughout the molecule: while the black spectrum displays a fairly symmetric resonance, the tail of the resonance of the red spectrum has a slower decay in the negative bias regime than in the positive one and the situation is reversed for the blue spectrum. As explained in chapter 3 section II, these variations of the resonance lineshape are caused by interferences between different tunnelling paths for the electrons. In order to quantify these changes we fit the spectra with a Frota-Fano function [61]:

$$F(\omega) = -A\Im(ie^{i\phi}\sqrt{\frac{i\Gamma/2}{\omega - \omega_0 + i\Gamma/2}}) \tag{7.1}$$

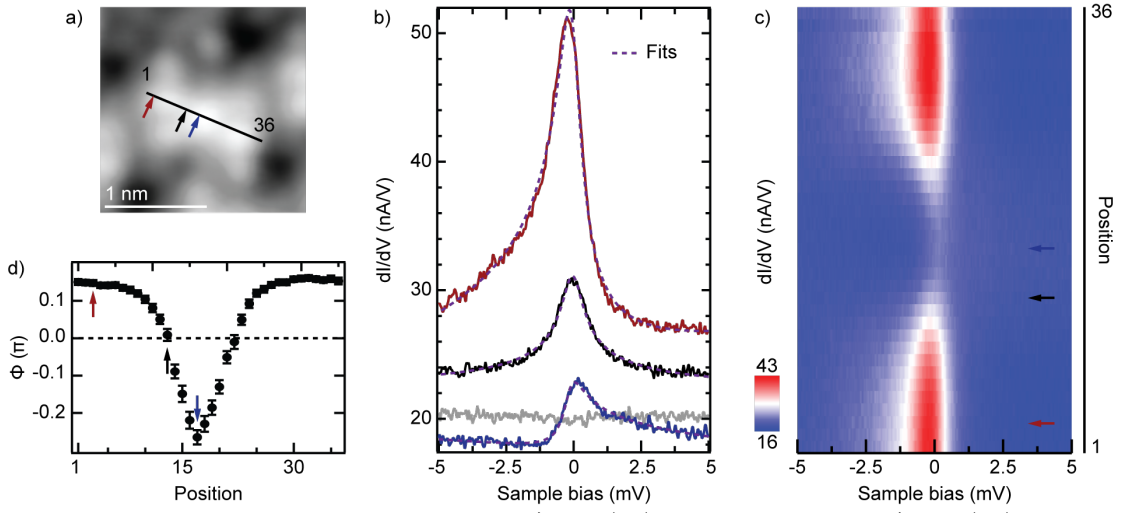

Figure 7.6.: a) Topography image of the investigated molecule ($V_{\text{bias}} = 5$ mV, $I = 100$ pA). b) $\mathrm{d}I/\mathrm{d}V$ spectra taken above the bare Pb substrate (grey) and above the molecule as shown in a) (feedback opened at $V_{\text{bias}} = 5$ mV, $I = 100$ pA and signal modulated with $V_{\text{rms}} = 100$ μeV). Fits of the resonances with Frota-Fano functions are shown by dashed violet lines. c) Set of $\mathrm{d}I/\mathrm{d}V$ spectra taken along the line shown in a). Evolution of the phase factor ϕ extracted by Frota-Fano fits of the spectra shown in b), error bars represent the fit error.

where A is the amplitude of the resonance, Γ its full width at half maximum (FWHM), ω_0 its position and ϕ is the phase parameter that characterizes its shape. As explained in [61], this phase parameter is related to the q-factor of the Fano formula by $\tan(\phi/2) = q$. Along the investigated line we find that the width of the resonance barely scatters around $\Gamma = 0.77$ meV with a standard deviation of ± 0.03 meV. This indicates that the Kondo resonance is caused by the same impurity spin everywhere in the molecule, consistently with our findings for the YSR state. On the contrary, the phase factor presents significant variations as shown in Fig. 7.6d. It mimics the behavior of the asymmetry of the YSR state with, in particular, a sign reversal over the Fe center of the molecule as compared to its ligand.

In order to comprehend in more detail the similarities between the observed YSR state and Kondo resonance we record a set of spectra along the grid shown in Fig. 7.7. We show in Fig. 7.7b the intensity of the $\mathrm{d}I/\mathrm{d}V$ signal at $V_{\text{bias}} = 0$ V that reproduces, to a first approximation, the intensity of the resonance over the molecule. The signal is most intense

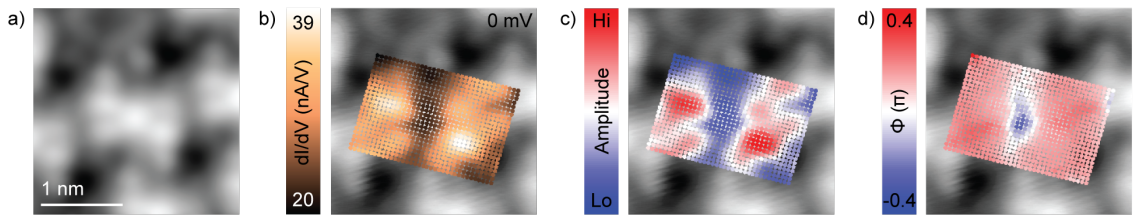

Figure 7.7.: a) Topography image ($V_{\text{bias}} = 5$ mV, $I = 100$ pA) of the molecule above which a grid of spectra was recorded as shown in b-d). (feedback opened at $V_{\text{bias}} = 5$ mV, $I = 100$ pA and signal modulated with $V_{\text{rms}} = 100$ μeV). b) Intensity of the $\mathrm{d}I/\mathrm{d}V$ signal at $V_{\text{bias}} = 0$ mV. Each spectrum of the grid was fitted with a Frota-Fano function and we present in c) and d) the variations of the obtained amplitude and phase factor parameters, respectively.

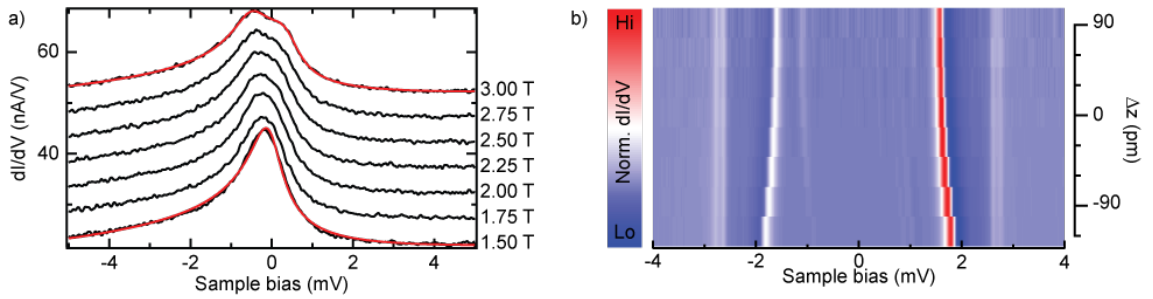

Figure 7.8.: a) Evolution of the Kondo resonance under an external magnetic field (feedback opened at $V_{\text{bias}} = 5$ mV, $I = 100$ pA and signal modulated with $V_{\text{rms}} = 100$ μeV). The spectra are offset for clarity. Red curves are fits with one and two Frota-Fano function for a magnetic field of 1.5 T and 3 T, respectively. b) Set of dI/dV spectra in the superconducting state, normalized to their conductance at $V_{\text{bias}} = 5$ mV taken at different tip offsets Δz after opening the feedback with $V_{\text{bias}} = 5$ mV, $I = 100$ pA (signal modulated with $V_{\text{rms}} = 15$ μeV).

above the four pyrrole groups of the molecule with a distribution that is very similar to the one of the YSR state at positive bias in Fig. 7.5b. Here again the intensity of the signal over the center of the molecule appears by contrast very weak but we emphasize that the Kondo resonance is still present there as shown in Fig. 7.6. The Kondo state has thus the same localization as the YSR state which is expected since they stem from the same phenomenon. Fig. 7.7c and d show the evolution of the amplitude and phase factor resulting from fitting the spectra of the grid by Frota-Fano functions. The amplitude reproduces the variation of the dI/dV signal at $V_{\text{bias}} = 0$ V which ensures a good quality of the fits. The phase factor shows a sign reversal above the Fe center that is interestingly in a one-to-one correspondence with the variations of the asymmetry of the YSR state in Fig. 7.5c.

Sign reversals of the interference factor have already reported in literature [146, 162]. Theory calculations have shown that a sign reversal can occur upon a lateral displacement of the tip with respect to the impurity due to Friedel-like oscillations of the scattering cloud [216]. However, it was estimated in [216] that no significant change in the lineshape of the Kondo resonance should happen on a lengthscales shorter than ~ 10 Å. Experimental observations of sign reversal on shorter lengthscales have thus been related either to the presence of several impurities each coupling individually to the electron bath and giving rise to a resonance with a specific asymmetry [162] or to possible interference effects of projected bulk states that thus affect the direct tunnel path to the substrate [146]. In the following we first discuss the possibility of several magnetic centers. We then investigate the relevance of the interference paths that are usually considered to explain the Fano lineshape of the Kondo resonance.

As mentioned earlier the spin of the molecule in gas phase is 1. Yet, usually the observation of a Kondo resonance is associated with the presence of a half-integer spin whose axial anisotropy is such that the ground state is $|ms_s = \pm 1/2\rangle$ to allow for a spin flip of the substrate electrons. For a spin 1, the Kondo effect can still take place between the $|+\rangle$ and $|-\rangle$ states if $D > 0$, $E \neq 0$ (see 3 Fig. 3.1f) [95]. In order to estimate the likeliness of this scenario we extract the intrinsic width of the resonance by accounting for the thermal ($T = 1.1$ K) and instrumental ($V_{\text{rms}} = 100\mu$V) broadening [1]:

[1] We do not include the Zeeman splitting in order to get an upper boundary for Γ_{intrisic}. Within our energy resolution, it is indeed not clear if one should include it or not: if the magnetic field B is below the critical magnetic field B_c of the Kondo state, the resonance should not split. But if $B > B_c$ we should observe a Zeeman splitting. Since we argue that the width of the resonance is small compared to the expected

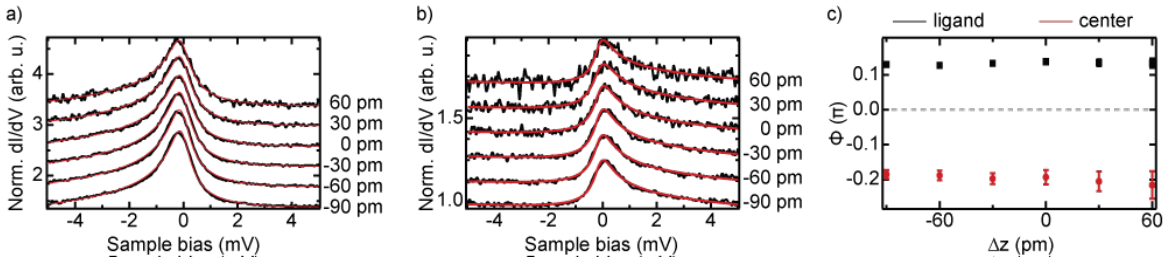

Figure 7.9.: Evolution of the Kondo resonance under tip approach above the ligand a) and center b) of the molecule (under an external magnetic field of 1.5 T). The $\mathrm{d}I/\mathrm{d}V$ spectra are normalized to their conductance at $V_{\mathrm{bias}} = 5$ mV and offset for clarity. They are recorded at different offset Δz as indicated in the Figure after opening the feedback at $V_{\mathrm{bias}} = 5$ mV, $I = 100$ pA (signal modulated with $V_{\mathrm{rms}} = 100$ μeV). Red curves are Frota-Fano fits to the $\mathrm{d}I/\mathrm{d}V$ spectra. c) Evolution with Δz of the phase of the interference factor obtained from the fits.

$$\Gamma_{\mathrm{intrisic}} = \Gamma_{\mathrm{measured}} - \sqrt{(2V_{\mathrm{rms}})^2 + (3.5k_BT)^2} \tag{7.2}$$

$$= \Gamma_{\mathrm{measured}} - 390\mu\mathrm{eV} \tag{7.3}$$

$$= 380\mu\mathrm{eV} \tag{7.4}$$

The obtained value is within our energy resolution. Due to the saddle shape conformation of the Fe-TPyP molecule, both axial and transversal anisotropy are expected to set in for spin large than 1/2. The value of the axial anisotropy is usually in the order of $\sim$ meV and one would therefore expect steps in $\mathrm{d}I/\mathrm{d}V$ outside the Kondo resonance corresponding to inelastic spin excitations [175]. Since it is not the case it seems unlikely that the Kondo resonance stems from a spin larger than 1/2. Nonetheless, we should mention that the behavior of the Kondo resonance in an external magnetic field is singular (see Fig. 7.8a): the splitting of the resonance under an external magnetic field is much stronger than expected. At 3 T we observe a splitting of $\sim 900\mu$eV which is three times the value expected for a free electron carrying a spin 1/2 ($2\mu_B B \sim 350\mu$eV). The nature of the spin state remains thus unclear.

If more the impurity spin is larger than 1/2, the impurity can show more than one YSR state on a superconducting substrate. The multiplicity of the YSR state is then either due to the independent coupling of the unpaired electrons to the substrate or to the magnetic anisotropy. In order to ensure that there is only one YSR state per FeP molecule we performed approach experiments similarly to what was presented in chapter 6. We show in Fig. 7.8b a set of spectra taken above the molecular ligand at different tip offset Δz after opening the feedback with $V_{\mathrm{bias}} = 5$ mV and $I = 100$ pA. A shift of the resonance toward the gap indicates a free-spin ground state (see chapter 6) which is consistent with the small width of the Kondo resonance. Importantly, no additionnal YSR state is observed, neither above the ligand nor above the center of the molecules (see [3] for more complete approach sets).

All in all, we do not have indication of a high spin state. In particular, we can conclude from the approach experiments that it is the same impurity in the entire molecule that induces the Kondo and YSR states. For simplicity, and despite the peculiar behavior of the Kondo resonance in a magnetic field, we therefore assume in the following that this impurity is a spin 1/2. Yet, we emphasize that this assumption is not at all restrictive for our model.

anisotropy values, we chose to take the largest possible intrinsic width.

The sign reversal of the Kondo resonance is thus not due to the presence of several unpaired electrons. As explained in chapter 3 section II, the lineshape of the Kondo resonance in STS is usually interpreted as resulting from interference between a tunneling path to the resonance and another one to the substrate. [131]. In our case the impurity is embedded in a molecular ligand and lies therefore a few Ångströms above the surface. Because of the exponential decay of the wavefunctions into the vacuum a change of the tip height should have a significant effect on the relative strength of those two paths. We present in Fig. 7.9a and b two sets of spectra taken at different tip offset Δz after opening the feedback with $V_{\text{bias}} = 5$ mV, $I = 100$ pA above the center and the ligand of the molecule, respectively. The width of the resonance does not vary within our energy resolution and, as one can see, the lineshape of the molecule is not affected by this approach experiment. In particular, Fig. 7.9c shows the evolution of the phase factor obtained by Frota-Fano fits and one does not observe a sign reversal upon tip approach. Therefore, we should consider other interference channels to explain the lineshape variations of the resonance.

III. Proposed model of orbital cotunneling

We have seen in the previous section that the localizations of the YSR state and Kondo resonance were closely related. This is expected as they stem from the same phenomenon: scattering of electron at a magnetic impurity. Interestingly, the localization of these many-body states bears resemblances with those of the HOMO and LUMO as shown in the first section. Moreover, we have noticed that the asymmetry of the YSR state and the interference factor of the Kondo resonance have the exact same pattern across the molecule with a sign reversal above the Fe center. This sign reversal cannot be explained by the common interference model for the Kondo resonance. In this section we propose a model in which the HOMO and LUMO serve as intermediate states in the scattering of electrons at the magnetic impurity. We first propose a modified version of the Anderson model and then discuss how the relative overlaps of the HOMO and LUMO with the tip can affect the $\mathrm{d}I/\mathrm{d}V$ signals.

We first motivate the key assumption behind our model: the involvement of the HOMO and LUMO into the scattering of electrons at the magnetic impurity. Two effects can support this claim. First of all, their wavefunctions can have a slower decay toward the surface and/or the vacuum than the one of the d level carrying the unpaired electron. Indeed, we have seen in the first section that these orbitals are detected in $\mathrm{d}I/\mathrm{d}V$ but that we could not identify one carrying an unpaired electron. Second of all, the HOMO and LUMO may lie closer to Fermi energy than the singly and doubly-occupied orbitals hosting a magnetic moment. As a result, a multi-scattering process via the HOMO or LUMO might be more likely than a direct one to the magnetic orbital.

We sketch in Fig. 7.10 a modified version of the Anderson model for the scattering of electrons at an impurity. We consider a single orbital carrying an unpaired electron at e_d with a Coulomb repulsion energy U that lifts the doubly occupied orbital above Fermi energy. Similarly to chapter 3 Fig. 3.4, the scattering of electrons at the impurity can happen via two virtual paths in which an electron is either added (upper path of Fig. 7.10) or substracted (lower path of Fig. 7.10) to the molecule. In the first case, an electron from the Fermi sea is first added to the LUMO before it occupies the impurity level. Then, one of the two electrons at $e_d + U$ relaxes to the Fermi sea via the LUMO. In the second case, an electron from the HOMO first scatters to the Fermi sea and is then replaced by the one at e_d. One of the two electrons of the HOMO then occupies back the impurity level and is replaced by one of the electron at the Fermi sea. In both cases, this can effectively lead to a spin-flip of the impurity as in Fig. 3.4. However, we note that when only the impurity level is considered,

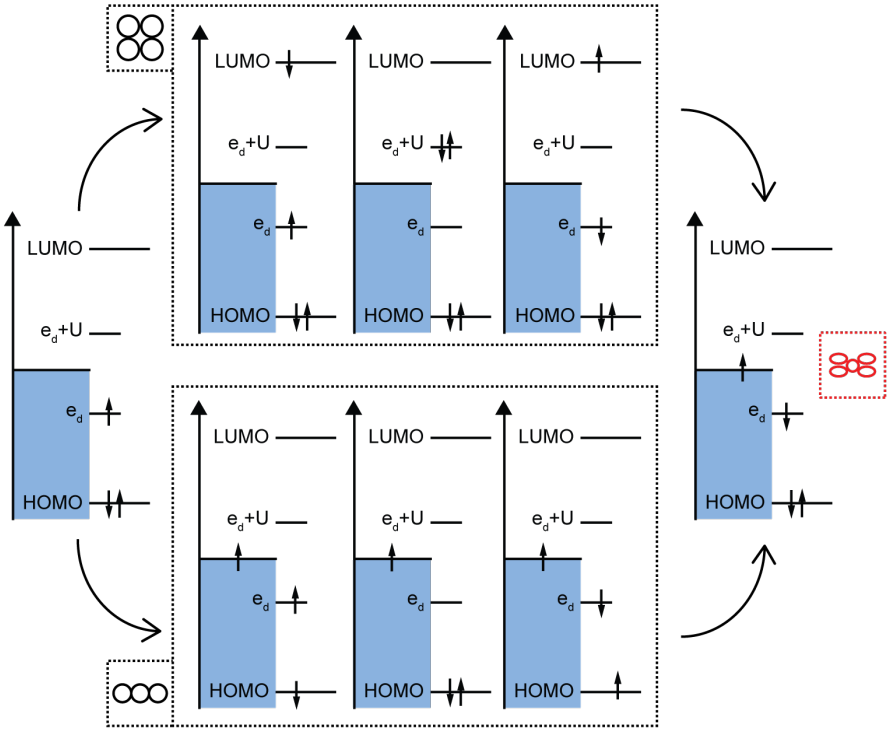

Figure 7.10.: Modified Anderson model for the scattering of electrons at the impurity. Two virtual paths are considered in which one electron is added (upper path) or subtracted (lower path) from the impurity. In both cases the scattering at the impurity level happens via the LUMO (upper path) or the HOMO. The intensity of the scattering events are thus modulated by the wavefunctions of these two orbitals (sketches next to the two paths). As a result, the resulting many-body states have a spatial distribution that result from a convolution of both wavefunctions.

the probabilities for an electron (Fig. 3.4b) or hole (Fig. 3.4c) to be scattered at the impurity have the same spatial distributions, namely the one of the magnetic orbital. Here, these probabilities are modulated by the wavefunction of the LUMO for an electron and of the HOMO for a hole, as sketched in black next to the two paths. The many-body states arise from a multitude of such scattering events and should thus adopt a pattern that corresponds to a convolution of both shapes (see red sketch).

In more detail, we have seen in 3 that the potential scattering K depends on the electron-hole asymmetry of the scattering problem. Here we argue that the HOMO and LUMO effectively modify this asymmetry and thereby modulate the lineshapes of the Kondo and YSR states.

More precisely, the LUMO has a double nodal plane above the Fe center of the molecule. As a result, at this position, the weight of hole excitation (corresponding to the tunneling path going through the HOMO) is expected to be higher than the one of electron excitation (corresponding to the tunneling path going through the LUMO). We know from the approach experiment of Fig. 7.8b that the YSR state is in a free-spin ground state. The excitation probed in STS corresponds thus to $\gamma^\dagger = uc_\alpha^\dagger - vc_\beta$. The hole component is thus detected at negative bias (see chapter 3 section III.2 or chapter 6). We observe indeed that the asymmetry of the YSR state is negative above the Fe center (see Fig. 7.5). Above the ligand the reversed asymmetry indicates a stronger weight of the electron component of the YSR state and would

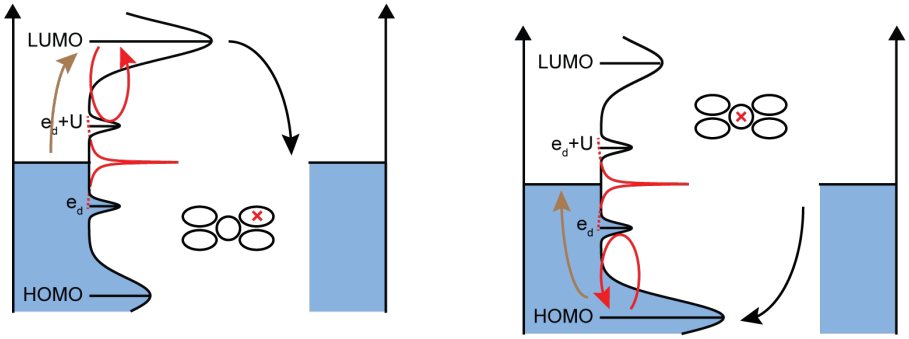

Figure 7.11.: Cotunneling via the HOMO and LUMO into the Kondo resonance. Paths to the impurity (brown-red-black) and to the substrate (brown-black) interfere with one another given rise to a Fano lineshape of the resonance. When the tip is placed above the ligand (left sketch), cotunneling events through the LUMO dominate the transport properties. Above the center, the overlap with the HOMO is stronger and cotunneling events through this resonance prevail. As result, the electron-hole asymmetry of the excitation spectrum is reversed from one position to another.

thus relate to a stronger hybridization of the LUMO than the HOMO with the substrate.

As for the Kondo resonance, it has been shown in [55] that a reversal of the sign of interference factor corresponds effectively to a reversal of the electron-hole asymmetry of the scattering problem. Here, we argue that the variations of relative weights of the wavefunctions of the HOMO and LUMO may be at the origin of this local inversion of the electron-hole asymmetry. A more rigorous derivation of the proposed scattering model would be necessary to confirm this proposal.

We now consider the spatial variations of the relative overlaps of the HOMO and LUMO with the tip and discuss these as a possible alternative explanation for the observed localization and asymmetry of the YSR and Kondo states. We illustrate in Fig. 7.11 two situations in which the tip is placed above the ligand (left) or center (right) of the molecule. Here again, we assume that the interaction with the magnetic impurity takes place after tunneling first via the HOMO or the LUMO. Usually, tunneling to the Kondo resonance is sketched as a direct path to the resonance. Here we chose to present this tunneling path by a scattering of electrons at the singly and doubly occupied levels, similarly to the Anderson model. In each case we have therefore two interfering paths: one that interacts with the impurity (brown-red-black arrows) and one that does not (brown-black) arrows. When the tip is placed above the ligand of the molecule (left), it overlaps more strongly with the LUMO than the HOMO, the many-body states are thus probed dominantly by electron excitation. Above the Fe center (right), the situation is reversed with a stronger overlap with the HOMO resonance leading to a prevalence of hole-excitation.

In analogy with the previous discussion, these different paths effectively modify the electron-hole asymmetry of the tunneling electrons. This effective reversal would therefore lead to a reversal of the YSR asymmetry and interference factor of the Kondo resonance.

IV. Conclusion

In this chapter we have established a clear correlation between the lineshapes of the Kondo resonance and the YSR state induced by a magnetic impurity on a metallic and superconduct-

ing substrate, respectively. In particular, we have observed a reversal of the YSR asymmetry and of the sign of the interference factor of the Kondo resonance above the Fe center of the molecule. Both reversals relate to a local inversion of the electron-hole asymmetry. Usually, the lineshape of the Kondo resonance is interpreted as resulting from interference between two tunneling paths: one to the impurity and the other one to the substrate. However, in our case, this model fails to explain the variation of the lineshape of the resonance, both laterally and vertically (for the tip position with respect to the molecule). The localization of the YSR state and Kondo resonance seem indeed to indicate that the HOMO and LUMO are involved in the scattering of electrons onto the impurity. We have therefore proposed in the last section two models in which the frontier orbitals intervene as intermediate states in these scattering events. For both scenarios, the change of the Kondo and YSR state lineshapes are explained by an effective reversal of the electron-hole asymmetry of the scattering problem.

Chapter 8

Magnetic coupling in a molecular lattice

Coupling of magnetic impurities is often studied as a platform to create new entangled states, especially within the framework of strongly correlated electrons such as Yu-Shiba-Rusinov (YSR) states and Kondo lattices. For instance, lately, the hybridization of YSR states has been investigated enthusiastically as it can, under certain conditions, lead to the formation of Majorana fermions [154, 153, 167, 143, 108, 105]. Most experimental works rely either on growth of chains or islands that lack an atomic control of the structures, or on atomic or molecular manipulation to engineer a well-defined structural geometry of the investigated system. These manipulations are often time-demanding which thus limits the size of the systems to around a hundred impurity sites. Here, we show that molecular self-assembly is a valid alternative as it allows for a long-range molecular arrangement while keeping a molecular/atomic precision. Beyond a simple proof of principle, the lattice that we study, the Kagome lattice, is long-searched for in experiments, both for its magnetic (high frustration of antiferromagnets) and electronic structure (presence of a flat-band) [98, 80, 90, 77, 196, 207, 204, 157]. In this chapter, we prove the experimental implementation of such a lattice with exactly one fermion per site and coupling between nearest neighbors, reproducing exactly its elementary theoretical description.

In order to do so, we characterize in the first section the properties of FeP molecules in various environments before any coupling, both in the superconducting and in the normal state of the Pb substrate. The second section is dedicated to the investigation of the YSR coupling within the Kagome lattice. We demonstrate that the YSR states indeed hybridize under certain conditions and discuss a theoretical description of the coupling mechanism. In the third section, we try to determine if this YSR coupling translates to the formation of a Kondo lattice when Pb is in its normal state.

I. Influence of the different molecular environments

The FeP molecules in the Kagome lattice are surrounded by molecules and Cl adatoms (see chapter 4, section II.3). Here, we investigate the influence of these two types of adsorbates on the fingerprints of the FeP molecules, both in the superconducting and the normal state

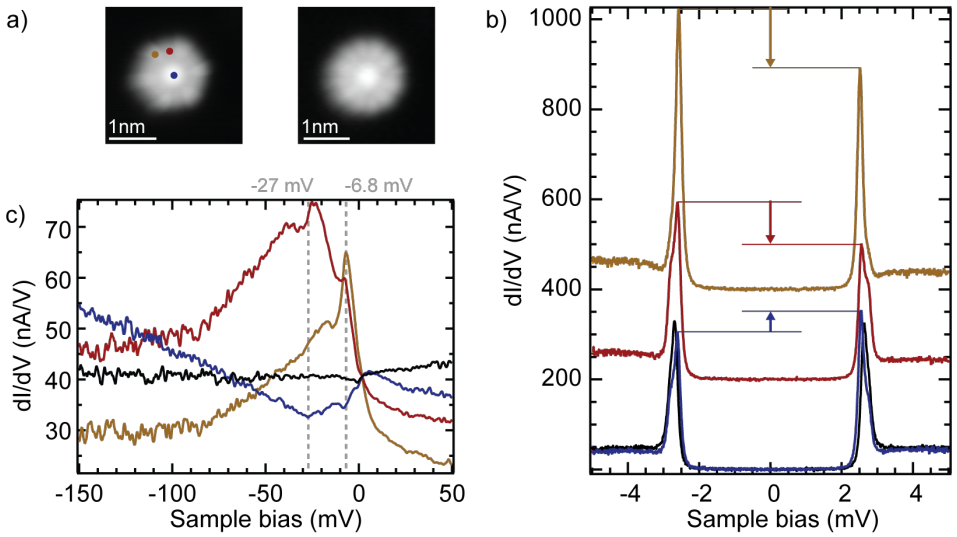

Figure 8.1.: a) Topography images of a molecule dragged out of an island (left: $V_{\text{bias}} = 5$ mV, $I = 200$ pA right: $V_{\text{bias}} = -45$ mV, $I = 100$ pA). b) $\mathrm{d}I/\mathrm{d}V$ spectra recorded with a superconducting tip above the positions shown in a and above the bare Pb surface (black) (feedback opened at $V_{\text{bias}} = 5$ mV, $I = 200$ pA and signal modulated with $V_{\text{rms}} = 15$ μeV, spectra are offset for clarity). c) $\mathrm{d}I/\mathrm{d}V$ spectra recorded above the same positions as in b but in the normal state of Pb with an external magnetic field $B = 800$ mT (feedback opened with $V_{\text{bias}} = 5$ mV, $I = 200$ pA and signal modulated with $V_{\text{rms}} = 500$ μeV, spectra offset for clarity).

of the substrate. In order to do so, we study the properties of the FeP molecules in the phase where chlorine adatoms are present but with a FeP-Cl ratio lower than 1/2, giving us access to the Kagome building blocks, as explained in chapter 4

1. Influence of neighboring molecules

We first characterize in Fig. 8.1 the fingerprints of a molecule that has been dragged out of an island. The topography images of Fig. 8.1a, recorded with different set points (left: $V_{\text{bias}} = 5$ mV, $I = 200$ pA and right: $V_{\text{bias}} = -45$ mV, $I = 100$ pA) show a six-fold symmetry of the molecule. This can be attributed to the fast rotation of the FeP molecule between three different adsorption configurations that are equivalent due to the symmetry of the surface (same adsorption site but different orientations of the molecule) [91, 186, 199]. This rotation was observed irrespective of the feedback parameters that were used. The energy of this rotation is thus very low, as it is either activated by temperature of by the tunneling electrons. Fig. 8.1b shows the properties of the molecule in the superconducting state of Pb at positions shown on the left topography image in Fig. 8.1a. Comparing these spectra to the reference spectrum recorded above the bare Pb surface (black curve), we do not see the appearance of additional peaks within the superconducting gap. Rather, an asymmetry of the intensity of the coherence peaks is observed. This could correspond to the presence of a YSR state very close to the gap edge that can not be resolved or due to the background. Approach experiments shown in the appendix (Fig. 1 page 148) show that there is indeed a YSR state very close to the gap edge.

The spectroscopic properties on a broader energy range are shown in Fig. 8.1c. The spectra are recorded under an external magnetic field of 800 mT to suppress superconductivity in the

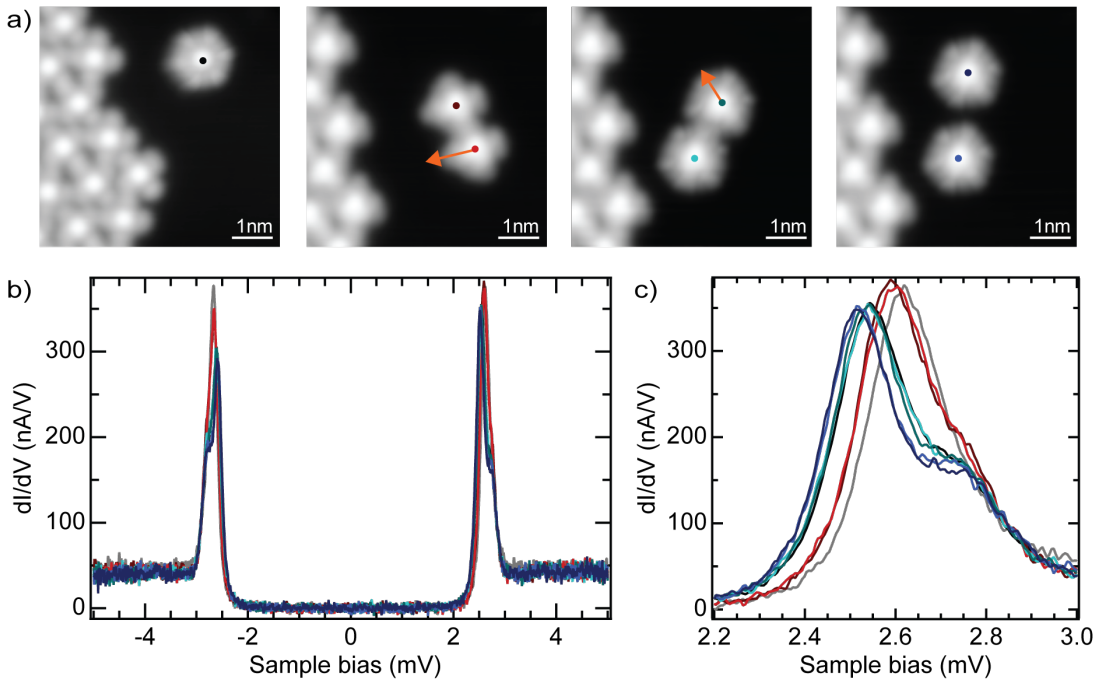

Figure 8.2.: a) Topography images of one (left) and two (three right panels) molecules dragged out of an island ($V_{\text{bias}} = 5$ mV, $I = 200$ pA). The position of the molecules relative to each other is modified by moving them as indicated by the orange arrows. b) $\mathrm{d}I/\mathrm{d}V$ spectra (feedback opened with $V_{\text{bias}} = 5$ mV, $I = 200$ pA and signal modulated with $V_{\text{rms}} = 15$ μeV) taken above the centers of the molecules as shown in a as well as above the bare Pb substrate (gray). c) Enhanced view of the spectra shown in b.

sample and the tip. This could only be partially achieved for the tip as one can see a shallow dip around the Fermi energy in the reference spectrum taken above the bare Pb surface (black curve). Above the ligand (red and orange curves), a broad resonance in the negative bias range is observed. Above the center, a shallow resonance is seen around $V_{\text{bias}} = 0$ V and a steady increase in $\mathrm{d}I/\mathrm{d}V$ in the negative bias range indicates the onset of an orbital at higher energies. Additionally, a peak (dip) is seen above the ligand (Fe center) at $V_{\text{bias}} = -6.8$ mV and another feature can be perceived at $V_{\text{bias}} = -27$ mV (dashed grey lines). The relative intensity of these two features is different at the two positions probed above the ligand of the molecule (compare red and orange curves). We assign the feature at -6.8 mV to a Kondo resonance; its lineshape variations are caused by changes in the interfering paths as discussed in chapter 7. It is possible that the feature at -27 mV is a vibration-mediated excitation of the Kondo resonance [51]. Its broader lineshape could be explained by the higher current flowing through the junction at $V_{\text{bias}} = -27$mV. The variations in its intensity relative to the Kondo resonance would then relate to local variations in the efficiency of the excitation. Normally, one would then also expect a vibrational Kondo resonance at $V_{\text{bias}} = 27$ mV (see chapter 2 section II.3). The absence of such a resonance in our case could be due to the fact that there is no orbital in the positive bias regime that could mediate the excitation of the vibrational mode [165].

We then investigate the influence of the presence a neighboring molecule. We display in Fig. 8.2a topography images ($V_{\text{bias}} = 5$ mV, $I = 200$ pA) of the different molecular configurations that are to be compared. The left topography image shows the molecule of Fig. 8.1 without neighbor. In the three other cases a second molecule has been pulled out

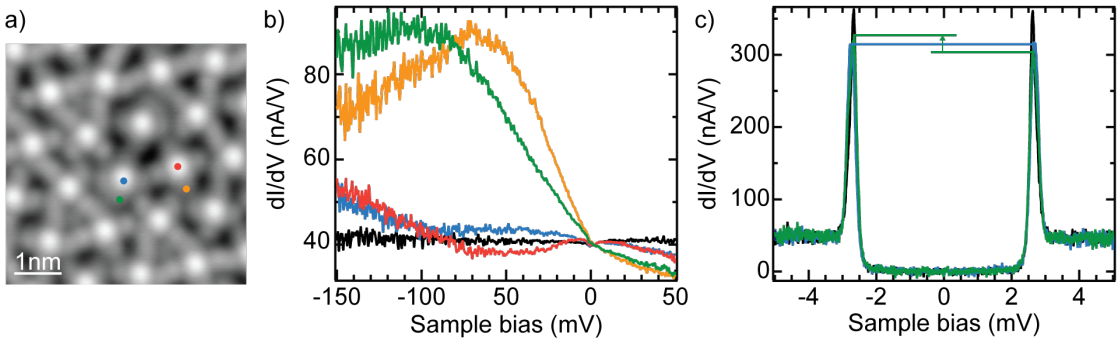

Figure 8.3.: a) Topography image ($V_{\text{bias}} = 5$ mV, $I = 200$ pA) of a preparation where less than two chlorine per three FeP molecule is present. Some molecules have thus no chlorine in their vicinity (see chapter 4). b) dI/dV spectra recorded above such molecules (see positions in a) with an external magnetic field of 800 mT (feedback opened at $V_{\text{bias}} = 5$ mV, $I = 200$ pA and signal modulated with $V_{\text{rms}} = 500$ μeV). A reference spectrum taken above the bare Pb substrate is shown in black. c) dI/dV spectra recorded with a superconducting tip above the center (blue) and ligand (green) of a molecule without neighboring Cl (see a) as well as above the bare Pb substrate (feedback opened at $V_{\text{bias}} = 5$ mV, $I = 200$ pA and signal modulated wirh $V_{\text{rms}} = 15$ μeV). The green spectra shows an asymmetry of the coherence peaks but the blue one does not.

of the island and placed in the vicinity of the first one, the relative positions of these two molecules are changed by manipulating them along the paths indicated by the orange arrows in Fig. 8.2a. As one can see in Fig. 8.2b, the dI/dV spectra recorded above the centers of the molecules in these different configurations are very similar (a reference spectrum is also shown in gray). Fig. 8.2c shows an enhanced view of the coherence peaks in the positive bias. Small variations are detected between the different configurations. Yet, the energy shift is not particularly strong and we note that the spectrum taken above the molecule without neighbor (black spectrum) is in between the red and blue spectra (identical to the green ones) so that the trend is not clear.

Interestingly, the situation is quite different when the molecules are within a molecular island, as shown in Fig. 8.3. There, we investigate the spectroscopic properties of molecules that are not surrounded by Cl adatoms (see topography image in Fig. 8.3a). In the normal state of Pb, these molecules do not show any resonance near the Fermi level (see Fig. 8.3b, a reference spectrum above the bare Pb substrate is shown in black) indicating the absence of the Kondo effect. A broad resonance is still detected in the negative bias regime above the ligand of the molecules but at higher (absolute) energies than in Fig. 8.1c. The position of this orbital appears moreover to vary from one molecule to another (compare green and orange spectra in Fig. 8.3b). In the superconducting state of Pb, the spectra taken above the Fe center of the molecule is symmetric (blue) and the one taken above the ligand (green) is slightly asymmetric with a more intense coherence peak in the negative bias regime (a reference spectrum is shown in black). These fingerprints are very similar to the one displayed by the FeP molecules in Fig. 4.9 where no Cl adatoms are present within the molecular islands. In this case, contrary to what is observed for the molecule dragged out of an island an approach of the tip does not reveal the presence of a YSR state near the gap edge (see appendix Fig. 1). The asymmetry of the coherence peaks above the ligand is thus presumably due to the broad orbital in the negative bias regime and there is no evidence of a magnetic

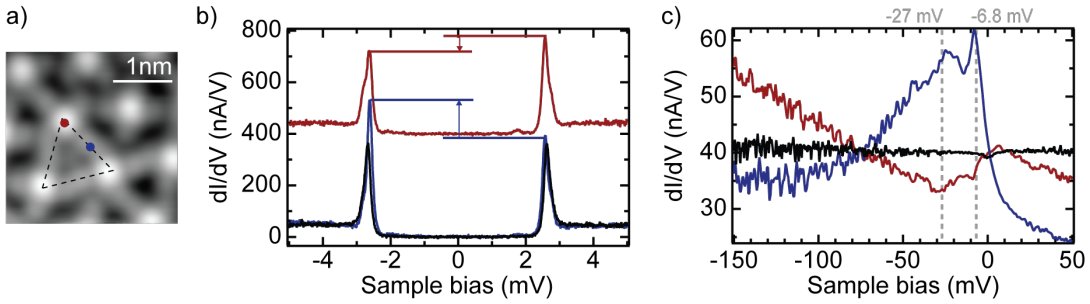

Figure 8.4.: a) Topography image with a triangular unit made of three FeP molecule and one chlorine adatom as indicated by black dashed lines ($V_{\text{bias}} = 5$ mV, $I = 200$ pA). b) dI/dV spectra above the center (red, offset for clarity) and ligand (blue) of a molecule in the triangle (see a) as well as a reference spectrum (black) taken on Pb (feedback opened at $V_{\text{bias}} = 5$ mV, $I = 200$ pA and signal modulated with $V_{\text{rms}} = 15$ μeV). c) dI/dV spectra taken above the same locations as in b but under an external magnetic field of 800 mT (feedback opened at $V_{\text{bias}} = 5$ mV, $I = 200$ pA and signal modulated with $V_{\text{rms}} = 500$ μeV).

fingerprint for these molecules.

All in all, the molecular assembly affects the coupling of the molecules to the substrate and this effect is particularly important when the molecules are embedded in a molecular island (without neighboring Cl adatoms). A possible explanation may be that, as the molecules adsorb on the substrate, a charge redistribution occurs at the interface. This could affect the hybridization strength between the impurity and the substrate electrons as well as the position of the FeP levels with respect to the Fermi level (we indeed see a shift of the HOMO in Fig. 8.3c and Fig. 8.1c). This could change the charge and spin state of the molecules or affect the coupling strength of the impurities to the substrate (see chapter 3 section II).

2. Influence of chlorine

We now characterize the effect of chlorine on the properties of the molecules. As we have seen in chapter 4 in Fig. 4.6, the unit cell of the Kagome lattice is made of two adjacent triangles where one triangle is composed of three FeP molecules at its vertexes and a Cl adatom in its center. Here, we characterize the properties of molecules in small structures made out of one and two such triangles both in the superconducting and the normal state of the Pb substrate.

One triangular unit

In the topography image of Fig. 8.4a one can recognize three molecules rotated by 30° with respect to each other with a chlorine adatom in-between them (see triangle black dashed lines and chapter 4 for identification of chlorine). No other chlorine adatom is present in their direct surroundings. dI/dV spectra recorded above the center (red) and ligand (blue) of these molecules in the superconducting state of Pb (Fig. 8.4b) show no resonances within the superconducting gap (a reference spectrum taken on Pb is shown in black) but an asymmetry of the coherence peaks, similar to the molecule dragged out of an island (see Fig. 8.1b). Approach experiments recorded above the center of the molecule (see appendix II Fig. 2) reveal here again the presence of a YSR state near the gap edge. In the normal state of Pb (Fig. 8.4c, the spectra are recorded under an external magnetic field of 800 mT), the spectra have also the same characteristics as those observed for a molecule dragged out of an island in Fig. 8.1c. In particular we observe a Kondo resonance at $V_{\text{bias}} = -6.8$ mV. This indicates that

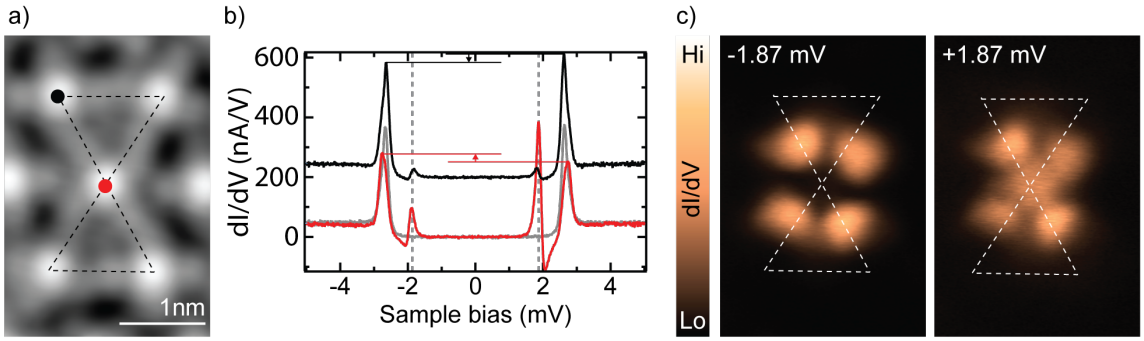

Figure 8.5.: a) Topography image of a structure that corresponds to the Kagome unit cell (see black dashed lines, set point: $V_{\text{bias}} = 5$ mV, $I = 200$ pA). b) $\mathrm{d}I/\mathrm{d}V$ spectra recorded above the centers of a molecule at the edge of the structure (black, offset for clarity) and of the central molecule (red) along with a reference spectrum taken above the bare Pb surface (grey) (feedback opened at $V_{\text{bias}} = 5$ mV, $I = 200$ pA and signal modulated with $V_{\text{rms}} = 15$ μeV). c) $\mathrm{d}I/\mathrm{d}V$ maps recorded at $V_{\text{bias}} = \pm 1.87$ mV with the tip following the height profile of the topography image in a (signal modulated with $V_{\text{rms}} = 25$ μeV). The dashed lines are the replica of those in a and help identify the molecules' positions. The $\mathrm{d}I/\mathrm{d}V$ signal is present only above the central molecule of the structure.

the coupling between the substrate electrons and impurity spin of the molecules is similar for molecules adsorbed alone on the substrate and those in islands but with one chlorine adatom in their direct vicinity. The presence of chlorine near the molecule compensate thus the effect caused by the molecular assembly. We speculate that a charge redistribution occurs at the interface between the molecular island and the surface. Here, it seems reasonable that the presence of chlorine modifies this charge redistribution since it tends to attract electrons [23].

The Kagome unit cell

Fig. 8.5a shows a topography image of a structure that corresponds to the Kagome unit cell (see black dashed-lines): five FeP molecules and two chlorine adatoms. We first characterize the properties of the molecules in the superconducting state of Pb. As one can see in Fig. 8.5b, the molecules at the edge of the structure (black spectrum) show the same asymmetry of the coherence peaks as in the previous structure (see Fig. 8.4) (a reference spectrum taken above Pb is shown in grey). Additionally, a shallow pair of resonances is seen at $V_{\text{bias}} = \pm 1.87$ mV. This pair of resonances originates from the molecule at the center of the structure (red spectrum in Fig. 8.5b) and marks the presence of a YSR state well inside the superconducting gap. In Fig. 8.5c we show the corresponding $\mathrm{d}I/\mathrm{d}V$ maps recorded while following the height profile of the topography image shown in Fig. 8.5a. The YSR state is only localized above the molecule at the center of the structure (the white dashed lines help to identify the molecules' positions). At positive bias four protrusions are seen above the molecular ligand and one above the Fe center. At negative bias, the same protrusions are seen above the ligand but the intensity above the Fe center is, by contrast, much reduced. Yet, the $\mathrm{d}I/\mathrm{d}V$ spectrum shown in Fig. 8.5 indicates that the YSR resonance at negative bias is still detected there. Approach experiments performed above the center of the molecule (see appendix II Fig. 3) show that the YSR state is in a screened ground state (see chapter 6). The coherence peaks over the Fe center are asymmetric, with an asymmetry reversed when compared to the one observed above the centers of the molecules at the edge of the structure. As we see show next, this asymmetry can be explained by the background conductance. For the molecules at

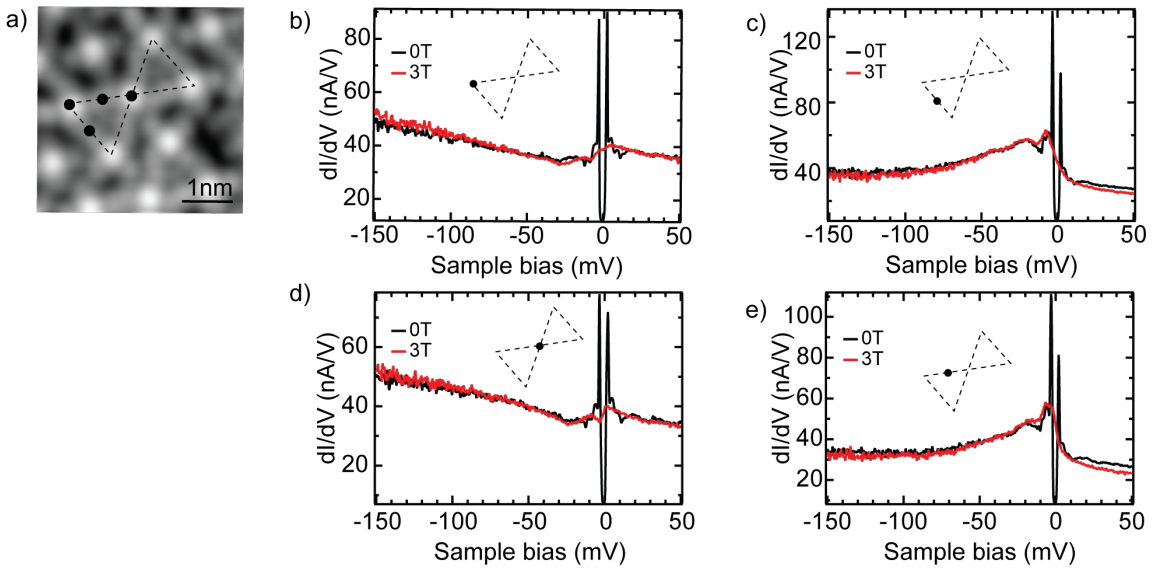

Figure 8.6.: a) Topography image of a structure consisting of the Kagome unit cell (see black dashed line, set poin: $V_{\text{bias}} = 5$ mV, $I = 200$ pA). b-e) $\mathrm{d}I/\mathrm{d}V$ spectra taken above the center and ligand of the molecules in the structure as indicated by the sketches that reproduces the one drawn in a with the various positions investigated. The spectra are recorded in the superconducting (black) and normal (red, external magnetic field $B = 3$ T) states (feedback opened at $V_{\text{bias}} = 5$ mV, $I = 200$ pA and signal modulated by $V_{\text{rms}} = 500$ μeV).

the edges, approach experiments reveal the presence of a YSR state near the gap while this is not the case for the central molecule (see appendix Fig. 4 page 150). Therefore, it appears that each molecule displays only one YSR state, but that lies at different energies depending on the number of Cl adatoms surrounding the molecule (one for the four molecules at the edge of the structure with a YSR at the gap edge and two for the central molecule with a YSR state well inside the gap).

The spectroscopic signatures of the molecules on a larger energy range are shown in Fig. 8.6 both in the superconducting state (black spectra) and in the normal state (red spectra) of the substrate under an external magnetic field of 3 T. In the normal state of Pb, the spectra are very similar to the triangular unit (see Fig. 8.4c). A broad resonance is seen above the ligand in the negative bias, a more shallow one is detected above the Fe centers around the Fermi energy and a Kondo resonance with its replica is also discernible (this is more clearly seen next in Fig. 8.7). We see that the spectra recorded in the superconducting state of Pb follow exactly the same variations with the exception of the presence of the superconducting gap around the Fermi level. In particular, the intensity of the coherence peaks is modulated by the variations of the differential conductance in the background (the higher modulation of the $\mathrm{d}I/\mathrm{d}V$ signal enhances here this effect when compared to Fig. 8.5).

We investigate in Fig. 8.7 in further detail how the spectroscopic fingerprints in the normal state of Pb evolve from the central molecule to one at the border of the structure. Fig. 8.7 shows as a 2D color plot a set of spectra recorded along the line shown in the topography image of Fig. 8.7a. The signal is most intense above the molecular ligand where the resonance in the negative bias is localized and where the Kondo resonance is detected as a peak. However, the position of the resonance is shifted from $V_{\text{bias}} = -6.8$ mV for the molecule at the border of the structure to $V_{\text{bias}} = -1.8$ mV above the molecule at the center of the structure (see grey dashed lines). This is more clearly seen when comparing the spectra above the centers

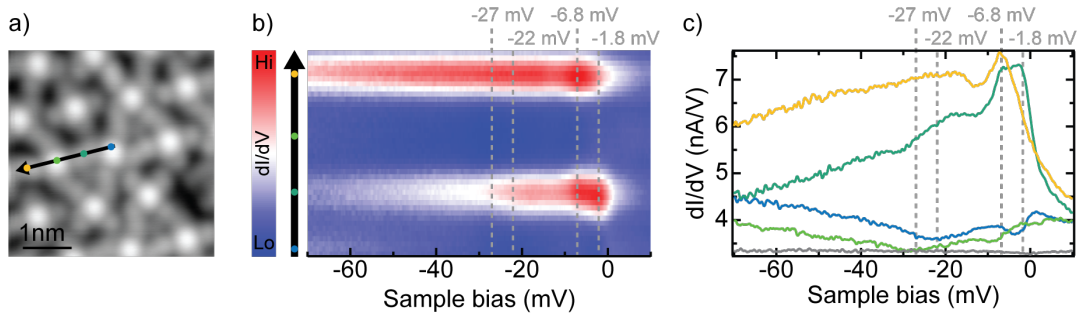

Figure 8.7.: a) Topography image of the same structure as in Fig. 8.6a (set point: $V_{\text{bias}} = 5$ mV, $I = 200$ pA b) Set of dI/dV spectra recorded along the line shown in a (feedback opened at $V_{\text{bias}} = 150$ mV, $I = 500$ pA and signal modulated with $V_{\text{rms}} = 700$ μeV) and under an external magnetic field $B = 600$ mT. c) The spectra recorded above the centers (blue and light green) and ligands (dark green and yellow) of the molecules show a shift by 5 mV of the Kondo resonance and its replica (see grey dashed lines). A reference spectrum recorded above Pb is shown in grey.

and ligands of the two molecules shown in Fig. 8.7c (a reference spectrum taken above Pb is shown in grey). The replica of the Kondo resonance is also shifted to lower bias by 5 mV (see grey dashed lines and compare the blue and light green spectra). This is in accordance with the assignment of this feature to a vibrational-assisted excitation of the Kondo resonance. In between the molecules, the two resonances are detected simultaneously (dark green spectrum) and do not show any sign of interference by a modification of their lineshape.

All in all, inside the unit cell of the Kagome lattice, the molecules exhibit one YSR state and one Kondo resonance. However, for the central molecule (two neighboring Cl adatoms), the energy of the YSR state and the position of the Kondo resonance is shifted compared to the molecules at the border of the structure (one neighboring Cl). More precisely, these show the same features as in the triangular unit (see Fig. 8.4). This is logical since they have the same environment with only one Cl adatom in their direct vicinity. The central molecule on the contrary is surrounded by two Cl adatoms. As discussed previously, these adatoms most likely modify the charge distribution at the interface. The shift in position of the Kondo resonance corroborates this claim as it indicates a change in the local electron-hole asymmetry [216, 209] (see chapter 3 section II). We show in the next section that in the Kagome lattice the YSR state induced by these molecules with two neighboring Cl adatoms hybridize with one another and form a YSR band. In order to set the framework for the discussion of a magnetic coupling in the normal state of Pb in the third section we characterize in more detail the Kondo resonance seen above the central molecule.

In Fig. 8.8b we show in black a dI/dV spectrum recorded above the Fe center of the central molecule of the Kagome unit cell (see topography image in Fig. 8.8a) in the normal state of Pb (external magnetic field $B = 600$ mT). A fit of the resonance with a Frota-Fano function [61] is shown in red and yields a full width at half maximum (FWHM) $\Gamma = 2.2 \pm 0.09$ meV. The intrinsic width of the resonance is then (see chapter 7) $\Gamma_{\text{intrinsic}} = 1.86$ meV which corresponds to a Fano width of $\Gamma^{\text{Fano}} = 4.72$ meV ($\Gamma^{\text{Fano}} \sim 2.54\Gamma_{\text{intrinsic}}$ [61]) and a Kondo temperature $T_K = 54.8$ K ($k_B T_K = \Gamma^{\text{Fano}}$ [231]) and a critical magnetic field of $B_c = 20$ T ($g\mu_B B_c = 0.5 k_B T_K$ [35]). This Kondo resonance is thus the counterpart of the YSR state observed at $V_{\text{bias}} = \pm 1.87$ mV in the superconducting state of Pb.

Finally, we note that the FeP molecules have a spin 1 in gas phase (see chapter 4) and that bright molecules can exhibit more than one YSR state after deposition on a sample held at

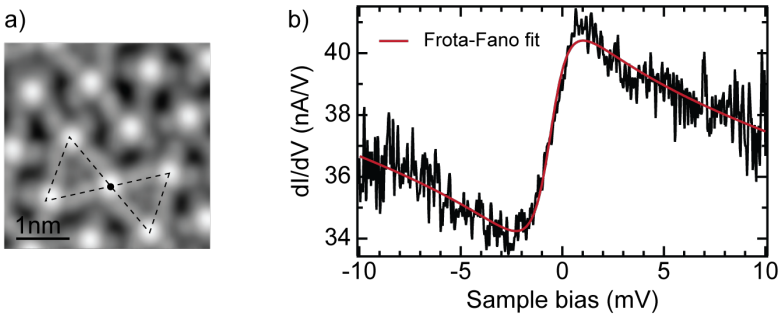

Figure 8.8.: a) Topography image with a structure corresponding to the unit cell of the Kagome lattice ($V_{\text{bias}} = 5$ mV, $I = 200$ pA) b) dI/dV spectrum (black) recorded above the Fe center of the central molecule of this structure (feedback opened at $V_{\text{bias}} = 5$ mV, $I = 200$ pA and signal modulated with $V_{\text{rms}} = 50$ μeV) along with a Frota-Fano fit (red).

cold temperatures (see appendix page 139). It is thus most likely that the bright molecules have here also a spin 1. However, the origin of the multiple YSR states is most likely the independent coupling of unpaired electrons to the substrate, each giving rise to one YSR state (see appendix page 139). Here, we observe only one YSR state and a Kondo resonance and do not have indication for a high spin state. It thus seems that even if more than one electron is unpaired, only one of them gives rise to the observed YSR state at $V_{\text{bias}} = \pm 1.87$ mV and its corresponding Kondo resonance in the normal state of the Pb substrate. We therefore for simplicity treat each FeP molecule as a spin 1/2 impurity.

II. Coupling of Yu-Shiba-Rusinov states

In this section we show that the YSR states induced by FeP molecules with two surrounding Cl adatoms hybridize with one another giving rise to a YSR band in the Kagome lattice. In order to do so, we first focus on small structures in which only a few impurities couple to each other and investigate a theoretical description of the YSR hybridization mechanism in the spirit of what has been so far reported in literature [182, 57]. We show that this model describes correctly the small structures but that the different symmetries of the substrate and molecules set the limits of our analytical description. Finally, we characterize the properties of the YSR band observed in the Kagome lattice and discuss the origin of the coupling between the molecules.

1. Coupling of two and three Yu-Shiba-Rusinov states

We first investigate a structure (see dashed black lines in the topography image of Fig. 8.9a) in which two molecules are surrounded by two Cl adatoms (their centers are marked with a blue and a black dot). The molecules at the edges of the structure, with only one surrounding Cl adatom, exhibit the same spectroscopic fingerprints (brown spectrum in the top panel of Fig. 8.9b) as the triangular unit (see Fig. 8.4b) and edge molecules of the Kagome unit cell (black spectrum of Fig. 8.5b) with an asymmetry of the coherence peaks (the dI/dV spectra are recorded with the same tip). This is in accordance with the fact that these molecules have the same surroundings (one neighboring Cl adatom). We do not observe any evolution of the spectra of such molecules (with one neighboring Cl adatom) when increasing the size of the investigated structures and therefore do not focus on these molecules in the following. The

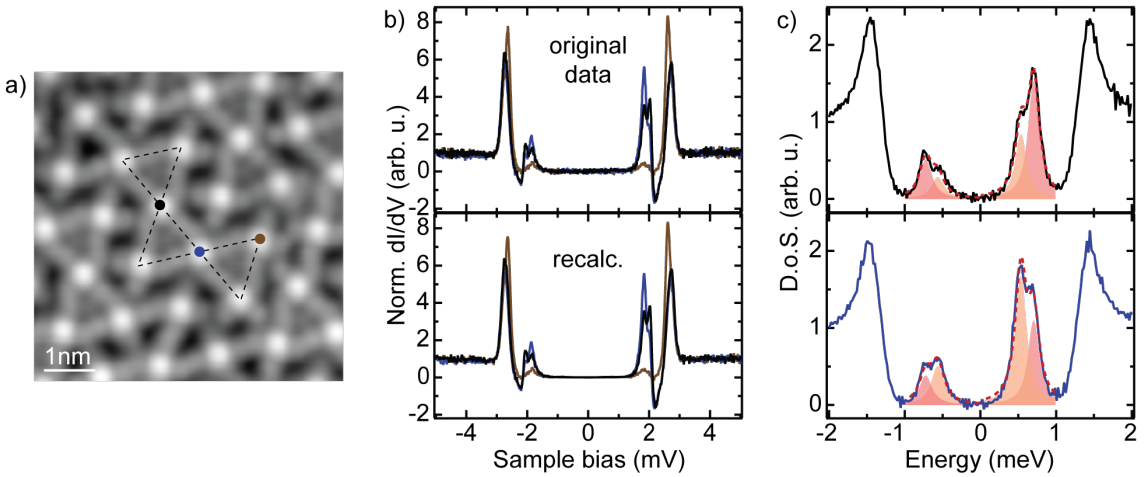

Figure 8.9.: a) Topography image ($V_{\text{bias}} = 5$ mV, $I = 200$ pA) of a structure with two moleculesn that have two neighboring Cl adatoms (see black dashed lines). b) Upper panel: $\mathrm{d}I/\mathrm{d}V$ spectra obtained with a superconducting tip above the centers of the molecules as shown in a (feedback opened at $V_{\text{bias}} = 5$ mV, $I = 200$ pA and signal modulated with $V_{\text{rms}} = 15$ μeV). Lower panel: reconvolved $\mathrm{d}I/\mathrm{d}V$ spectra that ensure the consistency of the deconvolution procedure used to obtained the sample density of states (DOS) shown in c (see appendix page 145). c) The presence of two YSR states are seen in the sample DOS as two peaks inside the superconducting gaps that can be fitted by two Lorentzians both at positive and negative energies (see red dashed curves). The contribution of each Lorentzian peak is shown by the filled curves.

$\mathrm{d}I/\mathrm{d}V$ spectra recorded above the central molecules (black and blue in Fig. 8.9b, upper panel) are, on the contrary, different than the red spectrum of Fig. 8.5b. We now observe two pairs of resonances within the superconducting gap at $V_{\text{bias}} = \pm 2$ mV and $V_{\text{bias}} = 1.9$ mV. Only one pair is observed for the central molecule of the Kagome unit cell in Fig. 8.5. Because the molecules have the same surroundings (two neighboring Cl adatoms) we attribute this to a hybridization of the YSR states induced by each molecule, similarly to [107, 182, 31]. In order to support this claim we investigate the localization of the YSR states over the structure. However, as explained in chapter 3 (Fig. 3.13), the $\mathrm{d}I/\mathrm{d}V$ spectra are a convolution of the tip and sample DOS. Because the YSR state at $V_{\text{bias}} = \pm 2$ mV lies in the negative differential resistance (NDR) of the YSR state at $V_{\text{bias}} = \pm 1.9$ mV the intensity of the $\mathrm{d}I/\mathrm{d}V$ signal at $V_{\text{bias}} = \pm 2$ mV does not only reflect the weights of the electron and hole parts of this YSR state. In order to circumvent this problem we obtain the sample local DOS by deconvolving the $\mathrm{d}I/\mathrm{d}V$ spectra as explained in appendix page 145. To ensure the consistency of the deconvolution procedure we show in the lower panel of Fig. 8.9b the recalculated $\mathrm{d}I/\mathrm{d}V$ spectra (reconvolution of the obtained sample DOS with the tip DOS that is used in the deconvolution procedure) that are in very good agreement with the original data. The sample DOS above the centers of the molecules are displayed in Fig. 8.9c. The two YSR states are now seen as two pairs of resonances at ± 0.71 meV and ± 0.55 meV and the spectra can be fitted by the sum of two Lorentzian functions both at positive and negative energies (see red dashed lines for the fits and filled curves that indicate the contribution of each Lorentzian peak). The amplitude of the Lorentzian can now be used in order to quantify the weights of the two YSR states.

In order to get more insight into the localization of the YSR states we record a $\mathrm{d}I/\mathrm{d}V$

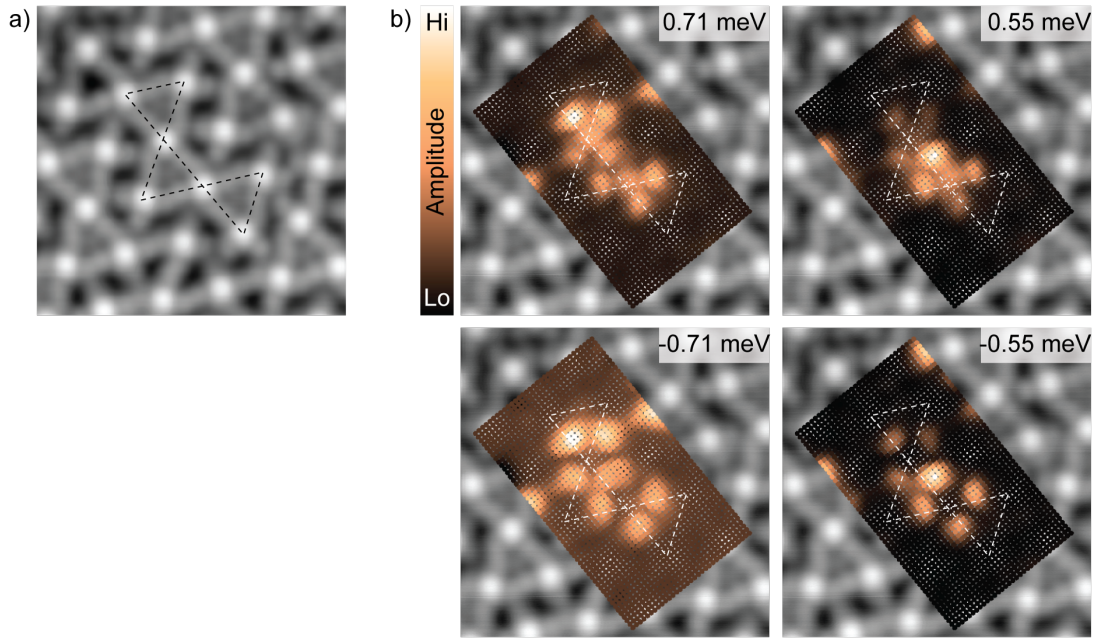

Figure 8.10.: a) Topography image ($V_{\text{bias}} = 5$ mV, $I = 200$ pA) of the structure (indicated by black dashed lines) above which a grid of spectra (see b) is recorded (feedback opened at $V_{\text{bias}} = 5$ mV, $I = 200$ pA and signal modulated with $V_{\text{rms}} = 15$ μeV). The spectra are deconvolved (appendix II) and fitted at positive and negative energies by Lorentzian peaks whose positions and width are kept the same. b) Variations of the amplitude of the Lorentzian peaks (the peaks' energies are indicated in the top right corner of each image). The white dashed lines are the replica of the black dashed lines in a.

spectrum at each point of the grid shown in Fig. 8.10b. The $\mathrm{d}I/\mathrm{d}V$ spectra are then deconvoled as explained in appendix II and fitted by Lorentzian peaks as shown in Fig. 8.9c. The broadening and positions of the Lorentzian peaks are kept the same for all spectra of the grid and we show in Fig. 8.10 the variations of the amplitude of each peak (the corresponding energy is shown in the top right corner of the images). The white dashed lines in Fig. 8.10b are the replica of the black dashed lines in Fig. 8.9a that indicate the investigated structure and serve as a guide to eye to identify the positions of the molecules. Both YSR states are localized above the two central molecules of the structure. This is in accordance with what one expects for YSR dimers with the formation of a symmetric and an antisymmetric YSR state whose probability amplitudes are enhanced and nullified at the center of the dimer [107, 182, 31], respectively. In our case, the YSR state at ± 0.55 meV shows a clear maximum between the two molecules but we do not observe a nodal plane for the one at ± 0.71 meV. Despite this lack of a nodal plane we assign these two YSR states to the symmetric (± 0.55 meV) and antisymmetric (± 0.71 meV) YSR hybrid states.

To further confirm the hybridization of YSR states we study in Fig. 8.11 a structure with now three molecules that have two neighboring Cl adatoms (see black dashed lines in the topography image in a). The $\mathrm{d}I/\mathrm{d}V$ spectra recorded above their centers are shown in Fig. 8.11b and an enlarged view of their YSR states is shown in Fig. 8.11c (we use the same tip as for the previous structures). Three resonances can be identified with different intensities depending on the investigated molecule: the brown and black spectra are identical with a main peak around $V_{\text{bias}} = 1.9$ mV and two shoulders at $V_{\text{bias}} = 1.6$ mV and $V_{\text{bias}} = 2.0$ mV while the blue spectrum only exhibits the two outer YSR states and no central peak. Here

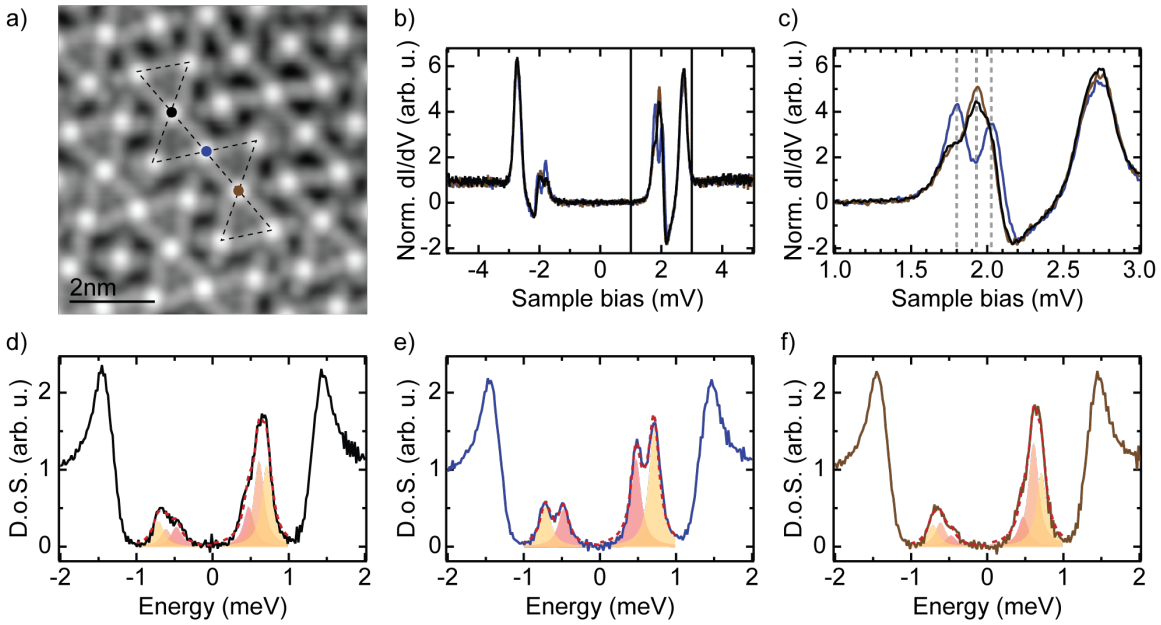

Figure 8.11.: a) Topography image ($V_{\text{bias}} = 5$ mV, $I = 200$ pA) with a structure (see black dashed lines) that contains three molecules with two neighboring Cl adatoms (their centers are indicated by dots). b) $\mathrm{d}I/\mathrm{d}V$ spectra (feedback opened with $V_{\text{bias}} = 5$ mV, $I = 200$ pA and signal modulated with $V_{\text{rms}} = 15$ μeV) taken above their centers with the same tip as in Fig. 8.5. c) Enlarged view of their YSR states with the presence of three resonances that have different intensities. d-f) Sample DOS at these three positions obtained from a deconvolution of the $\mathrm{d}I/\mathrm{d}V$ spectra as explained in appendix page 145. The spectra are fitted both at positive and negative energies with a sum of three Lorentzian peaks (see red dashed lines), the contribution of each Lorentzian peak is indicated by a filled curve.

again, we obtain the sample DOS above the three centers (see Fig. 8.11d-f) by deconvolving the $\mathrm{d}I/\mathrm{d}V$ spectra as explained in appendix II. Now, these can be fitted by the sum of three Lorentzian peaks (see red dashed lines) both at positive and negative energies. For all three centers, the energy positions of the Lorentzian peaks are the same but their intensities vary as one would expect for a coupled system.

The localization of the YSR states across this structure is shown in Fig. 8.12. There, we employed the same methodology as presented before when two molecules are coupled. A set of $\mathrm{d}I/\mathrm{d}V$ spectra is recorded at each point of the grid shown in the topography images. These $\mathrm{d}I/\mathrm{d}V$ spectra are then deconvolved and the resulting DOS are fitted by Lorentzians with the same energies and broadening for all spectra. The variations of the amplitude of each peak is then mapped in Fig. 8.12 (the corresponding energy is indicated in the top-right corner of each image) where the white dashed lines are the replica of the black dashed lines in Fig. 8.11a and help identifying the molecules' positions. Again, the extent of the YSR states is limited to the three central molecules of the structure. The lowest YSR state (± 0.48 meV) is mainly present above the central molecule and has a weak intensity above the two outer ones. By contrast, the YSR state at ± 0.61 meV is not seen above the central molecule but only above the two outer ones. Finally, the higher YSR state at ± 0.71 meV is localized above the three molecules with a slightly higher intensity above the central one. We show next that this dispersion of the YSR states is well accounted for by a theoretical description of the YSR hybridization as reported in literature [182, 57].

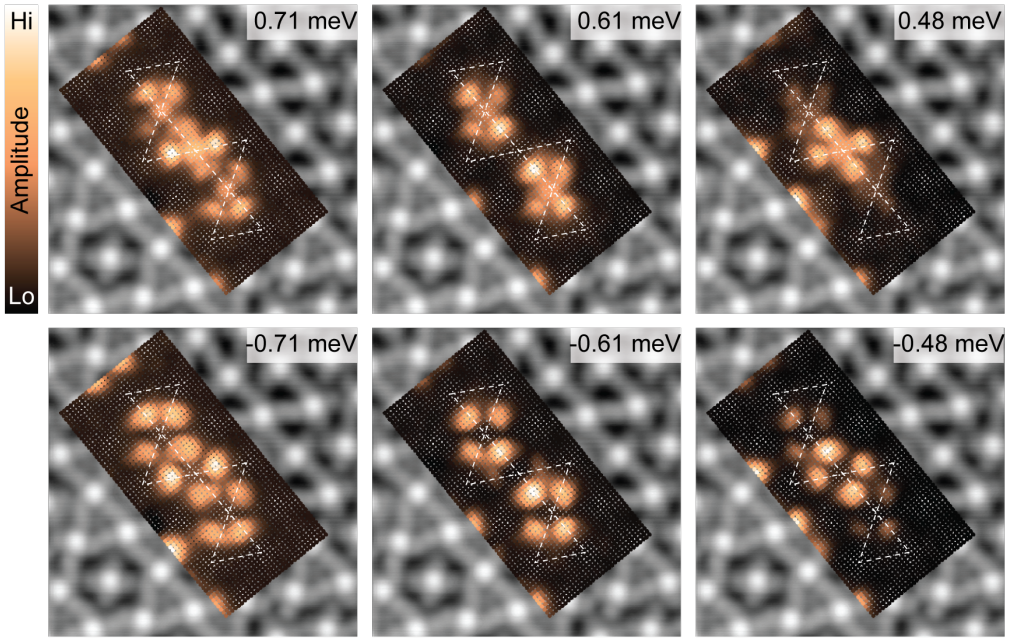

Figure 8.12.: Dipersion of the three YSR states across the structure shown in Fig. 8.11a (see white dashed lines). Spectra are recorded at each point of the grid (feedback opened with $V_{\text{bias}} = 5$ mV, $I = 200$ pA and signal modulated with $V_{\text{rms}} = 15$ μeV), deconvolved as explained in appendix II and fitted at positive and negative energies by three Lorentzian peaks whose width and positions are the same for all spectra. We show here the variations in the amplitudes of these peaks (the corresponding energies are shown in the top-right corners of the images).

2. Theoretical model

Hybridization of YSR states

In order to describe the hybridization of neighboring YSR states we follow the approach of [182]. The coupling of a single magnetic moment (oriented in the z direction and defined as the origin) to the superconducting substrate is described by the following Hamiltonian:

$$H = H_s + J(\mathbf{r})\sigma_z, \tag{8.1}$$

where H_s is the Hamiltonian describing the superconductor, $J(\mathbf{r})$ the exchange potential between the magnetic impurity and substrate electrons and σ_z the Pauli matrix in spin-space. The potential scattering term is for simplicity neglected. This yields two eigenvectors, the YSR states, that follow particle-hole symmetry. In particular, one can fix $\sigma_z = 1$ to find a solution with $-\Delta < E < \Delta$ and obtain the second one (corresponding to $\sigma_z = -1$) with energy $-E$ by particle-hole symmetry.

We now consider a set of N impurities localized at positions $\mathbf{r}_i, i = 1, \cdots, n$ that do not interact directly with one another. Assuming an indirect ferromagnetic coupling via Ruderman-Kittel-Kasuya-Yoshida (RKKY) interaction (see chapter 3 section I.2), the Hamiltonian of the system is then described by:

$$H = H_s + \sum_{i=1}^{N} J(\mathbf{r} - \mathbf{r}_i)\sigma_z \tag{8.2}$$

As explained above we then fix $\sigma_z = 1$. The hybrid YSR states are to a first approximation linear combinations of the original states [182]. We therefore make the variational ansatz that the eigenvectors of the system are of the form $\psi(\mathbf{r}) = \sum_{i=1}^{N} c_i \phi_i(\mathbf{r})$ where ϕ_i satisfies

$$[H_s + J(\mathbf{r} - \mathbf{r}_i)]\phi_i(\mathbf{r}) = E_s \phi_i(\mathbf{r}), \quad |E_s| < \Delta \tag{8.3}$$

Using the following notations $J_i = J(\mathbf{r} - \mathbf{r}_i)$, $|\phi\rangle = \phi_i(\mathbf{r})$ and $|\psi\rangle = \psi(\mathbf{r})$ the eigensystem to solve is then:

$$H|\psi\rangle = E|\psi\rangle \tag{8.4}$$

$$[H_s + \sum_{i=1}^{N} J_i] \sum_{j=1}^{N} c_j |\phi_j\rangle = E \sum_{i=1}^{N} c_i |\phi_i\rangle \tag{8.5}$$

$$\sum_{i=1}^{N} [H_s + J_i] c_i |\phi_i\rangle + \sum_{i=1}^{N} \sum_{\substack{j \neq i \\ j=1}}^{N} J_j c_i |\phi_i\rangle = E \sum_{i=1}^{N} c_i |\phi_i\rangle \tag{8.6}$$

$$\sum_{i=1}^{N} E_s c_i |\phi_i\rangle + \sum_{i=1}^{N} \sum_{\substack{j \neq i \\ j=1}}^{N} J_j c_i |\phi_i\rangle = E \sum_{i=1}^{N} c_i |\phi_i\rangle \tag{8.7}$$

By multiplying each side by $\langle \phi_k|$ we find:

$$E_s c_k + \sum_{\substack{i=1 \\ i \neq k}}^{N} E_s c_i \langle \phi_k | \phi_i \rangle + \sum_{\substack{j=1 \\ j \neq k}}^{N} c_k \langle \phi_k | J_j | \phi_k \rangle + \sum_{\substack{i,j=1 \\ i \neq k \\ j \neq i}}^{N} c_i \langle \phi_k | J_j | \phi_i \rangle = E c_k + E \sum_{\substack{i=1 \\ i \neq k}}^{N} c_i \langle \phi_k | \phi_i \rangle \tag{8.8}$$

Here, one can identify the overlap ($S_{i,k}$), Coulomb-like ($C_{i,k}$) and exchange-like ($D_{i,k}$) integrals between two YSR states ϕ_i and ϕ_k that are defined in analogy with the textbook model for the H_2 molecule as:

$$S_{i,k} = \langle \phi_k | \phi_i \rangle = \int d\mathbf{r} \phi_i(\mathbf{r})^\dagger \phi_k(\mathbf{r}) \tag{8.9}$$

$$C_{i,k} = \langle \phi_k | J_i | \phi_k \rangle = \int d\mathbf{r} \phi_k(\mathbf{r})^\dagger J(\mathbf{r} - \mathbf{r}_i) \phi_k(\mathbf{r}) \tag{8.10}$$

$$D_{i,k} = \langle \phi_k | J_k | \phi_i \rangle = \int d\mathbf{r} \phi_k(\mathbf{r})^\dagger J(\mathbf{r} - \mathbf{r}_k) \phi_i(\mathbf{r}) \tag{8.11}$$

For the different structures that we investigate, one should therefore solve the matrix equation (8.8) to determine the eigenstates of the system. Because we want to compare the results with our experimental findings, we first describe how we choose to simulate the unhybridized YSR state, corresponding to the wave-function $\phi(\mathbf{r})$ described above.

Simulation of a single YSR state

As mentioned earlier, studies of magnetic atoms on superconductors have shown that the YSR state inherits the symmetry of the orbital carrying the unpaired electron which it stems from [180, 32]. In our case, this orbital could not be identified in scanning tunneling spectroscopy (STS) and, as discussed in chapter 7, tunneling to frontier orbitals may also influence the YSR scattering pattern. The YSR state is localized over the center and ligand of the molecule

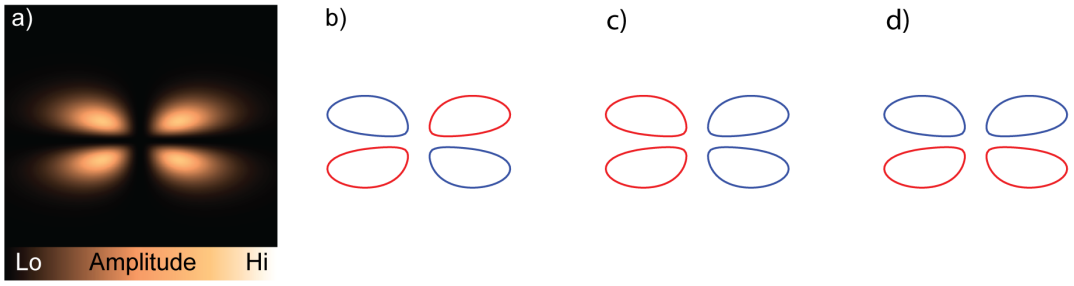

Figure 8.13.: Simulation of a single YSR state ϕ. a) Probability amplitude $|\phi|^2$. b) Iso-contour showing the alternating phase of the lobes. c-d) Alternative phase configurations that have the same probablity amplitude as in a.

(see Fig. 8.5c); it seems that it arises from a hybridization of an Fe d level with the π states of the ligand (see chapter 4 section I). For simplicity, we choose to use solely a d orbital in order to simulate the YSR state: we neglect the protrusion above the Fe center mostly seen at positive energies and focus on rendering the four lobes over the ligand. As one can see from the dI/dV maps of Fig. 8.5c, these four lobes only have a two-fold symmetry and we thus use a distorted d orbital in order to render this C_{2v} symmetry. Most precisely, with Φ_{nlm} being the hydrogen wavefunction with quantum number n, m and l we define ϕ as

$$\phi(x,y) = \frac{1}{\sqrt{2}}\left(\Phi_{322} - \Phi_{32-2}\right)(x/2, y, 0) \tag{8.12}$$

We show in Fig. 8.13a the corresponding amplitude probability $|\phi|^2$ over space and in Fig. 8.13b an iso-contour of the wavefunction indicating the alternating phase of the four lobes. Yet, since we do not know from which orbital the unpaired electron stems from we plot in Fig. 8.13c and d alternative phase configurations that would also yield the amplitude probability plotted in a. Indeed, Fig. 8.13b corresponds to a d_{xy} or $d_{x^2-y^2}$ orbital and c and d rather to the d_π orbital. We first consider the phase configuration shown in b and discuss in section II.3 the relevance of the others.

Coupling of two YSR states

We now consider the structure of Fig. 8.10 where two YSR states are coupled. From equation (8.8) we should solve the matrix equation:

$$\begin{pmatrix} E_s + C & E_s S + D \\ E_s S + D & E_s + C \end{pmatrix} \begin{pmatrix} c_1 \\ c_2 \end{pmatrix} = \begin{pmatrix} E & ES \\ ES & E \end{pmatrix} \begin{pmatrix} c_1 \\ c_2 \end{pmatrix} \tag{8.13}$$

The two eigenstates are $|+\rangle = \begin{pmatrix} 1 \\ 1 \end{pmatrix}$ and $|-\rangle = \begin{pmatrix} 1 \\ -1 \end{pmatrix}$

with eigenenergies

$$E_\pm = E_s + \frac{C \pm D}{1 \pm S} \tag{8.14}$$

Using the simulation of $\phi(\mathbf{r})$ of equation (8.12), Fig. 8.14 c-d) and f-g) show the probability amplitude and iso-contours of the resulting eigenvectors. More precisely, one can consider two different phase configurations for the unhybridized YSR states as shown in Fig. 8.14a and e: the lobes along the bonding axis having either the same (Fig. 8.14a) or opposite (Fig. 8.14e)

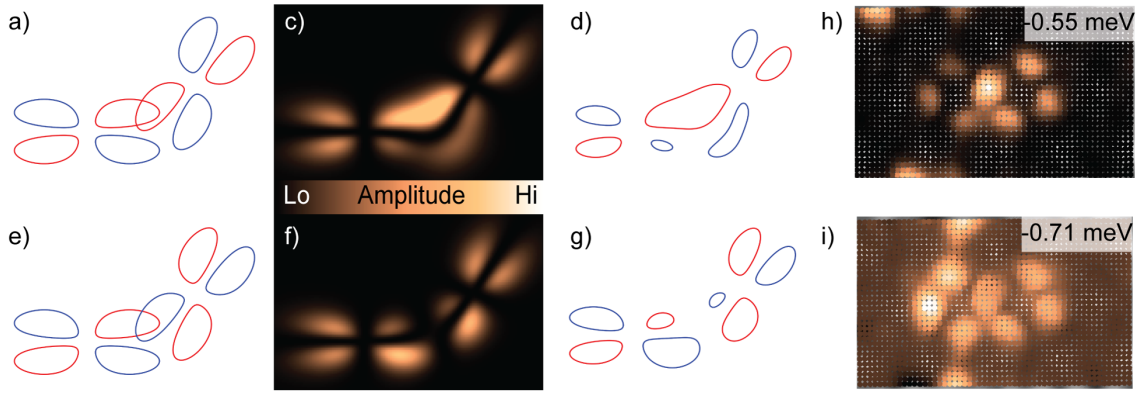

Figure 8.14.: Simulation of the coupling of two YSR states. a) Configuration of the YSR before hybridization. Hybridization of the two YSR states leads to the formation of two hybrid YSR states: $|+\rangle$ and $|-\rangle$ c) Probability amplitude of the $|+\rangle$ YSR state across the structure. d) Iso-contour of the $|+\rangle$ state. f) Probability amplitude of the $|-\rangle$ state. g) Iso-contour of the $|-\rangle$ state. e) Alternative configuration of the YSR states. In this case the $|+\rangle$ and $|-\rangle$ exchange their role. h-i) Experimental data of Fig. 8.10b, reproduced here to facilitate the comparison.

phases. In the first (second) case, the YSR state shown in Fig. 8.14c-d is the $|+\rangle$ ($|-\rangle$) eigenstate and the one in Fig. 8.14f-g the $|-\rangle$ ($|+\rangle$) eigenstate. To facilitate the comparison with the experimental data we reproduce in Fig. 8.14h and i the grids of Fig. 8.10b. We assign the simulated YSR state of Fig. 8.14c to the experimental data of Fig. 8.14h and the simulation of Fig. 8.14f to the experimental data of Fig. 8.14i. Despite the lack of nodal plane mentioned earlier for the YSR state at ± 0.71 meV, we find a good agreement between the simulation and the experimental data.

Coupling of three YSR states

We now demonstrate that a good agreement can also be found when considering the coupling of three YSR states as observed in Fig. 8.11 and Fig. 8.12. For simplicity we consider only interaction between nearest neighbors and assume that the overlap (S), Coulomb (C) and exchange (D) integrals are the same for the two pairs of nearest neighbohrs. The matrix equation to solve is then:

$$\begin{pmatrix} E_s + C & E_s S + D & 0 \\ E_s S + D & E_s + 2C & E_s S + D \\ 0 & E_s S + D & E_s + C \end{pmatrix} \begin{pmatrix} c_1 \\ c_2 \\ c_3 \end{pmatrix} = \begin{pmatrix} E & ES & 0 \\ ES & E & ES \\ 0 & ES & E \end{pmatrix} \begin{pmatrix} c_1 \\ c_2 \\ c_3 \end{pmatrix} \tag{8.15}$$

One of the eigenvector is $\begin{pmatrix} -1 \\ 0 \\ 1 \end{pmatrix}$ with eigenvalue $E = E_s + C$. The other two eigenvectors and their corresponding eigenvalues can be determined analytically but depend in a non-trivial way on the values of S, C and D. Because we want to demonstrate that the model can reproduce the experimental data we choose a set of parameters for which the agreement is good but underline that other sets of values for S, C and D could also have been chosen.

We show in Fig. 8.15 the results of a simulation of three YSR states arranged as shown in Fig. 8.15a and using the set of values: $S = -0.3$, $C = 0$ and $D = 0.7$. Fig. 8.15b-d displays

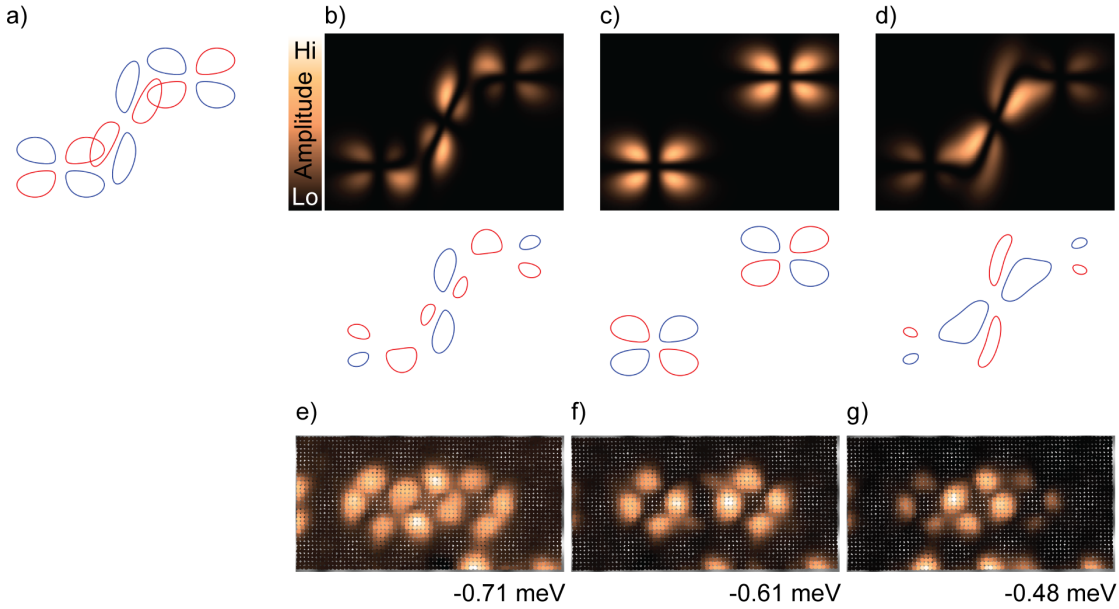

Figure 8.15.: Simulation of the coupling of three YSR states. a) Configuration of the YSR states before hybridization. b-d) Probability amplitude (top graphs) and iso-contours (lower graphs) of the hybrid states. e-g) To facilitate a comparison with the experimental data presented in Fig. 8.12 we reproduce here the negative energy intensity grids of the YSR states.

the eigenstates' probabilities amplitudes (top graphs) and iso-contours (lower graphs). To aid the comparison with the experimental data shown in Fig. 8.12, we reproduce in Fig. 8.15 the negative energy intensity grids of the YSR states of Fig. 8.12. Here again, the simulation reproduces well the experimental data. The YSR state of Fig. 8.15b is seen above the three molecules with a slightly higher intensity over two lobes of the central molecules and is thus assigned to the YSR state of Fig. 8.15b. The YSR state of Fig. 8.15c is only localized above the two outer molecules (it is the eigenvector $\begin{pmatrix}-1 & 0 & 1\end{pmatrix}$) and corresponds to the YSR state of Fig. 8.15f. Finally, the YSR state of Fig. 8.15g is assigned to Fig. 8.15d with the highest intensity above the central molecule. We chose the phase configuration shown in Fig. 8.15a because of the symmetry of the YSR states in Fig. 8.12. A reversal of the phase of the central molecule would give rise to the same eigenstates with the two of Fig. 8.15b and d being swapped.

3. Coupling of four Yu-Shiba-Rusinov states

So far, the experimental data can be explained by considering a ferromagnetic coupling of the impurities, including interactions between nearest neighbors only and assuming that each pair of nearest neighbors have the same overlap, exchange and Coulomb integrals. We now discuss a structure for which these assumptions fail to provide a satisfying description of the YSR coupling.

The structure of interest is shown in the topography image of Fig. 8.16a by black dashed lines. Four molecules (their centers are marked with dots) have two neighboring Cl adatoms. The sketch of the structure is reproduced in Fig. 8.16b where we label the positions of these molecules with A, B, C and D. The $\mathrm{d}I/\mathrm{d}V$ spectra (with the same tip as in Fig. 8.11) recorded above their Fe centers are shown in Fig. 8.16b (an enlarged view of the YSR states at positive

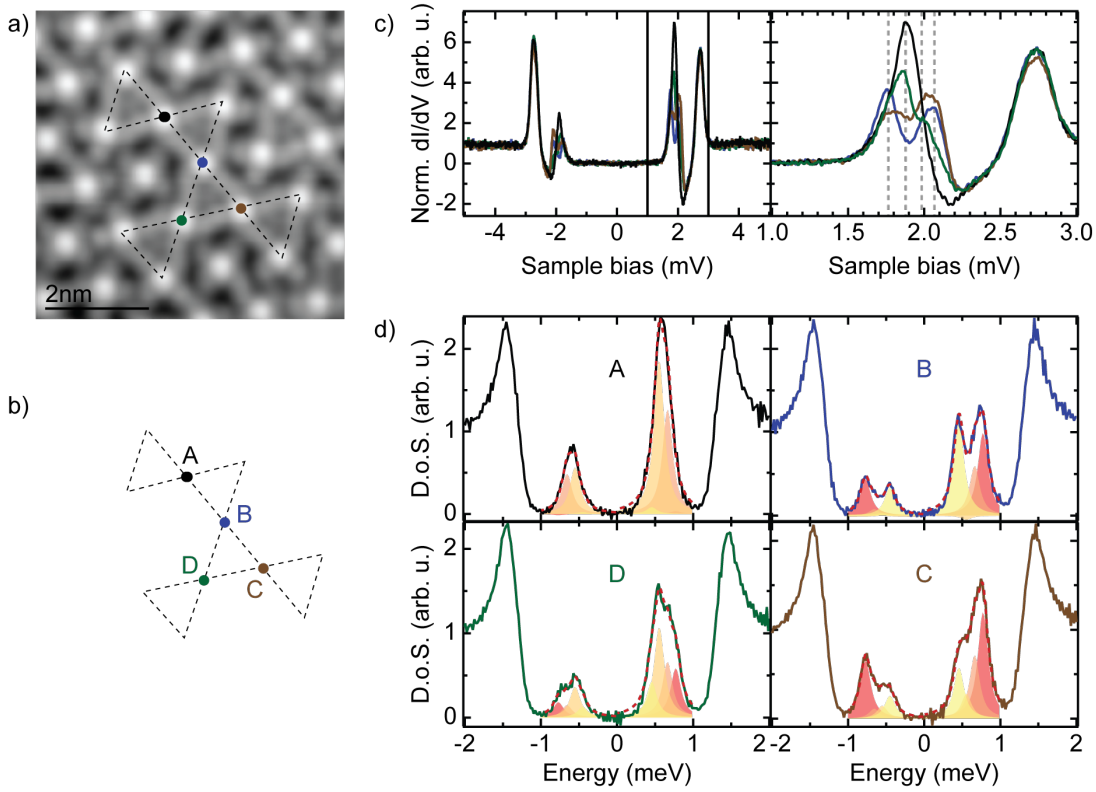

Figure 8.16.: Topography image ($V_{\text{bias}} = 5$ mV, $I = 200$ pA) of a structure (see black dashed lines) with four molecules having two neighboring Cl adatoms (their centers are indicated by dots). b) Sketch of the structure with labels for the different sites whose YSR states are hybridized. c) dI/dV spectra recorded above the center of the molecules as shown in a (feedback opened with $V_{\text{bias}} = 5$ mV and $I = 200$ pA and signal modulated with $V_{\text{rms}} = 15$ μeV). An enlarged view of the YSR states at positives energies is shown in the right panel. d) Sample DOS above the same positions obtained by deconvolving the dI/dV spectra shown in b as explained in appendix II. Each spectrum is fitted by a sum of four Lorentzian peaks (see red dashed lines) and the contribution of each peak is indicated by a filled curve.

energies is shown in the right panel). One can distinguish four different resonances but we see that these are not always well separated indicating that we reach the limits of our resolution. Identically to what was done for the other structures, we deconvolve these dI/dV spectra in order to obtain the sample DOS at these positions as displayed in Fig. 8.16. The spectra are then fitted (see red dashed lines) with a sum of four Lorentzian peaks both at positive and negative energies, with filled curves indicating the contribution of each peak to the fit.

Similarly to Fig. 8.10 and Fig. 8.12, we record a spectrum at each point of the grid shown in Fig. 8.17. These dI/dV spectra are then deconvolved (see appendix page 145) and the obtained sample DOS are fitted at positive and negative energies by a sum of four Lorentzians. The width and positions of the Lorentzian peaks are kept the same for all spectra of the grid and we show in Fig. 8.17 the variations in the amplitude of these peaks (the corresponding energies are shown in the top-right corners of the images). To describe the localization of the states we use the labeling of the positions shown in Fig. 8.16. The YSR state at ± 0.77 meV is not seen above A but above the three other positions. The YSR state at ± 0.66 meV has it highest intensity above the position A and remains present on the other positions. The YSR

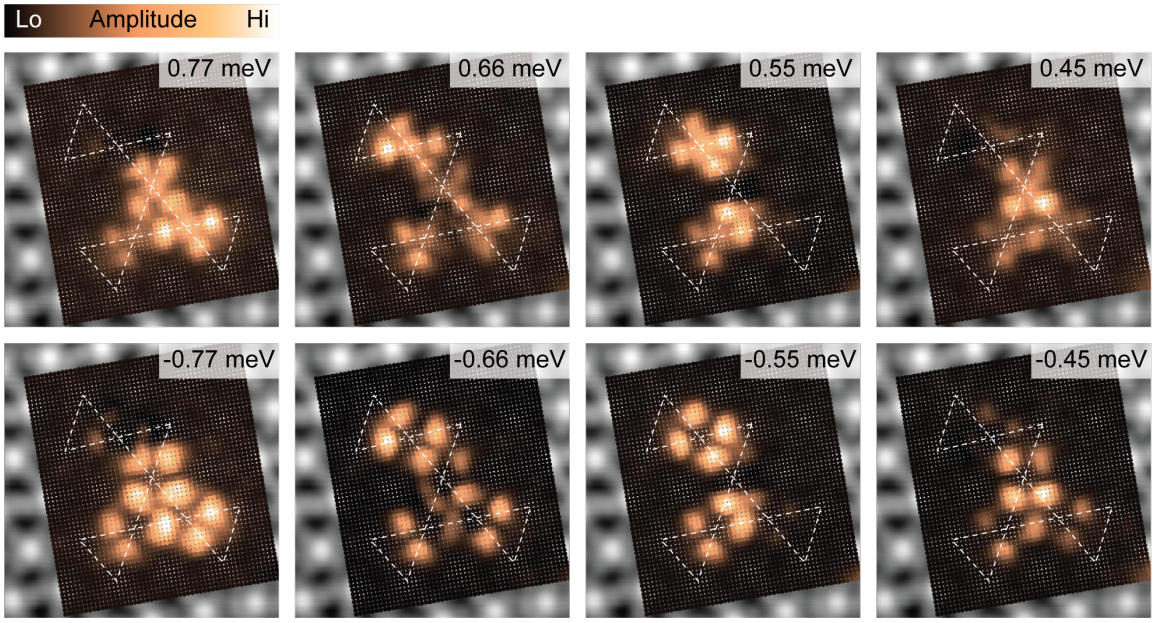

Figure 8.17.: Dipersion of the YSR states across the structure shown in Fig. 8.16a. The white dashed lines are a replica of the black dashed lines in Fig. 8.16a and help identify the positions of the molecules. $\mathrm{d}I/\mathrm{d}V$ spectra (feedback opened with $V_{\mathrm{bias}} = 5$ mV and $I = 200$ pA and signal modulated with $V_{\mathrm{rms}} = 15$ μeV) are recorded at each point of the grid, deconvolved as explained in appendix page 145 and the resulting sample DOS are fitted by a sum of four Lorentzian peaks at positive and negatives energies. The position and width of the peaks is kept the same for all spectra and we show the variations in their amplitude (the corresponding energies are indicated in the top-right corners of the images).

state at ± 0.55 meV is only seen above the positions A and D with similar intensity. Finally, the YSR state at ± 0.45 meV has its highest intensity above the position B and is also present above C and D. Here, we want to highlight the fact that none of these YSR states is seen only above the sites C and D or show even a higher intensity above these two sites when compared to A and B. Moreover, the YSR state at ± 0.55 meV shows clearly that these two sites are not equivalent. This assertion can already be made by comparing the brown and green $\mathrm{d}I/\mathrm{d}V$ spectra in Fig. 8.16b that exhibit different intensities of the various resonances.

We show now that this observation cannot be accounted for by the simplifications we made for the coupling model so far. Indeed, using equation (8.8), considering only nearest neighbor interactions and assuming the same overlap (S), exchange (D) and Coulomb (C) integrals for all pairs of neighbors we obtain the following matrix equation (we use the basis $\begin{pmatrix} A & B & C & D \end{pmatrix}$):

$$\begin{pmatrix} E_s + C & E_s S + D & 0 & 0 \\ E_s S + D & E_s + 3C & E_s S + D & E_s S + D \\ 0 & E_s S + D & E_s + 2C & E_s S + D \\ 0 & E_s S + D & E_s S + D & E_s + 2C \end{pmatrix} \begin{pmatrix} c_1 \\ c_2 \\ c_3 \\ c_4 \end{pmatrix} = \begin{pmatrix} E & ES & 0 & 0 \\ ES & E & ES & ES \\ 0 & ES & E & ES \\ 0 & ES & ES & E \end{pmatrix} \begin{pmatrix} c_1 \\ c_2 \\ c_3 \\ c_4 \end{pmatrix} \tag{8.16}$$

We note that we also neglected the terms

$$D'_{i,j,k} = \langle \phi_i | J_j | \phi_k \rangle \tag{8.17}$$

with $\{i,j,k\} \in S(\{B,C,D\})$, $S(\{B,C,D\})$ being the permutation group of $\{B,C,D\}$. From now on, we refer to these $D'_{i,j,k}$ expressions as exchange via common neighbor integrals.

The vector $\begin{pmatrix}0 & 0 & 1 & -1\end{pmatrix}$ is an eigenvector of (8.16) with eigenvalue $E = E_s + \frac{2C-D}{1-S}$. It corresponds to a YSR state localized only above the sites C and D of the structure. This is in direct contradiction with the experimental data as explained above. Indeed, in the coupling model that we used, the sites D and C are equivalent. We should review the hypotheses that were made and discuss their relevance.

We neglected the potential scattering U for each impurity site and assumed a ferromagnetic coupling between the impurities. We neglected interactions beyond nearest neighbor and the exchange via common neighbor integrals $D'_{i,j,k}$. We also assumed the same overlap (S), exchange (D) and Coulomb (C) integrals for all pairs of neighbors.

We now address the relevance of each hypothesis and discuss which one should be relaxed in order to find a better agreement with the experimental data.

Potential scattering. This term accounts for the electron-hole asymmetry of both the impurity and the substrate. It should therefore be the same for all impurities and would affect their YSR states in the same way. In particular, it would not break the symmetry of the problem for the C and D sites. While its importance is non negligible for a quantitative description of the coupling of YSR states, since we aim at a qualitative understanding, it is reasonable to neglect it.

Ferromagnetic coupling. A ferromagnetic coupling is usually assumed for the hybridization of YSR states because, for classical impurity spins, an anti-ferromagnetic coupling between two impurities would render their YSR states orthogonal to each other and thus prevent any hybridization between them [56]. Here, the observation of a Kondo resonance in the normal state of the Pb substrate (see next section) indicates that the impurities have a quantum and not a classical nature. Therefore, the observation of a splitting of the YSR state in Fig. 8.9 and Fig. 8.12 thus does not imply that the coupling between the impurities is ferromagnetic. However, the description of the coupling of two quantum impurities is not trivial and usually requires numerical renormalization group (NRG) calculations that go beyond the scope of this thesis [224, 187, 228, 104]. Yet, anti-ferromagnetic coupling between the impurities would lead to a frustration within the triangular arrangements of the sites B, C and D and could thus account for the different behaviors of the sites C and D. We propose a very naive implementation of this frustration consisting of a sign reversal in front of $J(\mathbf{r})\sigma_z$ for an impurity within this triangle as it would effectively correspond to a reversal of the spin eigenvalues in σ_z. A possible Hamiltonian would thus be:

$$H = H_s + J(\mathbf{r}-\mathbf{r}_A)\sigma_z + J(\mathbf{r}-\mathbf{r}_B)\sigma_z + J(\mathbf{r}-\mathbf{r}_C)\sigma_z - J(\mathbf{r}-\mathbf{r}_D)\sigma_z \tag{8.18}$$

which translates into a sign reversal of J_D. Using equations (8.10), (8.11) and (8.9) and assuming otherwise the same absolute values for the exchange, overlap and Coulomb integrals we can define S, C and D as:

$$S = S_{A,B} = S_{B,C} = S_{C,D} = S_{B,D} \tag{8.19}$$
$$C = C_{A,B} = C_{B,C} = -C_{D,C} = -C_{B,D} \tag{8.20}$$
$$D = D_{A,B} = D_{B,C} = -D_{D,C} = -D_{B,D} \tag{8.21}$$

Neglecting exchange via common neighbor integrals and interactions beyond nearest neighbors, we obtain the following matrix equation:

$$\begin{pmatrix} E_s+C & E_sS+D & 0 & 0 \\ E_sS+D & E_s+C & E_sS+D & E_sS-D \\ 0 & E_sS+D & E_s & E_sS-D \\ 0 & E_sS-D & E_sS-D & E_s-2C \end{pmatrix} \begin{pmatrix} c_1 \\ c_2 \\ c_3 \\ c_4 \end{pmatrix} = \begin{pmatrix} E & ES & 0 & 0 \\ ES & E & ES & ES \\ 0 & ES & E & ES \\ 0 & ES & ES & E \end{pmatrix} \begin{pmatrix} c_1 \\ c_2 \\ c_3 \\ c_4 \end{pmatrix} \tag{8.22}$$

One can verify that no vector of the form $\begin{pmatrix} 0 \\ 0 \\ \alpha \\ \beta \end{pmatrix}$, $\alpha, \beta \in \mathbb{R}$ can be an eigenvector of the system (we have $C \neq 0$ or $D \neq 0$ since we observe a splitting for two YSR states - see equation (8.14)).

The disagreement between the experimental data and the model may thus be avoided by considering a frustrated antiferromagnetic coupling between the sites B, C and D. Further simulations are still necessary in order to determine if this model can reproduce our experimental data.

Interactions beyond nearest neighbors. The integrals between states that are not nearest neighbors have been neglected. Indeed, the YSR wavefunctions decay exponentially with distance and it was observed in [180] that Mn dimers on Pb(001) show a clear YSR hybridization for an interatomic distance of 1.04 nm but barely any sign of coupling for an interatomic distance of 2.08 nm. Here, the intermolecular distance is 1.2 nm so that the integrals involving second (and higher orders) nearest neighbors can be considered as a perturbation with respect to the integrals involving nearest neighbors. Including them in our theoretical model would then only result in a perturbative modification of the eigenstates. Yet, we have seen in Fig. 8.17 that no YSR state is mostly localized above the sites C and D. Including higher orders for the interactions between the molecules would thus still not account for our experimental observations.

Exchange via common neighbor integrals. These integrals involve three distinct but neighboring sites (B, C and D). Because the three parts of these integrals have different spatial origins it is expected that these integrals are less important than the exchange integrals that involve only two sites. Moreover, here again, if we consider ferromagnetic coupling, the sites C and D would be affected the same way and would thus still be hosting the $\begin{pmatrix} 0 & 0 & 1 & -1 \end{pmatrix}$. As a result, the inclusion of these integrals alone would not suffice to have a better simulation of the experimental data.

Equality of the overlap, exchange and Coulomb integrals for all pairs of neighbors. The sites at which the YSR states are localized are arranged along lines that have a 60° angle between one another. The molecules at the different sites are rotated accordingly so that, when considering the probability amplitudes of neighboring molecules, the overlap is always the same. However, the phase of these molecules might be arranged in different ways. As we have illustrated in Fig. 8.14a and e, the phases of the overlapping lobes can either be the same (Fig. 8.14a) or opposite (Fig. 8.14e). As mentioned earlier, for the coupling of two and three YSR states across the structures investigated in this thesis, both configurations yield valid and equivalent results. Yet, for the coupling of four YSR states, due to the triangular formation of the sites B, C and D this might play a role as the phase configurations between the different sites are interdependent. Using the different phases shown in Fig. 8.13b-d, we sketch in Fig. 8.18 the different phase configurations obtained for a triangle depending on if an in-phase or out-of-phase overlap is preferred. As one can see, in some cases (indicated by a star), the favored overlap cannot be achieved between all pairs of molecules. In these cases, it could be possible to break the symmetry of the problem for the D and C sites if we consider

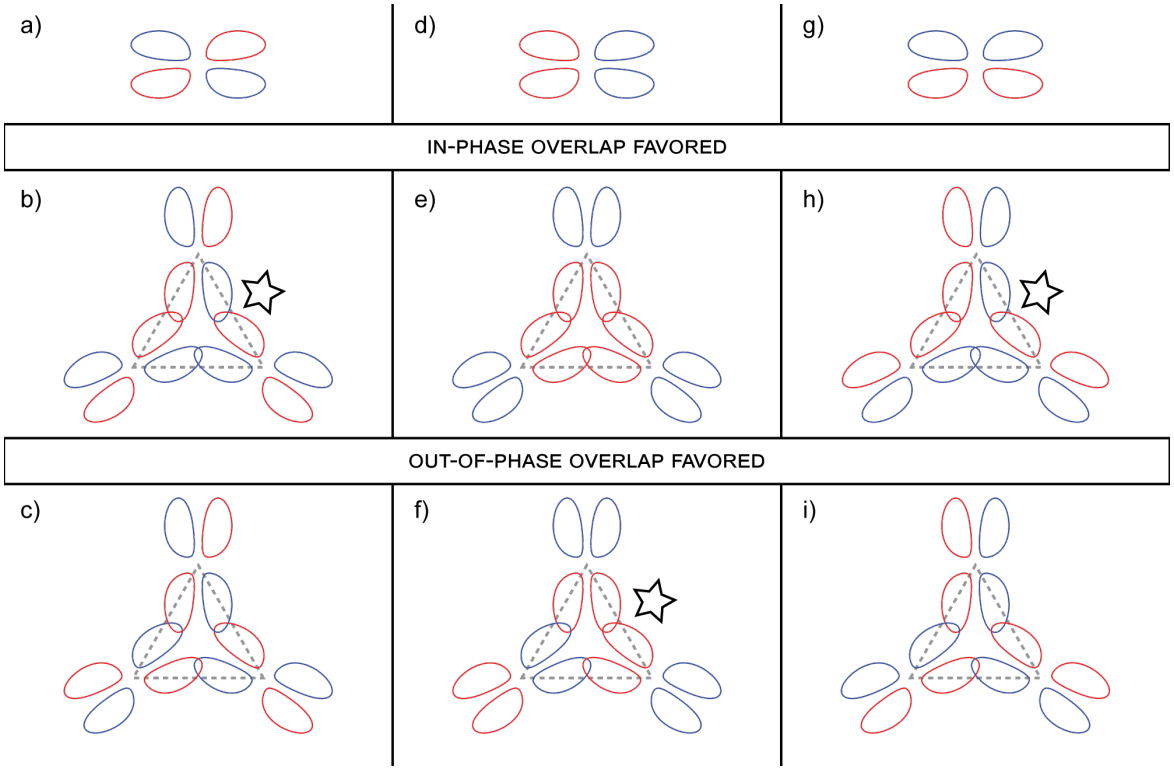

Figure 8.18.: Configurations obtained for a triangle of YSR states depending on which phase configuration is used to model a single YSR state (a, d and g - the according phase configurations for the triangles are then sorted vertically) and if an in-phase (b, e and h) or out-of-phase (c, f and i) overlap is favored. In some cases, marked by a star, the favored overlap cannot be achieved for all pairs of states.

that the S, D and C integrals depend on the relative phases of the overlapping lobes.

The simplest approach would be to consider that the in-phase and out-of-phase overlap only correspond to a sign reversal of one of the wavefunctions involved in the integrals. Namely, we want to compare the integrals between $|\phi_1\rangle$ and $|\phi_2\rangle$ and those between $Y\phi_1\rangle$ and $|\widetilde{\phi_2}\rangle = -|\phi_2\rangle$. We find:

$$S_{1,\tilde{2}} = \langle\widetilde{\phi_2}|\phi_1\rangle = -\langle\phi_2|\phi_1\rangle = -S_{1,2} \tag{8.23}$$

$$C_{1,\tilde{2}} = \langle\widetilde{\phi_2}|J_1|\widetilde{\phi_2}\rangle = \langle-\phi_2|J_1|-\phi_2\rangle = C_{1,2} \tag{8.24}$$

$$D_{1,\tilde{2}} = \langle\widetilde{\phi_2}|J_2|\phi_1\rangle = -\langle\phi_2|J_2|\phi_1\rangle = -D_{1,2} \tag{8.25}$$

Considering such a phase configuration for the structure of four YSR states with a frustration between the sites B and C we have:

$$S = S_{A,B} = S_{B,D} = S_{D,C} = -S_{B,C} \tag{8.26}$$

$$C = C_{A,B} = C_{B,D} = C_{D,C} = C_{B,C} \tag{8.27}$$

$$D = D_{A,B} = D_{B,D} = D_{D,C} = -D_{B,C} \tag{8.28}$$

We then obtain the following matrix equation

$$\begin{pmatrix} E_s+C & E_sS+D & 0 & 0 \\ E_sS+D & E_s+3C & -E_sS-D & E_sS+D \\ 0 & -E_sS-D & E_s+2C & E_sS+D \\ 0 & E_sS+D & E_sS+D & E_s+2C \end{pmatrix} \begin{pmatrix} c_1 \\ c_2 \\ c_3 \\ c_4 \end{pmatrix} = \begin{pmatrix} E & ES & 0 & 0 \\ ES & E & -ES & ES \\ 0 & -ES & E & ES \\ 0 & ES & ES & E \end{pmatrix} \begin{pmatrix} c_1 \\ c_2 \\ c_3 \\ c_4 \end{pmatrix} \tag{8.29}$$

Unfortunately, $\begin{pmatrix} 0 \\ 0 \\ 1 \\ 1 \end{pmatrix}$ is now an eigenvector which still corresponds to a state only localized above the sites C and D. If we consider the exchange via common neighbor integrals (see equation (8.17)) we have:

$$D' = D'_{B,C,D} = -D'_{C,B,D} = -D'_{C,D,B} \tag{8.30}$$

and the vector $\begin{pmatrix} 0 \\ 0 \\ 1 \\ 1 \end{pmatrix}$ remains an eigenvector of the resulting matrix equation.

As a result, if one wants to explain the experimental data with a ferromagnetic coupling of the YSR states, a directional dependence of the overlap, exchange and Coulomb integrals that goes beyond a simple sign reversal is necessary. This is sensible because the four-fold symmetry of the molecules is broken by the three-fold symmetry of the substrate. However, the numbers of parameters involved is then too large to make educated guesses about their values.

All in all, we can conclude that two hypotheses can be possibly relaxed in order to get a better agreement with our experimental data: one should consider either an antiferromagnetic coupling between the molecules (leading to frustration within a triangle) and/or a directional dependence of the overlap, exchange, (exchange via common neighbor) and Coulomb integrals between YSR states.

4. Yu-Shiba-Rusinov bands in a Kagome lattice

We now characterize the properties of the molecules in the superconducting state of Pb when a Kagome lattice is formed as presented in chapter 4. Fig. 8.19a shows a topography image of an island with a Kagome arrangement of the molecules in which blue lines indicate boundaries between different Kagome lattices. This is illustrated more precisely in Fig. 8.19b. There, the molecules at the top of the image have the regular arrangement of a Kagome lattice as indicated by red dashed lines. The molecules on the lower part of the island are also arranged in a Kagome lattice (see black dashed lines). There is however a lattice mismatch between the two arrangements (by one molecular column in the horizontal direction) that leads to a domain boundary between the two lattices for which the blue line stands.

We analyze Fig. 8.19d the spectroscopic properties of the molecules depending on their positions within the island and with respect to the Kagome arrangements. The molecules that are inside a Kagome lattice (i.e. with two neighboring Cl adatoms) show a broad resonance between $V_{\text{bias}} \sim 1.4$ mV and $V_{\text{bias}} \sim 1.9$ mV (green spectra). The intensity of the $\mathrm{d}I/\mathrm{d}V$ signal varies across this resonance and from one molecule to another. Since we have demonstrated an hybridization of the YSR states within the Kagome buildings blocks in the previous subsection we attribute this broad resonance to a YSR band. This broad resonance is not observed above the other molecules. The molecules inside a hole of the Kagome lattice

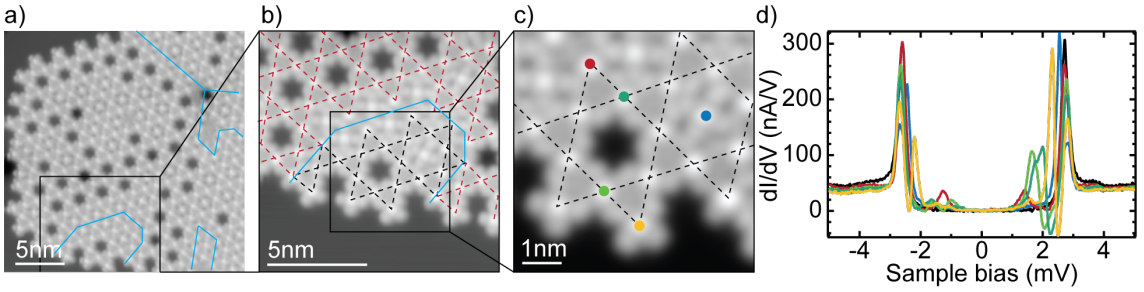

Figure 8.19.: a) Togography image ($V_{\text{bias}} = 5$ mV, $I = 50$ pA) of an island in which the molecules arrange in Kagome lattices. Domain boundaries between different lattices are marked with blue lines. b) Illustration of a domain boundary ($V_{\text{bias}} = -45$ mV, $I = 100$ pA): the two Kagome lattices indicated with red and black dashed lines mismatch each other by one molecular column along the horizontal direction. This gives rise to a domain boundary for which the blue line stands. c) Enhanced view of the area marked with a square in b) ($V_{\text{bias}} = -45$ mV, $I = 100$ pA). d) $\mathrm{d}I/\mathrm{d}V$ spectra taken with a superconducting tip above molecules with various positions inside the island and with respect to the Kagome lattice (see c), a reference spectrum taken on Pb is shown in black (feedback opened at $V_{\text{bias}} = 5$ mV, $I = 200$ pA and signal modulated wirh $V_{\text{rms}} = 20$ μeV).

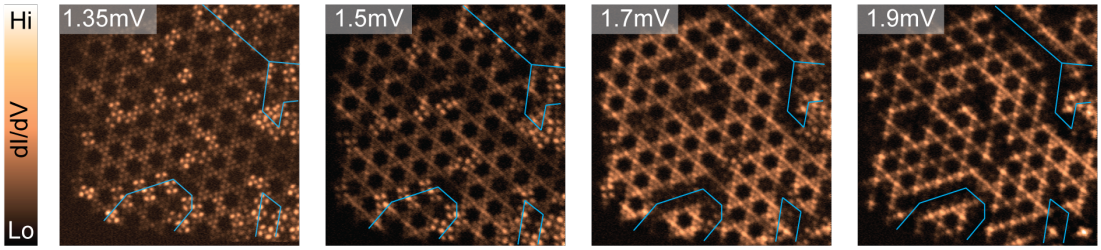

Figure 8.20.: Constant height $\mathrm{d}I/\mathrm{d}V$ maps taken above the same are as shown in the topography image of Fig. 8.19a and at different bias voltages as indicated in the top-lef corners of the maps (signal modulated with $V_{\text{rms}} = 25$ μeV). The $\mathrm{d}I/\mathrm{d}V$ maps are recorded with a superconducting tip: $V_{\text{bias}} = 1.35$ mV corresponds to the Fermi energy of the sample.

(blue spectrum) show a YSR state very close to the gap edge. Those at the edge of the island and thus also at the edge of the Kagome lattice (one neighboring Cl adatom) also show one sharp pair of resonances that is at higher energy than the YSR band and assigned to a single YSR state. Finally, we note that some molecules that are inside the molecular island but at the edge of a Kagome lattice (one neighboring Cl adatom - red spectrum) exhibit a symmetric pair of resonances at $V_{\text{bias}} = \pm 1.35$ mV which corresponds to the Fermi energy of the sample (we use a superconducting tip, a reference spectrum taken above the bare Pb substrate is shown in black).

Fig. 8.20 shows constant height $\mathrm{d}I/\mathrm{d}V$ maps over the same area as the topography image of Fig. 8.19a which allow for a better assessment of the localization of each feature. As a guide to the eye we indicate with blue lines domain boundaries between different Kagome lattices. At zero energy ($V_{\text{bias}} = 1.35$ mV), the $\mathrm{d}I/\mathrm{d}V$ signal is most intense above a few molecules, inside the molecular island and at domains boundaries. The signal is also present above the molecules that are part of the Kagome lattices (two neighboring Cl adatoms) with a few of them being brighter than the others. At higher biases the $\mathrm{d}I/\mathrm{d}V$ signal is more intense above the Kagome lattice than at the boundaries. Indeed, at $V_{\text{bias}} = 1.7$ mV and $V_{\text{bias}} = 1.9$ mV

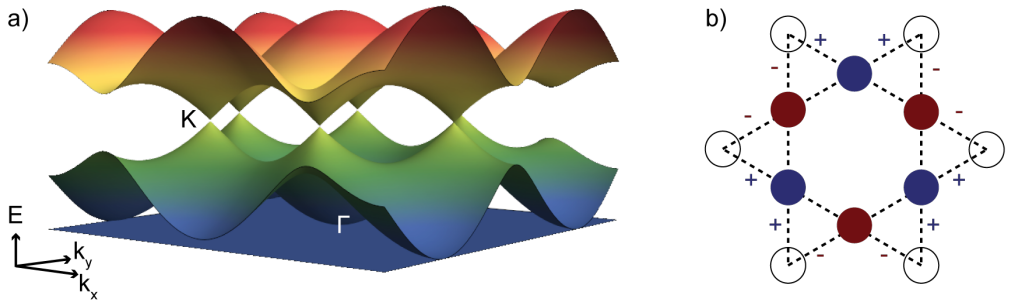

Figure 8.21.: a) Band structure of the Kagome lattice obtained from a tight-binding model with nearest neighbor hopping only. The two upper bands are dispersive with a linear dispersion at the K point. The third band is non-dispersive (flat-band) and touches the second one at the Γ point. b) Sketch of the first mode of the flat-band: it is localized above the six sites (filled circles) enclosing a Kagome hole with an alternating phase on adjacent sites (blue and red). This gives rise to destructive interferences at the neighboring sites (empty black circles) illustrating the localized nature of the state.

the $\mathrm{d}I/\mathrm{d}V$ signal is spread over the different Kagome lattices and the domain boundaries are identified as depressions between them. Noticeably, the holes of the Kagome lattices are always seen as depressions, irrespective of their occupation or not by a molecule. Finally, we note that, for each map, the intensity of the $\mathrm{d}I/\mathrm{d}V$ signal is modulated across the Kagome lattices. Unfortunately, because of their finite sizes, we can not extract a typical scattering lengthscale for each energy that would have helped characterize the energy dispersion of the YSR band.

All in all, these results are in good agreement with those obtained in the previous subsection about the building blocks of the Kagome lattice. The YSR states induced by molecules that are part of a Kagome lattice, with two neighboring Cl, hybridize with one another leading to the formation of a YSR band. The $\mathrm{d}I/\mathrm{d}V$ maps of the YSR band show clearly that the YSR hybridization only takes place for these specific molecules since we observe depressions at domain boundaries and above the holes of the Kagome lattice, despite them being sometimes occupied with a molecule. It is therefore relevant to discuss if the observed YSR band inherits the characteristics of the electronic structure of a Kagome lattice.

The Kagome lattice has been the subject of numerous studies because of the peculiar nature of its band structure and the high degree of frustration of antiferromagnets in such lattices [98, 80, 90, 77, 196]. We show in Fig. 8.21a the three bands obtained from a tight-binding model considering nearest-neighbor hopping only [149]. Two of these band are dispersive with, similarly to the honeycomb lattice, a linear dispersion at the K point of the Brillouin zone. The last band is degenerate and non-dispersive (therefore called a flat-band) that touches the second band at the Γ point. The emergence of this flat band lies at the core of the current inquiries about the Kagome lattice: strong interaction between many degenerate states makes it a perfect candidate for, for instance, the observation of a fractional quantum Hall effect [207, 204, 157]. Yet, this flat band has been observed for only few systems so far [128, 27, 26]. We show in Fig. 8.21b a schematics, in real space, of the fundamental mode of this flat band: a ring localized above six sites enclosing a hole of the Kagome lattice (filled circles). The alternative phases (blue and red) of the mode on adjacent sites lead to destructive interference at the neighboring sites (empty circles) demonstrating the non-dispersive nature of the state.

Because there is no band gap, it is hard to determine if the observed broad resonance in STS could reflect the band structure of Fig. 8.21a. We therefore compare our results to

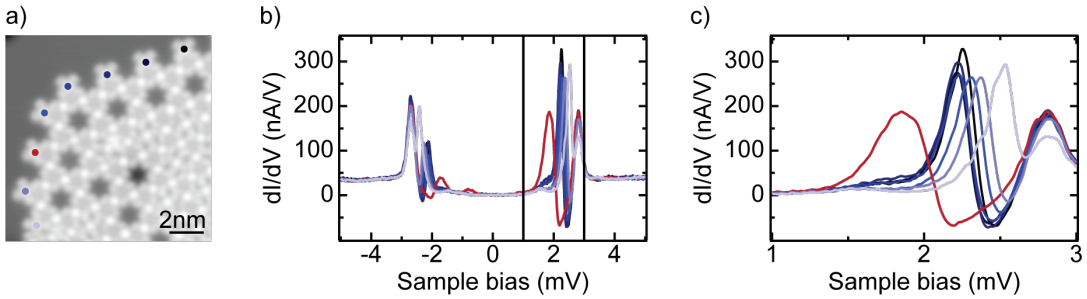

Figure 8.22.: a) Topography image ($V_{\text{bias}} = -45$ mV, $I = 100$ pA) of an island with Kagome arrangement of the molecules. b) Set of dI/dV spectra (feedback opened at $V_{\text{bias}} = 5$ mV, $I = 200$ pA and signal modulated with $V_{\text{rms}} = 20$ μeV), recorded with the same superconducting tip as in Fig. 8.19d above a set of molecules at the edge of an island, as shown in a. c) Enhanced view of the dI/dV spectra in b around the YSR states' energies.

another scanning tunneling microscopy (STM) experiment [128] that established the presence of the flat band in the electronic Kagome lattice induced by the Moiré patterns of twisted silicene multilayers. In this work, a single resonance in STS that has a Kagome pattern in dI/dV maps is attributed to the flat and Dirac bands of the lattice. This assignment is supported by density functional theory (DFT) calculations and the observation of an edge state as well as of higher energy bands that have a hexagonal pattern.

The pattern observed in the dI/dV maps of Fig. 8.21 is in very good agreement with the experimental data of [128] and the corresponding DFT calculations. It seems therefore reasonable that the broad resonance between $V_{\text{bias}} = 1.4$ mV to $V_{\text{bias}} = 1.9$ mV corresponds to the Kagome bands of Fig. 8.21a. Nevertheless, we note that we do not observe higher energy bands with a hexagonal pattern (i.e. localized above the holes of the Kagome lattice) nor the presence of an edge state. Yet in our case, the fermions involved in the lattice formation are single YSR states per site (see subsection I.2) while in [128] a local modulation of the potential leads to a scattering landscape that affects all electrons and creates an electronic Kagome lattice. It is therefore quite reasonable that in our case we do not observe higher energy bands and only those corresponding to the pure hopping model with one fermion per site. As a result, it seems that the observed YSR band observed in STS indeed corresponds the band structure of Kagome lattice. We also note that the size of undisturbed Kagome lattices within the molecular islands varies from one preparation to another and can involve several hundreds of molecules (see appendix Fig. 1 page 154), overcoming the usual limitation of systems obtained by atomic or molecular manipulation [31, 105, 107].

Still, we should mention that the tight-binding model with nearest neighbor hopping is a simplification of the hybridization model discussed in subsection II.2 (with periodic boundaries and assuming $S = 0$) for which it was shown in subsection II.3 that improvements were necessary. A better understanding of the driving mechanism behind the YSR coupling would help in this matter. In this perspective we now investigate in more detail the fingerprints of molecules that are not inside a Kagome lattice (i.e. with one or no neighboring Cl).

The dI/dV spectra of a set of molecules at the edge of an island (and thus of a Kagome lattice) are investigated in Fig. 8.22. As one can see in Fig. 8.22b (and the enhanced view of Fig. 8.22c), the majority of the molecules (blue spectra) show a sharp pair of resonances at relatively high bias voltages ($|V_{\text{bias}}| > 2$ mV). As explained above, these are assigned to single YSR states that are localized at each molecules and do not hybridize with neighbors. Interestingly, the energy of this pair of resonance varies from molecule to another and the

YSR band is actually present above one of the investigated molecule (red spectrum). The YSR state induced by this molecule thus hybridizes with its neighbor despite being a different environment (only one surrounding Cl adatom). Molecules inside a molecular island but not inside the Kagome lattice (either at the edge of the lattice or inside the Kagome holes) exhibit a similar behavior (see appendix II Fig. 2, Fig. 3): presence of a YSR state at high energy (except for a few molecules that exhibit it at zero energy - see red spectrum in Fig. 8.19d) but with variations in this energy position between molecules.

We have seen in section I.2 that the Cl adatoms influence the energy of the YSR states of the surrounding molecules. Here, it appears that the formation of Kagome lattices also affects the energy of the YSR state of neighboring molecules but in a non-homogeneous way. As one can infer from the red spectrum of Fig. 8.22, when the energy of this YSR state is low enough, it couples to the YSR band. Within an island, at domain boundaries, molecules having only one neighboring Cl adatom are often nearest neighbor of one another (see Fig. 8.19b). Yet, there is no clear sign of YSR hybridization between them (see appendix II Fig. 3). We can thus formulate two hypotheses for the YSR coupling mechanism. Either it is mediated by the Cl adatoms via, in all likelihood, a super-exchange interaction. Or, the YSR energy must be, prior to hybridization, in a given energy range to allow for a coupling. Indeed, it is shown in [223] that an enhanced antiferromagnetic interaction between YSR states occurs via their hybridization with the Cooper pair condensate. This interaction is thus all the more substantial when the YSR energy is close to the Fermi level. In both cases, an antiferromagnetic interaction is most likely to occur between molecules and we underline that this was indeed one of the proposed solution for the improvement of the coupling model in subsection II.3.

III. Magnetic fingerprints in the normal state of Pb

Since we observe a magnetic coupling in the superconducting state of the substrate we now want to determine if this translates to the formation of a Kondo lattice in the normal state of Pb. In this case, as explained in chapter 3 section II.3, two (three) energies scale compete with each other: the coupling of the impurities to the substrate and the coupling between impurities (as well as the temperature of the experiment). Similarly to what was done in the previous section, we first investigate the properties of the molecules in the building blocks of the Kagome lattice and in a second part those of the molecules inside the Kagome lattice. We find that the coupling of the impurities to the substrate dominates over the coupling between impurities but that there is no coherent coupling over the lattice, necessary for the formation of a heavy fermion band.

1. The Kondo effect inside the Kagome building blocks

In this subsection we focus on the properties of the molecules in the building blocks of the Kagome lattice (i.e. structures made out of a few triangular units) for which it was shown in section II that the YSR states of molecules with two neighboring Cl adatoms hybridize with one another.

Fig. 8.23a shows a topography of a structure in which three molecules have two neighboring Cl adatoms (same structure as in Fig. 8.11 and Fig. 8.12). The $\mathrm{d}I/\mathrm{d}V$ spectra recorded on a broad energy range above the molecules inside this structure (see Fig. 8.23b) are very similar to those recorded above the Kagome unit cell in which no YSR coupling takes place (see Fig. 8.6

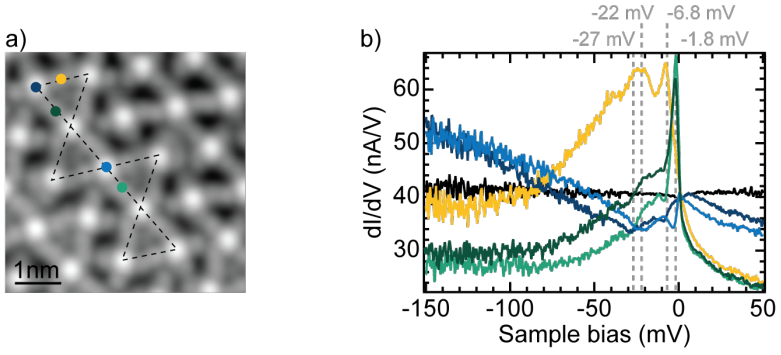

Figure 8.23.: a) Topography image ($V_{\text{bias}} = 5$ mV, $I = 200$ pA) with a structure in which three molecules have two surrounding Cl adatoms (see black dashed lines - same structure as in Fig. 8.11). b) Set of dI/dV spectra (feedback opened at $V_{\text{bias}} = 5$ mV, $I = 200$ pA and signal modulated with $V_{\text{rms}} = 500$ μeV) taken above the centers and ligands of the molecules in the structure as indicated by the dots in a. To quench superconductivity in the substrate, we applied an external magnetic field of 800 mT (a reference spectrum taken on Pb is shown in black).

and Fig. 8.7). Namely, molecules with one surrounding Cl adatom show a broad orbital above their ligand (yellow spectrum), a Kondo resonance at $V_{\text{bias}} = -6.8$ mV and a replica at $V_{\text{bias}} = -27$ mV (dark blue spectrum). Inside the structure, molecules with two surrounding Cl adatoms show also a broad resonance above their ligand (green spectra) with a shift of the Kondo resonance and its replica to $V_{\text{bias}} = -1.8$ mV and $V_{\text{bias}} = -6.8$ mV, respectively. The intensity of the broad resonance seen above the molecular ligand seems to decrease as the number of surrounding molecules with two neighboring Cl adatoms increases (yellow spectrum: 0 such molecule, dark green spectrum: 1 such molecule, light green spectrum: 2 such molecules) while the intensity of the Kondo resonance, inversely, increases. Similar results were obtained for all other investigated structures made out of a few triangular units.

In order to determine if the coupling of YSR states of the previous section translates into the formation of a Kondo lattice in the normal state, we now focus on the characteristics of the Kondo resonance seen above molecules with two neighboring Cl adatoms. Fig. 8.24a shows a topography image with a structure in which four molecules have two surrounding Cl adatoms (see black dashed lines) and for which the three possible molecular orientations with respect to the underlying Pb lattice are present (compare the orientations of the three molecules whose center are marked with a circle). dI/dV spectra taken in the normal state (external magnetic field of 600 mT) on a small energy range above three of these molecules with different orientations are shown in Fig. 8.24b along with a reference spectrum taken above the bare Pb substrate (grey spectrum). The three spectra are extremely similar and show the same interference pattern of the Kondo resonance that can be fitted with Frota-Fano functions [61] (see brown curves). We compare in Fig. 8.24c the intrinsic width of the resonance obtained from Frota-Fano fits of such dI/dV spectra taken above the Fe centers of molecules with two surrounding Cl adatoms in various Kagome building blocks. We sorted the data according to the number of coupled molecules in the superconducting state of Pb (x axis) and use a color code to identify their orientation with respect to the underlying Pb lattice. As one can see, we do not observe any dependence on either of these parameters: the intrinsic width of the resonance scatters around 1.5 meV. This confirms that all molecules with two surrounding Cl exhibit the same coupling strength between their magnetic center and the electrons of the substrate. This was implicitly assumed in the description of the

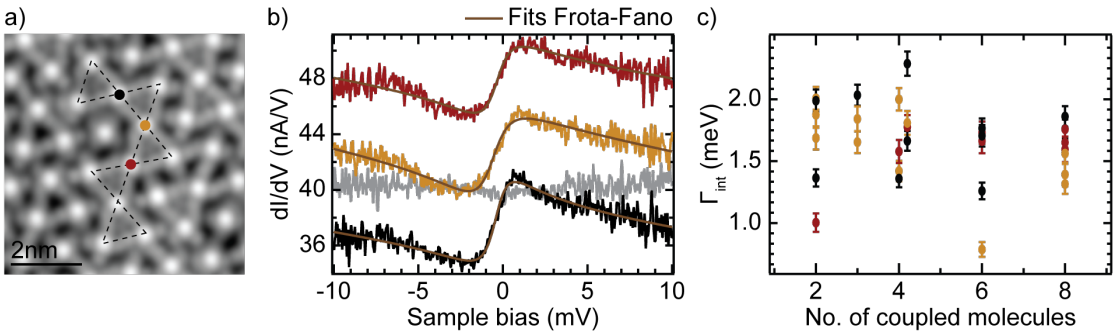

Figure 8.24.: a) Topography image ($V_{\text{bias}} = 5$ mV, $I = 200$ pA) of a structure in which four molecules have two surrounding Cl adatoms (see black dashed lines). The three molecules whose centers are marked with a dot have different orientation with respect to the underlying Pb substrate. b) $\mathrm{d}I/\mathrm{d}V$ spectra recorded above the centers of these three molecules with Frota-Fano fits in brown. To quench superconductivity, we applied an external magnetic field of 600 mT, a reference spectrum taken on Pb is shown in grey (feedback opened at $V_{\text{bias}} = 5$ mV, $I = 200$ pA and signal modulated with $V_{\text{rms}} = 50$ μeV). c) Intrinsic width of the Kondo resonances of molecules having two neighboring Cl adatoms extracted from Frota-Fano fits as shown in b. The data is sorted according to the number of coupled molecules in the superconducting state of Pb (x axis) and the color indicates the different orientations of the molecules as shown in a.

YSR hybridization in the previous section and is a pre-requisite for the formation of a Kondo lattice. Yet, this result does not give any indication pointing toward a coupling between the Kondo clouds of neighboring molecules.

In order to address this aspect more specifically we investigate in Fig. 8.25 the variations of the intensity of the Kondo resonance across a structure in which three molecules have two neighboring Cl adatoms (same structure as in Fig. 8.23, Fig. 8.11 and Fig. 8.12). The $\mathrm{d}I/\mathrm{d}V$ map of Fig. 8.25b is recorded with $V_{\text{bias}} = 0$ mV and while the tip follows the height profile of the topography image of Fig. 8.25a ($V_{\text{bias}} = 5$ mV, $I = 200$ pA). As a guide to the eye we indicate the structure with black dashed lines in both images. The $\mathrm{d}I/\mathrm{d}V$ signal is localized above the ligands of the three molecules with two neighboring Cl adatoms since this is where

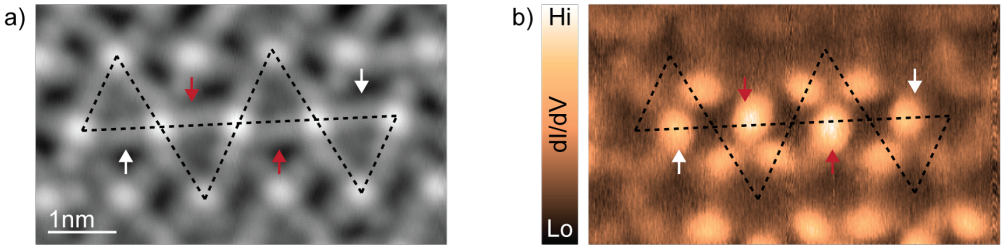

Figure 8.25.: a) Topography image ($V_{\text{bias}} = 5$ mV, $I = 200$ pA) of a structure with three molecule having two neighboring Cl adatoms (see black dashed lines - same structure as in Fig. 8.23, Fig. 8.11). b) $\mathrm{d}I/\mathrm{d}V$ map recorded at $V_{\text{bias}} = 0$ V (signal modulated with $V_{\text{rms}} = 500$ μeV) under an external magnetic field of $B = 800$ mT and following the height profile of the topography image in a.

the Kondo resonance is seen as a peak in $\mathrm{d}I/\mathrm{d}V$ at $V_{\mathrm{bias}} = -1.8$ mV. [1] Interestingly, we note that the intensity of the $\mathrm{d}I/\mathrm{d}V$ signal is higher between these molecules than above the parts of the ligands facing molecules at the edge of the structure (compare the lobes marked with red and white arrows).

We compare our results to those of [152] where the formation of a Kondo lattice was studied by investigating the evolution of the Kondo resonance upon the creation of a chain of Co adatoms on Ag(111). Similarly to our case, the width of the Kondo resonance is the same for single Co adatoms and when these are part of a chain. This shows that the Kondo coupling of the impurities to the substrate overcomes any type of magnetic coupling between the impurities. The emergence of a Kondo lattice is deduced from the intensity variations of the resonance that indicate a redistribution of the local DOS of the many-body state. For a Co dimer, the intensity of the resonance is enhanced in between the Co atoms while chains whose length are in a peculiar range show a clear increase of the Kondo resonance intensity at their ends. Employing a multi-impurity Anderson model, the authors show that the redistribution of the Kondo resonance intensity through the chains is due to the coherent screening of the magnetic impurities and that these chains are thus in the heavy Fermi liquid regime (see chapter 3 section II.3). The transition from the independent Kondo screening of the impurities to the heavy Fermi liquid phase is controlled by the inter-atomic distance and length of the chains.

Here, because we do not observe a splitting or broadening of the Kondo resonance when increasing the number of molecules that could couple with one another we can conclude that the coupling of the impurities to the substrate also overcomes any magnetic coupling between the impurities [104, 15, 215]. Indeed, an increase of the magnetic field (see appendix II, Fig. 4) or the temperature (see appendix II Fig. 5) does not affect the spectra of the molecules with two surrounding Cl adatoms differently than the ones with only one surrounding Cl adatom. The fact that we are in the regime of a strong coupling of the impurities to the substrate is consistent with the approach experiments (see chapter 6 and appendix II Fig. 3) in the superconducting phase that showed that the YSR states were in a screened-spin ground state. This also supports the omission of any direct interaction between the impurities in the theoretical description of the YSR hybridization in subsection II.2. We should now determine if the screening of the impurities is coherent, as in [152] (heavy Fermi liquid phase), or incoherent. The intensity variations in Fig. 8.25 do not allow to discard any scenario. Indeed, from [152] an increase of the intensity between the impurities could be the sign of a coherent coupling. Theoretical calculations would be necessary in order to know if this scenario is realistic given the inter-impurity distance and Fermi wavelength of the substrate. Yet, an incoherent screening of the impurities would also account for such an intensity distribution: when the tip is placed above a molecular ligand between two Kondo centers (red arrows in Fig. 8.25), the intensity increase can be accounted for by the sum of the two (independent and thus non-interfering) tunneling channels to the two Kondo resonances.

As explained in chapter 3 section II.3, in the Fermi liquid phase, a gap around Fermi should develop as the heavy fermion band is formed. Here, the limited number of impurities involved might hinder the observation of the gap (no gap was indeed observed in [152]), we therefore investigate next the properties of the molecules when a Kagome lattice is formed.

[1] The intensity distribution of the Kondo resonance is very similar to the one of the YSR states (summing over all coupled states). We describe in chapter 7 the correlations between the localization and lineshape variations of the two many-body states. Threfore, we do not further investigate these two aspects in this chapter.

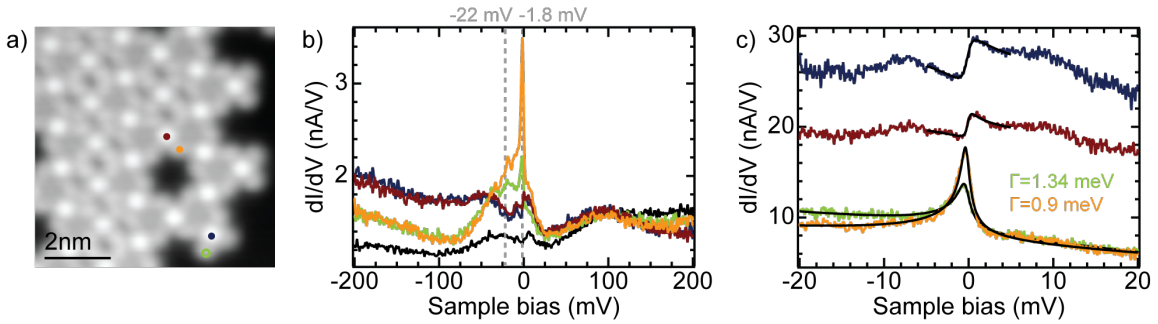

Figure 8.26.: a) Topography image ($V_{\text{bias}} = -45$ mV, $I = 30$ pA) of a molecular island in which a Kagome lattice is formed. b) dI/dV spectra (feedback opened at $V_{\text{bias}} = 200$ mV, $I = 300$ pA and signal modulated with $V_{\text{rms}} = 1$ mV) recorded above the centers and ligands of two molecules as shown in a. An external magnetic field of 200 mT was applied and a reference spectrum taken above Pb is shown in black (for the reference spectrum the magnetic field is 100 mT). c) dI/dV spectra (feedback opened above the ligand of the molecules -for both positions: center and ligand- at $V_{\text{bias}} = 20$ mV, $I = 150$ pA and signal modulated with $V_{\text{rms}} = 50$ μV) taken above the same positions as in b but recorded over a smaller energy range (still under an external magnetic field of 200 mT). The black curves are Frota-Fano fits and the Γ values are the width of the resonances extracted from the fits for the two different molecules.

2. The Kondo effect inside the Kagome lattice

We compare in Fig. 8.26 the properties of a molecule indside the Kagome lattice (two surrounding Cl adatoms - red spectra) to those at the edge of an island and thus also of the Kagome lattice (one surrounding Cl adatom - blue spectra). On a large energy range (Fig. 8.26), the two molecules have very similar characteristics. A broad resonance in the negative bias regime is seen above the ligand (orange and green spectra) and a Kondo resonance and its replica are seen at $V_{\text{bias}} = -1.8$ mV and $V_{\text{bias}} = -22$ mV, respectively. These results are comparable to those observed in the previous section except for the position of the Kondo resonance of the molecule at the edge of an island. Indeed, so far, molecules with only one neighboring Cl adatom have been shown to exhibit this resonance at $V_{\text{bias}} = -6.8$ mV (see Fig. 8.4, Fig. 8.7, Fig. 8.23). Yet, this shift of the Kondo resonance closer to the Fermi level is in accordance with the shift of the YSR state away from the gap edge in the superconducting state of Pb (see Fig. 8.19 and Fig. 8.22). Because the position of the Kondo resonance relates to the local electron-hole asymmetry of the system, this shift furthermore supports the conclusion of section I proposing that the presence of Cl adatoms leads to a charge redistribution at the interface between the molecular islands and the substrate.

Spectra recorded over a smaller energy range (Fig. 8.26) confirm the absence of a gap around the Fermi level. The two molecules have very similar dI/dV characteristics with the presence of a Kondo resonance that appears as a peak above the molecular ligands and rather like a step above the molecules' centers. A fit of the resonances with a Frota-Fano function indicates a larger width and thus stronger coupling for the molecule at the edge of an island. Beside these different widths, the two molecules behave similarly upon a change of temperature or external magnetic field (see appendix page 159 Fig. 7 and Fig. 6). The behavior of the Kondo resonance in the Kagome building blocks and Kagome lattice is thus very similar with only a shift in position for the moelcules with one neighboring Cl and a small decrease of the Kondo width in the lattice. A possible explanation for this small

decrease might again be that the charge distribution at the surface is affected as it would also affect the exchange coupling strength (see chapter 3 equation (8.11)).

All in all, our results indicate an incoherent screening of the magnetic impurities with independent Kondo clouds arranged in a Kagome lattice. In all likelihood, a decrease of the temperature is necessary to reach the heavy fermion limit with a coherent screening of the impurities. Besides the temperature, we know from the investigation of the YSR hybridization that the coupling between the impurities is most likely not mediated by the RKKY interaction. This may also contribute in decreasing the long range coherence of the Kondo screening that is necessary for the formation of a heavy fermion band.

IV. Conclusion and outlook

In this chapter, we have studied the coupling of magnetic impurities both in the superconducting and the normal case. In the first part, we have investigated the influence of different environments on the coupling of a single impurity to the substrate. In particular, we have shown that the presence of surrounding adatoms modifies this coupling by influencing the charge distribution at the interface between the molecular island and the surface. In the second part, we have investigated the hybridization of YSR states. The coupling between the YSR states induced by molecules with two surrounding Cl adatoms was demonstrated by the study of small structures which constitute building blocks of the Kagome lattice. A description of this coupling with a simple theoretical model yields a good agreement for the coupling of two and three YSR states. Yet, it has been shown that some of the assumptions had to be relaxed to account for the experimental data: we should consider either an antiferromagnetic coupling between the impurities (leading to frustration inside triangular arrangements of the molecules) or directional-dependent overlap, exchange and Coulomb integrals. Above the Kagome lattice, we observe a broad YSR band whose distribution agrees well with another STM work that studied the electronic Kagome band structure obtained in silicene multilayers. The origin of the coupling mechanism has been assigned either to a mediation by the Cl adatoms via a super-exchange interaction or to the hybridization of the YSR states with the Cooper pair condensate (this leads to an enhanced antiferromagnetic coupling when the YSR energy is close to the Fermi level). We have thus shown that, beyond atom manipulation, molecular self-assembly could be used in order to create complex long-range networks for the engineering of YSR coupling. Finally, we wanted to determine in the third section if this YSR hybridization translates into the formation of a Kondo lattice when the substrate is in its normal state. We found that the coupling of the magnetic impurities to the substrate overcomes any type of coupling between the impurities. Moreover, we established that the screening of the impurities is incoherent with the presence of independent Kondo clouds arranged in a Kagome lattice. A lowering of the temperature is most probably necessary in order to reach the transition to the heavy Fermi liquid phase. Yet, since the origin of the coupling between the impurities in the superconducting state of Pb is not mediated by a RKKY interaction, it could also be that the coupling mechanism itself hinders the formation of a delocalized heavy-fermion band.

Chapter 9

Conclusions

In this thesis we have investigated the properties of porphine molecules on a Pb(111) substrate by means of scanning tunneling microscopy (STM), scanning tunneling spectroscopy (STS) and atomic force microscopy (AFM). We studied the mechanisms that dictate their electronic and magnetic properties and tried to take advantage of them in order to tune various types of interactions.

First, we characterized the molecular self-assembly of iron-porphine (FeP) molecules after sublimation of FeP-Cl molecules on a Pb(111) substrate. By investigating the preparations obtained after deposition on cold and warm surfaces, with and without a post-annealing, we were able to identify different molecular phases. We have shown that the formation of these different phases are related to different FeP/Cl ratio on the surface and established that the most stable arrangement is obtained when this ratio is between 1/2 and 2/3. There, the Cl adatoms and FeP molecules form a Honeycomb-Kagome lattice (referred to as Kagome lattice for simplicity). Importantly, the formation of these different phases generate various surroundings for the FeP molecules that affect both their electronic and magnetic properties. The rest of the thesis is devoted to their specific study.

Second, we studied the electronic properties of the FeP molecules in the molecular phase obtained when the FeP/Cl ratio is lower than 1/2. In this phase, we have identified at low bias voltages two types of molecules, bright and dark. Using AFM we verified that the origin of these two types is not due to a chemical modification of some of the molecules but was related to differences in their charge distributions that are then reflected in distinct electronic properties. The random distribution of Cl adatoms throughout the molecular islands was found to be most likely at the root of this diversity. Furthermore, we observed quite some diversity in the fingerprints displayed by dark molecules in STS. There again, this diversity was attributed to the non homogeneous influence of Cl adatoms within the island. We studied in detail one of these fingerpints: the occurence of oscillations in the $\mathrm{d}I/\mathrm{d}V$ spectrum of some molecules. Based on a model that we proposed in the first chapter in order to explain the detection of charging rings in STS, we ascribed these oscillations to the manifestation of local gating effects. More precisely, we introduce a model in which the numbers of image potential states is modulated by the electric field of the tip. Thereby we demonstrated that molecules directly adsorbed on a metal substrate can still be gated by an STM tip.

The remainder of this thesis was then dedicated to the study of magnetism and superconductivity. We started by investigating single Yu-Shiba-Rusinov states. Most precisely, taking advantage of the molecules' flexibility, we were able to tune the energy of a YSR state and

by considering the forces at hand, we identified the ground state of the system. Moreover, this approach experiment allowed for the tuning of the system through the quantum phase transition (QPT), from a screened- to a free-spin ground state, and we could highlight its hallmark characteristics in STS: as the YSR state energy crosses the Fermi level, the electron and hole weights of the excitation spectrum exhibit discontinuous changes, which are reflected in a reversal of the YSR asymmetry. Finally, we investigated the different types of transport processes that occur through the junction as its conductance is increased and showed that the YSR state could be excited not only by single electrons but also by multiple Andreev reflections.

Then we focused on another aspect of the YSR state: the spatial variations of its asymmetry. Studying iron-tetra-pyridyl-porphyrin (FeTPyP) molecules on Pb(111), we established that there is a clear correlation between the spatial variations of the YSR state these molecules induce on a superconducting substrate and the spatial variations of the lineshape of the Kondo resonance induced on a metallic substrate. Interestingly, these distributions and their variations are very similar to the relative local weights of the highest occupied molecular orbital (HOMO) and lowest unoccupied molecular orbital (LUMO) of the molecules. We therefore proposed that these orbitals serve as intermediate states in the scattering of electrons onto the impurity level. We argued that such a model would lead to a local modulation of the electron-hole asymmetry of the scattering events, leading in the end to the observed sign reversal of the YSR asymmetry and Frota-Fano interference factor from the molecular ligand to the Fe center.

Finally, we investigated in FeP molecules the magnetic coupling of YSR states in the Kagome lattice. We first characterized the influence of neighboring molecules and Cl adatoms on the magnetic fingerprints of the molecules. We found that inside an island, when the molecules have exactly two Cl adatoms in their direct surroundings, they generate a YSR state well inside the superconducting gap. The small building blocks of the Kagome lattice exhibit a clear hybridization of the YSR states of such neighboring molecules. Using a model reported in literature to describe this YSR hybridization, we could reproduce partially the experimental data. The limitations of the model indicate that the coupling of the molecules is either anisotropic or antiferromagnetic. We also established that this coupling was mediated either by a superexchange interaction via the Cl adatoms or by an hybridization of the YSR states with the Cooper pairs condensate. The YSR band formed in large Kagome domains was found to agree well with a previous STM experiment reporting on the observation of the electronic Kagome flat band on silicene multilayers. All in all, this study proved that molecular self-assembly is a good alternative to atom or molecular manipulation in order to engineer well-defined networks in which YSR couple. Finally, we described the magnetic fingerprints of the molecules when the Pb(111) substrate is in its normal state and discussed the requirements for the emergence of a Kondo lattice.

In a nutshell, this research work shed more light onto the fundamental mechanisms that govern the electronic and magnetic properties of molecules on superconductors. We have highlighted that these depend on the fine details of the molecules' environment and can be influenced by the presence of an STM tip.

Appendices

Additional information for molecules in the mixed phase

I. Bright/Hybrid molecule displaying oscillations

In this section, we show that the oscillations characterized in chapter 5 have also been observed above a bright molecule at the edge of an island. It is not clear if this is due to the presence of an impurity but we present the observed features in order to give an exhaustive description of the oscillations.

The molecule of interest is indicated by an arrow in the topography images of Fig. 1a. It is localized at the edge of an island and is surrounded by a bright and two dark molecules. One of these neighboring dark molecules is at the edge of the island which is unusual and might indicate the presence of an impurity that we have not yet identified. The three topography images in Fig. 1b-d are taken under the very same conditions, but one can see that the molecule has a different appearance in Fig. 1c. More precisely, it is in this case an hybrid molecule with its right corner appearing dark. The change of appearance between Fig. 1b and Fig. 1c was caused by a small tip forming resulting in a modification of the tip apex. The second change from the hybrid appearance (Fig. 1c) to a bright type (Fig. 1d) was provoked by a tip approach toward the center of the molecule, as shown later in this paragraph. In Fig. 1e we show the $\mathrm{d}I/\mathrm{d}V$ spectra recorded above the center of the molecule in these three different cases. In the three cases, the molecule exhibits the same features as presented in Fig. 5.5a: a broad orbital crossing Fermi energy localized on the center and a sharp resonance

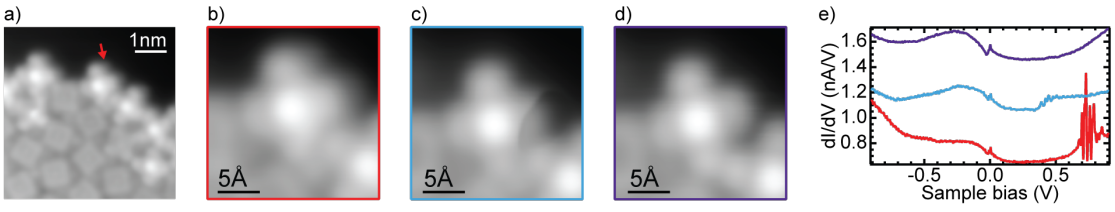

Figure 1.: a) Topography image ($V_{\mathrm{bias}} = 5$ mV, $I = 200$ pA) of a molecular island with an arrow indicating the investigated molecule. b-d) Topography image of the same molecule with the same set point ($V_{\mathrm{bias}} = 5$ mV, $I = 200$ pA) but with different tip apexes (b and c) and before and after a switch of the molecule from hybrid (c) to bright (d). e) $\mathrm{d}I/\mathrm{d}V$ spectra taken above the center of the molecule in the different cases b to d (feedback opened at $V_{\mathrm{bias}} = 900$ mV, $I = 300$ pA and signal modulated wit $V_{\mathrm{rms}} = 5$ mV, the spectra are offset for clarity and their colors refer to the frame colors of the topography images).

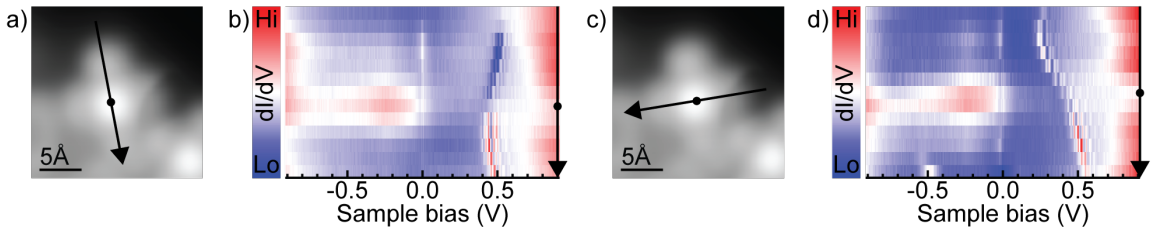

Figure 2.: a) and c) Topography images of the investigated molecule ($V_{\text{bias}} = 5$ mV, $I = 200$ pA). c) and d) Sets of dI/dV spectra (feedback opened with $V_{\text{bias}} = 900$ mV, $I = 300$ pA and signal modulated with $V_{\text{rms}} = 5$ mV) taken along the line shown in the topography image in a) and c), respectively.

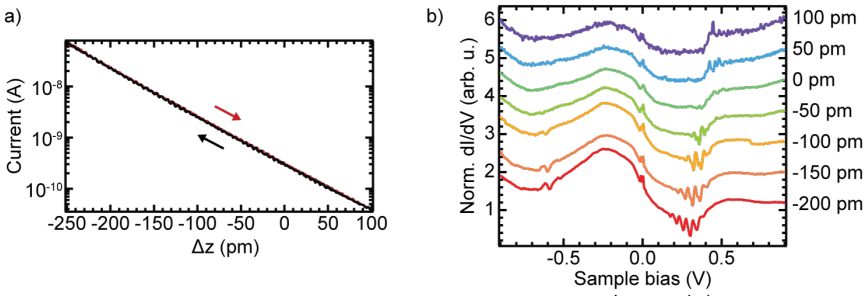

Figure 3.: Tip approach above the center of the molecule shown in the topography images of Fig. 111. a) Evolution of the current (applied bias $V_{\text{bias}} = 900$ mV) with tip offset Δz (feedback opened at $V_{\text{bias}} = 900$ mV, $I = 300$ pA). b) Set of dI/dV spectra normalized to their conductance at $V_{\text{bias}} = 900$ mV at different tip offsets as indicated next on the right of the spectra (spectra are offset for clarity, feedback opened at $V_{\text{bias}} = 900$ mV, $I = 300$ pA and signal modulated with $V_{\text{rms}} = 5$ mV).

at zero bias assigned to a Kondo resonance. However, the spectra differ quite strongly in the positive bias regime: the red and blue spectra show oscillations while the violet one does not. Moreover, we notice that the oscillations of the red and blue spectrum are at different energies and have different intensities the model proposed in chapter 5 that relate these feature to a local gating due to the electric field of the tip.

The spatial variations of the oscillations of the molecule in a hybrid state (Fig. 1c) is investigated in more details in Fig. 2. There, we show in Fig. 2b and Fig. 2d as 2D color-plots the evolution of the dI/dV spectra taken along the lines shown in Fig. 2a and Fig. 2c, respectively. In both cases we see that the position of the oscillations shift with the tip position. More precisely, when the tip is placed above the right corner of the molecule, these oscillations appear at the lowest energy. Here, we note that the tip position was stabilized with $V_{\text{bias}} = 900$ mV and $I = 300$ pA before opening the feedback for each spectrum. The absolute height of the tip with respect to the sample plane changes thus from one spectrum to another. This height modulation makes it harder to relate the shift of the oscillations position to variations of the electric field but one can still recognize a similar dispersion as in Fig. 5.13. Furthermore, we see in Fig. 2d that the oscillations change progressively from a series of peaks to one of dips as the tip is moved from the lowest corner to the top corner of the corner. This behavior is quite similar to the reversal of the rings' intensity observed in Fig. 5.12d.

Finally, we show in Fig. 3 the evolution of the electronic fingerprint above the center of the

molecule with the tip height. In Fig. 3a, we show the evolution of the current with the tip height that ensures the stability and reproducibility of the experiment. Similarly to Fig. 5.7 and Fig. 5.14, we stay in the tunneling regime throughout the approach. The evolution of the $\mathrm{d}I/\mathrm{d}V$ spectra is shown in Fig. 3b (the spectra are normalized to their conductance at $V_{\mathrm{bias}} = 900$ mV). When the tip is far away form the molecule a peak is barely visible around $V_{\mathrm{bias}} = 450$ mV, it is progressively replaced by a series of dips that developed at lower energies when the tip is brought closer to the molecule. Taking a spectrum with $\Delta z = -250$ pm resulted in the switching of the molecule back to a bright type (see topography image of Fig. 1D) that do not show the oscillations features anymore.

Because these oscillations have a very similar behavior to the one of those observed above dark molecules we argue that they should be caused by the same effect: a local gatinf by the electric field of the tip via a modification of the number of image potential states.

II. Magnetic properties of the molecules

We now characterize the magnetic properties of the bright and dark molecules.

We first analyze the spectra obtained above bright molecules. We display in Fig. 4a $\mathrm{d}I/\mathrm{d}V$ spectra recorded above the center (red) and ligand (blue) of a bright molecule as shown in the topography image of Fig. 4a. Both the center and the ligand of the molecule show the presence of multiple resonances inside the superconducting gap of Pb (a reference spectrum taken on bare Pb is shown in black). These can be assign to two and three Yu-Shiba-Rusinov (YSR) states above the center and ligand of the molecule, respectively (as explained in chapter 6 we measure the $\mathrm{d}I/\mathrm{d}V$ spectra with a superconducting tip so that the resonances below $V_{\mathrm{bias}} = \pm 1.35$ mV are assigned to thermal excitations).

In order to explain the origin of these different number of YSR states we show in Fig. 4c and d the evolution with tip height of the $\mathrm{d}I/\mathrm{d}V$ spectra above the center and ligand of the molecule, respectively. The spectra are normalized to their conductance at $V_{\mathrm{bias}} = 5$ mV and we define $\Delta z = 0$ pm as the distance at which the feedback was opened with $V_{\mathrm{bias}} = 5$ mV, $I = 200$ pA (note that this corresponds to different absolute height of the tip with respect to the Pb surface for the two approach sets). As one can see, when the tip is far away the spectra are similar with two pairs of resonances, labeled α and β, at ± 1.55 mV and ± 2.35 mV. As the tip is brought closer, the energy of the YSR states change but not in a uniform way. This change in energy under tip approach is due to the deformation of the molecule as is explained in details in the next chapter. Above the center, the α YSR state shifts away from Fermi energy while the β resonance shifts first away from the gap edge and then back toward it (from $\Delta z = -20$ pm to $\Delta z = -60$ pm). Above the ligand, the α YSR state stays at the same energy while the β YSR state shifts significantly toward Fermi energy. Additionally, at $\Delta z = 15$ pm, a third SYR state, labeled γ is seen emerging from the gap edge and shifting toward Fermi energy. Interestingly, in both cases, the YSR states seem to vanish as the tip is brought close to the molecule: around $\Delta z = -60$ pm for the center position and around $\Delta z = -30$ pm for the ligand position. As one can see from the $I - Z$ curves of Fig. 4e, this vanishing of the YSR states correlate to a drop in the current above the center and a plateau above the ligand. The origin of this behavior might be caused by a switching of the molecule to a dark type (as we will see in the following, these do not induce YSR state) but is outside the scope of this thesis.

Several phenomena lead to the appearance of multiple YSR states: coupling of single YSR states [182, 31, 107], magnetic anisotropy in the case of spin systems higher than 1/2 [82], presence of several unpaired electrons that couple individually to the substrate [150, 180], or detection of multiple scattering channels with different angular momentum ($l = 0$, $l = 1$,

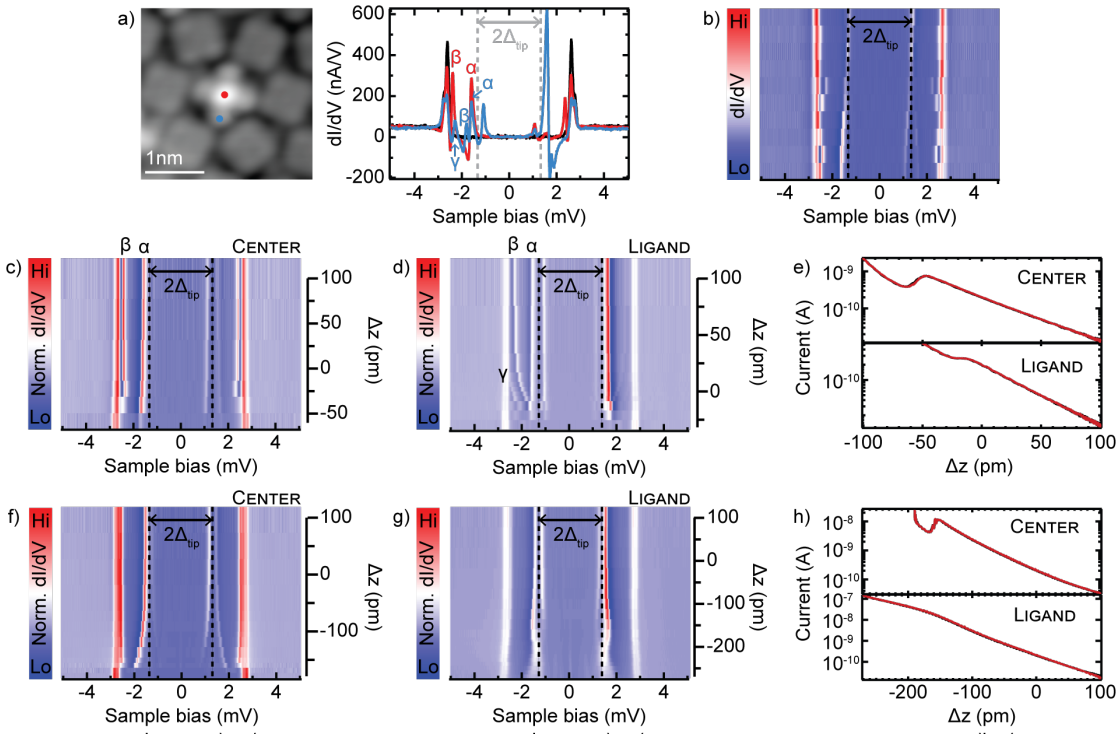

Figure 4.: a) Sepctra taken with a superconducting above the center (red) and ligand (blue) of a bright molecule along with a reference spectrum taken above the bare Pb surface (feedback opened at $V_{\text{bias}} = 5$ mV, $I = 200$ pA and signal modulated with $V_{\text{rms}} = 15$ μeV) b) Set of spectra taken above the center of bright molecules that do not have bright neighbor. The spectra are sorted arbitrarily according to the energy of the α YSR state. c-d) Set of spectra normalized to their conductance at $V_{\text{bias}} = 5$ mV taken at different tip offsets (feedback opened at $V_{\text{bias}} = 5$ mV, $I = 200$ pA and signal modulated with $V_{\text{rms}} = 15$ μeV) above the center and ligand of the molecule shown in the topography image in a). e) Evolution of the current with tip offset Δz above the center and liagnd of the same molecule. f-h) Similar experiment as in c-d) but performed above another bright molecule, that does not have any bright nearest neighbor.

etc.) from the substrate [56]. Since no bright molecule is in the direct surroundings of the investigated molecule (in Fig. 4) and since the dark molecules do not show YSR states (see Fig. 5 and following discussion) a coupling between YSR states seems unlikely. In order to test the other hypothesis we compare in Fig. 4b dI/dV spectra taken above the center of other bright molecules that do not have any bright molecule as a nearest neighbor. The spectra are arbitrarily sorted according to the energy of the α YSR state. We do not see any correlation of this energy to the β YSR state position. Therefore we can dismiss the hypothesis of several scattering channels from the surface and the one of a high spin system with magnetic anisotropy. Indeed, it was shown in [58] that the expected trend cannot explain the variations in the energy position of the β YSR state neither for the three lowest spectra of Fig. 4 nor for the approach set shown in Fig. 4c. Multiple YSR states due to magnetic anisotropy are usually much closer in energy should shift in concerted manner, which does not appear to be the case for the α and β YSR states. It is thus more likely that these two YSR states arise form the independent coupling of two unpaired electrons. Approaching the tip toward to the center or the ligand of the molecule affects the coupling parameters of these unpaired electrons differently resulting in uncorrelated shift of the YSR states. Interestingly,

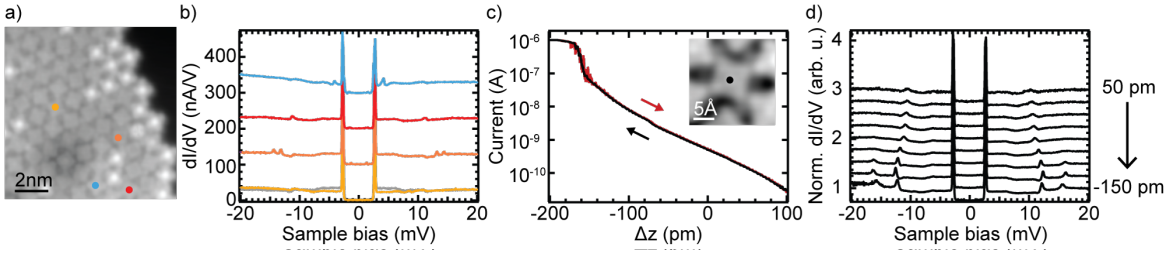

Figure 5.: a) Topography image ($V_{\text{bias}} = 20$ mV, $I = 500$ pA) of a molecular island. b) $\mathrm{d}I/\mathrm{d}V$ spectra (feedback opened at $V_{\text{bias}} = 20$ mV, $I = 500$ pA and signal modulated with $V_{\text{rms}} = 50$ μeV) taken above the centers of dark molecules as indicated in a). c) Evolution of the current with tip offset Δz (feedback opened at $V_{\text{bias}} = 20$ mV, $I = 500$ pA) above the center of the molecule shown in the inset. d) Set of $\mathrm{d}I/\mathrm{d}V$ spectra normalized to their conductance at $V_{\text{bias}} = 20$ mV taken above the center of the molecule shown in the inset of b and at different tip offsets Δz (feedback opened at $V_{\text{bias}} = 20$ mV, $I = 500$ pA and signal modulated with $V_{\text{rms}} = 50$ μeV).

the γ YSR state seems to follow the variations in energy of the β YSR state in Fig. 4d. This may be related to one of the two hypothesis discussed above (magnetic anisotropy or multiple scattering channels).

However, we also note that the behavior of the YSR states under tip approach vary rather significantly from one molecule to another. Fig. 4f and g show such evolution of the $\mathrm{d}I/\mathrm{d}V$ spectra recorded above the center and ligand of another bright molecule that does not have any direct bright neighbor. There, above the center, one can see that the variation in energy of the α YSR state is stronger than in Fig. 4c before vanishing at $\Delta z = -180$ pm. More noticeable are the differences in the tip approach performed above the ligand of the molecules: in Fig. 4g we do not observe a shift of the β YSR state nor the appearance of another YSR state upon approach but only variations of the α YSR energy. The evolution of the current above both molecules (shown in Fig. 4e and h is quite comparable, notably with a drop above the center of the molecule at close distance (small variations in the $I - Z$ curves above the ligands are most likely related to slight differences in the tip positions). All in all, these results indicate that the bright molecules have at least two unpaired electrons that are coupled to the superconducting substrate. Small variations in the surroundings of the molecules, most likely related to the presence of chlorine adatoms, seems to have an important impact on the energy position of the YSR states induced by these unpaired electrons.

We now investigate the magnetic fingerprints of dark molecules. Fig. 5b show four exemplary spectra recorded above dark molecules as shown in the topography image in Fig. 5a. A reference spectrum taken above the bare Pb(111) surface is also shown in grey. As one can see from the red and orange spectra, some molecules show pairs of symmetric peaks around Fermi energy and outside the superconducting gap that we attribute to inelastic spin excitation. Fig. 5d shows the evolution of the $\mathrm{d}I/\mathrm{d}V$ spectra above such a molecule upon tip approach (see topography image in the inset of Fig. 5c). When the tip is far away, one can distinguish a pair of small peaks at $V_{\text{bias}} = \pm 10.5$ mV. As the tip is brought closer, these peaks become sharper and shift slightly toward higher energy. Conjointly, a second peak starts to become visible at higher energy. When $\Delta z = -150$ pm, the two peaks appear to shift slightly back to Fermi energy. As mentioned above we assign these peaks to inelastic spin excitation: such peaks have been observed at similar energies for FeTPyP molecules on Pb(111) [3] and the energy shift with tip height seems to be in accordance with studies performed above Fe-OEP molecules on Pb(111) [88]. More precisely, the energy shift is caused by a modification of the

ligand field and resulting anisotropy parameters due to the small distortion of the molecule under the tip. As will be explained in details in the next chapter, at the beginning of the tip approach, the molecule is attracted to the tip which results in a decrease of the coupling strength between the magnetic impurity and the substrate. This leads to an increased lifetime of the excited states and explains the fact that the peaks becomes sharper upon tip approach. Because we observe up to two pairs of symmetric steps and since the molecule in gas phase has a spin 1 it is most likely that the spin state of the dark molecules is as well 1. The inelastic excitations would then correspond to the transitions $|m_s = 0\rangle \leftrightarrow |m_s = \pm 1\rangle$ in the case of a single peak and $|m_s = 0\rangle \leftrightarrow |+1\rangle \pm |-1\rangle$ (see chapter 3).

The behavior of the relative intensities of the two pairs of peaks in Fig. 5b is then quite peculiar: if the underlying excitation are $|0\rangle \rightarrow |+1\rangle - |-1\rangle$ and $|0\rangle \rightarrow |+1\rangle + |-1\rangle$ then the two peaks should have the same intensities. Yet, the second excitation is not visible at high tip-sample distance and remains slightly less intense than the first one at shorter distance. A possible explanation might lie in a stronger coupling of this excited state to the environment which then strongly decrease its lifetime and make it too broad to be detected. Indeed, in the case of Fig. 5d, the first excitation stays below 10 meV while the second one is above 13 meV so that the latter may couple to the second phonon band of Pb [213] while the former does not. In order to confirm this hypothesis further analysis should be performed since it appears that the energy of the inelastic excitations vary from one molecule to another. Furthermore, above some molecules, no clear peak is visible in the energy range of ± 20 mV as is demonstrated by the yellow spectrum of Fig. 5b. Finally, we mention that less than 1% of the investigated dark molecules show asymmetric peak in energy outside the superconducting gap (blue spectrum of Fig. 5b). An influence of the electric field on the excitation may be related to this difference in energy depending on the bias polarity but a more careful study should be carried out in order to explain this peculiar behavior.

All in all, we see that the magnetic fingerprints of the bright and dark molecules differ quite strongly and we note that the former have a much stronger coupling to the substrate than the latter since they display YSR states that are absent above dark molecules.

Deconvolution of dI/dV spectra

As explained in chapter 2 and 3, the use of a superconducting tip leads to a convolution of both tip and sample density of states (DOS) in the dI/dV spectra. We present here the numerical deconvolution procedure used to obtain the sample DOS from dI/dV spectra. This is done similarly to [32].

The tunneling current is given by equation 2.6 as in chapter 2

$$I \propto \int [f(\omega - eV) - f(\omega)]\rho_t(\omega - eV)\rho_s(\omega)d\omega \tag{1}$$

The differential conductance is thus the sum of two integrals.

$$\frac{dI}{dV} = \int -e[f(\omega - eV) - f(\omega)]\frac{\partial \rho_t}{\partial E}|_{E=(\omega - eV)}\rho_s(\omega)d\omega + \int -e\frac{\partial f}{\partial E}|_{E=\omega - eV}\rho_t(\omega - eV)\rho_s(\omega)d\omega, \tag{2}$$

These two integrals are of the form $\int K(\omega)\rho_s(\omega)d\omega$ with

$$K_1(\omega) = [f(\omega - eV) - f(\omega)]\frac{\partial \rho_t}{\partial E}|_{E=(\omega - eV)} \tag{3}$$

$$K_2(\omega) = \frac{\partial f}{\partial E}|_{E=\omega - eV}\rho_t(\omega - eV) \tag{4}$$

These integrals can be numerically approximated if the sampling on the energy ω is fine enough to capture the main features and if one chooses a cutting energy ω_{max} that is high enough: $\omega = [-\omega_{max} : d\omega : \omega_{max}] \quad \omega_i, i = 1...N$. Similarly, we discretize the voltage range over which the dI/dV spectra are recorded: $V = [-V_{max} : dV : V_{max}] \quad V_j, j = 1...M$.

The difference conductance is then a matrix product:

$$\frac{dI}{dV} = K \times \rho_s, \tag{5}$$

where $K = K_1 + K_2$ depends only on the tip DOS that we assumed to be BCS like (see equation 3.39).

The sample DOS is then obtained by pseudo-inverting the matrix K:

$$\rho_s = K^{-1} \times \frac{dI}{dV}, \tag{6}$$

To ensure the consistency of the deconvolution procedure we reconvolve the resulting DOS with the K matrix and verify that the obtained spectrum corresponds to the original dI/dV data.

Approach series

We present in this appendix approach series recorded above the centers of FeP molecules in various environments. As explained in chapter 6, if the FeP molecule carries a spin, such measurements affect its exchange coupling strength to the substrate electrons. This change of coupling strength is usually reflected in a shift of the corresponding Yu-Shiba-Rusinov (YSR) state.

Most of the approach series we present are thus shown to evidence the presence (or absence for Fig. 5) of a YSR state that is very close to the gap edge when the tip is far away. For all spectra, the feedback was opened at $V_{\text{bias}} = 5$ mV and $I = 200$ pA and the tip height varied by an offset Δz as indicated in the Figures ($\Delta z > 0$ corresponding to a tip retraction). All $\mathrm{d}I/\mathrm{d}V$ spectra are recorded with a modulation of the lock-in voltage by $V_{\text{rms}} = 15$ μeV. The spectra are normalized to their conductance at $V_{\text{bias}} = 5$ mV. The $I - Z$ curves are recorded under a bias voltage of $V_{\text{bias}} = 5$ mV.

Molecule out of an island

We first show the approach experiment performed above the Fe center of a molecule dragged out of an island as shown in the topography image of Fig. 1a. The six-fold symmetry of the molecule is attributed to its fast rotation as explained in chapter 8. The $I - Z$ curve of Fig. 1b shows that the approach experiment is stable and reproducible. The set of $\mathrm{d}I/\mathrm{d}V$ spectra recorded at various tip offsets Δz is shown as a 2D-color plot in Fig. 1c. As the tip is brought closer to the molecule, a YSR state shifts from the gap edge towards the Fermi level. For $\Delta z > -260$ pm the shift reverses back toward the gap edge which could indicate the crossing of the quantum phase transition (QPT) (see chapter 6, the intensity changes are unfortunately not clear within our resolution).

One triangular unit

We analyze in Fig. 2, the effect of a tip approach above the center of a molecule that is part of a triangular unit which constitutes the Kagome building block (see chapter 4). The triangular unit is indicated by black dashed lines in the topography image of Fig. 2 and a black dot indicates the position at which the approach experiment is carried out. The $I - Z$ curve of Fig. 2b shows that the approach is stable and reproducible. The set of $\mathrm{d}I/\mathrm{d}V$ spectra shown in Fig. 2c demonstrates the presence of a YSR state at the gap edge when the tip is relatively far away.

The Kagome unit cell

We now characterize the fingerprints of molecules that are part of a structure that consists of two triangular units (this is the Kagome unit cell, see chapter 4) as indicated by black dashed

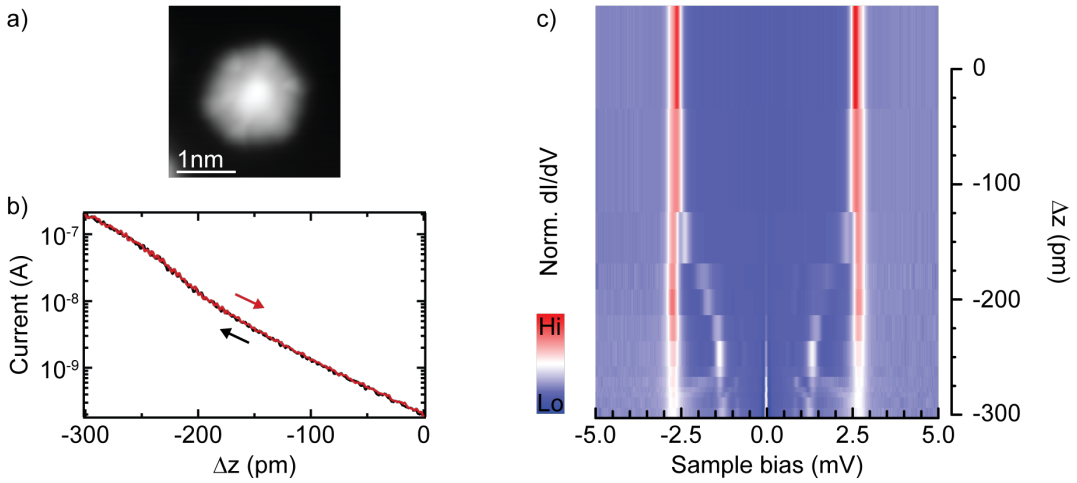

Figure 1.: a) Topography image ($V_{\text{bias}} = 5$ mV, $I = 200$ pA) of a molecule dragged out of an island. b) $I - Z$ curve recorded above its Fe center showing the stability of the experiment. c) Set of dI/dV spectra taken at different tip offsets Δz that show the presence of a YSR state close to the gap edge when the tip is (relatively) far away.

lines in the topography image of Fig. 3a. We first analyze the properties of the molecule that is surrounded by two Cl adatoms (its center is indicated by a black circle in Fig. 3a). The $I - Z$ curve recorded above its Fe center ensures the stability and reproducibility of the approach experiment. The set of dI/dV spectra shown in Fig. 3c shows that the YSR state at ± 1.9 initially shifts toward the Fermi level upon tip approach. This indicates that the YSR state is in a screened-spin ground state (see chapter 6). Importantly, no additionnal YSR state is seen shifting away from the gap edge. The assymetry of the coherence peaks at $\Delta z = 0$ pm (see chapter 8) is thus due to the background conductance.

In Fig. 4, we analyze the effect of a tip approach above the center of a molecule at the edge of the structure consisting of the Kagome unit cell (see black dashed lines and black dot in the topography image of Fig. 3a). Here again, the $I - Z$ curve shows that the tip approach is stable and reproducible. The set of dI/dV spectra of Fig. 4c show that a YSR state shifts away from the gap edge as the tip is brought closer.

FeP pure phase

We finally show the results for molecules in the phase in which no Cl adatom is present (see chapter 4, section II.4). In Fig. 5b we display the $I - Z$ curve recorded above the center of one of these molecules: the approach experiment is stable and reproducible. At $\Delta z = 0$ pm, no asymmetry of the coherence peaks is seen and upon approach we do not see the emergence of any YSR statea. The peaks seen at $\Delta z = -150$ pm and $\Delta = -200$ pm are caused by multiple Andreev reflections (see chapter 6, the grey dashed lines indicate $(\Delta_{\text{tip}} + \Delta_{\text{sample}})/n$ where $n = 2, 3, \ldots, 7$).

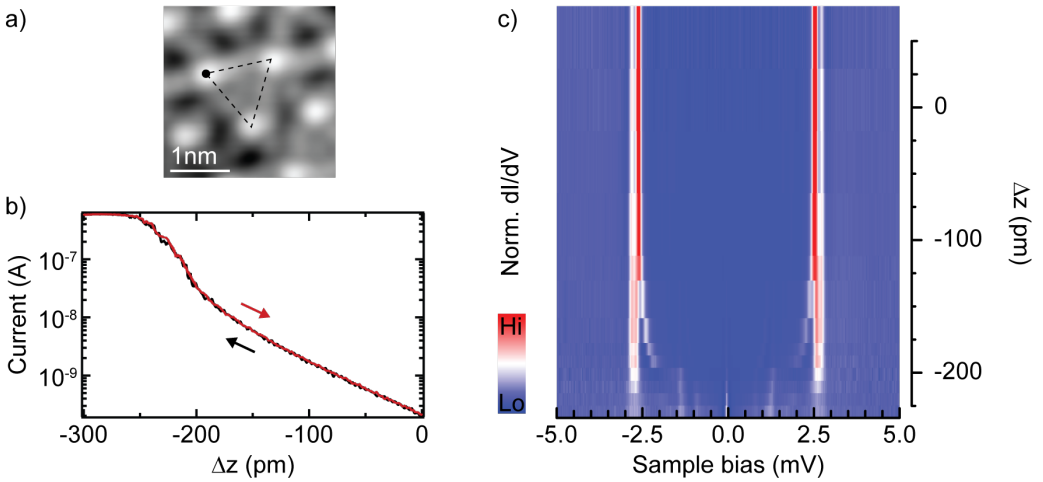

FIGURE 2.: Topography image ($V_{\text{bias}} = 5$ mV, $I = 200$ pA) of a triangular building block of the Kagome lattice, as indicated by black dashed lines (see chapter 4). b) $I - Z$ curve recorded at the position indicated by the black dot in a. c) Set of $\mathrm{d}I/\mathrm{d}V$ spectra recorded at the same position with different tip offsets that evidence the presence of a YSR state close to the gap edge when the tip is relatively far away.

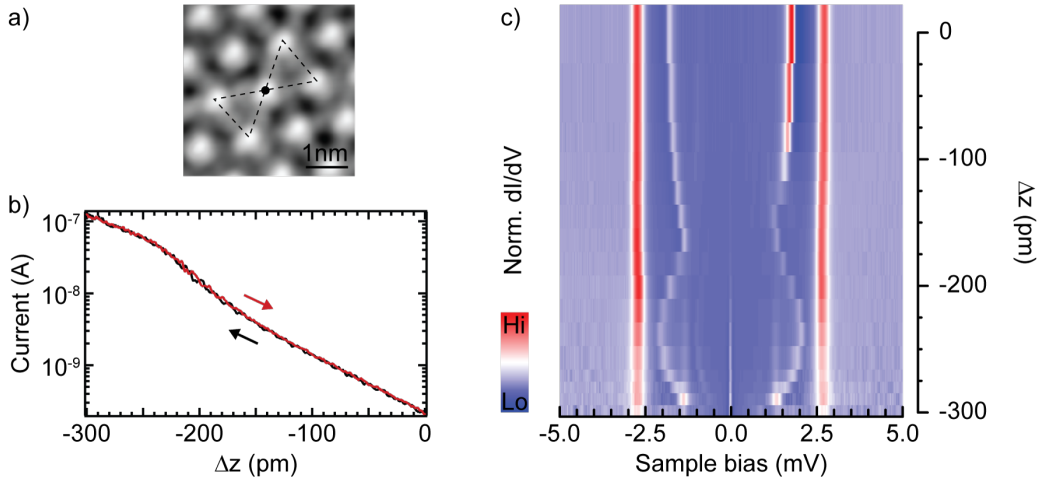

FIGURE 3.: a) Topography image ($V_{\text{bias}} = 5$ mV, $I = 200$ pA) with a structure that consists of the Kagome unit cell (see chapter 4), as indicated by black dashed lines. b) $I - Z$ curve recorded above the center of the central molecule of the structure, as indicated by the black circle in y. c) Set of $\mathrm{d}I/\mathrm{d}V$ spectra recorded above the same position that show that the YSR state is in a screened-spin ground state. Importantly, no additionnal YSR state is seen shifting from the gap edge.

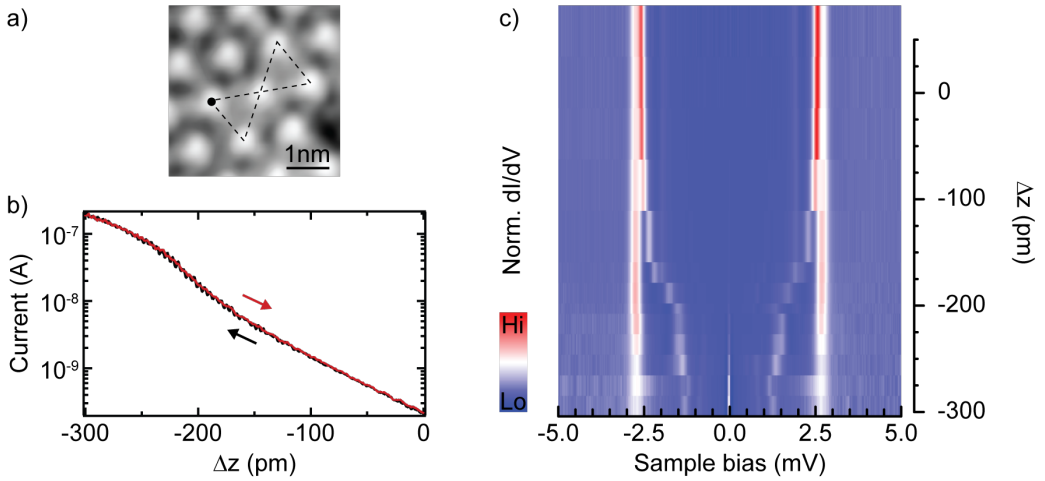

Figure 4.: a) Topography image ($V_{\text{bias}} = 5$ mV, $I = 200$ pA) of a structure consisting of the Kagome unit cell (see chapter 4). b) $I - Z$ curve recorded above the center of a molecule at the edge of the structure as indicated by the black circle in a. c) Set of $\mathrm{d}I/\mathrm{d}V$ spectra at different tip offsets Δz that show the presence of a YSR state at the gap edge at $\Delta z = 0$ pm.

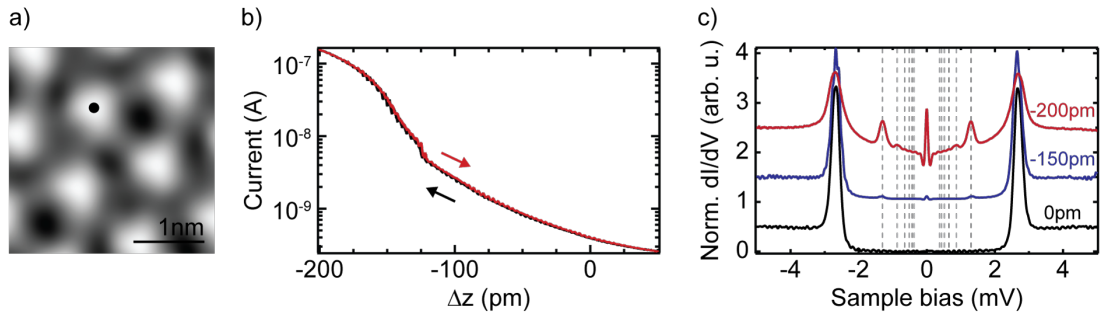

Figure 5.: a) Topography image ($V_{\text{bias}} = 5$ mV, $I = 200$ pA) of the molecular arrangement obtained when no Cl adatom is present (see chapter 4 section II.4). b) $I - Z$ curve recorded above the center of a molecule. c) $\mathrm{d}I/\mathrm{d}V$ spectra recorded at different tip offsets as indicated in the graph. The grey dashed lines indicate the position of the multiple Andreev reflections (see chapter 6).

Kagome lattice - additional information

I. Molecular assembly

The size of the Kagome lattices shown in the main part of this thesis are relatively small. We show in Fig. 1 a topography image of an island in which much larger Kagome domains are formed, as indicated by the red and blue lines in the top of the topography image. A fine tuning of the annealing temperature and post-cooling of the sample is probably necessary to optimize the growth of these large domains. Still, from these large domains it is clear that the molecular self-assembly described in chapter 4 is indeed a very good alternative (as compared to lateral manipulation of adatoms) for the growth of system in which Yu-Shiba-Rusinov (YSR) states are coupled (see chapter 8).

II. Magnetic fingerprints in the superconducting state

In chapter 8 we demonstrate that the YSR states induced by the molecules inside the Kagome lattice, i.e. with two neighboring Cl adatoms (see chapter 4), hybridize with one another and form YSR bands. Here, we show that the other molecules inside such islands (with one or no neighboring Cl adatoms) do not exhibit signs of YSR coupling.

In Fig. 2a we show a topography image of an island in which a Kagome lattice is formed (see black dashed lines) and whose holes are partially occupied by FeP molecules. These molecules have no Cl adatoms in their surroundings. In Fig. 2b we present the $\mathrm{d}I/\mathrm{d}V$ spectra recorded with a superconducting tip above three of these molecules (as indicated by dots in Fig. 2a) along with a reference spectrum taken above the bare Pb surface (black). They exhibit a YSR state very close to the gap edge (an enhanced view of the spectra is shown in the right panel), but with small variations in its energy from one moleule to another.

In order to study molecules at Kagome domain boundaries we show in Fig. 3b-f $\mathrm{d}I/\mathrm{d}V$ maps recorded while following the height profile of the topography image in Fig. 3a. In this topography image one can identify several Kagome lattice that are indicated with lines of different colors. The $\mathrm{d}I/\mathrm{d}V$ maps are taken with a superconducting tip so that $V_{\mathrm{bias}} = 1.34$ mV corresponds to the Fermi energy of the sample. At zero energy (Fig. 3b), the $\mathrm{d}I/\mathrm{d}V$ signal is intense above some of the domain boundaries (for instance in the left part of the image, between the red, orange and green lattices) but not all (*e.g.* the central part of the image between the red and violet lattices). At $V_{\mathrm{bias}} = 1.7$ mV, the signal is intense above the Kagome lattices and vanishes at the domain boundaries: this corresponds to a YSR band

as discussed in chapter 8. At higher energies, molecules at the edge of the island show a YSR state (see Fig. 3d), but here again with energy variations from one molecule to the other (see chapter 8 Fig. 8.22). The same is observed for molecules at domain boundaries within the island: for instance in Fig. 3f, a clear $\mathrm{d}I/\mathrm{d}V$ signal is detected between the red and blue lattices (top-right) but not between the blue and violet ones.

All in all this indicates that the presence of chlorine is crucial to enable the YSR coupling and other mechanisms than the Ruderman-Kittel-Kasuya-Yoshida (RKKY) coupling (see chapter 3 section I.2) have to be considered, as discussed in chapter 8.

III. Magnetic fingerprints in the normal state

Since the YSR states show a coupling inside the Kagome lattice, we are interested if a Kondo lattice forms in the normal state. This should then happen between molecules that have two neighboring Cl adatoms. Here, we show additional information that the Kondo resonance behaves the same upon a change of magnetic field or temperature, for molecules that should couple and those that should not.

1. Kagome building blocks

In Fig. 4, we investigate the Kondo effect in a structure with two molecules having two neighboring Cl adatoms (see black dashed lines). We compare the spectra taken above the center and ligand of one of these molecule (that might be coupled) to those taken above a molecule at the edge of the structure (which should show no sign of coupling). For both molecules, the spectra taken with an external magnetic field of 800 mT (black) and 3 T (red) are extremely similar.

We investigate in Fig. 5 a similar structure and analyze the temperature dependence of the $\mathrm{d}I/\mathrm{d}V$ spectra. Besides a broadening that can be fully explained by the Fermi-Dirac broadening, no change is observed in the $\mathrm{d}I/\mathrm{d}V$ lineshape. Both results seem to dismiss any type of coupling between the two molecules having two neighboring Cl adatoms.

2. Kagome lattice

To confirm the similarities between molecules that should couple and the ones that should not we study the temperature dependence of the Kondo resonances when the Kondo lattice is formed. The resonances are more intense and better resolved above the molecular ligands (see Fig. 6), we therefore use these positions to carry out the analysis. For each molecule investigated in Fig. 6b, we record a $\mathrm{d}I/\mathrm{d}V$ spectrum at various temperature and fit it with a Frota-Fano function. Fig. 6c shows one of the data set (lowest molecule at the edge - dark blue circle in Fig. 6a). As explained in chapter 7, equation 7.3, we extract the intrinsic width of the resonance and convert it to a Fano width [61]. The evolution of the Fano width of the resonances with temperature is shown in Fig. 6d (filled dots, the error bars correspond to the standard deviations of the fits and the different colors to the different positions as shown in Fig. 6) and can be fitted (solid lines) for all four molecules with [155, 231]:

$$\Gamma^{\mathrm{Fano}}(T) = 2\sqrt{(\alpha k_B T)^2 + (k_B T_K)^2} \tag{1}$$

where Γ^{Fano} is the full Fano width of the resonance, T the temperature, T_K the Kondo temperature and α a phenomenological fit parameter.

This confirms that the molecules at the edge of the island exhibit a stronger coupling to the substrate and also shows that the behavior for all molecules is very similar, discrediting the hypothesis of a coherent Kondo lattice.

Similarly, we show in Fig. 7 the evolution of the Kondo resonance under an external magnetic field. Here again, no difference is detected between the molecules, besides different width.

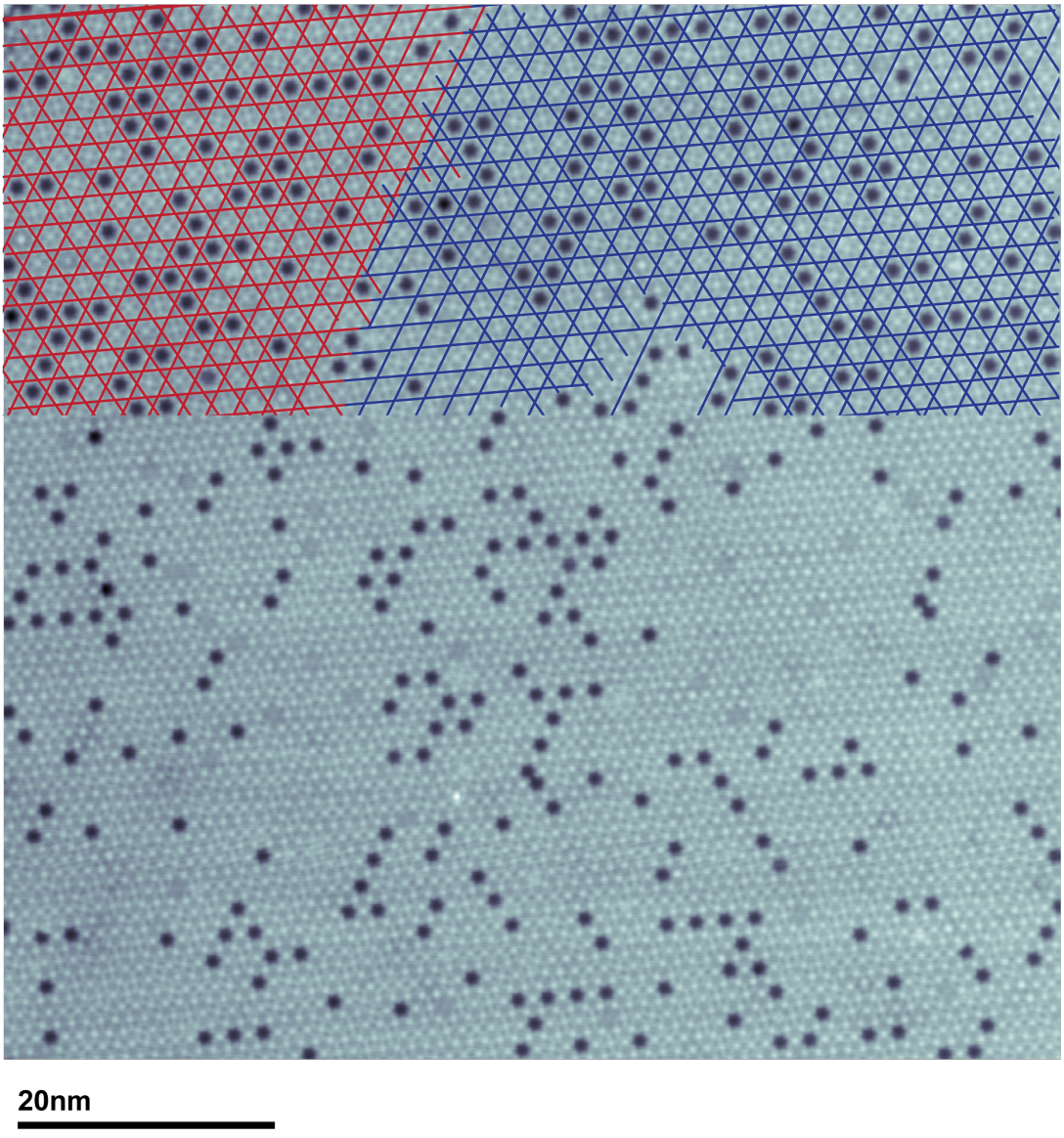

Figure 1.: Topography image ($V_{\text{bias}} = -45$ mV, $I = 30$ pA) of an island in which large Kagome domains are formed as indicated in the top part with blue and red lines.

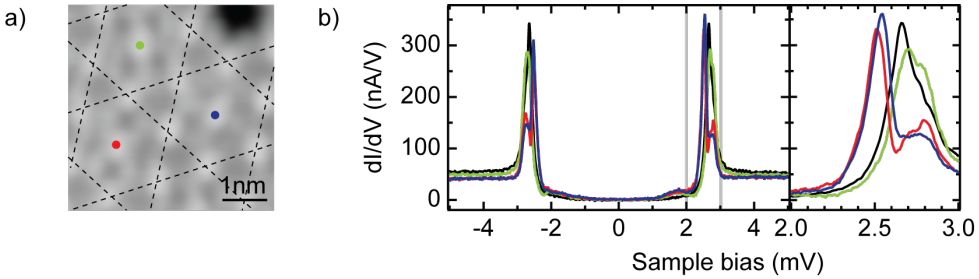

Figure 2.: a) Topography image ($V_{\text{bias}} = -45$ mV, $I = 50$ pA) of a molecular island in which the Kagome lattice (see chapter 4) is formed as indicated by the black dashed lines. b) $\mathrm{d}I/\mathrm{d}V$ spectra taken above molecules that occupy holes of the Kagome lattice as shown in a. The spectra are taken with a superconducting tip and a reference spectrum is shown in black (feedback opened at $V_{\text{bias}} = 5$ mV, $I = 200$ pA and signal modulated with $V_{\text{rms}} = 25$ μeV).

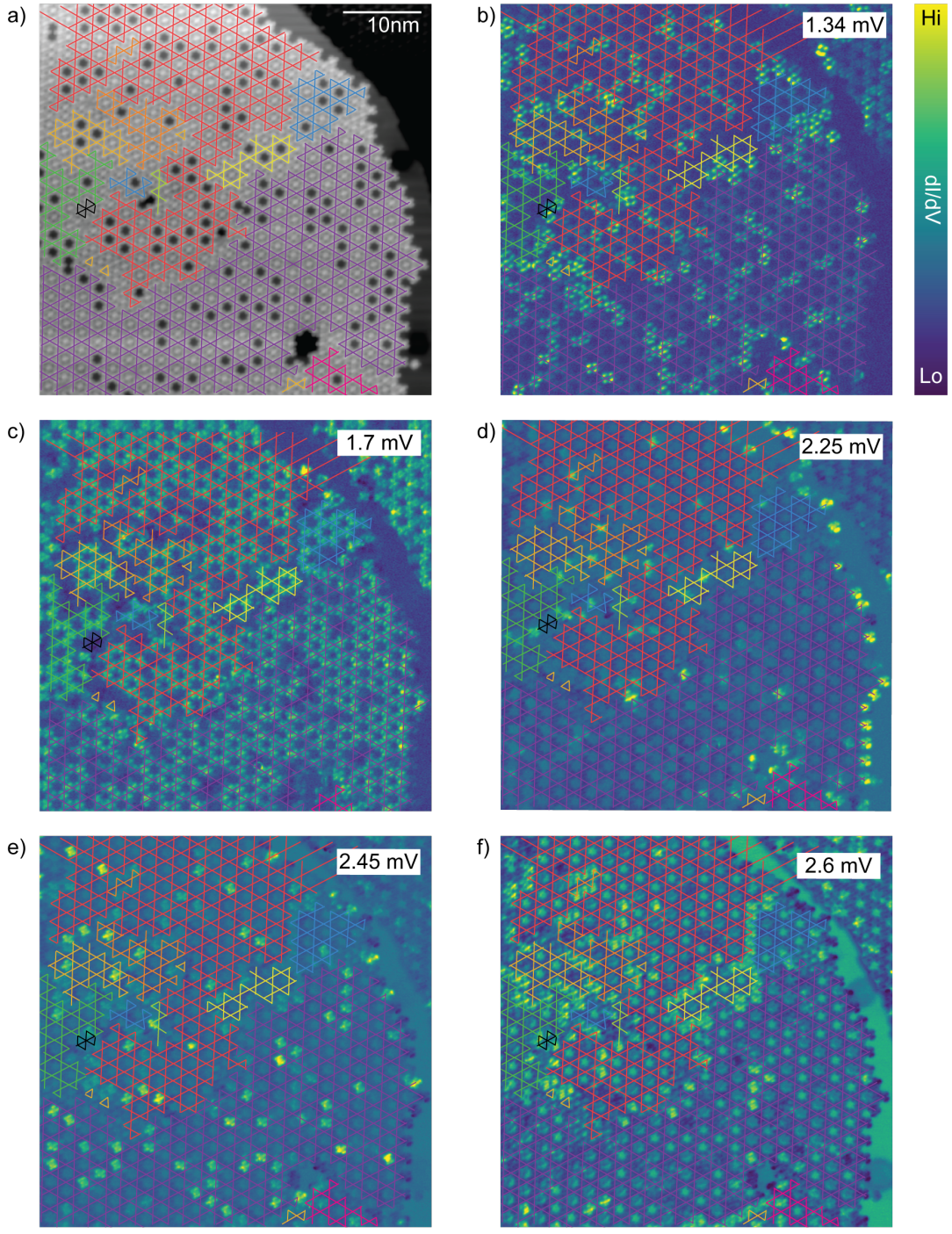

Figure 3.: a) Topography image ($V_{\text{bias}} = 5$ mV, $I = 50$ pA) of a molecular island in which several Kagome lattices can be identified, as indicated by color lines. b-f) $\mathrm{d}I/\mathrm{d}V$ maps ($V_{\text{rms}} = 25$ μeV) recorded with a superconducting tip ($V_{\text{bias}} = 1.34$ mV corresponds to the Fermi energy of the sample) following the height profile of the topography image of a. Domains boundaries show YSR states at various and diverse energies.

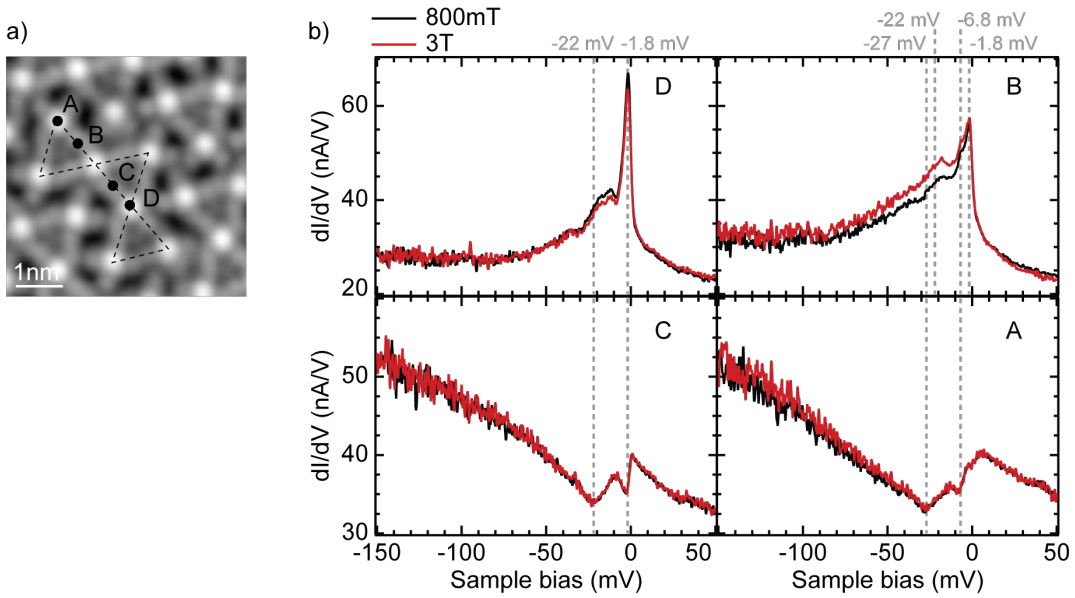

Figure 4.: a)Topography image ($V_{\text{bias}} = 5$ mV, $I = 200$ pA) of a structure with two molecules having two neighboring Cl adatoms (see black dashed lines). b) $\mathrm{d}I/\mathrm{d}V$ spectra (feedback opened at $V_{\text{bias}} = 5$ mV, $I = 200$ pA and signal modulated with $V_{\text{rms}} = 500$ μeV) taken above the centers and ligands of the molecules as indicated by the letters and under an external magnetic field of 800 mT (black), 3 T.

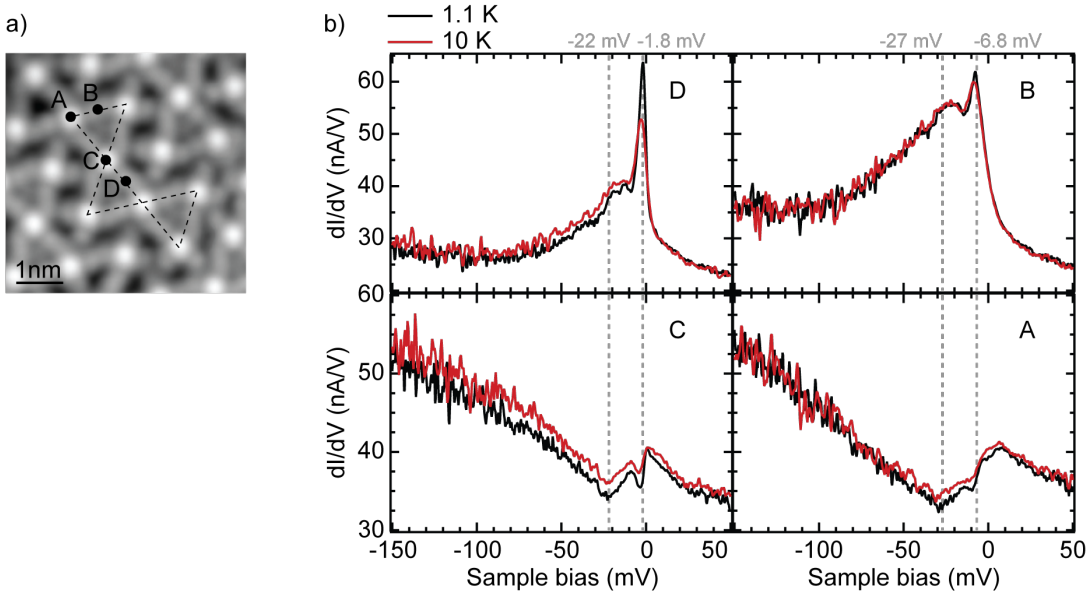

Figure 5.: a)Topography image ($V_{\text{bias}} = 5$ mV, $I = 200$ pA) of a structure with two molecules having two neighboring Cl adatoms (see black dashed lines). b) $\mathrm{d}I/\mathrm{d}V$ spectra (feedback opened at $V_{\text{bias}} = 5$ mV, $I = 200$ pA and signal modulated with $V_{\text{rms}} = 500$ μeV) taken above the centers and ligands of the molecules as indicated by the letters at 1.1 K (black) and 10 K (red).

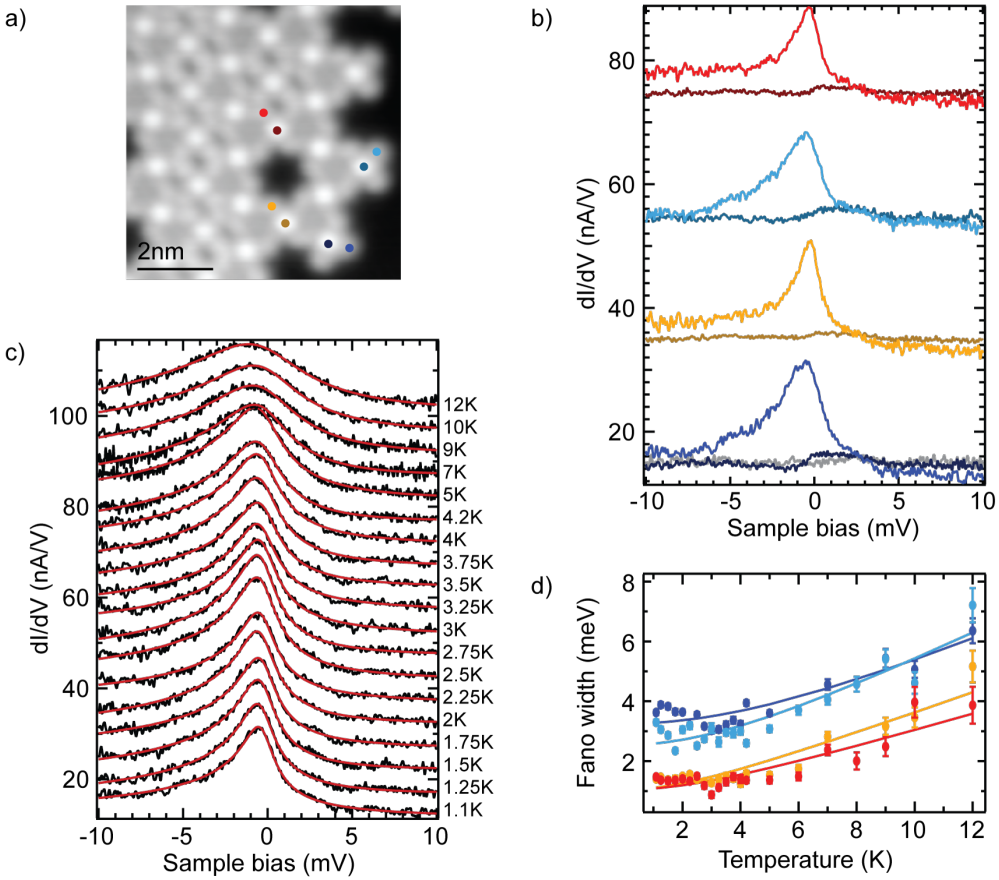

Figure 6.: a) Topography image ($V_{\text{bias}} = -45$ mV, $I = 30$ pA) of an island where the Kagome lattice is formed. b) $\mathrm{d}I/\mathrm{d}V$ spectra (feedback opened at $V_{\text{bias}} = 10$ mV, $I = 150$ pA and signal modulated with $V_{\text{rms}} = 50$ μeV) taken above the centers and ligands of molecules as shown a. Evolution of the Kondo resonance above the ligand of the lowest molecule in a (dark blue) with temperature with Frota-Fano fits in red. d) Evolution with temperature of the width of the Kondo resonance for the four molecules shown in a. Error bars are the standard deviation of the Frota-Fano fits and lines are fits of the data with $2\sqrt{(\alpha k_B T)^2 + (k_B T_K)^2}$ [155, 231].

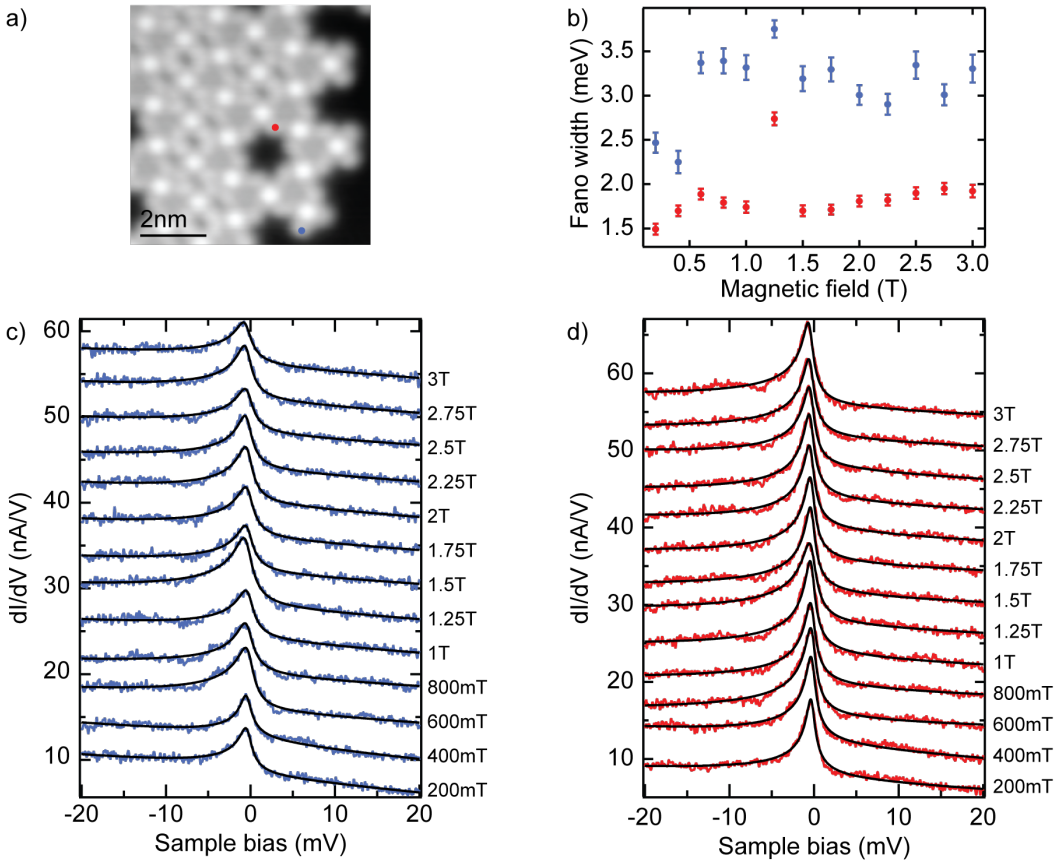

Figure 7.: a) Topography image ($V_{\text{bias}} = -45$ mV, $I = 30$ pA) of an island in which the Kagome lattice is formed. b) Evolution of the width of the Kondo resonance above the two positions shown a) as obtained from Frota-Fano fits of the sets of $\mathrm{d}I/\mathrm{d}V$ spectra (feedback opened at $V_{\text{bias}} = 10$ mV, $I = 150$ pA and signal modulated with $V_{\text{rms}} = 50$ μeV) displayed in c) and d).

Bibliography

[1] N. Abdurakhmanova et al. *Superexchange-mediated ferromagnetic coupling in two-dimensional Ni-TCNQ networks on metal surfaces*. Phys. Rev. Lett. **110**.2 (2013), p. 027202. DOI: 10.1103/PhysRevLett.110.027202 [cited on page 32].

[2] J. Adair, E. Suvaci, and J. Sindel. *Surface and Colloid Chemistry*. In: *Encyclopedia of Materials: Science and Technology*. Ed. by K. J. Buschow et al. Oxford: Elsevier, 2001, pp. 1–10. DOI: 10.1016/B0-08-043152-6/01622-3 [cited on page 17].

[3] G. Ahmadi. *Metal-organic networks and metal-porphyrins on superconducting Pb(111): structural, electronic and magnetic properties*. PhD thesis. Freie Universität, 2017 [cited on pages 89, 90, 93, 97, 143].

[4] G. Ahmadi and K. J. Franke. *Self-assembly of tetracyanonaphtho-quinodimethane (TNAP) based metal–organic networks on Pb (1 1 1): Structural, electronic, and magnetic properties*. Appl. Surf. Sci. **373** (2016), pp. 2–7. DOI: 10.1016/j.apsusc.2015.10.232 [cited on page 52].

[5] M. E. Ali, B. Sanyal, and P. M. Oppeneer. *Electronic structure, spin-states, and spin-crossover reaction of heme-related Fe-porphyrins: a theoretical perspective*. J. Phys. Chem. B **116**.20 (2012), pp. 5849–5859. DOI: 10.1021/jp3021563 [cited on pages 30, 49, 50].

[6] J. Alicea. *New directions in the pursuit of Majorana fermions in solid state systems*. Rep. Prog. Phys. **75**.7 (2012), p. 076501. DOI: 10.1088/0034-4885/75/7/076501 [cited on page 2].

[7] H. Alloul. *Physique des électrons dans les solides*. Vol. 1. Éditions de l'école Polytechnique, 2007 [cited on page 8].

[8] B. M. Andersen et al. *Nonequilibrium Transport through a Spinful Quantum Dot with Superconducting Leads*. Phys. Rev. Lett. **107**.25 (2011), p. 256802. DOI: 10.1103/PhysRevLett.107.256802 [cited on page 88].

[9] P. W. Anderson. *Localized magnetic states in metals*. Phys. Rev. **124**.1 (1961), p. 41. DOI: 10.1103/PhysRev.124.41 [cited on page 33].

[10] W. Auwärter et al. *Self-assembly and conformation of tetrapyridyl-porphyrin molecules on Ag (111)*. J. Chem. Phys. **124**.19 (2006), p. 194708. DOI: 10.1063/1.2194541 [cited on page 90].

[11] W. Auwärter et al. *Conformational adaptation and selective adatom capturing of tetrapyridyl-porphyrin molecules on a copper (111) surface*. J. Am. Chem. Soc. **129**.36 (2007), pp. 11279–11285. DOI: 10.1021/ja071572n [cited on page 90].

[12] W. Auwärter et al. *Controlled metalation of self-assembled porphyrin nanoarrays in two dimensions*. ChemPhysChem **8**.2 (2007), pp. 250–254. DOI: 10.1002/cphc.200600675 [cited on page 90].

[13] W. Auwärter et al. *Site-specific electronic and geometric interface structure of Co-tetraphenyl-porphyrin layers on Ag (111)*. Phys. Rev. B **81**.24 (2010), p. 245403. DOI: 10.1103/PhysRevB.81.245403 [cited on page 91].

[14] P. Aynajian et al. *Visualizing heavy fermions emerging in a quantum critical Kondo lattice*. Nature **486**.7402 (2012), p. 201. DOI: 10.1038/nature11204 [cited on page 39].

[15] P. Aynajian et al. *Visualizing the formation of the Kondo lattice and the hidden order in URu2Si2*. Proceedings of the National Academy of Sciences **107**.23 (2010), pp. 10383–10388. DOI: 10.1073/pnas.1005892107 [cited on pages 39, 132].

[16] J. Bardeen. *Tunnelling from a many-particle point of view*. Phys. Rev. Lett. **6**.2 (1961), p. 57. DOI: 10.1103/PhysRevLett.6.57 [cited on page 9].

[17] J. Bardeen, L. N. Cooper, and J. R. Schrieffer. *Microscopic theory of superconductivity*. Phys. Rev. **106**.1 (1957), p. 162. DOI: 10.1103/PhysRev.106.162 [cited on pages 39, 40].

[18] J. Bardeen, L. N. Cooper, and J. R. Schrieffer. *Theory of superconductivity*. Phys. Rev. **108**.5 (1957), p. 1175. DOI: 10.1103/PhysRev.108.1175 [cited on pages 39, 40].

[19] C. Barraclough, A. Gregson, and S. Mitra. *Interpretation of the magnetic properties of manganese (II) phthalocyanine*. J. Chem. Phys. **60**.3 (1974), pp. 962–968. DOI: 10.1063/1.1681174 [cited on page 32].

[20] J.-L. Basdevant and J. Dalibard. *Mécanique quantique*. Vol. 1. Éditions de l'école Polytechnique, 2012 [cited on page 7].

[21] S. Baumann et al. *Electron paramagnetic resonance of individual atoms on a surface*. Science **350**.6259 (2015), pp. 417–420. DOI: 10.1126/science.aac8703 [cited on page 1].

[22] P. Benioff. *Quantum mechanical Hamiltonian models of Turing machines*. Journal of Statistical Physics **29**.3 (1982), pp. 515–546. DOI: 10.1007/BF01342185 [cited on page 2].

[23] U. Berzinsh et al. *Isotope shift in the electron affinity of chlorine*. Phys. Rev. A **51**.1 (1995), p. 231. DOI: 10.1103/PhysRevA.51.231 [cited on page 108].

[24] S. Bhandary et al. *Correlated electron behavior of metal-organic molecules: Insights from density functional theory combined with many-body effects using exact diagonalization*. Phys. Rev. B **93**.15 (2016), p. 155158. DOI: 10.1103/PhysRevB.93.155158 [cited on pages 30, 49, 50].

[25] G. Binnig and H. Rohrer. *Scanning tunneling microscopy—from birth to adolescence*. Rev. Mod. Phys. **59**.3 (1987), p. 615. DOI: 10.1103/RevModPhys.59.615 [cited on page 1].

[26] Y. Cao et al. *Correlated insulator behaviour at half-filling in magic-angle graphene superlattices*. Nature **556**.7699 (2018), p. 80. DOI: 10.1038/nature26154 [cited on page 127].

[27] Y. Cao et al. *Unconventional superconductivity in magic-angle graphene superlattices*. Nature **556**.7699 (2018), p. 43. DOI: 10.1038/nature26160 [cited on page 127].

[28] C.-T. Chen. *Scanning tunneling spectroscopy studies of high-temperature cuprate superconductors*. PhD thesis. California Institute of Technology, 2006 [cited on page 14].

[29] X. Chen et al. *Probing superexchange interaction in molecular magnets by spin-flip spectroscopy and microscopy*. Phys. Rev. Lett. **101**.19 (2008), p. 197208. DOI: 10.1103/PhysRevLett.101.197208 [cited on page 32].

[30] X. Chen et al. *Conformational adaptation and manipulation of manganese tetra (4-pyridyl) porphyrin molecules on Cu (111)*. J. Chem. Phys. **146**.9 (2017), p. 092316. DOI: 10.1063/1.4974313 [cited on page 90].

[31] D.-J. Choi et al. *Influence of Magnetic Ordering between Cr Adatoms on the Yu-Shiba-Rusinov States of the β- Bi 2 Pd Superconductor*. Phys. Rev. Lett. **120**.16 (2018), p. 167001. DOI: 10.1103/PhysRevLett.120.167001. [cited on pages 46, 112, 113, 128, 141].

[32] D.-J. Choi et al. *Mapping the orbital structure of impurity bound states in a superconductor*. Nat. Commun. **8** (2017), p. 15175. DOI: 10.1038/ncomms15175 [cited on pages 94, 116, 145].

[33] E. Chulkov et al. *Lifetimes of image-potential states on copper surfaces*. Phys. Rev. Lett. **80**.22 (1998), p. 4947. DOI: 10.1103/PhysRevLett.80.4947 [cited on page 75].

[34] T. L. Cocker et al. *An ultrafast terahertz scanning tunnelling microscope*. Nat. Photonics **7**.8 (2013), p. 620. DOI: 10.1038/nphoton.2013.151 [cited on page 1].

[35] T. Costi. *Kondo effect in a magnetic field and the magnetoresistivity of Kondo alloys*. Phys. Rev. Lett. **85**.7 (2000), p. 1504. DOI: 10.1103/PhysRevLett.85.1504 [cited on page 110].

[36] M. F. Crommie, C. P. Lutz, and D. M. Eigler. *Confinement of electrons to quantum corrals on a metal surface*. Science **262**.5131 (1993), pp. 218–220. DOI: 10.1126/science.262.5131.218 [cited on page 1].

[37] D. Dai, H. Xiang, and M.-H. Whangbo. *Effects of spin-orbit coupling on magnetic properties of discrete and extended magnetic systems*. J. Comput. Chem. **29**.13 (2008), pp. 2187–2209. DOI: 10.1002/jcc.21011 [cited on page 31].

[38] W. De Haas and G. Van den Berg. *The electrical resistance of gold and silver at low temperatures*. Physica **3**.6 (1936), pp. 440–449. DOI: 10.1016/S0031-8914(36)80009-3 [cited on page 36].

[39] R. S. Deacon et al. *Tunneling Spectroscopy of Andreev Energy Levels in a Quantum Dot Coupled to a Superconductor*. Phys. Rev. Lett. **104**.7 (2010), p. 076805. DOI: 10.1103/PhysRevLett.104.076805 [cited on page 79].

[40] R. Deacon et al. *Tunneling spectroscopy of Andreev energy levels in a quantum dot coupled to a superconductor*. Phys. Rev. Lett. **104**.7 (2010), p. 076805. DOI: 10.1103/PhysRevLett.104.076805 [cited on page 44].

[41] D. van Delft and P. Kes. *The discovery of superconductivity*. Europhys. News **42**.1 (2011), pp. 21–25. DOI: 10.1051/epn/2011104 [cited on page 39].

[42] S. Doniach. *The Kondo lattice and weak antiferromagnetism*. Physica B+C **91** (1977), pp. 231–234. DOI: 10.1016/0378-4363(77)90190-5 [cited on page 38].

[43] V. Dose et al. *Image-potential states observed by inverse photoemission*. Phys. Rev. Lett. **52**.21 (1984), p. 1919. DOI: 10.1103/PhysRevLett.52.1919 [cited on page 75].

[44] D. Dougherty et al. *Tunneling spectroscopy of Stark-shifted image potential states on Cu and Au surfaces*. Phys. Rev. B **76**.12 (2007), p. 125428. DOI: 10.1103/PhysRevB.76.125428 [cited on page 75].

[45] R. Dynes, V. Narayanamurti, and J. P. Garno. *Direct measurement of quasiparticle-lifetime broadening in a strong-coupled superconductor*. Phys. Rev. Lett. **41**.21 (1978), p. 1509. DOI: 10.1103/PhysRevLett.41.1509 [cited on page 42].

[46] P. Echenique et al. *Image-potential-induced states at metal surfaces*. J. Electron Spectrosc. Relat. Phenom. **126**.1 (2002). Special Issue in Honor of Neville V. Smith and Charles Fadley's 60th Birthdays, pp. 163–175. DOI: 10.1016/S0368-2048(02)00150-0 [cited on page 74].

[47] D. M. Eigler and E. K. Schweizer. *Positioning single atoms with a scanning tunnelling microscope*. Nature **344**.6266 (1990), p. 524. DOI: 10.1038/344524a0 [cited on page 1].

[48] U. Fano. *Effects of configuration interaction on intensities and phase shifts*. Phys. Rev. **124**.6 (1961), p. 1866. DOI: 10.1103/PhysRev.124.1866 [cited on page 37].

[49] L. Farinacci et al. *Tuning the Coupling of an Individual Magnetic Impurity to a Superconductor: Quantum Phase Transition and Transport*. Phys. Rev. Lett. **121**.19 (2018), p. 196803. DOI: 10.1103/PhysRevLett.121.196803 [cited on pages 79, 80, 83].

[50] S. Fatayer et al. *Molecular structure elucidation with charge-state control*. Science **365**.6449 (2019), pp. 142–145. DOI: 10.1126/science.aax5895 [cited on page 62].

[51] I. Fernández-Torrente, K. Franke, and J. Pascual. *Vibrational Kondo effect in pure organic charge-transfer assemblies*. Phys. Rev. Lett. **101**.21 (2008), p. 217203. DOI: 10.1103/PhysRevLett.101.217203 [cited on page 105].

[52] I. Fernández-Torrente et al. *Gating the charge state of single molecules by local electric fields*. Phys. Rev. Lett. **108**.3 (2012), p. 036801. DOI: 10.1103/PhysRevLett.108.036801 [cited on pages 20, 72].

[53] R. Feynman. *Plenty of Room at the Bottom" at California Institute of Technology*. 1959 [cited on page 1].

[54] R. P. Feynman. *Simulating physics with computers*. Int. J. Theor. Phys. **21**.6 (1982), pp. 467–488 [cited on page 2].

[55] J. Figgins and D. K. Morr. *Differential conductance and quantum interference in Kondo systems*. Phys. Rev. Lett. **104**.18 (2010), p. 187202. DOI: 10.1103/PhysRevLett.104.187202 [cited on page 100].

[56] M. E. Flatté and J. M. Byers. *Local electronic structure of a single magnetic impurity in a superconductor*. Phys. Rev. Lett. **78**.19 (1997), p. 3761. DOI: 10.1103/PhysRevLett.78.3761 [cited on pages 122, 142].

[57] M. E. Flatté and D. E. Reynolds. *Local spectrum of a superconductor as a probe of interactions between magnetic impurities*. Phys. Rev. B **61**.21 (2000), p. 14810. DOI: 10.1103/PhysRevB.61.14810 [cited on pages 46, 111, 114].

[58] M. E. Flatté and J. M. Byers. *Local Electronic Structure of a Single Magnetic Impurity in a Superconductor*. Phys. Rev. Lett. **78**.19 (1997), pp. 3761–3764. DOI: 10.1103/PhysRevLett.78.3761 [cited on page 142].

[59] M. E. Flatté and J. M. Byers. *Local electronic structure of defects in superconductors*. Phys. Rev. B **56**.17 (1997), pp. 11213–11231. DOI: 10.1103/PhysRevB.56.11213 [cited on page 83].

[60] N. Fournier et al. *Force-controlled lifting of molecular wires.* Phys. Rev. B **84**.3 (2011), p. 035435. DOI: 10.1103/PhysRevB.84.035435 [cited on page 18].

[61] S. Frank and D. Jacob. *Orbital signatures of Fano-Kondo line shapes in STM adatom spectroscopy.* Phys. Rev. B **92**.23 (2015), p. 235127. DOI: 10.1103/PhysRevB.92.235127 [cited on pages 38, 94, 95, 110, 130, 152].

[62] K. J. Franke, G. Schulze, and J. I. Pascual. *Competition of Superconducting Phenomena and Kondo Screening at the Nanoscale.* Science **332**.6032 (2011), pp. 940–944. DOI: 10.1126/science.1202204 [cited on page 89].

[63] K. J. Franke and J. I. Pascual. *Effects of electron–vibration coupling in transport through single molecules.* J. Phys.: Condens. Matter **24**.39 (2012), p. 394002. DOI: 10.1088/0953-8984/24/39/394002 [cited on page 91].

[64] K. J. Franke, G. Schulze, and J. I. Pascual. *Excitation of Jahn- Teller Active Modes during Electron Transport through Single C60 Molecules on Metal Surfaces.* J. Phys. Chem. Lett. **1**.2 (2009), pp. 500–504. DOI: 10.1021/jz900260v [cited on page 73].

[65] K. Franke, G. Schulze, and J. Pascual. *Competition of superconducting phenomena and Kondo screening at the nanoscale.* Science **332**.6032 (2011), pp. 940–944. DOI: 10.1126/science.1202204 [cited on page 47].

[66] K. Giesen et al. *Effective mass of image-potential states.* Phys. Rev. B **35**.3 (1987), p. 975. DOI: 10.1103/PhysRevB.35.975 [cited on page 75].

[67] K. Giesen et al. *Two-photon photoemission via image-potential states.* Phys. Rev. Lett. **55**.3 (1985), p. 300. DOI: 10.1103/PhysRevLett.55.300 [cited on page 75].

[68] F. J. Gießibl. *A direct method to calculate tip–sample forces from frequency shifts in frequency-modulation atomic force microscopy.* Appl. Phys. Lett. **78**.1 (2001), pp. 123–125. DOI: 10.1063/1.1335546 [cited on page 16].

[69] F. J. Giessibl. *Advances in atomic force microscopy.* Rev. Mod. Phys. **75**.3 (2003), p. 949. DOI: 10.1103/RevModPhys.75.949 [cited on page 15].

[70] F. J. Giessibl. *Forces and frequency shifts in atomic-resolution dynamic-force microscopy.* Phys. Rev. B **56**.24 (1997), p. 16010. DOI: 10.1103/PhysRevB.56.16010 [cited on page 14].

[71] V. L. Ginzburg and L. D. Landau. *On the theory of superconductivity.* In: *On Superconductivity and Superfluidity.* Springer, 2009, pp. 113–137 [cited on page 39].

[72] J. M. Gottfried. *Surface chemistry of porphyrins and phthalocyanines.* Surf. Sci. Rep. **70**.3 (2015), pp. 259–379. DOI: 10.1016/j.surfrep.2015.04.001 [cited on pages 49, 90].

[73] L. Gross et al. *Measuring the charge state of an adatom with noncontact atomic force microscopy.* Science **324**.5933 (2009), pp. 1428–1431. DOI: 10.1126/science.1172273 [cited on pages 19, 20].

[74] L. Gross et al. *Organic structure determination using atomic-resolution scanning probe microscopy.* Nat. Chem. **2**.10 (2010), p. 821. DOI: 10.1038/nchem.765 [cited on page 61].

[75] L. Gross et al. *The chemical structure of a molecule resolved by atomic force microscopy.* Science **325**.5944 (2009), pp. 1110–1114. DOI: 10.1126/science.1176210 [cited on pages 17, 18, 61, 62].

[76] M. Gruber, A. Weismann, and R. Berndt. *The Kondo resonance line shape in scanning tunnelling spectroscopy: instrumental aspects*. J. Phys.: Condens. Matter **30**.42 (2018), p. 424001. DOI: 10.1088/1361-648x/aadfa3 [cited on page 38].

[77] H.-M. Guo and M. Franz. *Topological insulator on the kagome lattice*. Phys. Rev. B **80**.11 (2009), p. 113102. DOI: 10.1103/PhysRevB.80.113102 [cited on pages 103, 127].

[78] H. C. Hamaker. *The London—van der Waals attraction between spherical particles*. Physica **4**.10 (1937), pp. 1058–1072. DOI: 10.1016/S0031-8914(37)80203-7 [cited on page 17].

[79] S. K. Hämäläinen et al. *Intermolecular contrast in atomic force microscopy images without intermolecular bonds*. Phys. Rev. Lett. **113**.18 (2014), p. 186102. DOI: 10.1103/PhysRevLett.113.186102 [cited on pages 61, 62].

[80] T.-H. Han et al. *Fractionalized excitations in the spin-liquid state of a kagome-lattice antiferromagnet*. Nature **492**.7429 (2012), p. 406. DOI: 10.1038/nature11659 [cited on pages 103, 127].

[81] P. K. Hansma and J. Kirtley. *Recent advances in inelastic electron tunneling spectroscopy*. Acc. Chem. Res. **11**.12 (1978), pp. 440–445. DOI: 10.1021/ar50132a002 [cited on page 13].

[82] N. Hatter et al. *Scaling of Yu-Shiba-Rusinov energies in the weak-coupling Kondo regime*. Nat. Commun. **8**.1 (2017), p. 2016. DOI: 10.1038/s41467-017-02277-7 [cited on pages 89, 141].

[83] G. Heimel et al. *The interface energetics of self-assembled monolayers on metals*. Acc. Chem. Res. **41**.6 (2008), pp. 721–729. DOI: 10.1021/ar700284q [cited on page 67].

[84] A. J. Heinrich et al. *Single-Atom Spin-Flip Spectroscopy*. Science **306**.5695 (2004), pp. 466–469. DOI: 10.1126/science.1101077 [cited on page 13].

[85] B. W. Heinrich et al. *Protection of excited spin states by a superconducting energy gap*. Nat. Phys. (2013). DOI: 10.1038/nphys2794 [cited on pages 51, 53].

[86] B. W. Heinrich, J. I. Pascual, and K. J. Franke. *Single magnetic adsorbates on s-wave superconductors*. Prog. Surf. Sci. **93**.1 (2018), pp. 1–19. DOI: 10.1016/j.progsurf.2018.01.001 [cited on page 2].

[87] B. W. Heinrich et al. *Change of the magnetic coupling of a metal-organic complex with the substrate by a stepwise ligand reaction*. Nano Lett. (2013). DOI: 10.1021/nl402575c [cited on page 53].

[88] B. W. Heinrich et al. *Control of Oxidation and Spin State in a Single-Molecule Junction*. ACS Nano (2018). DOI: 10.1021/acsnano.8b00312 [cited on pages 53, 143].

[89] B. W. Heinrich et al. *Tuning the Magnetic Anisotropy of Single Molecules*. Nano Lett. (2015). DOI: 10.1021/acs.nanolett.5b00987 [cited on page 53].

[90] J. Helton et al. *Spin dynamics of the spin-1/2 kagome lattice antiferromagnet* $ZnCu_3(OH)_6Cl_2$. Phys. Rev. Lett. **98**.10 (2007), p. 107204. DOI: 10.1103/PhysRevLett.98.107204 [cited on pages 103, 127].

[91] N. Henningsen et al. *Inducing the rotation of a single phenyl ring with tunneling electrons*. J. Phys. Chem. C **111**.40 (2007), pp. 14843–14848. DOI: 10.1021/jp0741861 [cited on page 104].

[92] A. C. Hewson. *The Kondo problem to heavy fermions*. Vol. 2. Cambridge university press, 1997 [cited on pages 33, 36, 37].

[93] W. Ho. *Single-molecule chemistry*. J. Chem. Phys. **117**.24 (2002), pp. 11033–11061. DOI: 10.1063/1.1521153 [cited on pages 13, 73].

[94] I. Horcas et al. *WSXM: a software for scanning probe microscopy and a tool for nanotechnology*. Rev. Sci. Instrum. **78**.1 (2007), p. 013705. DOI: 10.1063/1.2432410 [cited on page 24].

[95] D. Jacob and J. Fernández-Rossier. *Competition between quantum spin tunneling and Kondo effect*. Eur. Phys. J. B **89**.10 (2016), p. 210. DOI: 10.1140/epjb/e2016-70402-2 [cited on page 96].

[96] S. P. Jarvis et al. *Physisorption controls the conformation and density of states of an adsorbed porphyrin*. J. Phys. Chem. C **119**.50 (2015), pp. 27982–27994. DOI: 10.1021/acs.jpcc.5b08350 [cited on page 90].

[97] Y. Jiang et al. *Real-space imaging of Kondo screening in a two-dimensional O2 lattice*. Science **333**.6040 (2011), pp. 324–328. DOI: 10.1126/science.1205785 [cited on page 39].

[98] G.-B. Jo et al. *Ultracold atoms in a tunable optical kagome lattice*. Phys. Rev. Lett. **108**.4 (2012), p. 045305. DOI: 10.1103/PhysRevLett.108.045305 [cited on pages 103, 127].

[99] C. Joachim et al. *Electronic Transparence of a Single* C_{60} *Molecule*. Phys. Rev. Lett. **74**.11 (1995), pp. 2102–2105. DOI: 10.1103/PhysRevLett.74.2102 [cited on page 81].

[100] J. E. Jones. *On the determination of molecular fields.—II. From the equation of state of a gas*. Proc. R. Soc. Lond. A. **106**.738 (1924), pp. 463–477. DOI: 10.1098/rspa.1924.0082 [cited on page 16].

[101] T. Jung, Y. Mo, and F. Himpsel. *Identification of metals in scanning tunneling microscopy via image states*. Phys. Rev. Lett. **74**.9 (1995), p. 1641. DOI: 10.1103/PhysRevLett.74.1641 [cited on page 75].

[102] A. Kahn. *Fermi level, work function and vacuum level*. Mater. Horiz. **3**.1 (2016), pp. 7–10. DOI: 10.1039/C5MH00160A [cited on page 67].

[103] A. Kahn, N. Koch, and W. Gao. *Electronic structure and electrical properties of interfaces between metals and π-conjugated molecular films*. J. Polym. Sci., Part B: Polym. Phys. **41**.21 (2003), pp. 2529–2548. DOI: 10.1002/polb.10642 [cited on page 67].

[104] A. Kamlapure et al. *Investigation of the Yu-Shiba-Rusinov states of a multi-impurity Kondo system*. arXiv preprint arXiv:1911.03794 (2019) [cited on pages 39, 47, 122, 132].

[105] A. Kamlapure et al. *Engineering the spin couplings in atomically crafted spin chains on an elemental superconductor*. Nat. Commun. **9**.1 (2018), p. 3253. DOI: 10.1038/s41467-018-05701-8 [cited on pages 103, 128].

[106] T. Kasuya. *A theory of metallic ferro- and antiferromagnetism on Zener's model*. Prog. Theor. Phys. **16**.1 (1956), pp. 45–57. DOI: 10.1143/PTP.16.45 [cited on page 32].

[107] S. Kezilebieke et al. *Coupled Yu–Shiba–Rusinov states in molecular dimers on NbSe2*. Nano Lett. **18**.4 (2018), pp. 2311–2315. DOI: 10.1021/acs.nanolett.7b05050 [cited on pages 46, 112, 113, 128, 141].

[108] H. Kim et al. *Toward tailoring Majorana bound states in artificially constructed magnetic atom chains on elemental superconductors*. Sci. Adv. **4**.5 (2018), eaar5251. DOI: 10.1126/sciadv.aar5251 [cited on page 103].

[109] Y. Kim, T. Komeda, and M. Kawai. *Single-molecule reaction and characterization by vibrational excitation*. Phys. Rev. Lett. **89**.12 (2002), p. 126104. DOI: 10.1103/PhysRevLett.89.126104 [cited on pages 73, 91].

[110] A. Y. Kitaev. *Unpaired Majorana fermions in quantum wires*. Phys.-Usp. **44**.10S (2001), p. 131. DOI: 10.1070/1063-7869/44/10s/s29 [cited on page 2].

[111] N. Koch et al. *Conjugated organic molecules on metal versus polymer electrodes: Demonstration of a key energy level alignment mechanism*. Appl. Phys. Lett. **82**.1 (2003), pp. 70–72. DOI: 10.1063/1.1532102 [cited on page 67].

[112] N. Kocić et al. *Forces from periodic charging of adsorbed molecules*. J. Chem. Phys. **146**.9 (2017), p. 092327. DOI: 10.1063/1.4975607 [cited on page 18].

[113] N. Kocić et al. *Periodic charging of individual molecules coupled to the motion of an atomic force microscopy tip*. Nano Lett. **15**.7 (2015), pp. 4406–4411. DOI: 10.1021/acs.nanolett.5b00711 [cited on pages 20, 21, 72].

[114] T. Komeda. *Chemical identification and manipulation of molecules by vibrational excitation via inelastic tunneling process with scanning tunneling microscopy*. Prog. Surf. Sci. **78**.2 (2005), pp. 41–85. DOI: 10.1016/j.progsurf.2005.05.001 [cited on page 73].

[115] J. Kondo. *Resistance minimum in dilute magnetic alloys*. Prog. Theor. Phys. **32**.1 (1964), pp. 37–49. DOI: 10.1143/PTP.32.37 [cited on page 36].

[116] S. Krause et al. *Magnetization reversal of nanoscale islands: How size and shape affect the Arrhenius prefactor*. Phys. Rev. Lett. **103**.12 (2009), p. 127202. DOI: 10.1103/PhysRevLett.103.127202 [cited on page 64].

[117] L. Kronik and Y. Morikawa. *Understanding the Metal–Molecule Interface from First Principles*. In: *The Molecule–Metal Interface*. John Wiley & Sons, Ltd, 2013. Chap. 3, pp. 51–89. DOI: 10.1002/9783527653171.ch3 [cited on page 69].

[118] O. Kurnosikov et al. *Long-range electron interferences at a metal surface induced by buried nanocavities*. Phys. Rev. Lett. **102**.6 (2009), p. 066101. DOI: 10.1103/PhysRevLett.102.066101 [cited on page 24].

[119] J. Lambe and R. Jaklevic. *Molecular vibration spectra by inelastic electron tunneling*. Phys. Rev. **165**.3 (1968), p. 821. DOI: 10.1103/PhysRev.165.821 [cited on page 10].

[120] N. Lang. *Spectroscopy of single atoms in the scanning tunneling microscope*. Phys. Rev. B **34**.8 (1986), p. 5947. DOI: 10.1103/PhysRevB.34.5947 [cited on page 11].

[121] M. Langer et al. *Giant frictional dissipation peaks and charge-density-wave slips at the* $NbSe_2$ *surface*. Nat. Mater. **13**.2 (2014), p. 173. DOI: 10.1038/nmat3836 [cited on page 15].

[122] L. Lauhon and W. Ho. *Single-molecule chemistry and vibrational spectroscopy: pyridine and benzene on Cu (001)*. J. Phys. Chem. A **104**.11 (2000), pp. 2463–2467. DOI: 10.1021/jp991768c [cited on pages 73, 91].

[123] E. J. H. Lee et al. *Scaling of subgap excitations in a superconductor-semiconductor nanowire quantum dot*. Phys. Rev. B **95**.18 (2017), p. 180502. DOI: 10.1103/PhysRevB.95.180502 [cited on page 79].

[124] E. J. Lee et al. *Scaling of subgap excitations in a superconductor-semiconductor nanowire quantum dot*. Phys. Rev. B **95**.18 (2017), p. 180502. DOI: 10.1103/PhysRevB.95.180502 [cited on page 44].

[125] E. J. Lee et al. *Spin-resolved Andreev levels and parity crossings in hybrid superconductor–semiconductor nanostructures*. Nat. Nanotechnol. **9**.1 (2014), p. 79. DOI: 10.1038/nnano.2013.267 [cited on page 44].

[126] E. J. Lee et al. *Spin-resolved Andreev levels and parity crossings in hybrid superconductor–semiconductor nanostructures*. Nat. Nanotechnol. **9**.1 (2014), p. 79. DOI: 10.1038/nnano.2013.267 [cited on page 79].

[127] L.-L. Li and E. W.-G. Diau. *Porphyrin-sensitized solar cells*. Chem. Soc. Rev. **42**.1 (2013), pp. 291–304. DOI: 10.1039/C2CS35257E [cited on page 49].

[128] Z. Li et al. *Realization of flat band with possible nontrivial topology in electronic Kagome lattice*. Sci. Adv. **4**.11 (2018), eaau4511. DOI: 10.1126/sciadv.aau4511 [cited on pages 127, 128].

[129] J. S. Lindsey and D. F. Bocian. *Molecules for charge-based information storage*. Acc. Chem. Res. **44**.8 (2011), pp. 638–650. DOI: 10.1021/ar200107x [cited on page 49].

[130] L. Liu et al. *Interplay between energy-level position and charging effect of manganese phthalocyanines on an atomically thin insulator*. ACS Nano **9**.10 (2015), pp. 10125–10132. DOI: 10.1021/acsnano.5b03741 [cited on pages 20, 72].

[131] L. Liu et al. *Revealing the atomic site-dependent g factor within a single magnetic molecule via the extended Kondo effect*. Phys. Rev. Lett. **114**.12 (2015), p. 126601. DOI: 10.1103/PhysRevLett.114.126601 [cited on page 98].

[132] F. London and H. London. *The electromagnetic equations of the supraconductor*. Proc. R. Soc. London, Ser. A **149**.866 (1935), pp. 71–88. DOI: 10.1098/rspa.1935.0048 [cited on page 39].

[133] N. Lorente. *Mode excitation induced by the scanning tunnelling microscope*. Appl. Phys. A **78**.6 (2004), pp. 799–806. DOI: 10.1007/s00339-003-2434-8 [cited on page 91].

[134] S. Loth et al. *Measurement of fast electron spin relaxation times with atomic resolution*. Science **329**.5999 (2010), pp. 1628–1630. DOI: 10.1126/science.1191688 [cited on page 1].

[135] C. Lotze et al. *Driving a macroscopic oscillator with the stochastic motion of a hydrogen molecule*. Science **338**.6108 (2012), pp. 779–782. DOI: 10.1126/science.1227621 [cited on page 15].

[136] V. Madhavan et al. *Tunneling into a single magnetic atom: spectroscopic evidence of the Kondo resonance*. Science **280**.5363 (1998), pp. 567–569. DOI: 10.1126/science.280.5363.567 [cited on page 37].

[137] R. Maurand et al. *First-Order $0-\pi$ Quantum Phase Transition in the Kondo Regime of a Superconducting Carbon-Nanotube Quantum Dot*. Phys. Rev. X **2**.1 (2012), p. 011009. DOI: 10.1103/PhysRevX.2.011009 [cited on page 79].

[138] R. Maurand et al. *First-Order 0- π Quantum Phase Transition in the Kondo Regime of a Superconducting Carbon-Nanotube Quantum Dot*. Phys. Rev. X **2**.1 (2012), p. 011009. DOI: 10.1103/PhysRevX.2.011009 [cited on page 44].

[139] E. Maxwell. *Isotope effect in the superconductivity of mercury*. Phys. Rev. **78**.4 (1950), p. 477. DOI: 10.1103/PhysRev.84.691 [cited on page 40].

[140] F. Meier et al. *Revealing magnetic interactions from single-atom magnetization curves*. Science **320**.5872 (2008), pp. 82–86. DOI: 10.1126/science.1154415 [cited on page 33].

[141] S. Meierott, N. Néel, and J. Kröger. *Spectroscopic Line Shapes of Vibrational Quanta in the Presence of Molecular Resonances*. J. Phys. Chem. Lett. **7**.13 (2016), pp. 2388–2393. DOI: 10.1021/acs.jpclett.6b00923 [cited on page 73].

[142] W. Meissner and R. Ochsenfeld. *Ein neuer effekt bei eintritt der supraleitfähigkeit*. Naturwissenschaften **21**.44 (1933), pp. 787–788. DOI: 10.1007/BF01504252 [cited on page 39].

[143] G. C. Ménard et al. *Two-dimensional topological superconductivity in Pb/Co/Si (111)*. Nat. Commun. **8**.1 (2017), p. 2040. DOI: 10.1038/s41467-017-02192-x [cited on page 103].

[144] T. Meng et al. *Superconducting gap renormalization around two magnetic impurities: From Shiba to Andreev bound states*. Phys. Rev. B **92**.6 (2015), p. 064503. DOI: 10.1103/PhysRevB.92.064503 [cited on page 83].

[145] P. Merino et al. *Exciton dynamics of C 60-based single-photon emitters explored by Hanbury Brown–Twiss scanning tunnelling microscopy*. Nat. Commun. **6** (2015), p. 8461. DOI: 10.1038/ncomms9461 [cited on page 1].

[146] J. Meyer et al. *Influence of organic ligands on the line shape of the Kondo resonance*. Phys. Rev. B **93**.15 (2016), p. 155118. DOI: 10.1103/PhysRevB.93.155118 [cited on page 96].

[147] H. B. Michaelson. *The work function of the elements and its periodicity*. Journal of Applied Physics **48**.11 (1977), pp. 4729–4733. DOI: 10.1063/1.323539 [cited on page 70].

[148] Y. Miyahara, A. Roy-Gobeil, and P. Grutter. *Quantum state readout of individual quantum dots by electrostatic force detection*. Nanotechnology **28**.6 (2017), p. 064001. DOI: 10.1088/1361-6528/aa5261 [cited on page 15].

[149] T. Mizoguchi and M. Udagawa. *Flat-band engineering in tight-binding models: Beyond the nearest-neighbor hopping*. Phys. Rev. B **99**.23 (2019), p. 235118. DOI: 10.1103/PhysRevB.99.235118 [cited on page 127].

[150] C. P. Moca et al. *Spin-resolved spectra of Shiba multiplets from Mn impurities in MgB 2*. Phys. Rev. B **77**.17 (2008), p. 174516. DOI: 10.1103/PhysRevB.77.174516 [cited on page 141].

[151] F. Mohn et al. *Imaging the charge distribution within a single molecule*. Nat. Nanotechnol. **7**.4 (2012), p. 227. DOI: doi:10.1038/nnano.2012.20 [cited on page 18].

[152] M. Moro-Lagares et al. *Real space manifestations of coherent screening in atomic scale Kondo lattices*. Nat. Commun. **10**.1 (2019), p. 2211. DOI: 10.1038/s41467-019-10103-5 [cited on pages 39, 132].

[153] S. Nadj-Perge et al. *Proposal for realizing Majorana fermions in chains of magnetic atoms on a superconductor*. Phys. Rev. B **88**.2 (2013), p. 020407. DOI: 10.1103/PhysRevB.88.020407 [cited on page 103].

[154] S. Nadj-Perge et al. *Observation of Majorana fermions in ferromagnetic atomic chains on a superconductor*. Science **346**.6209 (2014), pp. 602–607. DOI: 10.1126/science.1259327 [cited on pages 46, 103].

[155] K. Nagaoka et al. *Temperature dependence of a single Kondo impurity*. Phys. Rev. Lett. **88**.7 (2002), p. 077205. DOI: 10.1103/PhysRevLett.88.077205 [cited on pages 37, 152, 158].

[156] G. Nazin, X. Qiu, and W. Ho. *Charging and interaction of individual impurities in a monolayer organic crystal*. Phys. Rev. Lett. **95**.16 (2005), p. 166103. DOI: 10.1103/PhysRevLett.95.166103 [cited on pages 20, 72].

[157] T. Neupert et al. *Fractional quantum Hall states at zero magnetic field*. Phys. Rev. Lett. **106**.23 (2011), p. 236804. DOI: 10.1103/PhysRevLett.106.236804 [cited on pages 103, 127].

[158] N. Okabayashi, Y. Konda, and T. Komeda. *Inelastic electron tunneling spectroscopy of an alkanethiol self-assembled monolayer using scanning tunneling microscopy*. Phys. Rev. Lett. **100**.21 (2008), p. 217801. DOI: 10.1103/PhysRevLett.100.217801 [cited on page 73].

[159] L. Olsson et al. *A method for in situ characterization of tip shape in ac-mode atomic force microscopy using electrostatic interaction*. Journal of Applied Physics (1998). DOI: 10.1063/1.368618 [cited on pages 20, 67].

[160] H. K. Onnes. *The superconductivity of mercury*. Leiden Commun. (1911), 120b [cited on page 39].

[161] F. von Oppen, Y. Peng, and F. Pientka. *Topological superconducting phases in one dimension*. Lecture Notes of the Les Houches Summer School: Topological Aspects of Condensed Matter Physics (2017), pp. 387–447. DOI: 10.1093/acprof:oso/9780198785781.003.0009 [cited on pages 43, 46].

[162] G. E. Pacchioni et al. *Two-orbital Kondo screening in a self-assembled metal–organic complex*. ACS Nano **11**.3 (2017), pp. 2675–2681. DOI: 10.1021/acsnano.6b07431 [cited on page 96].

[163] J. I. Pascual et al. *Adsorbate-substrate vibrational modes of benzene on Ag (110) resolved with scanning tunneling spectroscopy*. Phys. Rev. Lett. **86**.6 (2001), p. 1050. DOI: 10.1103/PhysRevLett.86.1050 [cited on pages 73, 91].

[164] L. L. Patera et al. *Mapping orbital changes upon electron transfer with tunnelling microscopy on insulators*. Nature **566**.7743 (2019), p. 245. DOI: 10.1038/s41586-019-0910-3 [cited on page 15].

[165] B. Persson and A. Baratoff. *Inelastic electron tunneling from a metal tip: the contribution from resonant processes*. Phys. Rev. Lett. **59**.3 (1987), p. 339. DOI: 10.1103/PhysRevLett.59.339 [cited on pages 91, 105].

[166] V. D. Pham et al. *Control of molecule–metal interaction by hydrogen manipulation in an organic molecule*. J. Phys. Chem. Lett. **7**.8 (2016), pp. 1416–1421. DOI: 10.1021/acs.jpclett.6b00476 [cited on page 90].

[167] F. Pientka, L. I. Glazman, and F. von Oppen. *Topological superconducting phase in helical Shiba chains*. Phys. Rev. B **88**.15 (2013), p. 155420. DOI: 10.1103/PhysRevB.88.155420 [cited on page 103].

[168] N. A. Pradhan et al. *Atomic scale conductance induced by single impurity charging*. Phys. Rev. Lett. **94**.7 (2005), p. 076801. DOI: 10.1103/PhysRevLett.94.076801 [cited on pages 20, 72].

[169] M. T. Randeria et al. *Scanning Josephson spectroscopy on the atomic scale*. Phys. Rev. B **93**.16 (2016), p. 161115. DOI: 10.1103/PhysRevB.93.161115 [cited on pages 86, 87].

[170] G. Reecht et al. *π-Radical Formation by Pyrrolic H Abstraction of Phthalocyanine Molecules on Molybdenum Disulfide*. ACS Nano (2019). DOI: 10.1021/acsnano.9b02117 [cited on page 91].

[171] G. Reecht et al. *Imaging isodensity contours of molecular states with STM*. New J. Phys. **19**.11 (2017), p. 113033. DOI: 10.1088/1367-2630/aa969a [cited on pages 12, 91].

[172] J. Repp et al. *Controlling the charge state of individual gold adatoms*. Science **305**.5683 (2004), pp. 493–495. DOI: 10.1126/science.1099557 [cited on page 59].

[173] J. Rjabinin and L. Shubnikow. *Magnetic properties and critical currents of supraconducting alloys*. Nature **135**.3415 (1935), p. 581. DOI: 10.1038/135581a0 [cited on page 39].

[174] D. Rolf. *Fundamental properties of atoms and molecules on surfaces*. PhD thesis. Freie Universtiät, 2018 [cited on page 91].

[175] D. Rolf et al. *Correlation of Vibrational Excitations and Electronic Structure with Submolecular Resolution*. J. Phys. Chem. C **123**.12 (2019), pp. 7425–7430. DOI: 10.1021/acs.jpcc.8b11776 [cited on pages 91, 97].

[176] D. Rolf et al. *Visualizing Intramolecular Distortions as the Origin of Transverse Magnetic Anisotropy*. J. Phys. Chem. Lett. **9**.22 (2018), pp. 6563–6567. DOI: 10.1021/acs.jpclett.8b03036 [cited on page 91].

[177] M. Ruby. *SpectraFox: A free open-source data management and analysis tool for scanning probe microscopy and spectroscopy*. SoftwareX **5** (2016), pp. 31–36. DOI: 10.1016/j.softx.2016.04.001 [cited on page 24].

[178] M. Ruby et al. *End states and subgap structure in proximity-coupled chains of magnetic adatoms*. Phys. Rev. Lett. **115**.19 (2015), p. 197204. DOI: 10.1103/PhysRevLett.115.197204 [cited on page 46].

[179] M. Ruby et al. *Experimental demonstration of a two-band superconducting state for lead using scanning tunneling spectroscopy*. Phys. Rev. Lett. **114**.15 (2015), p. 157001. DOI: 10.1103/PhysRevLett.114.157001 [cited on page 24].

[180] M. Ruby et al. *Orbital picture of Yu-Shiba-Rusinov multiplets*. Phys. Rev. Lett. **117**.18 (2016), p. 186801. DOI: 10.1103/PhysRevLett.117.186801 [cited on pages 94, 116, 123, 141].

[181] M. Ruby et al. *Tunneling Processes into Localized Subgap States in Superconductors*. Phys. Rev. Lett. **115**.8 (2015), p. 087001. DOI: 10.1103/PhysRevLett.115.087001 [cited on pages 84, 86, 87].

[182] M. Ruby et al. *Wave-function hybridization in Yu-Shiba-Rusinov dimers*. Phys. Rev. Lett. **120**.15 (2018), p. 156803. DOI: 10.1103/PhysRevLett.120.156803 [cited on pages 46, 111–116, 141].

[183] M. A. Ruderman and C. Kittel. *Indirect exchange coupling of nuclear magnetic moments by conduction electrons*. Phys. Rev. **96**.1 (1954), p. 99. DOI: 10.1038/nphys1514 [cited on page 32].

[184] A. Rusinov. *Superconductivity near a paramagnetic impurity*. JETP Lett. **9** (1969), p. 85 [cited on page 43].

[185] J. E. Sader and S. P. Jarvis. *Accurate formulas for interaction force and energy in frequency modulation force spectroscopy*. Appl. Phys. Lett. **84**.10 (2004), pp. 1801–1803. DOI: 10.1063/1.1667267 [cited on pages 16, 61, 62].

[186] Y. Sainoo et al. *Observation of cis-2-butene molecule on Pd (1 1 0) by cryogenic STM: site determination using tunneling-current-induced rotation*. Surf. Sci. **536**.1-3 (2003), pp. L403–L407. DOI: 10.1016/S0039-6028(03)00564-8 [cited on page 104].

[187] J. Saldaña et al. *Two-Impurity Yu-Shiba-Rusinov States in Coupled Quantum Dots*. arXiv preprint arXiv:1812.09303 (2018) [cited on pages 47, 122].

[188] M. I. Salkola, A. V. Balatsky, and J. R. Schrieffer. *Spectral properties of quasiparticle excitations induced by magnetic moments in superconductors*. Phys. Rev. B **55**.18 (1997), pp. 12648–12661. DOI: 10.1103/PhysRevB.55.12648 [cited on page 83].

[189] J. Schirmer. *Self-Energy and the Dyson Equation*. In: *Many-Body Methods for Atoms, Molecules and Clusters*. Cham: Springer International Publishing, 2018, pp. 111–134. DOI: 10.1007/978-3-319-93602-4_8 [cited on page 14].

[190] M. Schmid et al. *Quantum Wells and Electron Interference Phenomena in Al due to Subsurface Noble Gas Bubbles*. Phys. Rev. Lett. **76**.13 (1996), pp. 2298–2301. DOI: 10.1103/PhysRevLett.76.2298 [cited on page 24].

[191] J. R. Schrieffer and P. A. Wolff. *Relation between the anderson and kondo hamiltonians*. Phys. Rev. **149**.2 (1966), p. 491. DOI: 10.1103/PhysRev.149.491 [cited on page 34].

[192] B. Schuler et al. *Contrast formation in Kelvin probe force microscopy of single π-conjugated molecules*. Nano Lett. **14**.6 (2014), pp. 3342–3346. DOI: 10.1021/nl500805x [cited on page 18].

[193] S. Seiro et al. *Evolution of the Kondo lattice and non-Fermi liquid excitations in a heavy-fermion metal*. Nat. Commun. **9**.1 (2018), p. 3324. DOI: 10.1038/s41467-018-05801-5 [cited on page 39].

[194] H. Shiba. *Classical spins in superconductors*. Prog. Theor. Phys. **40**.3 (1968), pp. 435–451. DOI: 10.1143/PTP.40.435 [cited on page 43].

[195] N. Shirato et al. *Elemental fingerprinting of materials with sensitivity at the atomic limit*. Nano letters **14**.11 (2014), pp. 6499–6504. DOI: 10.1021/nl5030613 [cited on page 1].

[196] R. R. Singh and D. A. Huse. *Ground state of the spin-1/2 kagome-lattice Heisenberg antiferromagnet*. Phys. Rev. B **76**.18 (2007), p. 180407. DOI: 10.1103/PhysRevB.76.180407 [cited on pages 103, 127].

[197] W. Steurer et al. *Manipulation of the charge state of single Au atoms on insulating multilayer films*. Phys. Rev. Lett. **114**.3 (2015), p. 036801. DOI: 10.1103/PhysRevLett.114.036801 [cited on page 18].

[198] B. C. Stipe, M. A. Rezaei, and W. Ho. *Single-Molecule Vibrational Spectroscopy and Microscopy*. Science **280**.5370 (1998), pp. 1732–1735. DOI: 10.1126/science.280.5370.1732 [cited on page 13].

[199] B. Stipe, M. Rezaei, and W. Ho. *Inducing and viewing the rotational motion of a single molecule*. Science **279**.5358 (1998), pp. 1907–1909. DOI: 10.1126/science.279.5358.1907 [cited on page 104].

[200] D. Straub and F. Himpsel. *Spectroscopy of image-potential states with inverse photoemission*. Phys. Rev. B **33**.4 (1986), p. 2256. DOI: 10.1103/physrevb.33.2256 [cited on page 75].

[201] J. A. Stroscio, R. Feenstra, and A. Fein. *Electronic structure of the Si (111) 2× 1 surface by scanning-tunneling microscopy*. Phys. Rev. Lett. **57**.20 (1986), p. 2579. DOI: 10.1103/PhysRevLett.57.2579 [cited on page 11].

[202] K. Sugawara et al. *Interaction of Stark-shifted image potential states with quantum well states in ultrathin Ag(111) islands on Si(111)-$\sqrt{3} \times \sqrt{3}$−B substrates*. Phys. Rev. B **96**.7 (2017), p. 075444. DOI: 10.1103/PhysRevB.96.075444 [cited on page 75].

[203] Y. Sugimoto et al. *Chemical identification of individual surface atoms by atomic force microscopy*. Nature (2007). DOI: 10.1038/nature05530 [cited on page 61].

[204] K. Sun et al. *Nearly flatbands with nontrivial topology*. Phys. Rev. Lett. **106**.23 (2011), p. 236803. DOI: 10.1103/PhysRevLett.106.236803 [cited on pages 103, 127].

[205] Z. Sun et al. *Quantitative atomic force microscopy with carbon monoxide terminated tips*. Phys. Rev. Lett. **106**.4 (2011), p. 046104. DOI: 10.1103/PhysRevLett.106.046104 [cited on page 18].

[206] I. Swart, T. Sonnleitner, and J. Repp. *Charge state control of molecules reveals modification of the tunneling barrier with intramolecular contrast*. Nano Lett. **11**.4 (2011), pp. 1580–1584. DOI: 10.1021/nl104452x [cited on page 59].

[207] E. Tang, J.-W. Mei, and X.-G. Wen. *High-temperature fractional quantum Hall states*. Phys. Rev. Lett. **106**.23 (2011), p. 236802. DOI: 10.1103/PhysRevLett.106.236802 [cited on pages 103, 127].

[208] M. Ternes. *Spin excitations and correlations in scanning tunneling spectroscopy*. New J. Phys. **17**.6 (2015), p. 063016. DOI: 10.1088/1367-2630/17/6/063016 [cited on page 14].

[209] M. Ternes, A. J. Heinrich, and W.-D. Schneider. *Spectroscopic manifestations of the Kondo effect on single adatoms*. J. Phys.: Condens. Matter **21**.5 (2008), p. 053001. DOI: 10.1088/0953-8984/21/5/053001 [cited on pages 37, 110].

[210] M. Ternes et al. *Subgap structure in asymmetric superconducting tunnel junctions*. Phys. Rev. B **74**.13 (2006), p. 132501. DOI: 10.1103/PhysRevB.74.132501 [cited on page 86].

[211] J. Tersoff and D. Hamann. *Theory and application for the scanning tunneling microscope*. Phys. Rev. Lett. **50**.25 (1983), p. 1998. DOI: 10.1103/PhysRevLett.50.1998 [cited on page 9].

[212] M. Tinkham. *Introduction to superconductivity*. Courier Corporation, 2004 [cited on pages 40–42].

[213] P. Townsend and J. Sutton. *Investigation by electron tunneling of the superconducting energy gaps in nb, ta, sn, and pb*. Phys. Rev. **128**.2 (1962), p. 591. DOI: 10.1103/PhysRev.128.591 [cited on page 144].

[214] S. Trishin et al. *Resolution of intramolecular dipoles and the push-back effect of individual molecules on a metal surface*. in preparation [cited on page 67].

[215] N. Tsukahara et al. *Evolution of Kondo resonance from a single impurity molecule to the two-dimensional lattice*. Phys. Rev. Lett. **106**.18 (2011), p. 187201. DOI: 10.1103/PhysRevLett.106.187201 [cited on pages 39, 132].

[216] O. Újsághy et al. *Theory of the Fano resonance in the STM tunneling density of states due to a single Kondo impurity*. Phys. Rev. Lett. **85**.12 (2000), p. 2557. DOI: 10.1103/PhysRevLett.85.2557 [cited on pages 96, 110].

[217] C. Wagner et al. *Scanning quantum dot microscopy*. Phys. Rev. Lett. **115**.2 (2015), p. 026101. DOI: 10.1103/PhysRevLett.115.026101 [cited on page 18].

[218] P. Wahl et al. *Exchange interaction between single magnetic adatoms*. Phys. Rev. Lett. **98**.5 (2007), p. 056601. DOI: 10.1103/PhysRevLett.98.056601 [cited on page 33].

[219] P. Wahl et al. *Quantum coherence of image-potential states*. Phys. Rev. Lett. **91**.10 (2003), p. 106802. DOI: 10.1103/PhysRevLett.91.106802 [cited on page 75].

[220] W. Wang et al. *Intramolecularly resolved Kondo resonance of high-spin Fe (II)-porphyrin adsorbed on Au (111)*. Phys. Rev. B **91**.4 (2015), p. 045440. DOI: 10.1103/PhysRevB.91.045440 [cited on page 91].

[221] W. Weinberg. *Inelastic electron tunneling spectroscopy: a probe of the vibrational structure of surface species*. Annu. Rev. Phys. Chem. **29**.1 (1978), pp. 115–139. DOI: 10.1146/annurev.pc.29.100178.000555 [cited on page 13].

[222] H. Yamada, T. Shimada, and A. Koma. *Preparation and magnetic properties of manganese (II) phthalocyanine thin films*. J. Chem. Phys. **108**.24 (1998), pp. 10256–10261. DOI: 10.1063/1.476486 [cited on page 32].

[223] N. Y. Yao et al. *Enhanced antiferromagnetic exchange between magnetic impurities in a superconducting host*. Phys. Rev. Lett. **113**.8 (2014), p. 087202. DOI: 10.1103/PhysRevLett.113.087202 [cited on page 129].

[224] N. Y. Yao et al. *Phase diagram and excitations of a Shiba molecule*. Phys. Rev. B **90**.24 (2014), p. 241108. DOI: 710.1103/PhysRevB.90.241108 [cited on pages 47, 122].

[225] A. Yella et al. *Porphyrin-sensitized solar cells with cobalt (II/III)–based redox electrolyte exceed 12 percent efficiency*. Science **334**.6056 (2011), pp. 629–634. DOI: 10.1126/science.1209688 [cited on page 49].

[226] K. Yosida. *Magnetic properties of Cu-Mn alloys*. Phys. Rev. **106**.5 (1957), p. 893. DOI: 10.1103/PhysRev.106.893 [cited on page 32].

[227] L. Yu. *Bound state in superconductors with paramagnetic impurities*. Acta Phys. Sin **21**.1 (1965), pp. 75–91 [cited on page 43].

[228] R. Žitko. *Numerical subgap spectroscopy of double quantum dots coupled to superconductors*. Phys. Rev. B **91**.16 (2015), p. 165116. DOI: 10.1103/PhysRevB.91.165116 [cited on pages 47, 122].

[229] R. Žitko, O. Bodensiek, and T. Pruschke. *Effects of magnetic anisotropy on the subgap excitations induced by quantum impurities in a superconducting host*. Phys. Rev. B **83**.5 (2011), p. 054512. DOI: 10.1103/PhysRevB.83.054512 [cited on page 47].

[230] R. Zhang et al. *Chemical mapping of a single molecule by plasmon-enhanced Raman scattering*. Nature **498**.7452 (2013), p. 82. DOI: 10.1038/nature12151 [cited on page 1].

[231] Y.-h. Zhang et al. *Temperature and magnetic field dependence of a Kondo system in the weak coupling regime*. Nat. Commun. **4** (2013), p. 2110. DOI: 10.1038/ncomms3110 [cited on pages 110, 152, 158].

[232] L. Zhou et al. *Strength and directionality of surface Ruderman–Kittel–Kasuya–Yosida interaction mapped on the atomic scale*. Nat. Phys. **6**.3 (2010), p. 187. DOI: 10.1038/nphys1514 [cited on page 33].

List of Publications

L. Farinacci, G. Ahmadi, G. Reecht, M. Ruby, N. Bogdanoff, O. Peters, B. W. Heinrich, F. von Oppen, K. J. Franke, *Tuning the Coupling of an Individual Magnetic Impurity to a Superconductor: Quantum Phase Transition and Transport*, Phys. Rev. Lett. **121**, 196803 (2018)

L. Farinacci, G. Ahmadi, M. Ruby, G. Reecht, B. W. Heinrich, C. Czekelius, F. von Oppen, K. J. Franke, *Interfering tunneling paths through magnetic molecules on superconductors: Asymmetries of Kondo and Yu-Shiba-Rusinov resonances*, in preparation

Conference Contributions

2015

598^{th} WE-Heraeus Seminar, Frontiers in Scanning Probe Microscopy
Bad Honnef, Germany *2 Nov. - 5 Nov.*
poster Polymerization and metallation of porphin molecules on Au(111)

2016

DPG Spring Meeting of the Condensed Matter Section
Regensburg, Germany *6 Mar. - 11 Mar.*
poster Inelastic spin excitations and many-body effects in Fe-porphins

DIPC Workshop, Spins on Surfaces (SoS)
San Sebastian, Spain *5 Sep. - 9 Sep.*
talk From weak to strong Kondo coupling

2017

DPG Spring Meeting of the Condensed Matter Section
Dresden, Germany *19 Mar. - 24 Mar.*
poster Yu-Shiba-Rusinov states and inelastic excitations in Fe-porphine molecules on Pb(111)

MPI Workshop,
Exotic New States in Superconducting Devices: The Age of the Interface
Mainz, Germany *25 Sep. - 28 Sep.*
poster Yu-Shiba-Rusinov States of Iron Porphin molecules on Pb(111)

654^{th} WE-Heraeus Seminar,
Topical Insights into Nanoscience using Scanning Probes
Bad Honnef, Germany *19 Nov. - 23 Nov.*
poster Electronic properties of Fe-porphin molecules on Pb(111)

2018

IMPRS Workshop, From Models to Reality
Tegernsee, Germany *19 Feb. - 23 Feb.*
poster Coupling of Yu-Shiba-Rusinov States in a Molecular Lattice

DPG Spring Meeting of the Condensed Matter Section
Berlin, Germany *11 Mar. - 16 Mar.*
talk Tuning a Yu-Shiba-Rusinov state across a quantum phase transition

MPI Workshop,
New Platforms for Topological Superconductivity with Magnetic Atoms
Dresden, Germany *9 Apr. - 11 Apr.*
poster Coupling of Yu-Shiba-Rusinov states in a molecular lattice

SPSTM-7 LTSPM-1,
Advances in High-Precision and Low-Temperature Scanning Probe Microscopy
Nijmegen, Netherlands *28 Jul. - 30 Jul.*
poster Coupling of Yu-Shiba-Rusinov states in a molecular lattice

DIPC Workshop, Spins on Surfaces (SoS II)
San Sebastian, Spain *10 Sep. - 14 Sep.*
poster Coupling of Yu-Shiba-Rusinov states in a molecular lattice

Condensed Matter research group - Centre de Pysique Théorique - Institut polythechnique
Saclay, France *09. Oct*
invited talk Quantum phase transition and transport in Fe porphin molecules on Pb(111)

2019

DPG Spring Meeting of the Condensed Matter Section
Regensburg, Germany *31 Mar. - 5 Apr.*
talk Tuning the coupling of an individual magnetic impurity to a superconductor: quantum phase transition and transport
talk Proximity effects of a STM tip on the magnetic properties of Fe-porphyrin on Au(111)

MPI Workshop, Bound states in superconductors and interfaces
Dresden, Germany *8 Apr. - 10 Apr.*
talk Tuning the coupling of an individual magnetic impurity to a superconductor: quantum phase transition and transport

Journées du STM 2019, Microscopie et spectroscopie à effet tunnel
Palaiseau, France *6 Jun. - 7 Jun.*
talk Contrôle du couplage entre une impureté magnétique et un supraconducteur : transition de phase quantique et transport

IVC-21
Malmö, Sweden *1 Jul. - 5 Jul.*
talk Tuning the coupling of an individual magnetic impurity to a superconductor: quantum phase transition and transport

Otte Lab, Department of Quantum Nanoscience, TU Delft
Delft, Netherlands *12 Jul.*
invited talk Investigation of Yu-Shiba-Rusinov states in a molecular network: quantum phase transition, transport and coupling phenomena

Acknowledgements

L'essentiel est invisible pour les yeux

Le Petit Prince
Antoine de Saint-Exupéry

My journey to Berlin transformed circumstantially into an exploration of research and I am grateful to the persons who guided and supported me along its sinuous paths.

First and foremost, thank you Katharina. If it was not for you, I would probably never have imagined how lively and joyful research can be. Your devotion is inspiring and your kindness galvanize everyone around you to give the best of themselves. If magic starts somewhere, it must be there. Thank you for your openness and your patience, for listening to my myriad of ideas and theories, and for listening to me. My thanks go next to Wolfgang Kuch, for agreeing to be my second supervisor and his regular interest in my research work. Thank you as well for organizing the exchange program through which I first came to Berlin. I am also very appreciative of the theory support that Felix von Oppen gave us concerning the quantum phase transition and transport processes involving a Shiba state.

I received a great amount of help from Gaël Reecht, especially in the lab. You were always there when all sort of unexpected issues happened, providing a needed hand and an open ear, always ready to use to your expertise in blindly but exactly guessing an evaporation temperature or making the perfect tip forming! Besides that, thank you for always offering to help, reminding me that things do not always have to be complicated and thank you for becoming a good friend. Next I want to thank Christian Lotze. It is not too much to say that the labs would fall apart without you, and I have really appreciated to learn a tiny amount of your knowledge, that you are always sharing with great simplicity. The bubble would not be complete without Idan Tamir, with whom it was really nice to work within the last months. I really appreciated your wise and thoughtful pieces of advice, carefully provided with a pinch of sarcasm.

I believe that when I will think back of my time here in Berlin I will still hear some burst of laughter coming from my office. It was an honor to found the Kindergarten Office with Michael Ruby who always had time to play a few tricks while doing great research and having a neat time-schedule. And it was just great to continue it with Rika Simon (whose time-schedule might be less regular ;p), with whom it was so enlightening to share all sort of stories. I am really pleased I was your supervisor during your bachelor thesis and that you joined the office when you came back. It was so much fun to be around your calm, witty and ever so slightly sarcastic mind! Thank you especially for your support in the last months and the very last days, doing magic with LaTeX, proof-reading thoroughly consequent parts of this thesis and keeping me sane, or just the right amount of insane, when I started to be slightly (?) overwhelmed with stress. Johanna Richter made writing a lot easier by

sharing its burden along my side, beaming with optimism and full of ingenuity. Somehow, the Kindergarten Office would not be complete without Nils Bogdanoff, who never had his official desk here (that might have saved us from a total chaos) but whose irregular and frequent visits always bring some unforeseeable entertainment and who is always eager to share some more genius ideas. I would also like to mention Guoda Treciokaite, whom it was a pleasure to supervise during her bachelor thesis, and Jennifer Hartfiel who joined the office lately and whose personality fits just perfectly. Good luck to Rika and Jenny with keeping angry Pikachu happy despite Sergey Trishin's baseball training, the sweets provision running and Angus (and the other plant) alive, since its numerous predecessors (the mimosa, the chili, Vincent and Taylor) had relatively short but definitely happy lives here. Finally I want to thank Eva Liebhaber, for being the best, friend I had in Berlin. I will miss your everlasting smile and cheerful spirit, you were a great and valued colleague at work and will stay a close and cherished friend. And finally thanks to all former and current members of the AG Franke, for contributing to the somehow magical spirit around here, full of coffee, volleyball, cake, ice-cream and whatever clubs!

Finally I would like to thank my family and friends without whom I would not be half the person I am today. Thanks for bringing to my life burst of joy and stream of happiness through the nice but also the hard times.

Selbstständigkeitserklärung

Hiermit erkläre ich die vorliegende Arbeit selbstständig und ohne Zuhilfenahme von nicht angegebenen Quellen angefertigt zu haben. Wörtlich oder sinngemäß übernommene Stellen sind als solche gekennzeichnet. Zudem erkläre ich, dass diese Arbeit in keinem früheren Promotionsverfahren eingereicht und dort angenommen oder für ungenügend befunden wurde.

Berlin, den 18.12.2019

_____

Laëtitia Farinacci